Technische Universität Braunschweig

Thilo Viereck

Magnetic Particle Imaging

Applications of magnetic nanoparticles for analytics and imaging

Dissertation
Braunschweig 2015

Berichte aus dem **Institut für Elektrische Messtechnik und Grundlagen der Elektrotechnik**

Band 53

Hrsg. Prof. Dr. Meinhard Schilling

Magnetic Particle Imaging

Applications of magnetic nanoparticles for analytics and imaging

Von der Fakultät für Elektrotechnik, Informationstechnik, Physik
der Technischen Universität Carolo-Wilhelmina zu Braunschweig

zur Erlangung des Grades eines Doktors
der Ingenieurwissenschaften (Dr.-Ing.)

genehmigte Dissertation

von	Thilo Viereck (geb. Wawrzik)
aus	Wolfsburg

eingereicht am:	25.06.2015
mündliche Prüfung am:	04.12.2015
1. Referent:	Prof. Dr. rer. nat. Meinhard Schilling
2. Referent:	Prof. Dr. rer. nat. Olaf Dössel
Druckjahr:	2016

Dissertation an der Technischen Universität Braunschweig,
Fakultät für Elektrotechnik, Informationstechnik, Physik

Kurzfassung

Magnetic Particle Imaging (MPI) ist eine relativ neue Bildgebungsmodalität, die Volumenbilder mit hoher räumlicher und zeitlicher Auflösung liefert. Als Marker-basiertes Verfahren gehört es in eine Gruppe mit nuklear-medizinischen Bildgebungstechniken, wie der Positronen-Emissions-Tomographie (PET) oder der Einzelphotonen-Emissions-Computertomographie (SPECT). Im Gegensatz zu diesen Verfahren benötigt MPI aber keine potentiell schädigende ionisierende Strahlung. Außerdem liefert die Methode räumliche Auflösungen im Millimeter-Bereich und zeitliche Auflösungen im Sekundenbereich oder sogar Echtzeitfähigkeit. In dieser Hinsicht ist MPI eher vergleichbar mit den klinischen Standard-Verfahren, wie der Magnetresonanztomographie (MRT) und der Computertomographie (CT). Die Eigenschaften des nanopartikulären Markers, der im Bildgebungsvolumen anwesend einen Bildkontrast generiert, haben dabei direkten Einfluss auf die MPI-Performance. Die Magnetisierungsdynamik der superparamagnetischen Nanopartikel ist auch ein entscheidender Faktor im MPI Systemdesign. Ein eingehendes Verständnis und die numerische Modellierung der Partikel-Magnetisierungsdynamik kann ein Schlüssel zur Realisierung von funktionaler Bildgebung im MPI sein, die auf einer möglichen Funktionalisierung der Partikel beruht. Die Option einer Modifizierung der Tracer-Oberfläche zur spezifischen Bindung an Zellproteinen, Antigenen oder anderen chemischen oder biologischen Strukturen in Kombination mit der Detektion dieser Marker im Körper durch MPI eröffnet vielfältige Möglichkeiten in der zukünftigen medizinischen Forschung.

Diese Arbeit beschreibt die Entwicklung eines Magnetic Particle Imaging Scanners und der dazugehörigen Charakterisierungstechnik, der Magnetic Particle Spectroscopy (MPS). Die Geräte wurden dabei entwickelt, gebaut und getestet, um Einblicke in die Partikeldynamik zu geben und um als Prototyp-Plattform für die MPI-Forschung zu dienen. Das schließt sowohl die Scanner-Hardware als auch die Software zur Modellierung der dynamischen Partikelantwort und zur Bildrekonstruktion ein. Der Fokus liegt hierbei auf der Entwicklung des sogenannten 'Mobility MPI' (mMPI), welches eine Bestimmung der Partikelbeweglichkeit zusätzlich zur konventionellen konzentrations-gewichteten MPI-Bildgebung zulässt. Die Partikelbeweglichkeit umfasst dabei den hydrodynamischen Durchmesser der Partikel und die Viskosität des sie umgebenden Mediums. Durch die

Unterscheidung von Néel'schen und Brown'schen Beiträgen zur Magnetisierung ermöglicht mMPI in Verbindung mit einem geeigneten Marker die Bindungsdetektion im Bildgebungsvolumen.

Als Vorbereitung auf die abschließende Realisierung von mMPI werden das Harmonischen-Spektrum und die dynamische Magnetisierungsantwort des MPI-Markers im MPS untersucht. Außerdem wird die Durchführung von Bio-Assays auf der Basis von MPS erkundet, und die Ergebnisse werden mit entsprechenden numerischen Modellen verglichen, wobei ein einfaches Magnetisierungsmodell zur Beschreibung der komplex-wertigen Harmonischen in Abhängigkeit von der Partikelbeweglichkeit eingeführt wird. Darüber hinaus wird der Einfluss der Viskosität auf die MPI System-Matrix analysiert und verschiedene Ansätze zur Ableitung der Mobilitätsinformation der Partikel aus den MPI Messdaten untersucht.

Schließlich zeigt sich, dass nach bisheriger Einschätzung eine direkte Zeitbereichs-Auswertung des MPI-Signals die besten Aussichten auf Realisierung des mMPI-Verfahrens verspricht, da es sowohl die räumliche Partikelverteilung als auch den Mobilitätszustand der Partikel zugänglich macht.

Abstract

Magnetic Particle Imaging (MPI) is recognized as a relatively new imaging modality, that delivers tracer-based images with high spatial and temporal resolution. It is in class with nuclear medicine tomographic imaging techniques, i.e. positron emission tomographie (PET) and single-photon emission computed tomography (SPECT), but unlike these methods no potentially harmful radiation is involved in MPI and the method delivers spatial resolution in the millimeter regime and temporal resolution in the order of seconds or even real-time capability. In that regard, MPI is closer to clinical standard modalities, i.e. magnetic resonance imaging (MRI) and computed tomography (CT). The properties of the nanoparticular tracer, that needs to be present in the imaging volume for MPI to render image contrast, have direct impact on the MPI performance. The dynamics of the superparamagnetic nanoparticles are a critical factor in MPI system design. However, once understood and numerically modelled the particle's magnetization dynamics are key to enabling functional imaging with MPI based on particle functionalization. The ability to modify the surface of the tracer to specifically bind to cell proteins, antigenes or other chemical or biological substances and to detect those markers in the body opens a huge opportunity for future medical research.

This thesis describes the development of a magnetic particle imaging scanner and its accompanying particle characterization technique, magnetic particle spectroscopy (MPS). The devices have been designed, build and tested to deliver insights into particle dynamics and to function as a prototype platform for MPI research. That includes the scanner hardware as well as the software for modelling of the particle's magnetization response and image reconstruction. The main focus is on the development and evolution of the so called 'Mobility MPI' (mMPI), that promises to provide an estimate of the particle mobility, including the hydrodynamic diameter of the particles and the viscosity of the surrounding medium, in addition to the standard concentration-weighted MPI image. By allowing a discrimination between Néel and Brownian contributions, mMPI in conjunction with a suitable tracer enables binding detection in the imaging volume.

In preparation for a final mMPI demonstration, the harmonic spectrum connected with the dynamic magnetization response of the tracer is studied in MPS. The ability for conducting bio-assays with MPS is explored

and the results are compared and evaluated in context of appropriate numerical models, introducing a simple magnetization model that describes the complex-valued harmonics as a function of the particle mobility. Furthermore, the effect of viscosity on the MPI system matrix is studied and different approaches for deducing mobility information from an MPI experiment are investigated.

In summary, the direct time-domain evaluation of the MPI signal seems most promising for the realization of mMPI as it captures both the spatial particle distribution and the mobility state of the particles.

Glossary

ABS	acrylonitrile butadiene styrene
ACS	ac susceptometry
BA	biotin-agarose
BPF	band-pass filter
BSF	band-stop filter
CAD	computer-aided design
CT	computed tomography
DLF	Deutschlandfunk (german world service, radio station)
DNA	deoxyribonucleic acid
ELISA	enzyme-linked immunosorbent assay
EMG	Institut für Elektrische Messtechnik und Grundlagen der Elektrotechnik Institute of Electrical Measurements and Fundamental Electrical Engineering
FD	freeze dried
FEMM	finite element method magnetics (software)
FFL	field-free line
FFP	field-free point (→ Sec. 4)
FFT	fast Fourier transform
FOV	field of view (→ Sec. 4.1)
FWHM	full-width at half-maximum
LLG	Landau-Lifshitz-Gilbert equation
LTI	linear and time invariant
MIA	magnetic immunoassays
MNP	magnetic nanoparticles (→ Sec. 2)

MPI	magnetic particle imaging (→ Sec. 4)
mMPI	mobility magnetic particle imaging
MPS	magnetic particle spectroscopy (→ Sec. 3)
MRI	magnetic resonance imaging
fMRI	functional magnetic resonance imaging
MRX	magnetorelaxometry
NI	National Instruments (company)
NMR	nuclear magnetic resonance
ODE	ordinary differentiell equation
PA	power amplifier
PCR	polymerase chain reaction
PEEK	polyetheretherketone
PET	positron emission tomography
PSD	particle size distribution
PSF	point spread function
PVC	polyvinylchloride
RBF	radial basis function
SAR	specific absorption rate
SBR	signal-to-background ratio
SD	single-domain
SNR	signal-to-noise ratio
SP	superparamagnetic
SPECT	single-photon emission computed tomography
SPIO	superparamagnetic iron oxide particle
SVD	singular value decomposition
TEM	transmission electron microscopy
ULNA	(ultra) low noise amplifier

Symbols

$\boldsymbol{A}$	1	system matrix
a_{2k+1}	1	odd cosine series coefficients
a_n	1	n-th cosine Fourier coefficients
α	1	prefactor for the real part of the susceptibility
α	1	damping constant ($\rightarrow$ Sec. 2)
B	T	magnetic flux density
$\boldsymbol{b}$	1	signal vector
b_n	1	n-th sine Fourier coefficients
b_{noise}	1	noise distribution in the detection signal
β	1	prefactor for the imaginary part of the susceptibility
β	1	parameter of the model curve ($\rightarrow$ Sec. 2)
C_p	F	parallel capacity
c	mol/L	concentration
χ	1	magnetic susceptibility
$\chi 0$	1	initial or dc susceptibility
χ_n	1	susceptibility of n-th harmonic frequency
d	nm	particle diameter
$d_{\mathbf{c}}$	nm	particle core diameter
$d_{\mathbf{h}}$	nm	particle hydrodynamic diameter
d_s	nm	thickness of particle shell
E	J	energy
E_t	1	error term
e	1	principal direction
e^{μ}	1	geometric mean
e^{σ}	1	geometric standard deviation
η	Pa s	dynamic viscosity
ε	1	scaling exponent
F	1	frequency spectrum $F(\omega)$ / spectral component
F_n	1	n-th spectral component
f	Hz	frequency
f_{rep}	Hz	repetition frequency
f_{test}	Hz	test frequency
f_0	Hz	base frequency
G	T/m	gradient
γ	rad/sT	gyromagnetic ratio ($\frac{\gamma}{2\pi} = 28.025 \times 10^9$ Hz/T)
H	A/m	magnetic field
H_{AC}	A/m	ac field strength or excitation amplitude

H_C	A/m	coercitivity or critical field
H_DC	A/m	static field strength
H_FF	A/m	focus field strength/amplitude
H_GF	A/m	gradient (or selection) field strength
H_V	A/m	effective field strength
H_typ	A/m	typical field strength
H_0	A/m	equilibrium field strength/amplitude
K	$\mathrm{J/m^3}$	anisotropy constant
k	m/A	k factor ($= \mu_0 m / k_\mathrm{B} T$)
$k_\mathbf{B}$	J/K	vacuum permeability (1.38×10^{-23} J/K)
κ	1/m	reciprocal field of view ($= G/\mu_0 H_\mathrm{x}$)
L	1	Langevin function of superparamagnetism
L_s	H	series inductance
L_0	1	initial slope of the Langevin function
M	A/m	magnetization
M_R	A/m	remanent magnetization
M_S	A/m	saturation magnetization
M_V	A/m	virtual field magnetization
M_0	A/m	equilibrium magnetization
M_1	A/m	magnetization of the fundamental frequency
$M_{2\mathrm{k}+1}$	A/m	magnetization of odd harmonics
M_n	A/m	magnetization of n-th harmonic frequency
m	$\mathrm{A/m^2}$	magnetic moment
N	1	particle number
N_A	1/mol	Avogadro constant (6.022×10^{23} 1/mol)
n_d	$\mathrm{1/m^3}$	particle number density
ω	Hz	excitation angular frequency ($= 2\pi f$)
ω_0	Hz	base excitation angular frequency ($= 2\pi f_0$)
P	V A	power dissipation
p_i	1	finite probability
$\Phi_\mathbf{B}$	Wb	magnetic flux
R_p	Ω	parallel resistance
R_s	Ω	series resistance
$S(x)$	1	spatial sensitivity profile of a coil
S_x	1	coil sensitivity
$\sigma_\mathbf{c}$	1	standard deviation of particle core diameter
$\sigma_\mathbf{h}$	1	standard deviation of particle hydrodynamic diameter
T	K	temperature
T_rep	s	repetition period of Lissajous trajectory
τ	s	time constant
$\tau_\mathbf{B}$	s	Brownian time constant
$\tau_\mathbf{N}$	s	Néel time constant
$\tau_\mathbf{eff}$	s	effective time constant
$\tau_\parallel$	s	parallel part of time constant
$\tau_\perp$	s	perpendicular part of time constant
θ	°	field angle with easy axis
$U_\mathbf{ind}$	V	induced voltage

$\mu_\mathbf{0}$	T m/A	vacuum permeability ($4\pi \times 10^{-7}$ Vs/Am)
$\mu_\mathbf{c}$	nm	mean particle core diameter
$\mu_\mathbf{r}$	1	relative permeability
V	m^3	volume ($1\,\mu L = 1\,mm^3$)
$V_\mathbf{c}$	m^3	particle core volume
$V_\mathbf{h}$	m^3	particle hydrodynamic volume
$V_\mathbf{P}$	m^3	particle volume
v_f	1	particle volume fraction
$\bar{v}_\mathrm{f}$	1	particle volume fraction of aggregates
$\boldsymbol{x}$	m	spatial point vector
$\boldsymbol{x}_\mathbf{center}$	m	vector to FOV center
$x_\mathbf{i}$	1	harmonic index (MPS)
$\dot{x}$	m/s	FFP velocity
ξ	1	ξ factor ($= kH$)
$y_\mathbf{i}$	1	spectral amplitude of the harmonics

Contents

1 Introduction

Magnetic Particle Imaging (MPI) is a relativly new imaging modality that provides high spatial and temporal resolution [1–8]. As a tracer-based method, image contrast is mediated by a nanoparticular tracer in the imaging volume, whose nonlinear magnetization curve is exploited to generate a signal. It is in class with nuclear medicine tomographic imaging techniques, i.e. positron emission tomography (PET) and single-photon emission computed tomography (SPECT), but unlike these methods MPI involves no potentially harmful radiation. A spatial resolution in the millimeter regime and a temporal resolution in the order of seconds (or sub-seconds) is achievable [4]. Real-time imaging capability is typically contrasted with a high sensitivity, which at the cost of imaging speed is in league with the nuclear medicine imaging techniques. Because MPI does not generate any contrast without the tracer it requires reference images from clinical standard modalities, i.e. magnetic resonance imaging (MRI) and computed tomography (CT), for applications where (background) tissue contrast is requisite.
For the specific characterization of the MPI tracer with regard to signal and imaging performance Magnetic Particle Spectroscopy (MPS) has been developed as a supporting tool [9]. In conjunction with an appropriate magnetization model, MPS allows one to characterize the particles regarding their core size distribution.

Besides our group, only a handful of research groups in Germany (Lübeck and Würzburg) and the United States (Berkeley, CA) and two commercial groups in Germany (Philips Medical Systems, Hamburg and Bruker BioSpin, Ettlingen) are concerned with the development of MPI scanners. The existing designs can be categorized based on mainly two criteria: a) the reconstruction approach and b) the selection field geometry. While the groups in Germany (except Würzburg) follow the (traditional) F-space approach [10–12], where the MPI detection signal is translated into the frequency domain and reconstructed based on a previously recorded system matrix, the group in Berkeley favors the x-space approach [13–15], where reconstruction is simplified to a spatial gridding of the detection signal amplitude over the scanning trajectory. Originally, the MPI signal is contributed by the particles in close proximity to the field-free point

(FFP), i.e. a unique point in the field of view (FOV) where the dc field level from the selection field is cancelled. Alternatively, a field-free line (FFL) has been suggested [16–18], which promises a higher sensitivity (signal increase from more particles contributing to a 1-dimensional FFL in comparison to a 0-dimensional FFP), faster imaging and a simpler reconstruction via filtered back-projection [19].

Traditionally, MPI systems have been designed at a drive field frequency around 25 kHz. Due to safety considerations regarding the peripheral nerve stimulation (PNS) and energy absorption from radio frequencies (specific absorption rate, SAR) [20–23], Philips has moved to a higher frequency range (around 150 kHz) for their clinical prototype. The strategy is complemented by use of small drive field amplitudes which keep the active field of view (FOV) small. Coverage of an enlarged FOV is then achieved through the use of additional focus fields shifting the small FOV at a slow rate [5, 24].

Because MPI is a tracer-based imaging modality, the properties of the tracer have direct effect on the imaging performance. MPI has unique requirements on the tracer and on the methods used for its characterization. In a (over-)simplified picture, the tracer exhibits a steep magnetization curve, i.e. to produce a rich harmonic receive spectrum at small drive field amplitudes, and a small relaxation time constant, so it instantly follows the drive field (frequency). The MPS as a 0-dimensional MPI variant (without selection field) is exceptional at delivering MPI-relevant characterization data, that together with results from other techniques provides a comprehensive view on the tracer. Resovist® and FeraSpin™ R have been discovered to render a remarkably good MPI imaging performance (in comparison to other available particle systems) [25, 26], which can even be improved by fractionation [27]. Several attempts have been made to optimize the particles for MPI application [28–31] yielding an improvement in sensitivity and/or spatial resolution.

MPI is positioned at a junction point between two research areas: medical imaging and applications of magnetic nanoparticles. For the imaging aspect, MPI has to find its place in relation to existing imaging modalities, like MRI, CT and PET/SPECT. Although, MPI has some unique properties, it competes against well established methods. On the other hand, magnetic nanoparticles are used in a wide range of applications, i.e. the separation and purification (of cells), magnetic drug targeting and delivery and hyperthermia. Some of these applications have reached the state of clinical use. The functional imaging aspect of the so-called 'Mobility MPI' (mMPI) presents an essential extension to MPI, where the already established nanoparticular magnetic markers are evaluated to enable spatially resolved binding detection.

This thesis is concerned with the functional imaging aspect of MPI, where the particle mobility, representative of the particle binding state or local changes in the viscosity environment, is made accessible in addition to the

standard concentration-weighted images. Also, the frequency-dependence of the tracer's dynamic magnetization response is acknowledged and potential utilization in MPI applications is investigated. For that, MPI and MPS systems have been developed, so that the measuring setups are available for practical research on the above mentioned objectives.

The magnetic nanoparticles are an essential part of MPI. The theory of their static and dynamic properties is the basis for all applications in MPI and MPS and it defines system design guidelines for MPI hardware and software. In Chapter 2, the basic properties of magnetic nanoparticles are introduced and numerical models (→ Sec. 2.4) for the magnetization of the particles in response to an externally applied field are described.
MPS is implemented (→ Sec. 3) as a universal tool for the characterization of magnetic nanoparticles (→ Sec. 3.3.2) and for use in biological binding assays (→ Sec. 3.3.3). Our MPS system (→ Sec. 3.2), in extension to a traditional MPS, allows one to study the magnetization response of the particles at multiple excitation frequencies and with an additionally applied dc magnetic field. In Chapter 4, the MPI scanner developed for this thesis is presented (→ Sec. 4.2). It constitutes a complex design with two fast-scanning axes and an adjustable gradient in form of a compact system, which gives enough flexibility to enable a variety of different application scenarios (→ Sec. 4.5). Chapter 4.5.1 presents a collection of phantom images obtained with the system. In contrast to most other systems, the scanner operates at a drive field frequency of 10 kHz, where a significant Brownian contribution from Resovist® or FeraSpin™ R is observed. At 25 kHz the largest fraction of the particles (in FeraSpin™) is assumed to relax via the Néel mechanism. The mobility estimation in MPS and mMPI (→ Sec. 4.5.2) poses special requirements on the MNP marker. A different magnetization response is needed depending on whether the particles are in suspension or (at least partially) immobilized. In FeraSpin™ a constant Néel baseline is always observed, which does not show any modulation as a function of viscosity or binding. Nonetheless, a smaller fraction of particles in FeraSpin™ contributes via the Brownian mechanism and enables the realization of assays in MPS and MPI.

2 Magnetic Nanoparticles

Magnetic Particle Imaging (MPI) inherently depends on a nanoparticular tracer being present in the imaging volume. The tracer is excited and detected via its magnetic properties. For that reason, the properties of the tracer material, both the magnetic core as well as the protective shell around it, have direct effect on the MPI imaging performance.
The upcoming chapter covers the basics of magnetic nanoparticles: geometric and magnetic properties of the particles, models to describe their magnetization (→ Sec. 2.4) and characterization methods to determine the defining parameters of such particles.
As the name suggests, magnetic nanoparticles (MNPs) are particles with magnetic properties in the size range of several nm to a few hundred nm. Larger particles, above several hundred nm or in the µm range are referred to as magnetic beads. For MPI, particle core sizes are typically in the range of 20 – 30 nm. In the context of medical imaging and other biomedical applications, the particles are dispersed in a water-based suspension.
Over the last decades a variety of applications have been developed utilizing magnetic nanoparticles [32–36]. Applications of MNPs include homogeneous bio-assays, which are special in that they can be conducted in an opaque medium, e.g. blood, and they do not require any wash-out steps prior to readout. For cancer treatment, MNPs are injected (or magnetically guided) into the tumor region and an alternating magnetic field is applied in order to induce heat at the particle site causing apoptosis (programmed cell death) of the tumor cells and tissue.
Also, MNPs are used as a constrast-enhancing agent in magnetic resonance imaging (MRI). The first superparamagnetic contrast agent was Endorem, followed by Resovist® in 2001, both intended for specific imaging of liver and spleen [37, 38].

Ferrofluids

A ferrofluid is a stable colloidal suspension of magnetic nanoparticles in a liquid phase (e.g. water). The magnetic nanoparticles are generally designed and manufactured as "core-shell" particles, where a core of magnetic material is surrounded by a non-magnetic protective shell (→ Fig.

2.1). The size of the magnetic core is generally described via the core diameter d_c, while the diameter of the entire particle (i.e. including shell and associated surface molecules) is referred to as hydrodynamic diameter d_h.

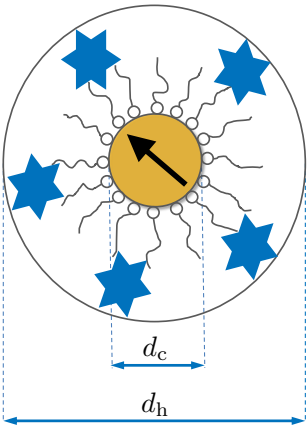

Figure 2.1: Core d_c and hydrodynamic d_h diameter: the magnetic core (yellow) is surrounded by a protective shell, where – for functionalized particles – other molecules attach (blue stars).

For bio-compatibility reasons, the choice of magnetic core material is mostly limited to iron oxide (although other materials, i.e. cobalt ferrite or nickel, are available as well and some of them are even superior in terms of magnetic properties). Composition, structure, size and shape of the core define the magnetic properties of the particles, although the shell might also have impact on the overall particle properties. For most applications, the diversity of particle sizes in synthetically fabricated particle suspensions is a disadvantage. Especially for medium-sized particles (15 – 50 nm), where the smaller particles are superparamagnetic and the largest ones are effectively multi-domain, the structure and shape is of great importance. One tries to have mono-sized particles, where each particle behaves alike any other, thus all particles have identical magnetic response to external fields. The ”perfect” particles are build by nature, produced by magnetosomes [39, 40], and chemists struggle to achieve similar quality. In summary, a controlled process of particle synthesis, stabilization and functionalization is crucial for the application of magnetic nanoparticles [36, 41–43].

Preparation and Functionalization

Coprecipitation and high-temperature decomposition of organic precursors are the most common methods for the synthesis of MNPs today. For coprecipitation, an aqueous iron salt solution is precipitated by addition of a base under inert atmosphere (and usually at room temperature or above) [42]. The main advantage of this method is the fact, that the particles are effectively produced in water. However, size, shape and composition – though reproducible in batch – are difficult to control upfront. In most cases, the size of precipitated particles is small with a large distribution width. Therefore, high-temperature decomposition is typically favoured for MNP production.
For high-temperature decomposition, the organometallic precursors (i.e. metal acetylacetonates, cupferronates or carboxyls) are dissolved in a high-boiling organic solvent, often under addition of surfactants (i.e. fatty acids, oleic acid, hexadecylamines), effect of stabilizing the particles during and after the synthesis [42]. The composition of the starting reagents and the environmental conditions in the reaction chamber control the resulting particle properties. Finally, hydrophobic particles have to be transferred into water phase (e.g. by ligand exchange or polymerization).
The surface chemistry of particles is critical when it comes to storage and (later) usage of the particles for biomedical applications. The surface corona ensures that the particles are solvable in water, or water-based solutions with around-neutral pH value, and it stabilizes the particle suspension against aggregation and agglomeration. An overview of relevant (nano-scale) forces is given by Bishop et al. [44]. Even under a strong magnetic field (e.g. the gradient field in MPI) the particle shell protects the ensemble of particles against (strong) interactions – most models assume non-interacting particles [45].
Typical coatings include polymeres (i.e. poly-ethylene-glycol, PEG), glucans (i.e. dextran, starch), silans or ionic residual groups (i.e. carboxyl groups in citric acid). It can also be a metal coating (i.e. gold) or multi-component encapsulation (i.e. micelles) [46]. In any case, steric hindering or repulsive forces keep the particles from interacting magnetically. Biocompatibility also includes non-cytotoxicity of MNPs at reasonable dose [43, 47, 48].
The small size of MNPs prepares them to infiltrate cells or to reside in extra-cellular space, which opens the opportunity for them to also bind to any cellular surface if functionalized properly. Functionalization of the particles, meaning that they specifically and functionally bind to surface proteins of tumor cells (for labeling) or via gene/anti-gene binding to certain (prepared) targets [41, 49], is especially useful for bioassays and functional imaging [35, 50]. The reader is refered to MPS bioassays (→ Ch. 3.3.3) and mMPI (→ Ch. 4.5.2) for exemplary applications.
One factor, that plays an important role for the stability of a MNP suspension and its application, is the concentration of iron in the tracer. For most bio-medical applications the amount of iron is limited by cytotoxic effects. Also, an increased iron concentration leads to unwanted particle-particle interations.

A small iron content entails a reduced magnetic signal compared to bulk material. To account for that, usually the volume fraction v_f of particles in the suspension is used. The particle volume V_P can be expressed in terms of the reciprocal particle number density n_d or the ratio of the volume fraction $v_\mathrm{f}V$ of a particle ensemble in solution to the number of particles N:

$$V_\mathrm{P} = \frac{1}{n_\mathrm{d}} = \frac{v_\mathrm{f}V}{N} \tag{2.1}$$

The molar concentration c is then given by

$$c = \frac{n_\mathrm{d}}{N_\mathrm{A}} = \frac{N}{v_\mathrm{f}VN_\mathrm{A}} = \frac{1}{V_\mathrm{P}N_\mathrm{A}} \tag{2.2}$$

Commercial agents

To conclude this section, we take a short look at commercially available tracers and their iron concentrations: Resovist® is the most widely-used tracer for MPI due to its rich harmonic spectrum. Also, Resovist® has been used in the early development phase of MPI and, after the initial publication in Nature 2005 [1], became the de-facto standard. In this thesis, the FeraSpin™ series, produced by nanoPET Pharma GmbH (Berlin, Germany), is considered a 'drop-in' replacement for the discontinued (as of 2009) Resovist® contrast agent. In contrast to Resovist® however, FeraSpin™ can be applied for pre-clinical animal studies, but it is not approved for use in humans. Still, sharing all relevant chemical, geometrical and magnetic properties FeraSpin™ is a highly-valuable substance, which we rely on for most of our studies.
The typical concentration of Resovist® is 500 mM, FeraSpin™ is available up to 700 mM, but usually delivered around 70 mM Fe. For a viscosity series or binding experiments, the MNP suspension is diluted to around 10 – 20 mM; functionalized particles or in-vivo concentrations are even lower. For Resovist® 10 µmol/kg are clinically approved and about 45 µmol/kg blood for bolus injection of a mouse [4, 38].

2.1 Static Properties

Magnetic properties, as discussed in this section, are constant in time. They can be observed as a stable state or under equilibrium measurement conditions. The most important quantity for magnetic nanoparticles is their static magnetization M and the associated magnetization curve $M(H)$.
The magnetic flux density B is connected to the magnetization M of the particles and the applied magnetic field H. The contribution from the particle's magnetization can also be described via the susceptibility χ

of the material or the relative permeability μ_r. M is sometimes called the "induced magnetization", in contrast to the residual magnetization or remanence. $M(H)$ is a function of the applied external field. In many cases, a non-linear relationship is observed for $M(H)$ and the susceptibility χ ($= \mathrm{d}M/\mathrm{d}H$) and also the permeability μ_r become field-dependent in (2.3b/c). The magnetic permeability in vacuum μ_0 is a constant of $4\pi \times 10^{-7}$ Vs/Am.

$$B = \mu_0(M + H) \tag{2.3a}$$
$$\approx \mu_0(\chi + 1)H \tag{2.3b}$$
$$= \mu_0\mu_r H \tag{2.3c}$$

Depending on the sign of the susceptibility χ, a distinction is made between diamagnetism ($\chi < 0$) and paramagnetism ($\chi > 0$).
Diamagnetism is a fundamental property of all materials, although sometimes overruled by other forms of magnetism, such as para- or ferromagnetism. Actual diamagnetic materials include carbon (graphite), copper and water (and therefore all water-based samples). In diamagnetism the angular momentum of electron orbitals creates a magnetic moment, which in sense is opposite to the applied magnetic field. For that reason, diamagnets to some degree repell external fields and the susceptibility is negative. Typical susceptibility values for diamagnets are $\chi_{\mathrm{water}} = -0.9 \times 10^{-5}$, $\chi_{\mathrm{copper}} = -1.0 \times 10^{-5}$ and $\chi_{\mathrm{graphite}} = -1.6 \times 10^{-5}$.
Paramagnetism on the other hand is observed only in materials with unpaired electrons. The electron spins behave as isolated magnetic dipoles with a moment of approximately one Bohr magneton. Due to the random orientation in the absence of an external field, no net magnetization is measured. However, when an external field is applied, the dipoles start to align and a magnetization becomes evident. For paramagnetic material, such as aluminium or iron oxide, the susceptibility is positive with typical susceptibility values of $\chi_{\mathrm{aluminium}} = 2.2 \times 10^{-5}$, $\chi_{\mathrm{FeO}} = 720.0 \times 10^{-5}$ and $\chi_{\mathrm{Fe2O3}} = 358.6 \times 10^{-5}$. In general, more unpaired electron spins contribute to large paramagnetic moments. The most succesful MNPs for contrast-enhanced MRI are made of gadolinium(III), which carries 7 unpaired electrons [51].
In case of a sufficiently large exchange energy between close-by dipoles, the material forms ferromagnetic (parallel alignment) or ferrimagnetic (anti-parallel alignment) domains. Only at higher temperatures, above the Curie temperature, the thermal agitation overcomes the interacting forces and the material behaves as a paramagnet.
The same principles, as discussed above, also apply in the case of magnetic nanoparticles. The Curie temperature of magnetite is about 850 K, which means that magnetite is ferrimagnetic at room temperature. However, for particles in the nm range the thermal energy becomes dominant against

the molecular level exchange energy. Here, every particle acts as a single magnetic domain and only the ensemble of particles behaves analogous to ferromagnets above their Curie temperature [52]. Because the susceptibility of such particle ensemble is large compared to other paramagnets, the effect is called superparamagnetism.

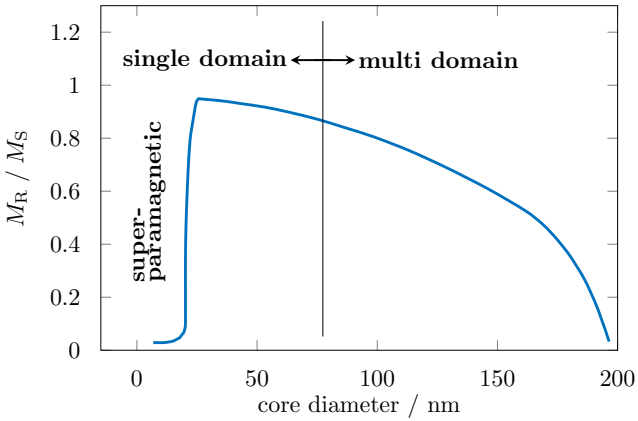

Figure 2.2: Coercivity: remanence magnetization M_R as a function of the core diameter d_c (adapted from [53]).

A magnetic domain refers to the largest unit of order in a magnetic material. That can either be a uniformely magnetized region or – more commonly – a region with closed magnetic loops or vortices. The non-uniform magnetization configuration of those regions reduces the self energy of the magnet with increasing particle size (→ Fig. 2.2). Very small particles (typ. $< 30\,\text{nm}$ for magnetite) are superparamagnetic (SP), medium-sized particles ($\approx 30 - 80\,\text{nm}$) form a single magnetic domain (single-domain, SD) with near-uniform magnetization and large particles ($> 80\,\text{nm}$) are suspect to show multiple magnetic domain configurations (multi-domain, MD). As a result, the net remanent magnetization M_R is reduced compared to the saturation magnetization M_S with increasingly non-uniform configuration in larger regions. For practical purposes, the bulk magnetic susceptibility is normalized to the particle volume or mass. Generally, the susceptibility is a complex function of temperature, applied field, orientation, mechanical stress and other factors. For applications of magnetic nanoparticles, which are typically in the range of $280 - 330\,\text{K}$ ($\Delta T \approx 50\,\text{K}$), the temperature dependence of the remanent magnetization is not a concern, although the saturation magnetization decreases slightly with increasing temperature.
It should be noted, that the coercitivity value also affects the relaxation time constant of the MNP core (→ Sec. 2.2.1).

2.1.1 Static Magnetization / Langevin Function

For a single particle, because the particle consists of a single magnetic domain, the magnetization is at its saturation magnetization. The overall magnetization M is then given by the sum of all contributing magnetic moments m_i in the volume V:

$$M = \frac{\sum m_\mathrm{i}}{V} \qquad \Longleftrightarrow \qquad m \sim \overline{m} = M_\mathrm{S} V_\mathrm{c} \tag{2.4}$$

In turn, the average magnetic moment $\overline{m}$ of a particle can be expressed as saturation magnetization M_S times the particle volume V_P. Because only the magnetic core contributes to the magnetization, the particle volume V_P is typically replaced with the particle core volume V_c.
As discussed in the previous section, for nanoparticles the thermal energy is in magnitude comparable to the exchange energy, thus a dynamic equilibrium is obtained. With that in mind, the $M(H)$ magnetization curve of superparamagnetic nanoparticles can be described via the Langevin function L of superparamagnetism (2.6).

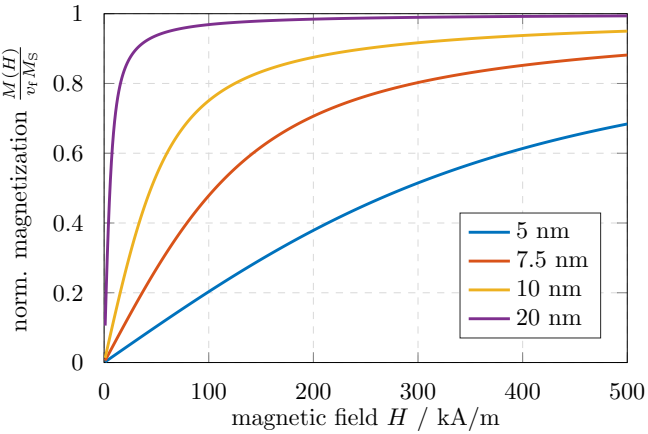

Figure 2.3: Langevin function L as a function of the applied magnetic field for particles with different core diameters (in the size range of 5 – 20 nm).

The static magnetization level M can be written as a function of the factor ξ, the ratio of magnetic energy $\mu_0 m H$ and thermal energy $k_\mathrm{B} T$:

$$\xi = \frac{\mu_0 m H}{k_\mathrm{B} T} \tag{2.5}$$

Factor ξ is connected to the k-Factor in x-Space MPI ($\rightarrow$ Sec. 4.1).
For a ferrofluid, the dilution factor v_f and the saturation magnetization M_S have to be taken into account. Thus, the static magnetization is finally given by:

$$L(\xi) = \frac{M(\xi)}{v_\mathrm{f} M_\mathrm{S}} = \coth(\xi) - \frac{1}{\xi} = \coth\left(\frac{\mu_0 m H}{k_\mathrm{B} T}\right) - \left(\frac{k_\mathrm{B} T}{\mu_0 m H}\right) \tag{2.6}$$

Inserting (2.4) into (2.6) reveals that the Langevin function is dominantely a function of the particle core volume V_c (or the core diameter d_c). Small magnetic cores possess a shallow magnetization curve with large fields required to saturate the particles. With increasing core diameter the magnetization curve becomes steeper and saturation is reached at moderate external fields ($\rightarrow$ Fig. 2.3).
For numerical treatment, the Langevin function can be approximated (around the origin) in terms of a Taylor series expansion $L^*(\xi)$ as follows:

$$L^*(\xi) = \frac{\xi}{3} - \frac{\xi^3}{45} + \frac{2\xi^5}{945} + ... \tag{2.7}$$

For some numerical evaluations, e.g. in fitting scenarios and to obtain the minimum amplitude for harmonics generation in MPS , the inverse of the Langevin function is also needed. A good overview of various approximations is given by Jedynak et al. [54].

2.1.2 DC Susceptibility

The magnetization characteristics of MNPs can also be described by looking at the susceptibility of the particles. This view is especially helpful in cases, where the magnetic field H varies in space (or time for ac susceptibility). The dc susceptibility χ is obtained as a derivative of the static magnetization curves discussed in the previous section:

$$\chi = \frac{\mathrm{d}M}{\mathrm{d}H} \tag{2.8}$$

An algebraic expression for the dc susceptibility is derived from (2.6):

$$\dot{L}(\xi) = \frac{1}{\xi^2} - \frac{1}{\sinh^2(\xi)} \tag{2.9}$$

with an equivalent Taylor series (around the origin) of:

$$\dot{L}^*(\xi) = \frac{1}{3} - \frac{\xi^2}{15} + \frac{2\xi^4}{189} + ... \tag{2.10}$$

As can be seen from (2.10), the zero/first order approximation of (2.9) is $\frac{1}{3}$. This value plays an important role and is frequently refered to as initial slope/susceptibility.

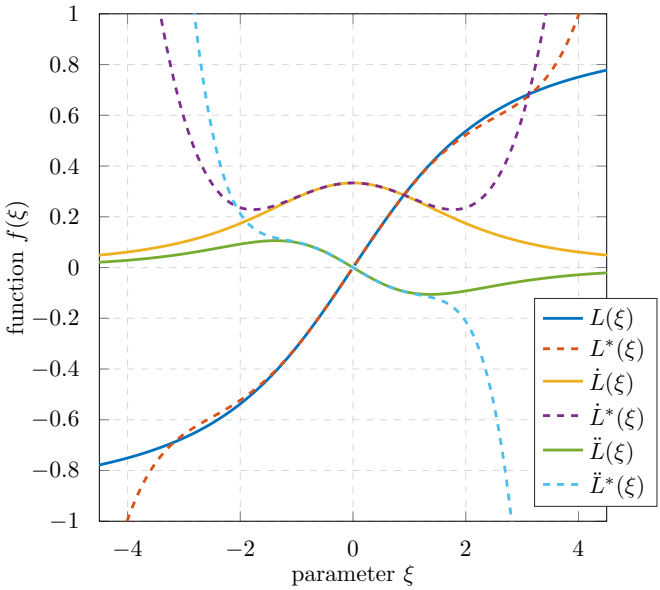

Figure 2.4: Langevin derivatives (solid lines) and approximations (dashed lines), $L(\xi)$ is the Langevin function and $\dot{L}(\xi)$ is the susceptibility.

For the sake of completeness and for use in later chapters (Sec. 3.3.2 and Sec. 4.1.1), an expression for the second derivative is also given:

$$\ddot{L}(\xi) = -\frac{2}{\xi^3} + \frac{2\coth(\xi)}{\sinh^2(\xi)} \tag{2.11}$$

with an equivalent Taylor expansion (around the origin) of:

$$\ddot{L}^*(\xi) = -\frac{2\xi}{15} + \frac{8\xi^3}{189} - \frac{2\xi^5}{225} + ... \tag{2.12}$$

Fig. 2.4 provides a plot of the Langevin function, its derivatives and the corresponding approximations. The maximum curvature of the Langevin function (i.e. were the harmonics are mostly generated) is found around $\xi \approx 1$, which gives a good estimate for the minimal excitation amplitude in MPS and MPI.

2.2 Dynamic Properties

Section 2.1 discussed properties which are constant in time or which are observable in an equilibrium state, dynamic properties are concerned with the temporal evolution of the MNP magnetization in time-varying external fields. Most magnetic characterization methods or application of MNPs object the particles to exciting magnetic fields. For ACS , MPS and MPI it is a sinusoidal field, for MRX a step function. In all cases, the magnetization response of the MNPs is governed by the two distinct relaxation time constants, namely the Néel relaxation of the magnetic core and the Brownian relaxation of the entire particle [55–63]. Fig. 2.5 depicts the two mechanisms in a schematic macroscopic view.

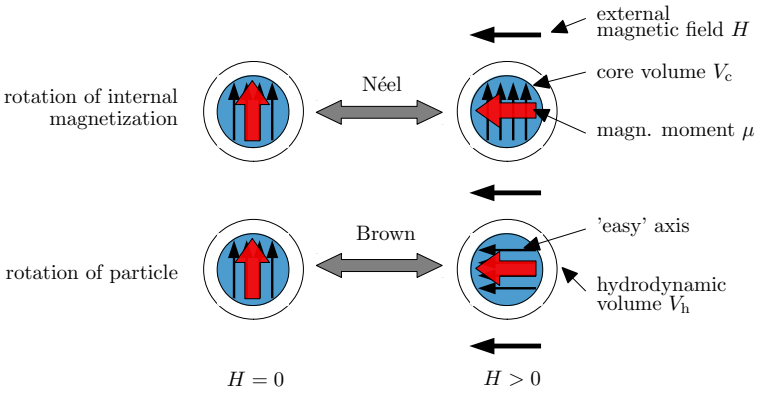

Figure 2.5: Néel vs. Brown relaxation mechanism: for the Néel mechanism the internal magnetization aligns with the applied field, for Brownian relaxation the particle rotates as a whole.

For the Néel mechanism, from applying an external field, the magnetization is rotated within the particle. The magnetization, at rest fixed along an 'easy' axis, is forced to align with the external field. In contrast, for the Brownian mechanism, the entire particle rotates to align its principal axis with the applied magnetic field.

2.2.1 Néel Relaxation

Due to a magnetic anisotropy, the magnetic moment has two stable orientations within the MNP crystallites defining the particle's 'easy' axis. The finite time constant that is associated with the probability for the magnetization to flip between the two directions is called the Néel time constant τ_N. The Néel time constant τ_N is determined by the magnetic

anisotropy constant K, the core volume V_c, the Boltzmann constant k_B and the temperature T via

$$\tau_N = \tau_0 \; exp\left(\frac{KV_c}{k_B T}\right) \cong \tau_0 \; exp\left(\frac{\pi K d_c^3}{6 k_B T}\right) \tag{2.13}$$

In fact, the anisotropy builds up an energy barrier KV_c separating the two stable orientations which is challenged by thermal fluctuations with energy $k_B T$. The Néel relaxation time exponentially depends on this energy ratio (→ Fig. 2.6). The figure shows that in most cases the particle is either superparamagnetic, i.e. it's Néel time constant $\tau_N \approx \tau_0$, or the particle is blocked, i.e. it's Néel time constant is very large (in the order of seconds). There exists only a small window of KV_c at room temperature where reasonable time constants are observed. For magnetite nanoparticles this window is found at a core diameter in the range of 20 – 30 nm. The Néel relaxation times for different particle diameters are shown in Fig. 2.7.

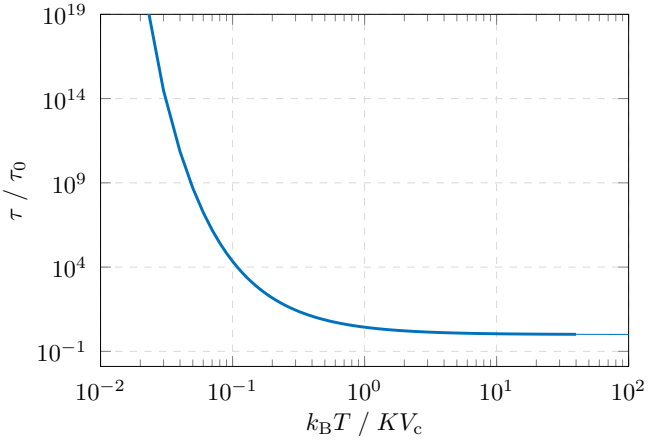

Figure 2.6: Néel relaxation time as a function of the energy ratio $k_B T$ / KV_c (thermal energy / anisotropy energy) [52].

The alignment process of the particle to an external magnetic field H, i.e. rotating the magnetization M to point into the direction of the applied field, can be described by the following equation:

$$2\tau_N \dot{M} = \frac{\mu_0 V_c}{k_B T}\left[\alpha^{-1} M_S M \times H + (M \times H) \times M\right] \tag{2.14}$$

An applied magnetic field H leads to a precession of the magnetization M around the field axis ($\dot{M} = \mu_0 \gamma M \times H$ with gyromagnetic ratio γ). The intensity and duration of the precession movement is also governed by the Néel time constant. The damping constant α in (2.14) can be determined by resolving $\tau_\mathrm{N} = \frac{\mu_0 V_\mathrm{c} M_\mathrm{S}}{2 k_\mathrm{B} T \gamma} \frac{1+\alpha^2}{\alpha}$ for α. In literature (2.14) is refered to as Landau-Lifschitz-Gilbert equation [64].
Anistropy and the associated Néel time constants are reponsible for hysteresis as described via the Stoner-Wohlfarth model [65, 66]. In the case, where the anisotropy energy KV_c is large compared to thermal energy $k_\mathrm{B}T$, the particle is considered 'blocked', i.e. the Néel relaxation time is too large with reference to the measurement duration, that the particle's magnetization does not change significantly during measurement. However, it must be considered, that the anisotropy and with it the Néel time constant is highly field-dependent (→ Sec. 2.2.1) [67, 68].

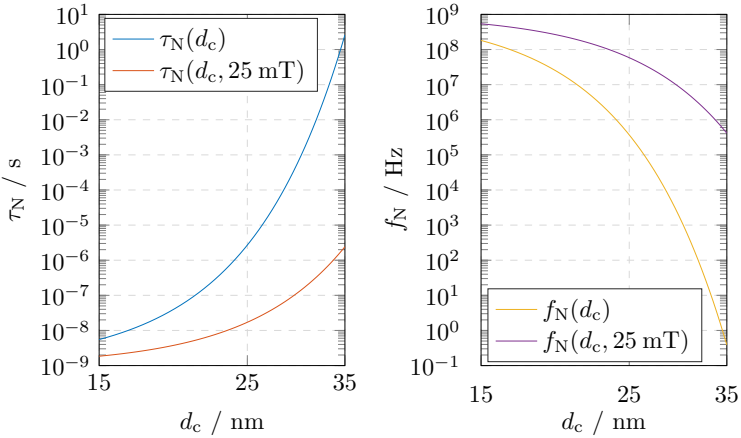

(a) time constant **(b)** characteristic frequency

Figure 2.7: Néel time constant and frequency equivalent over particle core diameter d_c (without/with field-dependence at 25 mT).

Field-dependent Néel Relaxation

The Stoner-Wohlfarth model can be expanded to account for the barrier height of the uniaxial potential in presence of an applied field [65, 69]. In that case, the maximum anisotropy energy $\Delta E = KV_\mathrm{c}$ is decreased to about $\Delta E = KV_\mathrm{c}(1 - \frac{H}{H_\mathrm{C}})^\varepsilon$, with the coercivity field H_C and scaling exponent ε. The field-dependent Néel time constant then becomes:

$$\tau_\mathrm{N}(H) = \tau_0 \; exp\left(\frac{KV_\mathrm{c}}{k_\mathrm{B}T}\left[1 - \frac{H}{H_\mathrm{C}}\right]^\varepsilon\right) \tag{2.15}$$

The scaling exponent ε typically varies around $\varepsilon = 2$ depending on the field angle θ with the 'easy' axis. It is exactly valid only for $\theta = 0$ and $\theta = 90°$. Eq. (2.15) is plotted in Fig. 2.7 for an amplitude of 25 mT, which reveals a strong field-dependence of the Néel relaxation time [68, 70–74].
For practical applications (i.e. in ACS , MPS and MPI) we deal with sinusoidal excitation fields. Although not strictly correct, the time constant can then be approximated by averaging over a sine period, i.e. using the quadratic mean of the field amplitude.

2.2.2 Brownian Relaxation

Nanoparticles in a suspension have an additional degree of freedom in that – as a response to an external field – they are able to rotate freely in space. In contrast to the internal reorientation of magnetic moments for the Néel process, relaxation via Brownian rotational motion does not have a fixed or prefered axis. It basically comes down to a torque equation, where the magnetic force acting on the magnetic moment of the particle is balanced by Stokes' frictional force.
The Brownian time constant τ_B is given by (2.16) and depends on the hydrodynamic volume of the particle V_h (or the hydrodynamic diameter d_h) and the viscosity of the medium η.

$$\tau_\mathrm{B} = \frac{3\eta V_\mathrm{h}}{k_\mathrm{B}T} \cong \frac{\eta\pi d_\mathrm{h}^3}{2k_\mathrm{B}T} \tag{2.16}$$

Fig. 2.8 shows the Brownian relaxation time as a function of particle diameter. Because the time constant τ_B connected to the Brownian alignment process depends on the hydrodynamic diameter of the particle d_h and viscosity of the surrounding medium η, it can be used as an indicator in biological binding assays (→ Sec. 3.3.3).
Analogous to the Néel process, the alignment motion of the particle to an external magnetic field H, i.e. rotating the entire particle into the direction of the applied field, can be described by the following equation:

$$2\tau_\mathrm{B}\dot{M} = \frac{\mu_0 V}{k_\mathrm{B}T}\left[(M \times H) \times M\right] \tag{2.17}$$

Equation (2.17) is identical to (2.14) with the precession term being omitted. A particle exercising the Brownian alignment process macroscopically behaves similar to a compass needle in the earth magnetic field.

Field-dependent Brownian Relaxation

The Brownian time constant is also field-dependent. In contrast to the field-dependent Néel time constant, no simple expression is known to

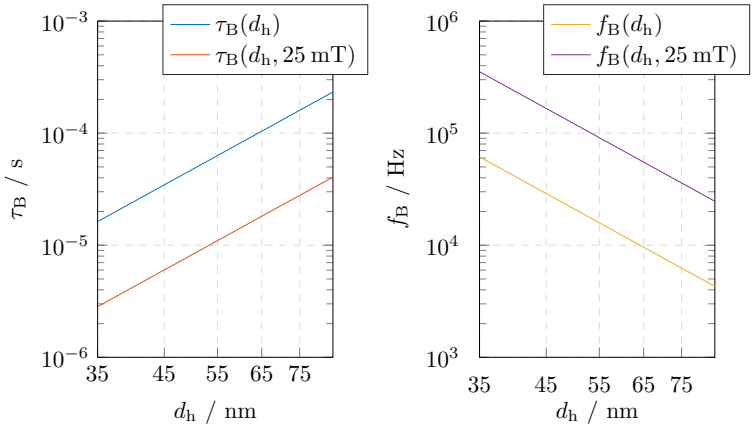

(a) time constant **(b)** characteristic frequency

Figure 2.8: Brownian time constant and frequency equivalent over particle hydrodynamic diameter d_h (without/with field-dependence at 25 mT).

describe the dependency. However, on the basis of solving the Fokker-Planck equation for the Brownian regime, Yoshida et al. [75] derived empirical expressions for a step response and sinusoidal excitation.

$$\tau_{B,\mathrm{step}}(H) = \frac{1}{\sqrt{1 + 0.21\xi^2}} \cdot \frac{\eta\pi d_h^3}{2k_B T} \tag{2.18a}$$

$$\tau_{B,\mathrm{sine}}(H) = \frac{1}{\sqrt{1 + 0.07\xi^2}} \cdot \frac{\eta\pi d_h^3}{2k_B T} \tag{2.18b}$$

The Brownian time constant as a function of the hydrodynamic particle diameter for different fields is plotted in Fig. 2.8. The diagram is calculated with (2.18) and assumes a sinusoidal excitation with an amplitude 25 mT.

2.2.3 Effective Relaxation

Whenever particles are in suspension, so that both relaxation mechanisms are enabled, a superposition of the Néel time constant τ_N and the Brownian time constant τ_B is observed [62]. The effective time constant τ_{eff} is then denoted by:

$$\tau_{\mathrm{eff}} = \frac{\tau_B\,\tau_N}{\tau_B + \tau_N} \quad \Longleftrightarrow \quad \frac{1}{\tau_{\mathrm{eff}}} = \frac{1}{\tau_B} + \frac{1}{\tau_N} \tag{2.19}$$

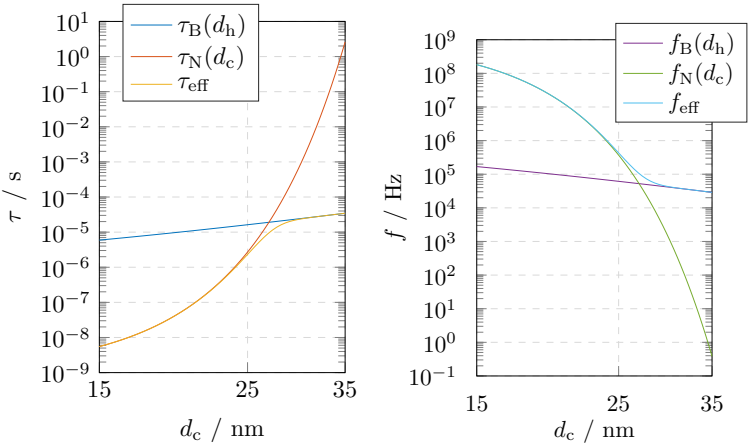

(a) time constant **(b)** characteristic frequency

Figure 2.9: Effective time constant and frequency equivalent over particle core diameter d_c for a fixed shell of 10 nm thickness.

Fig. 2.9 shows the effective time constant as a function of the hydrodynamic diameter (the thickness of the shell is kept constant at $d_s = 10\,\text{nm}$). For small particles, the Néel time constant is always dominant. For larger particles in suspension, the Brownian relaxation takes precedence at a hydrodynamic diameter of about 25 nm. In case one of the relaxation mechanism is prohibited, i.e. by immobilizing the particles the Brownian process is suppressed, the remaining mechanism is still valid.

2.2.4 AC Susceptibility

In Sec. 2.1.2 the susceptibility has been introduced as the derivative of the static magnetization curve. In addition, the ac susceptibility provides a formal description of the frequency-dependence of the susceptibility of MNPs with a time constant τ for a sinusoidal applied field. In general form, the ac susceptibility takes the initial susceptibility χ_0 and applies a frequency dependent term, resulting in a complex-valued function:

$$\chi = \frac{\chi_0}{1 + j\omega\tau} \tag{2.20}$$

Real and imaginary part of the susceptibility are typically separated by complex conjugate expansion, and $\chi' = \Re e\{\chi\}$ and $\chi'' = \Im m\{\chi\}$ are obtained:

$$\chi' = \chi_0 \frac{1}{1 + (\omega\tau)^2} \tag{2.21a}$$

$$\chi'' = \chi_0 \frac{\omega\tau}{1 + (\omega\tau)^2} \tag{2.21b}$$

For a detailed discussion of the ac susceptibility formalism, the reader is referred to the model section (→ Ch. 2.4.3).

2.3 Particle Taxonomy

In the last two sections, static and dynamic magnetic properties of MNPs were discussed. However, there is a complex interconnection between nanoscale or microscopic features of particles and the macroscopically observed magnetic properties. The macroscopic picture is typically obtained with our magnetic characterization techniques, while the microscopic features are discoverable by chemical analysis methods or structural decomposition.

2.3.1 Particle Size Distributions

The particle size distribution (PSD), i.e. the statistical distribution of particle diameters (not to be confused with PSD for power spectral density), represents a critical parameter for applications of magnetic nanoparticles. The reason for that is the strong dependence of MNP's magnetic properties, including the static magnetization and magnetization dynamics, on the particle core volume V_c.
The particle size distribution can be expressed in terms of a probability density function of particle diameters. In general, (2.22) expresses a discrete distribution function, in which each discrete particle diameter d is present with a finite probability p_i in the sample. Normalization requires $\sum p_\mathrm{i} = 1$.

$$f(d) = \sum_{i=1}^{n} p_\mathrm{i}\, \delta(d - d_\mathrm{i}) \tag{2.22}$$

In many cases, the probability density function is a continuous function, e.g. a normal or log-normal distribution. Then (2.22) gives a discrete approximation of the continuous function. Fig. 2.10 shows two distinct continuous distributions and the approximated discrete distribution in comparison. Of course, the granularity of discrete particle diameters defines the accuracy of the approximation. The number of discrete values to be distinguished in practical measurements, e.g. from MPS, ACS, etc.,

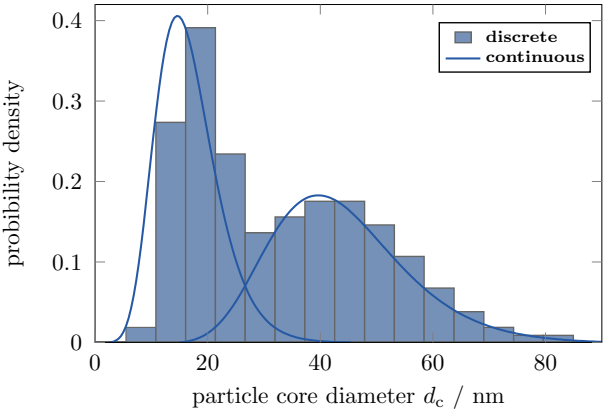

Figure 2.10: Two log normal size distributions with different mean (20 nm and 45 nm) together form a bimodal size distribution.

is largely limited by the dimension of the measurement space, e.g. the number of time- or frequency points (see Sec. 3.3.2 for an example).
For that reason, a certain (parameterized) distribution function is typically taken as a basis and its parameters are determined. The particle size distribution of MNP's has been observed to approach a log-normal distribution for most practical cases.
The probability density function of a log-normal distribution is defined as a function of the geometric mean e^{μ} and the geometric standard deviation e^{σ}:

$$f(d,\mu,\sigma) = \frac{1}{d\sigma\sqrt{2\pi}}\, e^{-\frac{(\ln d-\mu)^2}{2\sigma^2}} \tag{2.23}$$

The arithmetic mean, i.e. the expected value, is found at $E(d) = e^{\mu+\frac{1}{2}\sigma^2}$ and it is shifted against the distribution maximum towards larger diameters as a consequence of the asymmetry of the distribution with a tail of larger particles (→ Fig. 2.11a).
Fig. 2.11 depicts a log-normal size distribution for a mean diameter of $e^{\mu} = 25\,\text{nm}$ and $\sigma = 0.4$. The distribution tail is evident with large diameters of up to 60 nm. Because the log-normal distribution can be derived by performing a change-of-variable ($y = \ln x$) on a normal distribution, rescaling the abscissa of Fig. 2.11a to be logarithmic reveals the normal symmetric distribution (→ Fig. 2.11b). In this view, the absence of small particles (in contrast to the tail of large particles) is easily observed.

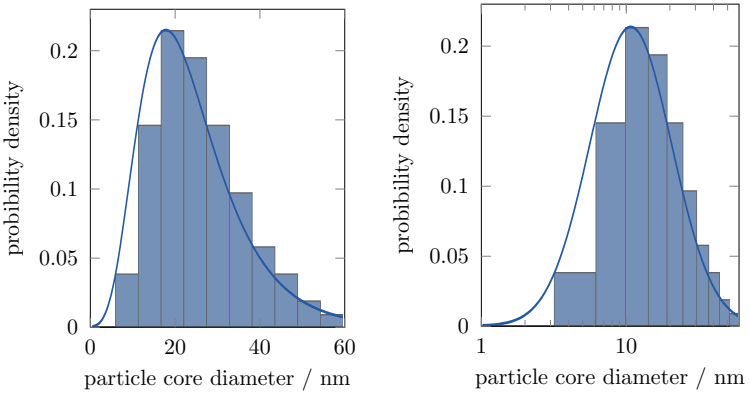

(a) linear axis **(b)** logarithmic axis

Figure 2.11: Log-normal distribution on a linear and logarithmic scale of the diameter axis in comparison. A log-scale abscissa reveals a normal distribution shape and shows the under-represented small particle sizes.

Closely related to the size distribution is the dispersity of the MNP sample. The dispersity designates the heterogeneity of particle diameters in a sample. A sample with near-uniform particle sizes is said to be mono-disperse. Usually, it can be described with a single log-normal size distribution, and its distribution function is monomodal. Other MNP samples, especially clustered particles or mixtures of different particle batches or types, where a large variety of different particle diameters are found, are called multi-dispersed. Multi-dispersity also reflects the fact that those samples can be described only by defining a sum of two (bimodal) or more (multi-modal) distributions.

2.3.2 Particle Classes

For the classification of MNPs, there is a clear distinction between single-core and multi-core (or clustered) particles. The fundamental building block of magnetic nanoparticles are the crystallites or cores. A crystallite describes the crystallographic unit representing one or more magnetic domains and created during chemical synthesis of the particles. An isolated crystallite or core is typically in the diameter range of 5 nm up to about 35 – 40 nm. The term 'single-core' nanoparticle denotes a particle made of a single crystallite. On the other hand, so called 'multi-core' particles are formed from multiple crystallites, which are typically tied together by the shell material.
For good MPI performance, MNPs are expected to show a steep magnetization curve (with moderate fields required for saturation) and a high saturation magnetization. Due to excitation frequencies in the order of

several kHz, fast magnetization dynamics with time constants comparable or faster than the excitation fields are required. However, the susceptibility and relaxation time constant of the particles increase proportionally with the particle volume (see Fig. 2.3 and Fig. 2.9). As a result, large particles with large magnetic moments and steep Langevin magnetization inherently show a limited dynamic response to an applied ac field.
With higher frequency, the magnetization starts to lag behind the driving magnetic field (due to a finite relaxation time) and an increase in hysteresis is observed. In magnetic hyperthermia [76–80] ac fields in the frequency range of several 100 kHz and large amplitudes are used to specifically heat the MNPs in the body for therapeutical purposes. The power dissipation P is proportional to the imaginary (or loss) component χ'' of the ac susceptibility, the squared amplitude power dissipation H_{AC} and frequency f of the applied field [76]:

$$P = \mu_0 \pi f \chi'' {H_{\mathrm{AC}}}^2 \tag{2.24}$$

As a consequence for MPI, the MNPs must not present a major hysteresis loop and/or the field and frequency parameters of the excitation field must be kept within a reasonable range to prevent heating of the MNPs. On the other hand, a small hysteresis loop was found to improve MPI signal because it leads to a higher susceptibility in the transient region of the magnetization curve [81]. A strong harmonic content of the MPI signal is a consequence of the divergence between ascending and descending branch of the magnetization curve.

Single-core Particles

Single-core nanoparticles, i.e. particles made of a single crystallite surrounded by a shell layer, are especially interesting in the context of magnetization models (→ Sec. 2.4) because the principles governing their magnetic properties are well understood (there are numerous models for single-core particles). They are also easier to characterize than their multi-core counterparts because all interaction effects can mostly be neglected. The basic question related to single-core particles refers to the coercitivity and the size of the magnetic domains. Three types of single-core particles can be identified:

superparamagnetic (SP)

Superparamagnetic nanoparticles respond instantaneously to an applied magnetic field and they do not show any hysteresis.

single-domain (SD)

Magnetization of single-domain nanoparticles with coercitivity $H_{\mathrm{C}} > 0$ follows a hysteresis loop, which – in most cases – can be described with uni-axial anisotropy (→ Sec. 2.2.1).

multi-domain (MD)

> Very large particles will also have multiple domains. However, all nanoparticles in the context of this thesis are much smaller than the multi-domain threshold diameter for magnetite particles (above ~100 nm).

As mentioned above, we usually refer to single-core particles with superparamagnetic (SP) or single-domain (SD) properties. Single-core particles also typically have monomodal size distributions.

Multi-core / Clustered Particles

Multi-core particles are composed of multiple crystallites covered in a joint shell. Due to small intra-particular spacing of the individual cores, magnetic (dipole-dipole) interaction of crystallites occurs. Therefore, multi-core particles effectively show a mixture of SP and SD characteristics. These mixtures have been studied extensively in geophysical research [82–84]. Here, it should suffice to highlight the enhancing effect of hysteresis (ascending versus descending branch), SP/SD mixtures and magnetic interaction on the MPI signal, i.e. a richer spectrum and higher harmonic content. To date, the connection between SP/SD mixtures and the modulated (spatial) MPI signal has not been studied, but the richer harmonic content certainly helps to pick-up the signal for improved sensitivity.

As mentioned above, the properties of MNPs for MPI are a compromise between the field requirements (saturation) and the relaxation time constant of the particles [28, 29, 31, 85–89]. Fast relaxing particles with a high saturation magnetization at moderate fields are an approximate optimum. The MPI community observed that Resovist® (or FeraSpin™) exhibits a remarkable rich spectrum which makes it suitable for MPI. An explicit analysis of the distribution of relaxation time constants against the corresponding effective magnetic moment (or particle size) revealed, that Resovist® consists of three fractions of contributing particles [26]. This complies with the observation that multi-core particles typically have a multi-modal size distribution when estimated from actual measurements [25, 85]. From numerical (Monte-Carlo) simulations the effective magnetic moment in multi-core nanoparticles is affected by dipole-dipole interactions and it is field-dependent [90–94].
For practical purposes, Yoshida et al. [27] analyzed the effective contributions of different fractions of an MNP sample to the MPI signal (→ Fig. 2.12). The fractions are numbered with type I, II and III. Type I refers to particles with small magnetic moments and very fast relaxation times, equivalent to a superparamagnetic fraction. Type III are particles with large magnetic moments and also very long relaxation times. For ac frequencies in the range of several kHz their magnetization is too steady to contribute significantly to the MPI signal. Therefore, the type III fraction effectively contributes via the Brownian mechanism and observes a viscosity dependence. Type II are particles with reasonable magnetic moments

and relaxation times in the appropriate time frame for an MPI experiment. We conclude, that the type II particles are dominant in generating an MPI response.

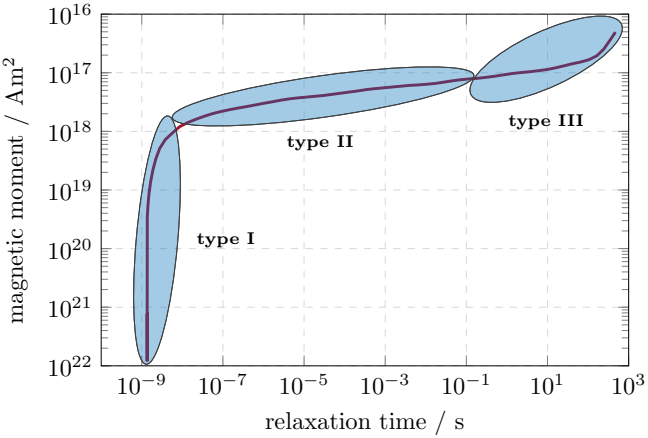

Figure 2.12: Empirical estimate on FeraSpin™ R of magnetic moment as a function of relaxation time (three major fraction types are identified) [27]. Type II is mainly responsible for good MPI performance.

For FeraSpin™ R, the volume fraction of type II particles was estimated to approximately 21 %. By performing size fractionation [95–100] on FeraSpin™ R, a series of samples ranging from FeraSpin™ S to FeraSpin™ XXL is produced and commercially available. FeraSpin™ L contributes the largest type II fraction with about 48 %. Similarly, Resovist® was fractionized [64, 81, 101–104] and evaluated for its MPI performance by Loewa et al. [27, 105].

2.4 Particle Magnetization Models

Numerical models describing the magnetization of magnetic nanoparticles are important to understand and simulate (or reconstruct based on simulation) the generation of signals in MPS and MPI (as well as for other methods, e.g. ACS , MRX , etc.). Some models (Langevin → Sec. 2.4.1 or Effective Field Method → Sec. 2.4.2) are valid only in the static case, where the magnetization process is slow enough (compared to the relaxation time constant) that an equilibrium state is obtained, or for periodic signals where a steady state is approached. In general, i.e. for arbitrary field geometries and time traces, models are more complex and put high demands on computing resources for solving. Two common approaches for theses complex models are found in literature.

The Fokker-Planck equation delivers an approach based on the time evolution of a non-equilibrium distribution function of magnetic moment orientations. It was derived by Brown et al. [58] from the stochastic Landau-Lifschitz-Gilbert equation (Gilbert equation in equivalent Landau-Lifschitz form) [106]. The stochastic Gilbert equation, in turn, is a nonlinear stochastic differential equation (SDE), also called the Langevin equation (not to be confused with the Langevin function) of the movement of a Brownian particle under the influence of a random force (i.e. thermal noise) [58, 64, 71, 101, 106–108].
Recently, the above mentioned models have been used to study the magnetization dynamics of magnetic nanoparticles [72, 75, 102, 103]. However, it remains challenging to model both the process of internal reorientation of the magnetic moment (Néel relaxation) and the Brownian rotational motion simultaneously.
The simpler models discussed in the upcoming chapter are still the ones used for practical evaluation of measurement data.

Note on notation:
The magnetization (and several other quantities) are represented as a spatial vector, meaning that they have a direction and a magnitude. All vector quantities are written in bold font, like $\boldsymbol{M}$, while their scalar counterparts (or the magnitude of the same quantities) are denoted in normal font M. Bold symbols with an overline bar, like $\bar{\boldsymbol{G}}$, denote a matrix or tensor.

2.4.1 Langevin Model

The Langevin function can be derived from the Brillouin function, developed for a quantum-mechanical description of paramagnets, in approach to the classical limit, where a quasi continuous (no quantization) alignment is obtained. For a large number of spins contributing to the total magnetic moment, the Langevin function depicts the macroscopic behavior of the material.
Basis for the Langevin function of superparamagnetism is an ensemble of nanoparticles with an average magnetic moment $\overline{m}$ for each particle at random orientations. The net magnetic moment of the entire sample is then expressed as the volume integral of all magnetic moments therein. The spatial average sums up to a zero net magnetization. However, with an applied magnetic field a predominant or preferred direction of the momentum axis develops. As a result, the volume integral no longer vanishes and a net magnetization of the ensemble is observed.
Sec. 2.1.1 introduced the scalar Langevin function $L(\xi)$ already in (2.6), it is repeated here for completeness and rewritten for a vector-valued field $\boldsymbol{H}$. To avoid confusion with the scalar Langevin function, the vector-valued Langevin model is denoted as $\tilde{L}$:

$$\tilde{\boldsymbol{L}}(\boldsymbol{H}) = \frac{\boldsymbol{M}(\boldsymbol{H})}{v_\mathrm{f} M_\mathrm{S}} = \underbrace{\left[\coth\left(\frac{\mu_0 m H}{k_\mathrm{B} T}\right) - \left(\frac{k_\mathrm{B} T}{\mu_0 m H}\right)\right]}_{L(\xi)} \frac{\boldsymbol{H}}{H} \tag{2.25}$$

The Langevin function is valid only in an equilibrium state, the (thermal) fluctuations in magnetization are small and they present zero average over time. Also the applied magnetic field is quasi-static, i.e. changes in the applied field (both in amplitude and direction) are slow compared to the time constant of the particles. In the Langevin model the resulting (equilibrium) magnetization $\boldsymbol{M}$ is always parallel to the applied magnetic field $\boldsymbol{H}$, i.e. $\boldsymbol{M} \times \boldsymbol{H} = 0$.
The applicability of the Langevin function is also limited to non-interacting particles. For MNP suspensions with a high volume fraction of particles or in the case of field-induced interactions (e.g. from aggregation or other transitional microstructures), the Langevin function needs to be modified. Li et al. derived a simple model for gaslike compression of previously non-interacting particles [109] with $\tilde{v_\mathrm{f}}$ the particle fraction of aggregates and v_f the total volume fraction of the sample:

$$L(\xi) = \coth(\xi) - \frac{1 + \ln(\tilde{v_\mathrm{f}}/v_\mathrm{f})}{\xi} \tag{2.26}$$

Eq. (2.26) causes a reduction of the saturation magnetization and a shallower slope of the magnetization curve in the region with highest curvature.

2.4.2 Effective Field Model

In physics, the effective-field technique provides a way of approximating the solution of an otherwise complex problem. Typically, a problem at small scale (particle-scale) is observed at larger scale (sample-scale). It is assumed that the system has an equilibrium state and that it approaches it in the absence of external disturbances. The transition from an arbitrary non-equilibrium state to the equilibrium might then be performed by introducing an additional field. The "auxilary external field [...] is constructed just for consideration of the non-equilibrium processes" [110].

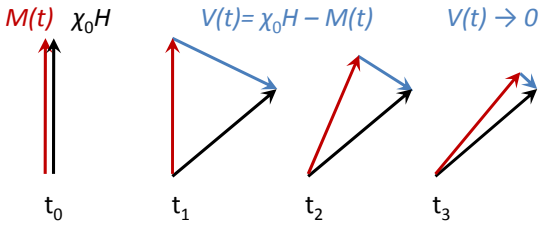

Figure 2.13: Illustration of the effective field approach with particle magnetization $M(t)$, equilibrium magnetization $\chi_0 H$ and (virtual) effective field $V(t)$.

In equilibrium state, there is a connection between the applied magnetic field $\boldsymbol{H}$ and the observed magnetization $\boldsymbol{M}$. In non-equilibrium state, the

deviation in magnetization $\boldsymbol{M}_\mathrm{V} = \boldsymbol{M} - \boldsymbol{M}_0$ can then be approximated from the effective field $\boldsymbol{H}_\mathrm{V}$ via the equilibrium function $\boldsymbol{M}_\mathrm{V} = L(\boldsymbol{H}_\mathrm{V})$. The magnetization $\boldsymbol{M}$ converges to its equilibrium value $\boldsymbol{M}_0$ over time in small quasi-equilibrium steps ($\boldsymbol{M}_\mathrm{V} \to 0$).
The linear approximation, given by the effective field method for dynamic magnetization of MNPs, is based on the fact that an arbitrary magnetization $\boldsymbol{M}$ can be represented as a sum of the equilibrium magnetization $\boldsymbol{M}_0$ and a small ($\boldsymbol{M}_\mathrm{V}/\boldsymbol{M}_0 \ll 1$) non-equilibrium contribution $\boldsymbol{M}_\mathrm{V}$. A (linearized) differential equation expressing the magnetization for an applied field is given by:

$$\dot{\boldsymbol{M}} = -\frac{1}{\tau_{||} H^2}\mathbf{H}\left[(\mathbf{M}-\mathbf{M}_0)\,\mathbf{H}\right] - \frac{1}{\tau_\perp H^2}\left[\mathbf{H}\times(\mathbf{M}\times\mathbf{H})\right] \tag{2.27}$$

A full derivation of (2.27) is provided in [110] and similarly in [101, 108, 111]. Eq. (2.27) is decomposed into two parts, parallel and orthogonal to the applied external field. For both components a corresponding relaxation time (longitudinal relaxation and transversal relaxation) can be defined as follows:

$$\tau_{||}(H) = \tau_\mathrm{B}\ \frac{d\ln L(\xi)}{d\ln\xi} \tag{2.28a}$$

$$\tau_\perp(H) = \tau_\mathrm{B}\ \frac{2L(\xi)}{\xi - L(\xi)} \tag{2.28b}$$

With (2.28), the time constants are found to be field-dependent and their values decrease for larger fields. The field dependence describes a hyperbola that draws near to τ_B for small fields. For high fields they approach $\tau_{||} = \tau_\mathrm{B}/\xi$ and $\tau_\perp = 2\tau_\mathrm{B}/\xi$ respectively. The field-dependence of the time constant is of great importance for MPI because of the large fields used for excitation. However, from the Fokker-Planck equation the field-dependence is found to be less pronounced (see Eq. (2.18)) [75].
For many scenarios, a dc field can be neglegted. Then the relaxation times converge again, and the pure ac excitation simplifies the model to the Debye form of the effective field model (→ Sec. 2.4.3), where the differential equation is reduced to contain only a single time constant τ and the virtual field magnetization $\boldsymbol{M}_\mathrm{V} = \boldsymbol{M} - \boldsymbol{M}_0$. The differential equation then simplifies to

$$\begin{aligned}\dot{\boldsymbol{M}} = \frac{d}{dt}\boldsymbol{M}(t) = -\frac{1}{\tau}\ \boldsymbol{M}_\mathrm{V}(t) &= -\frac{1}{\tau}\ \left[\boldsymbol{M}(t) - \boldsymbol{M}_0(t)\right] \\ &= -\frac{1}{\tau}\ \left[\boldsymbol{M}(t) - \chi_0\boldsymbol{H}(t)\right]\end{aligned} \tag{2.29}$$

In (2.29), the instantaneous magnetization $\boldsymbol{M}_0$ is approximated by the susceptibility χ_0 with $\boldsymbol{M}_0 = \chi_0\boldsymbol{H}(t)$. More generally, $\boldsymbol{M}_0$ might be defined via the Langevin function $\boldsymbol{M}_0 = m\boldsymbol{L}(\xi)$, which then also accounts for saturation in larger fields (→ Sec. 2.4.4).

2.4.3 Debye Model

For many applications (certainly for ACS and MPS), the applied field is a sine wave with amplitude H_0 and frequency $f = \frac{\omega}{2\pi}$, it can be denoted with:

$$\boldsymbol{H}(t) = H_0 \; e^{-i\omega t} \; \boldsymbol{e} \tag{2.30}$$

The harmonic excitation $\boldsymbol{H}(t)$ leads to an also harmonic change in magnetization $\dot{\boldsymbol{M}}$:

$$\dot{\boldsymbol{M}} = \frac{d}{dt}\boldsymbol{M}(t) = \frac{d}{dt}\boldsymbol{M}_0 \; e^{-i\omega t} = -i\omega \boldsymbol{M}(t) \tag{2.31}$$

Equating (2.31) with the effective field approximation (2.29), $-i\omega \boldsymbol{M}(t) = -\frac{1}{\tau} \; [\boldsymbol{M}(t) - \chi_0 \boldsymbol{H}(t)]$, and solving it for $\boldsymbol{\chi}(\omega) = \frac{\boldsymbol{M}(t)}{\boldsymbol{H}(t)}$ results in the Debye solution for the ac susceptibility [57, 112]:

$$\boldsymbol{\chi}(\omega) = \frac{\boldsymbol{M}(t)}{\boldsymbol{H}(t)} = \frac{\chi_0}{1 + i\omega\tau} \; \boldsymbol{e} \tag{2.32}$$

Eq. (2.32) is derived in the low-field limit and the initial magnetic susceptibility χ_0 can be obtained from the initial slope L_0 of the Langevin function as follows:

$$\chi_0 = \frac{dM}{dH} \approx \frac{M_\mathrm{S}}{H} L_0(\xi) = \frac{\mu_0 M_\mathrm{S}^2 V_\mathrm{P}}{3 k_\mathrm{B} T} \tag{2.33}$$

In measurement practice, it is common to detect a real (in-phase) part χ' and an imaginary (out-of-phase) part χ'', which can be derived from (2.32) by complex conjugate expansion.

$$\chi' = \chi_0 \alpha = \chi_0 \frac{1}{1 + (\omega\tau)^2} \tag{2.34}$$

$$\chi'' = \chi_0 \beta = \chi_0 \frac{\omega\tau}{1 + (\omega\tau)^2} \tag{2.35}$$

The expressions for α in (2.34) and β in (2.35) are representative for the Debye model. They are essentially pre-factors for the real and imaginary part of the susceptibility multiplied with the initial, frequency-independent susceptibility to obtain the frequency-dependent susceptibility. The factors are depicted in Fig. 2.14. There is a pronounced maximum in the imaginary part found at $\omega\tau = 1$ and $\chi'' = 0.5$. Its position is independent

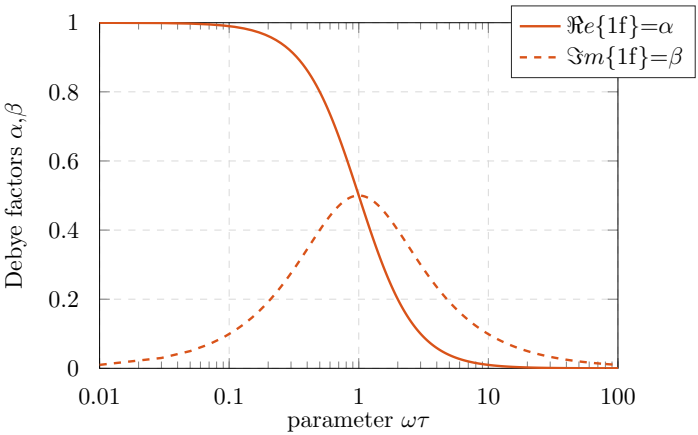

Figure 2.14: Real and imaginary part of the (normalized) Debye susceptibility as a function of $\omega\tau$.

of the MNP concentration and allows one to determine the effective/average time constant of the particles from a simple peak search. At the maximum of the imaginary part, the real part has dropped (from $\chi' = 1$ at small $\omega\tau$ values) to $\chi' = 0.5$, and continues to decrease towards larger $\omega\tau$.
Finally, a magnetization model $\boldsymbol{M}$ can be constructed from (2.32) applying a sinusoidal excitation (2.30) with an amplitude H_0 in the small-field limit, and the magnetization $\boldsymbol{M}_1$ (of the fundamental frequency) is denoted as follows:

$$\begin{aligned}
\boldsymbol{M}_1(t) &= H_0\ \chi(t)\ \boldsymbol{e} \\
&= H_0 \left[\chi' \cos(\omega t) + i\ \chi'' \sin(\omega t)\right]\ \boldsymbol{e} && \text{(2.36a)} \\
&= H_0 \chi_0 \left[\underbrace{\frac{1}{1+(\omega\tau)^2}}_{\alpha} \cos(\omega t) + i \underbrace{\frac{\omega\tau}{1+(\omega\tau)^2}}_{\beta} \sin(\omega t) \right] \boldsymbol{e} && \text{(2.36b)}
\end{aligned}$$

The Debye model, although it has the notion of parallel and perpendicular field components and time constants, is derived for a 1-dimensional excitation signal and the detection axis is identical/parallel to the axis of the excitation field. This principal direction is thereby denoted as $\boldsymbol{e}$ in equations (2.30) - (2.36).

In frequency space, the model simplifies to a single component at the excitation frequency:

$$\boldsymbol{M}_1(\omega) = H_0 \chi_0 \left(\alpha + i\beta\right) \ \boldsymbol{e} \tag{2.37}$$

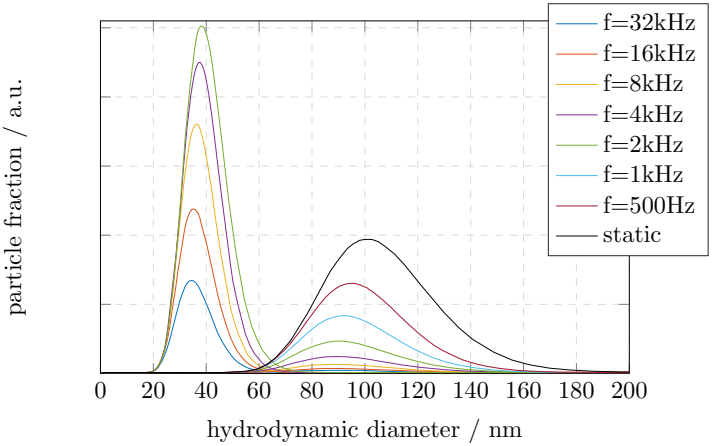

Figure 2.15: Effective size distribution of two samples (in different size ranges around 40 nm and 100 nm) for different excitation frequencies.

Since the time constant τ is a function of the particle diameter (via the Néel (Sec. 2.2.1) or Brownian (Sec. 2.2.2) time constant), the Debye factors α and β can be interpreted as a filter on the size distribution. Depending on the excitation frequency of an ACS or MPS experiment, a different effective size distribution contributes to the signal. Fig. 2.15 depicts the effect for the case of Brownian relaxation. For low frequencies, the majority of the particles contributes to the measurement signal. At higher frequencies, the large particles disappear from the effective size distribution due to their limited magnetization dynamics, and the size maximum of the contributing particle shifts towards smaller diameters.

2.4.4 Non-linear Debye Approximation Model

With the Debye approximation (→ Sec. 2.4.3) a dynamic magnetization model is given for the case of small excitation amplitudes (small-field limit). The model is inherently linear in response to the ac field, i.e. only the fundamental frequency (identical to the excitation frequency) is observed. For application in MPS (→ Sec. 3), where the non-linear response of the particles to a large excitation field (several mT in amplitude) is of interest, the Debye model is of limited use.
The non-linear Debye Approximation has been formulated [113] in this

thesis to fill a gap, where the Fokker-Planck method (or Langevin equation) [57, 75, 104, 114] is too slow and compute-intensive for large-scale simulations or curve fitting application and where the linear models do not apply.
A common approach for introducing a non-linear response replaces the small-field susceptibility χ_0 with the linearized slope of the Langevin function:

$$\chi_0(t) = \frac{dM}{dH} \approx \frac{M_\mathrm{S} L\left(H_0 \cos(\omega t)\right)}{H_0} \tag{2.38}$$

This also migrates the time-dependence of the model into the Langevin function (→ Sec. 2.4.1), i.e. the non-linearity of the Langevin function translates into a magnetization response containing harmonic frequencies $n\omega$ of the excitation angular frequency $\omega = 2\pi f$. The dynamic magnetization $M(t)$ in response to large sinusoidal excitation fields is then given by:

$$\begin{aligned} \boldsymbol{M}(t) &= M_\mathrm{S} L(t)\ \boldsymbol{e} \\ &= M_\mathrm{S} L\left(H_0 \cos(\omega t)\right) \left[\underbrace{\frac{1}{1+(\omega\tau)^2}}_{\alpha} + i \underbrace{\frac{\omega\tau}{1+(\omega\tau)^2}}_{\beta} \right] \boldsymbol{e} \end{aligned} \tag{2.39}$$

Eq. (2.39) implicitly poses a basic assumption: the generation of higher harmonics in the Langevin function L is separate from the modulation of the spectrum with regard to the time constant τ. Furthermore, it also requires that there is a single dominant time constant representative for the entire particle system. In fact, originally the generation of harmonics is limited by the particle dynamics itself. Thus (2.39), being a macroscopic model, violates a fundamental connection at the microscopic level (see introduction of Sec. 2.4) in favor of a simplified model expression.
The modulation of the harmonics in (2.40) is found to be identical for all harmonic indices, i. e. the frequency-dependence of all higher harmonics is the same, and it is described by the Debye factors α (2.34) and β (2.35). For the special case of a negligible dc field, only odd harmonic components are detectable, and the real and imaginary parts of the odd magnetization harmonics $M_{2\mathrm{k}+1}$ can be written as a function of the Debye factors and the cosine series coefficients $a_{2\mathrm{k}+1}$ of the Langevin function:

$$\Re e\left\{M_{2\mathrm{k}+1}\right\} = a_{2\mathrm{k}+1} \frac{1}{1+(\omega\tau)^2} \tag{2.40a}$$

$$\Im m\left\{M_{2\mathrm{k}+1}\right\} = (-1)^k a_{2\mathrm{k}+1} \frac{\omega\tau}{1+(\omega\tau)^2} \tag{2.40b}$$

The expressions in (2.40) for the modulation terms do not include a dependence on k in agreement with the above observation. Therefore, an alternative modulation approach is required for MPS.

In equivalence to (2.36), the new model provides an expression where the n-th harmonic component of the magnetization M_n is given from the corresponding susceptibility χ_n:

$$\begin{aligned}\boldsymbol{M}_\mathrm{n}(t) &= H_0\ \chi_\mathrm{n}(t)\ \boldsymbol{e} \\ &= H_0 \left[\chi_\mathrm{n}^{'} \cos(n\omega t) + i\ \chi_\mathrm{n}^{''} \sin(n\omega t)\right]\ \boldsymbol{e}\end{aligned} \tag{2.41a}$$

Here, the modulation can be different for each higher harmonic component. From the perspective of a consecutive model, where the generation of harmonics is decoupled from a subsequent modulation of the same, a 'dampening' of the harmonics according to their position on the $\omega\tau$ axis might be expected. Because of the finite relaxation time of the particle ensemble, the response is bandwidth-limited and described by low-pass characteristics. In other terms, the limited temporal dynamics of the particles, given by the respective time constant τ, translate into a smaller bandwidth in the observed response spectrum [113]. By replicating the Debye factors over frequency, the 'dampening' is adjusted to adhere the requirement of a low-pass system:

$$\chi_\mathrm{n}^{'} = \chi_0 \alpha_\mathrm{n} = \chi_0 \frac{1}{1 + (n\omega\tau)^2} \tag{2.42}$$

$$\chi_\mathrm{n}^{''} = \chi_0 \beta_\mathrm{n} = \chi_0 \frac{n\omega\tau}{1 + (n\omega\tau)^2} \tag{2.43}$$

Eqs. (2.42) and (2.43) can also be derived from the effective field approximation (→ Sec. 2.4.2) as a solution to the differential equation with an excitation frequency of $n\omega$ (instead of ω).
In order to find a closed expression for the harmonics of the magnetization, the Langevin function is first expressed in terms of a Fourier series:

$$M_\mathrm{S} L(t) = \sum_{n=1}^{N} a_\mathrm{n} \cos(n\omega t) + b_\mathrm{n} \sin(n\omega t) \tag{2.44}$$

Without any dc field ($a_0 = 0$), again only the odd harmonics are observed and only real Fourier coefficients a_n are present. In general, a single complex-valued magnetization component F_n is denoted by the cosine a_n and sine b_n coefficients of the Fourier series (2.44):

$$F_\mathrm{n} \left\{M_\mathrm{S} L(t)\right\} = (a_\mathrm{n} + i b_\mathrm{n}) \tag{2.45}$$

The n-th harmonic component of the magnetization M_n can then be described as follows:

$$\begin{aligned}\boldsymbol{M}_\mathrm{n}(\omega) &= (a_\mathrm{n} + ib_\mathrm{n})\,(\alpha_\mathrm{n} + i\beta_\mathrm{n})\;\; \boldsymbol{e} \\ &= (a_\mathrm{n} + ib_\mathrm{n}) \left(\underbrace{\frac{1}{1+(n\omega\tau)^2}}_{\alpha_\mathrm{n}} + i \underbrace{\frac{n\omega\tau}{1+(n\omega\tau)^2}}_{\beta_\mathrm{n}} \right) \boldsymbol{e} \end{aligned} \tag{2.46}$$

The Debye factors α and β in Sec. 2.4.3 are replaced with adjusted Debye factors α_n (2.42) and β_n (2.43) for each frequency component, and the susceptibility is expressed in terms of Fourier coefficients $(a_\mathrm{n} + ib_\mathrm{n})$ of the Langevin function. In comparison with (2.40), the real and imaginary part of the n-th harmonic can be written as:

$$\begin{aligned}\Re e\,\{M_n\} &= (a_\mathrm{n}\alpha_\mathrm{n} - b_\mathrm{n}\beta_\mathrm{n}) \\ &= \left(a_\mathrm{n} \frac{1}{1+(n\omega\tau)^2} - b_\mathrm{n} \frac{n\omega\tau}{1+(n\omega\tau)^2} \right) \end{aligned} \tag{2.47a}$$

$$\begin{aligned}\Im m\,\{M_n\} &= (b_\mathrm{n}\alpha_\mathrm{n} + a_\mathrm{n}\beta_\mathrm{n}) \\ &= \left(b_\mathrm{n} \frac{1}{1+(n\omega\tau)^2} + a_\mathrm{n} \frac{n\omega\tau}{1+(n\omega\tau)^2} \right) \end{aligned} \tag{2.47b}$$

Here, the real and imaginary parts are functions on both (real and imaginary) Fourier coefficients. This means the phase of the harmonics not only depends on the time constant τ, typically the Brownian time contant τ_B of the particles, but also on the particle's core properties, which translate into Fourier coefficients via the Langevin function (→ Sec. 2.1.1).
Because (2.46) is not an established model, it was verified in comparison with results from a Fokker-Planck simulation [75]. The Fokker-Planck solution represents an independent reference model, that is considered an accurate description of MNP magnetization dynamics [57, 75, 104]. A comparison of the complex-valued spectra (from $1f$ up to $7f$) for the models in this chapter with the Fokker-Planck results is given in Fig. 2.16. Here, the τ-dependence of the model is shown as a function of viscosity in the Brownian time constant τ_B (as would be observed in a viscosity series (→ Sec. 3.3.3)).
The Langevin model (→ Sec. 2.4.1) only considers core parameters and no dependence on the time constant is modelled (→ Fig. 2.16a). In the

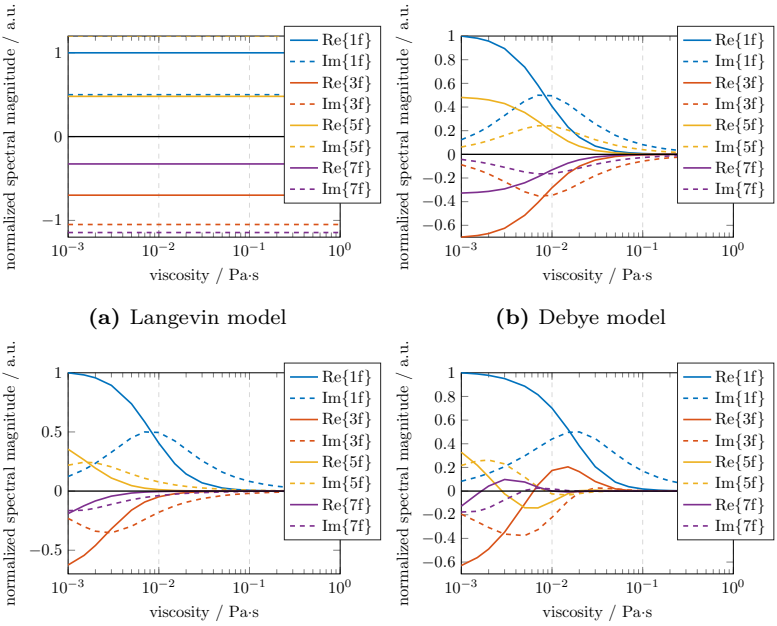

(a) Langevin model

(b) Debye model

(c) Non-linear Debye model

(d) Fokker-Planck model

Figure 2.16: Simulation results from Langevin, linear and non-linear Debye model in comparison with Fokker-Planck data ($d_c = 25\,\text{nm}$, $\sigma_c = 0.1$, $M_S = 250\,\text{kA/m}$, $d_h = 40\,\text{nm}$, $\sigma_h = 0.15$, $H_0 = 20\,\text{mT}$, $f = 1\,\text{kHz}$).

Debye model (→ Fig. 2.4.3) and the effective field model (→ Fig. 2.4.2) a single relaxation time constant is applied to all harmonics. Consequently, in Fig. 2.16b the modulation of the harmonic components over viscosity is identical for all harmonics, which is in conflict with experimental observations (→ Sec. 3.3.3) and with the results from Fokker-Planck simulations (→ Fig. 2.16d). The non-linear Debye approximation model (→ Sec. 2.4.4), with its dedicated time constants $n\tau$ for each harmonic frquency, gives a closest match to the Fokker-Planck reference (at a fraction of its complexity). However, non of the simple models is a replacement for the compute-intensive Fokker-Planck (or Langevin equation) simulations [64, 81, 101–104].

3 Magnetic Particle Spectroscopy

Magnetic particle spectroscopy (MPS) has been developed to supplement magnetic particle imaging (→ Sec. 4) (MPI) for particle characterization purposes [9, 26, 115–122]. MPI relies on the particles to generate higher magnetization harmonics if excited with a large-enough sinusoidal magnetic field. MPS builds on the same principle and allows the characterization of particle properties and provides insight into their MPI performance [9].
In contrast to ACS, MPS performs analysis beyond the small-field limit. It reveals the non-linearity of the magnetization curve (due to large excitation amplitudes) and it is consequently susceptible to the field-dependence of the relaxation time constants (→ Sec. 2.2). For that reason, MPS is a powerful tool for the characterization of MNPs, but it also makes MPS data more challenging to interpret correctly.

3.1 Basics

This section provides a review on MPS involving a description of the signal chain (transmit and receive chain), the signal generation process (particle response) and the basic engineering concepts for practical realization.
The physical principle of MPS is easily explained: A sinusoidal excitation signal is generated (Fig. 3.1a), amplified to a sufficient field amplitude ($\sim 20\,\mathrm{mT}$) in order to (at least partially) saturate the particles exposing a non-linear magnetization response (Fig. 3.1b). A pick-up coil is then used to derive a proportional induction signal (Fig. 3.1c), which reveals the higher harmonics after Fourier transform (Fig. 3.1d) into frequency space.
Generally, in (3.1) the exciting magnetic field $H(t)$ is composed of a sinusoidal component H_{AC} with frequency $f = \frac{\omega}{2\pi}$ and a static field component H_{DC}.

$$H(t) = H_{\mathrm{DC}} + H_{\mathrm{AC}} \cos(\omega t) \tag{3.1}$$

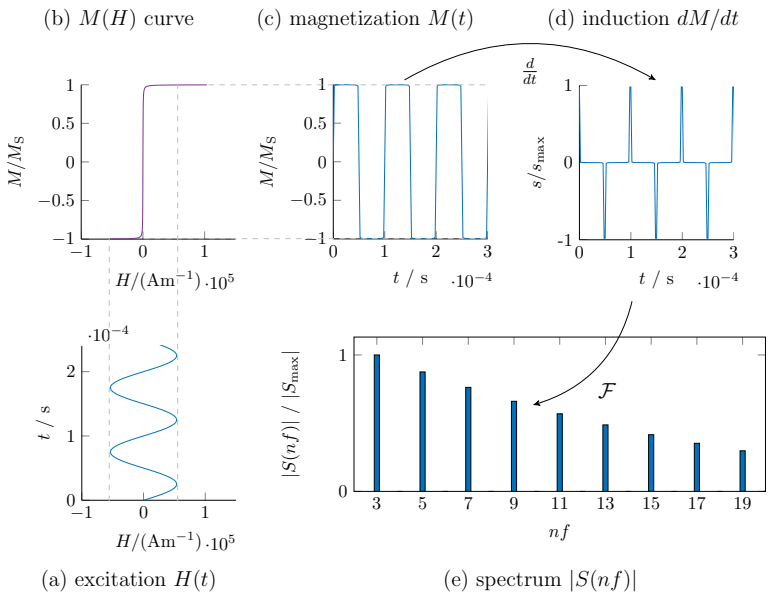

Figure 3.1: Basic principle of MPS: a sinusoidal excitation signal applied to the non-linear magnetization curve of the particles generates higher harmonics in the received induction signal.

The magnetization characteristics of the particles are described by the Langevin function of superparamagnetism (2.6) (→ Sec. 2.4.1). Inserting (3.1) into (2.6), and composing the resulting flux density $B(t)$ via (2.3a) obtains

$$\begin{aligned} B(t) &= \mu_0 \left[H(t) + M(t)\right] \\ &= \mu_0 H(t) + \mu_0 v_\mathrm{f} M_\mathrm{S} \left[\coth\left(\frac{\mu_0 m H(t)}{k_\mathrm{B} T}\right) - \left(\frac{k_\mathrm{B} T}{\mu_0 m H(t)}\right)\right] \end{aligned} \tag{3.2}$$

with the magnetic moment of the particles m, saturation magnetization M_S and volume fraction v_f. According to Faraday's induction law the detection signal $U_\mathrm{ind}(t)$ is proportional to the time-derivative of the magnetic flux density inside the pick-up coil:

$$U_\mathrm{ind}(t) = -N \frac{\mathrm{d}\Phi}{\mathrm{d}t} \tag{3.3a}$$

$$= -\sum_{\mathrm{x}\in\mathrm{V}} S(x) \frac{\mathrm{d}}{\mathrm{d}t} B(x,t) \tag{3.3b}$$

$$= -S_\mathrm{x} \frac{\mathrm{d}}{\mathrm{d}t} B(t) = -\mu_0 S_\mathrm{x} \frac{\mathrm{d}}{\mathrm{d}t} \left[H(t) + M(t)\right] \tag{3.3c}$$

In (3.3b) the time-derivative of the flux density $B(x,t)$ is multiplied with the spatial coil sensitivity $S(x)$ of the volume coil (calculated from Biot-Savart's law and the law of reciprocity, i.e. spatial magnetic field for unit current), so that the induction voltage is obtained from all field contributions over the sensitive volume V [123–125]. For a fixed geometry of the detection coil and homogenous sensitivity profile (or fixed sample geometry and position), the coil constant $S(x)$ can be expressed by a single constant factor S_x.
The flux density $B(t)$ and its time-derivative not only include the particle's magnetization $M(t)$ but also the exciting magnetic field $H(t)$. This is called 'direct feed-through' ($\frac{\mathrm{d}}{\mathrm{d}t}H(t)$ in (3.3c)) and expresses the fact that the fundamental frequency in the received signal is dominated by the excitation field (inductive coupling between excitation and detection coils), especially since for all relevant samples the volume fraction of particles in the sample is small ($\leq 1\%_\mathrm{vol}$) and with it the total magnetization $M(t)$.

Generally, the induction signal (as all periodic signals) can be written as a Fourier series. In the special case of a point-symmetric response (e.g. no dc offset), the induction voltage can be written as a cosine- (or sine-) series (3.4a), which makes it simple to find the time-derivative (3.4b) and to denote the individual frequency components a_n contained in the signal.

$$U_\mathrm{ind}(t) = -S_\mathrm{x} \frac{\mathrm{d}}{\mathrm{d}t} \sum_n a_\mathrm{n} \sin(n\omega t) \tag{3.4a}$$

$$= -S_\mathrm{x} \sum_n a_\mathrm{n} n\omega \cos(n\omega t) \tag{3.4b}$$

The harmonic spectrum $F(\omega)$, obtained by applying the Fourier-transform to the voltage readout $U_\mathrm{ind}(t)$, is therefore given by:

$$F(\omega) = \mathrm{FFT}\ \{U_\mathrm{ind}(t)\} = \mathrm{FFT}\ \left\{-S_\mathrm{x} \frac{\mathrm{d}}{\mathrm{d}t} B(t)\right\} \tag{3.5a}$$

$$= -S_\mathrm{x} \sum_n a_\mathrm{n} n\omega \tag{3.5b}$$

As visualized in Fig. 3.1d, the spectrum consists of the fundamental frequency (originally exposed to the sample) and a number of higher harmonic components. In the case of purely harmonic excitation ($H_\mathrm{DC} = 0$) due to point-symmetry of the magnetization curve $M(H)$ to the origin only the odd harmonics are present in the frequency spectrum.
Assuming an idealized step-response of the particles (instead of a Langevin function), the induction voltage is a periodic rectangular signal, revealing again only odd harmonic components with their spectral magnitudes

decreasing with $1/n$. However, due to induction law, which 'amplifies' signal components proportional to their frequency $n\omega$, a constant spectrum of odd harmonic components is be observed. For actual particles (with Langevin magnetization), we still find a pronounced decay in spectral magnitude towards higher harmonic indices.
It should be noted, that for the excitation function in (3.1) cosine and sine are interchangeble. Except, that applying an odd excitation function (i.e. sine) to the Langevin function (an odd function itself), results in an odd imaginary spectrum. However, an even excitation function (i.e. cosine) leads to a real spectrum.

3.2 Hardware

Hardware components required to build up an MPS system are dictated by the measuring principle (→ Sec. 3.1). Three main component blocks are generally proposed:

- Transmit components (Tx)
- Receive components (Rx)
- Coils system

Figure 3.2 provides a block diagram of the MPS components.

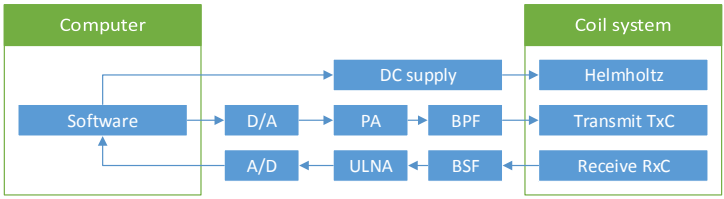

Figure 3.2: Block diagram of the MPS hardware components.

On the transmit side (Tx), the excitation signal is synthesized by a D/A converter card (Fig. 3.2, D/A). It is then amplified by a power amplifier (Fig. 3.2, PA) and passed through a passive band pass filter (Fig. 3.2, BPF) to improve spectral purity in order to drive the transmit coil (Fig. 3.2, TxC).
On the receive side (Rx), a receive coil (Fig. 3.2, RxC) is used as an inductive detector. It picks up the particle signal and the inductively coupled excitation signal from the transmit coil. A passive band stop filter (Fig. 3.2, BSF) rejects the (residual) fundamental frequency component before the detection signal is enlarged using a (ultra-)low-noise amplifier (Fig. 3.2, ULNA) and finally digitized by an A/D converter card (Fig. 3.2, A/D).

The measurement setup for MPS has been improved over time. While the fundamental design has not changed, individual components were replaced with newly designed or acquired ones. Power amplifiers, filter capacitors and coils system have gradually evolved. Because experiments (→ Sec. 3.3) were conducted at different states of the MPS evolution, Tab. 3.1 provides an overview of the MPS generations. Detailed description of individual components (Sec. 3.2.1 and Sec. 3.2.2) are only given for the latest generation in this thesis.

Table 3.1: Overview of MPS devices and generations.

	Generation 1	Generation 2	Generation 2b
H_{typ}	12.5 mT	25 mT	
f	arbitrary (2 kHz)	0.5 – 10 kHz	
D/A	NI PCI-6733 (1 MHz, 16 bit)		
PA	Custom (470 W, <0.04 %)	Omnitronic P-2000 (1000 W, <0.01 %)	Synq Digit 3K6 (1800 W, <0.04 %)
BPF	none	series	series + parallel
TxC	N = 3x270 (386.9 µH, 3.02 mT/A)	N = 4x360 (687.8 µH, 4.53 mT/A)	
RxC	N = 30/37 (320.0 nH)	N = 40/42 (677 nH)	
A/D	NI PCI-4462 (205 kS/s, 24 bit)	NI PCI-6133 (2.5 MS/s, 14 bit)	

The measurement setup is designed to fit our polystyrene sample vials (Nunc-immuno™ C8 PolySorp™ BreakApart™ modules #473539) with 250 µL working volume for adsorption of hydrophobic molecules (typical sample volume is 150 µL).

3.2.1 Coils

Figure 3.3 provides a schematic view of the spectrometer setup which consists of 3 coils: (a) the transmit coil (TxC) is constructed as a single elongated coil or solenoid, (b) the detection coil (RxC) is designed as a pair of differential receive coils and (c) the static field coils are arranged in a Helmholtz-type configuration.
A photograph of the MPS coils system is given in Fig. 3.4. It shows the frame and coil carriers of the MPS setup, which are made of plastic (Polyvinylchloride, PVC) to not interfere with magnetic fields, along with the copper windings of the coils.

Transmit Coil (TxC)

In order to periodically drive the particles under observation into the non-linear range of their magnetization curve, a drive field in the order of several mT is required. The original design (Tab. 3.1, Gen. I) allowed a

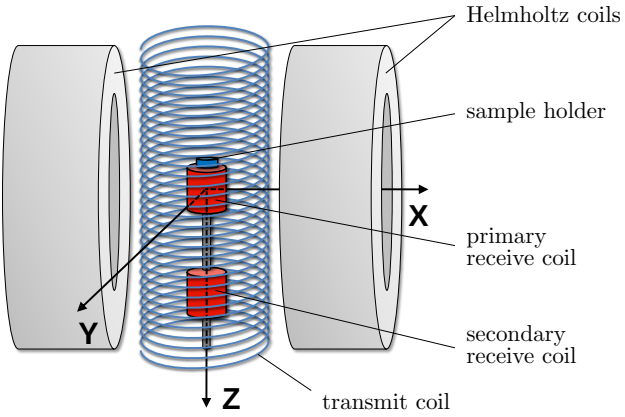

Figure 3.3: Schematic drawing of the MPS coils assembly.

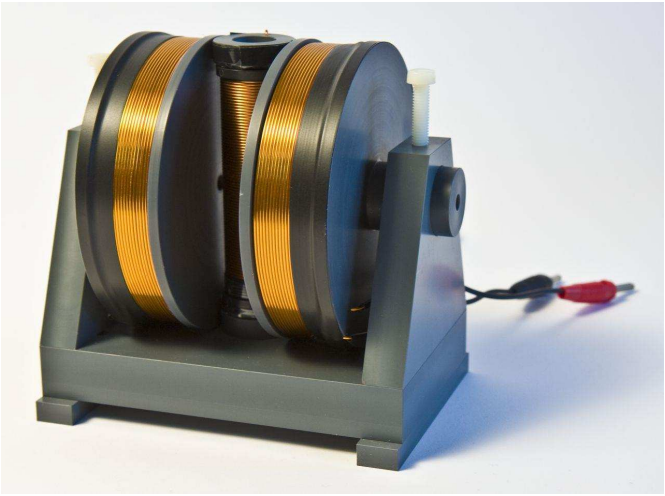

Figure 3.4: Photo of the MPS coils assembly.

drive field amplitude of 12.5 mT, but later designs settled on larger fields around 25 mT as a standard field requirement. Table 3.2 specifies the parameters of the transmit coil.

Table 3.2: Specifications of the MPS transmit coil TxC.

Wire gauge	0.79 mm^2 (⌀ 1 mm)
Radius (effective)	11 mm
Length	90 mm
Windings	360 (4 x 90)
Layers	4
Inductance	687.87 µH
Coil constant	4.53 mT/A
Current (typ.)	5 A ($\widehat{=}$ 22.65 mT)

The transmit coil is designed to homogeneously cover the differential detection coils (→ Sec. 3.2.1, differential receive coil (RxC)) and its contained sample.
Originally designed for 2 kHz, the transmit coil is made of solid copper wire of 1 mm diameter. Losses from eddy currents and the skin effect are in a range to permit operation up to 10 kHz and 25 mT. The coil carrier is made of PEEK (polyetheretherketone) to withstand the thermal stress. The transmit coil losses range from 25 W at 1 kHz to about 90 W at 10 kHz. Later designs (and the MPI coils) are made of Litz wire to accommodate high thermal losses.

Differential Receive Coil (RxC)

In order to deal with the 'feed-through' from the transmit coil (and the associated harmonics from the power amplifier), a differential pair of induction coils is used as the receiving detection coil arrangement [126]. The receive coil (RxC) specifications are given in Tab. 3.3.

Table 3.3: Specifications of the differential MPS receive coil RxC.

Wire gauge	0.2 mm^2
Radius (approx)	2.5 mm
Length (each)	7 mm
Coils distance (mean)	30 mm (adjustable)
Windings Sample	40
Windings Reference	42

Two coils with opposing sense of winding, approximately the same number of turns, are aligned along the axis and symmetrical to the center of the transmit coil. One coil is being equipped with the sample (i.e. sample coil or primary receive coil) and the second coil is used for compensation (i.e. reference coil or secondary receive coil). The excitation field

induces a voltage with opposite signs into the two coils of the detection arrangement, canceling all contributions from the transmit side. In practice, the balance of the differential coils is limited by geometrical precision (i.e. alignment with transmit coil and homogeneity of the drive field) and parasitic elements (i.e. capacitive coupling). For improved excitation field homogeneity at the sample position, both coils are shifted from their symmetrical arrangement towards one end of transmit coil. From this, the sample coil gets closer to the near-homogeneous center of the transmit coil, while the reference coil is pushed out to the border area of the transmit coil. The resulting imbalance (about 18 % of maximum) is compensated for with a few additional windings on the reference coil. For fine adjustments the compensation coil was designed to allow for small positional variations along the axis relative to the sample coil, although in practice no adjustments were made.
The distance between the sample and the reference coil determines the residual signal from the sample that is still detected from the differential coil pair. At 3 cm distance in this setup a residual signal of 0.23 % (at the borders) and 0.08 % (at the center) were calculated from a FEMM simulations (D. C. Meeker, Finite Element Method Magnetics) [127].

Static Field Coil

In MPI a magnetic field gradient is used for spatial encoding (→ Sec. 4.1.1). With the static field coils in the MPS design, some positions according to different static field levels can be simulated. The static field coils are oriented perpendicular to the transmit and receive coils. They are built as a Helmholtz-type coil pair, which has the advantage of generating a homogeneous field between the pair while providing enough space to install the transmit solenoid. Generally, a static field parallel to the ac field can be applied by superimposing a dc current to the excitation signal (in congruence to a 1D MPI scan along the x-axis, → Sec. 4.5.1). The orthogonal arrangement was chosen since it allows one to study arbitrary configurations between ac and dc background field as it is important for MPI. The specifications of the static field coils are given below (→ Tab. 3.4).

Table 3.4: Specifications of the static field coils in MPS.

Wire gauge	$0.79\,\mathrm{mm}^2$ ($\varnothing$ 1 mm)
Radius (effective)	49 mm
Coils distance (mean)	49 mm
Windings	200
Layers	10
Coil constant	3.12 mT/A
Current (continuous)	4 A ($\widehat{=}$ 12.5 mT)
Current (duty-cycled)	8 A ($\widehat{=}$ 25 mT)

The coils satisfy the conditions for a Helmholtz-type pair (radius of each coil = distance between coils). The effective radius and diameter have been manually optimized from a FEMM magnetic field simulation. The static field coils can be operated at up to 25 mT (equivalent to 8 A) for a limited duration. The high current density of $10\,\mathrm{A/mm^2}$ is feasible for duty-cycled operation only and a continuous current of 4 A or 12.5 mT should not be exceeded in order to stay within the thermal margins of about $3 - 5\,\mathrm{A/mm^2}$. Static field coils are powered by a dc voltage/current source (EA Elektro-Automatik EA-PS 5016-20, 16V/20A).

3.2.2 Signal Chain (Electronics)

A magnetic particle spectrometer has a signal chain equivalent to that of an MPI scanner (→ Sec. 4.2). However, due to a convenient filling factor for the sample inside the receive coil (RxC), simplifications can be made especially on the receive side.
For the transmit side, the excitation signal is generated at the workstation by a D/A converter card NI PCI-6773 (1 MS/s, 16 bit). The signal is then amplified with a standard audio amplifier Synq Digit 3K6 (1800 W) and passed through a passive band-pass filter (see below) to drive the MPS's transmit coil (TxC). In order to keep a well-defined current through the transmit coil, the current flow is monitored with an ac current sensor Allegro ACS750xCA-050 [128, 129]. The signal is used to form a control loop and to set the amplitude of the generated excitation signal.
To obtain a sinusoidal signal with high spectral purity, the passive band-pass filter between the power amplifier and the transmit coil is crucial. The typical filter design includes a combination of an LC series and parallel resonating band-pass. For the MPS, a simple design is used, where the inductive component of the LC filter is provided by the transmit coil itself. Series resistance R_{in} and the capacitive divider $C_{\mathrm{p}}/C_{\mathrm{s}}$ help to match the load inductance to the amplifier, while R_{in} and C_{p} also form a low-pass filter for the unwanted harmonics from the power amplifier. Figure 3.5 gives the circuit diagramm of the transmit filter.

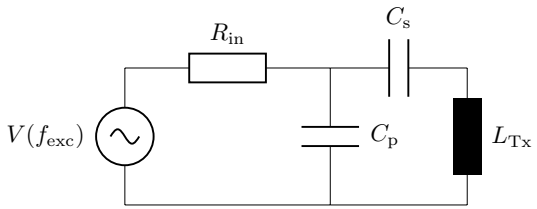

Figure 3.5: Transmit filter of the MPS.

The detection signal from the differential receiver pair, which cancels most of the feed-through, is amplified and leveled or directly connected to an A/D converter card NI PCI-6133 (2.5 MS/s, 14 bit). Since we are interested in the complex-valued spectrum, a phase-locked acquisition of the time-domain signal is performed.

3.3 Applications

The following section provides insights into some MPS applications. It uses the MPS measuring system designed and introduced in the previous section (→ Sec. 3.2). Unless noted otherwise, the MPS is operated at 10.05 kHz and a field amplitude of 25 mT, 2×10^6 samples are acquired at a sampling rate of 2 MS/s, resulting in a total measuring time of 1 s.

Nanoparticle Samples

In context of the application section various different iron oxide nanoparticles are considered. Depending on the manufacturer and/or the target application, the magnetic nanoparticles are sometimes referred to as 'contrast agent' or 'tracer'. The main differentiation here is that a contrast agent increases and improves the pre-existing native contrast of the imaging modality. A tracer generates contrast where there was none before. From that perspective, MPI is a tracer-based imaging modality, because it requires magnetic nanoparticles as a tracer to generate contrast, whereas MRI and CT show native tissue contrast without the contrast agent. That said, most commercially available superparamagnetic nanoparticles were originally designed as a contrast-enhancing agent. This is also true for the omnipresent Resovist® (or its 'drop-in' replacement FeraSpin™ R). For that reason, the datasheets typically refer to the material as a contrast agent, although in context of MPI it is actually a tracer.
The following list gives an overview of some iron oxide nanoparticles used in the MPS applications section.

FeraSpin™ R (nanoPET Pharma)

FeraSpin™ R is an MRI contrast agent, manufactured by nanoPET Pharma GmbH (Berlin, Germany). FeraSpin™ exhibits a multi-core structure made of small 5 – 6 nm crystallites. The particles were found to be very stable, both long-term as well as in a large variety of different media. FeraSpin™ R also generates one of the richest MPS spectra, except for some MPI-tailored particles, and it is used as 'default' tracer in all our MPI experiments.

ShortName	FSxx
Coating	dextrane
Core diameter d_c	5 – 6 nm (TEM)
Hydrodyn. diameter d_h	10 – 90 nm (typ. 60 nm)
Iron concentration	70 mg/mL

SHP-25 (Ocean NanoTech)

The SHP series from Ocean NanoTech (San Diego, CA, USA) are single core particles with a narrow core size distribution. They are most suitable as a model particle system in MPS.

ShortName	ONxx
Coating	carboxylic acid
Core diameter d_c	25 nm (TEM)
Hydrodyn. diameter d_h	32 nm
Iron concentration	5 mg/mL

fluidMag 12 (P)AS (chemicell)

The fluidMag series from chemicell GmbH (Berlin, Germany) was designed for MRI diagnostics and magnetic drug targeting applications. The particles have a multi-core structure with a broad size distribution. The product is also available in a streptavidin-functionalized variant (ShortName: CCCR).

ShortName	CCAx
Coating	polyacrylic acid
Core diameter d_c	12 nm (TEM)
Hydrodyn. diameter d_h	100 nm
Iron concentration	25 mg/mL

3.3.1 Particle Characterization

Figure 3.6 shows a basic magnetization response spectrum measured on a reference sample of FeraSpin™ R with default parameters. FeraSpin™ R is an equivalent replacement for the discontinued Resovist® (→ Sec. 3.3), which has been used during the development of MPI. FeraSpin™ generates a rich harmonic spectrum despite the small crystallite size of typ. 5 nm; its clustered structure generates a much larger effective magnetic moment [90, 91].
In Fig. 3.6 the odd harmonic components ($3f$, $5f$, $7f$, ...) of the received spectrum are shown. The even harmonics are typically not considered in MPS (in contrast to MPI), because without a dc field component the even harmonics are ideally non existent. Because our MPS setup uses differential receive coils instead of a band-stop filter, the fundamental frequency $1f$ is accessible in addition to the higher harmonics. The MPS spectrum gives a characteristic harmonic decay for a particle sample, FeraSpin™ R in this case.
Comparing a water-based sample (Fig. 3.6, FSR-B) of the particles with a freeze-dried immobilized sample (Fig. 3.6, FSR-N/FD) of the same batch, it is apparent that the first few harmonics are close, but at the higher harmonics there is a strong effect of the immobilization. From embedding the particles into a D-Mannitol sugar matrix one effectively blocks the Brownian rotation, i.e. the particles are immobilized within the matrix, and only the internal Néel relaxation mechanism is contributing to the spectrum. The label "N/FD" in Fig. 3.6 is short for a Néel-dominated sample from freeze-drying (FD). Immobilization is a powerful tool to separate the Brownian and Néel contributions (applicable – of course – to

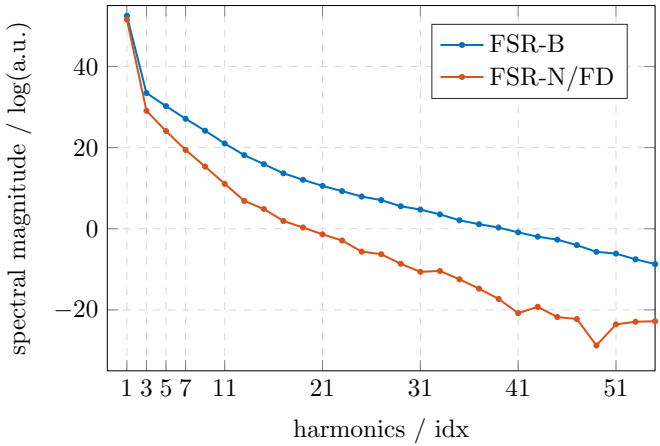

Figure 3.6: Reference MPS spectrum of FeraSpin™ R (B = suspension, N/FD = freeze-dried Néel sample) showing the odd harmonic components.

other magnetic characterization techniques (ACS, MRX, etc.) as well).
Note: Because the system is not calibrated to the unit of magnetic moment, the spectral magnitude (or real and imaginary ampitude) are typically given in arbitrary units. However, the data is only rescaled from the raw spectrum, which is given in dB Volts (dB_V, 1 V reference) so the ordinate of the plots is still in logarithmic scale.
The simplest evaluation of the spectrum involves a linear regression ($ax+b$) analysis on the first few harmonics. The harmonic decay is representative of the average particle core size according to the Langevin model (→ Sec. 2.4.1). A slightly more sophisticated version uses a second-order polynomial ($ax^2 + bx + c$), which also captures the change in slope around the 10th harmonic index (→ Fig. 3.6), which is typically observed for multicore particles only (these particles often show a bimodal size distribution). Alternatively, to obtain a core size distribution, the harmonic spectrum is fitted (in least-squares sense) with one of the dynamic magnetization models introduced in Sec. 2.4.
For all applications, but especially for applications of the MPS system for bio-/immunoassays, the stability of the measuring setup and its sensitivity for small concentrations are of great importance. The reproducibility of the MPS results has been studied from repeating measurements on the same 150 µL (standard volume) sample Ocean NanoTech SHP-25 under identical measurement conditions. It was found to be around 0.50 % (with intermittent sample replacement) and therefore qualifies for binding experiments, where the tolerance should be below 1 %. The system stability is also greatly affected by temperature changes. For series measurements, a duty cycle is introduced to keep thermal impact on the measurement results minimal. DIN 32645 defines the concentration limit for a system where the signal scales linearly with the analyte concentration and

a normal distribution of measurement points is assumed. The limit of determination [130], i.e. the minimal amount detectable by the system, and the limit of detection, i.e. the smallest quantifiable amount, have been determined for the MPS system. Because in MPS (and MPI) the detection signal, its spectral magnitude and the harmonic decay depend greatly on the given sample, a worst-case assessment has been conducted. For that, a chemicell fluidMag 12 (P)AS sample was prepared as a dilution/concentration series. The MPS results on that series are depicted in Fig. 3.7.

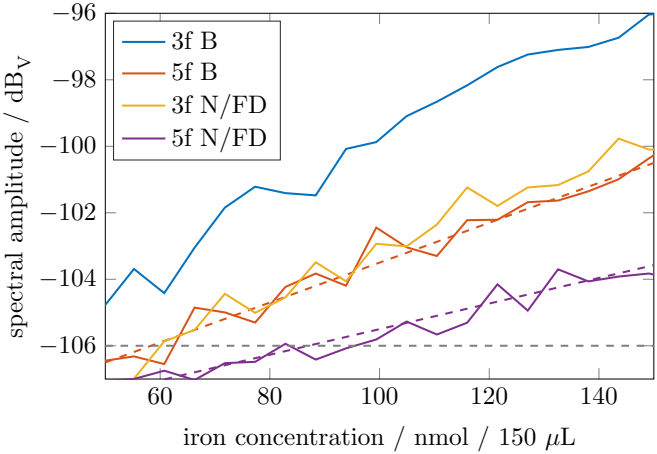

Figure 3.7: Limit of determination/detection: 3rd and 5th harmonic of mobile (B = suspension) and immobilized (N/FD = freeze-dried Néel sample) concentration series on fluidMag 12 (P)AS. Dotted line is guide to the eye.

We assume, that at least the 3rd and 5th harmonic must be determinable, so that a linear regression analysis is possible (for fitting purposes, i.e. size distribution, at least 5 to 10 harmonics are needed). Figure 3.7 shows the 3rd and 5th harmonic for a mobile sample (Fig. 3.7, B) and immobilized sample (Fig. 3.7, N/FD) tending towards the noise floor ($-106\,\mathrm{dB_V}$). The corresponding value for concentration limits are given in Tab. 3.5.

Table 3.5: Limits of determination and detection of the MPS V2 on fluidMAG 12.

	Limit of detection	Limit of determination
mobile	55.2 mM (3.1 mg/mL)	44.2 mM (2.4 mg/mL)
immobile	81.0 mM (4.5 mg/mL)	66.1 mM (3.7 mg/mL)

The MPS V2 system was not optimized for sensitivity, e.g. it supports a relativly large volume of 150 µL in order to be compatible with most of the other MNP characterization setups in the institute. However, the observed limits are reasonable for measuring immunoassays and viscosity or dilution series derived from concentrated MNP solutions. Also, the above plot shows the quantitative properties of the MPS (and MPI) technique.

The typical representation of MPS data, as displayed in Fig. 3.6, shows the spectral magnitude of the detection signal as a function of the harmonic index. Although such a plot is sufficient for characterization purposes of the particles, it does not reveal some details hidden in real and imaginary part of the same spectrum. A complex-valued picture is given in Fig. 3.8. Especially with regard to binding processes (or viscosity changes), the complex-valued harmonics plot is advantageous, because it exposes the phase relations of the harmonics which are directly related to the magnetization dynamics of the particles. For a mobile sample the real and imaginary parts show an interlacing pattern, which on a non-logarithmic scale would have opposite signs.

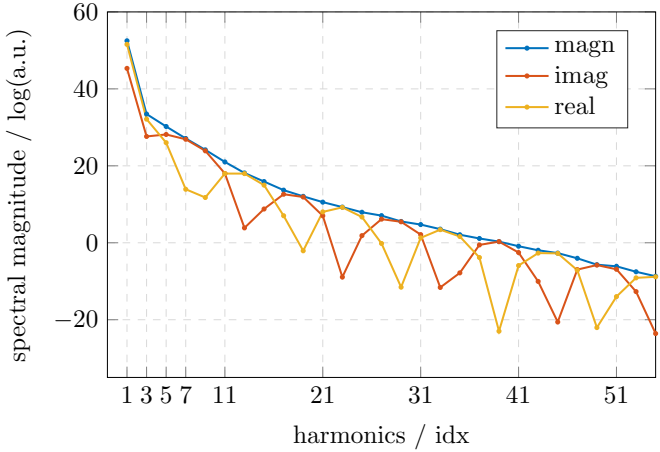

Figure 3.8: Reference spectrum (complex-valued view) of FeraSpin™ R (magn = magnitude, imag = imaginary part, real = real part) showing the odd harmonic components.

Alternative to a simple harmonic plot, the data obtained from an MPS measurement can be used to reconstruct a dynamic magnetization curve $M(H)$ or the data can be converted into a dynamic susceptibility $\mathrm{d}M/\mathrm{d}H$ view. The susceptibility plot is equivalent to the point spread function in 1-dimensional x-space MPI (cp. Fig. 4.69) and it provides an intuitive way for understanding the magnetization process of the particles.

Reference Characterization Methods

The methods of ac susceptometry (ACS) and magnetorelaxometry (MRX) are well understood and they are used as a reference for the analysis of the particles response in comparison with MPS. In ACS, the particles are exposed to an ac magnetic field of small amplitude (typically 100 µT or less) resulting in a magnetization response from the linear range of the magnetization curve. The fundamental frequency (identical to the applied excitation field frequency) is recorded and the susceptibility (slope of the magnetization curve) of the sample is calculated. A full ac susceptibility measurement includes a frequency sweep, where the linear susceptibility is obtained as a function of frequency. The resulting ACS spectrum can be interpreted using the Debye magnetization model (→ Sec. 2.4.3) [131].

Magnetorelaxometry (MRX) is a time-domain method. The particle sample is exposed to a static magnetic field in the order of 2 mT and the particle's magnetic moments align to the field according to the Langevin function (→ Sec. 2.1.1). Once the magnetization field is switched off (in about 100 µs) the magnetic moments of the particles relax to zero. The exponential decay of the magnetization expresses the relaxation time constant of the particles. MRX is used for characterization purposes, but is also highly useful for performing bio-/immuno-assays on magnetic nanoparticles [132–137].

3.3.2 MultiVariate MPS

Multivariate MPS describes the idea, that additional information, beyond the core size or core size distribution, can be extracted from an MPS experiment, if the sample is measured multiple times under different measurement conditions [138–140]. The parameters of interest are the dc field level and the ac excitation amplitude and frequency [141, 142].
For that, the MPS V2 is equipped with Helmholtz-coils to generate a static field and the excitation frequency is switchable between multiple fixed frequencies. With the setup it is then possible to measure the generation of higher harmonics in dependence of the excitation signal amplitude H_{AC} (0 – 25 mT) and the field strength H_{DC} of the static offset field (0 – 30 mT) for different excitation frequencies $f = \omega/2\pi$ (0.49 kHz, 1.30 kHz, 2.11 kHz, 3.85 kHz, 6.43 kHz and 9.96 kHz).
All experiments in this section were performed on a 150 µL (standard volume) sample of Ocean NanoTech SHP-25.

Parameter: DC Field

Figure 3.9 shows the rise of the even harmonics with increasing static offset field amplitude. Due to the symmetry of the Langevin function no even harmonics are expected at zero static field. As can be seen the increase of the curves is still present at 30 mT. For larger particles or at

higher field values (outside the measurement window), the rising slope of the even harmonics reaches a maximum followed by a decay. The odd harmonics are not shown here, but in contrast to the even harmonics, they start at high spectral magnitude and steadily decline with increasing static field to below the noise floor. For a parallel orientation of the ac and dc fields, the dc field dependence is equivalent to the encoding scheme of a 1-dimensional MPI experiment, where the dc field level at a given point in the field of view is specified by the selection field.

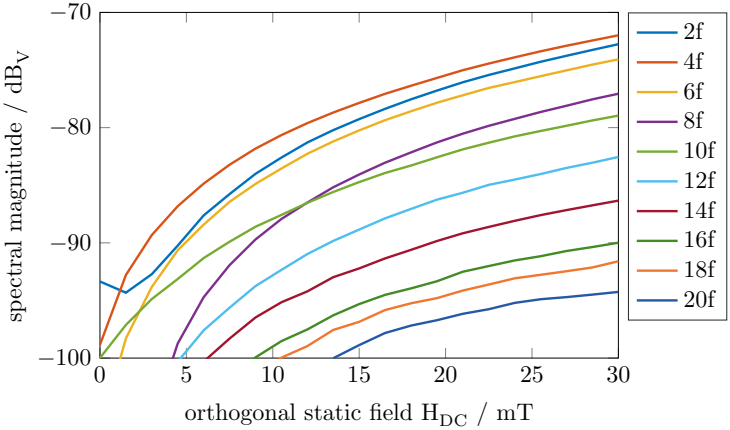

Figure 3.9: Orthogonal DC field dependence of the harmonic spectrum (even harmonics only) measured with $H_{AC} = 20\,\mathrm{mT}$ and $f = \omega/2\pi = 9.96\,\mathrm{kHz}$.

Parameter: AC Field

Figure 3.10 shows the dependence of the harmonic's spectral magnitude on the ac field amplitude. The amplitude of the ac field is responsible for the generation of higher harmonics. For small ac amplitudes the particles are excited in the linear range of their magnetization curve and only the fundamental frequency is evident in the harmonic spectrum. For larger ac amplitudes the particles are driven into the non-linear region of their $M(H)$ curve and higher harmonics are expressed.

Parameter: AC Frequency

Ac- and dc-field amplitudes have strong influence on the magnetization state of the core, and therefore they are connected to the core diameter [143]. In contrast, the hydrodynamic diameter of the MNPs comes into play via the Brownian relaxation time τ_B. Consequently, information on the hydrodynamic particle size can be obtained from the excitation

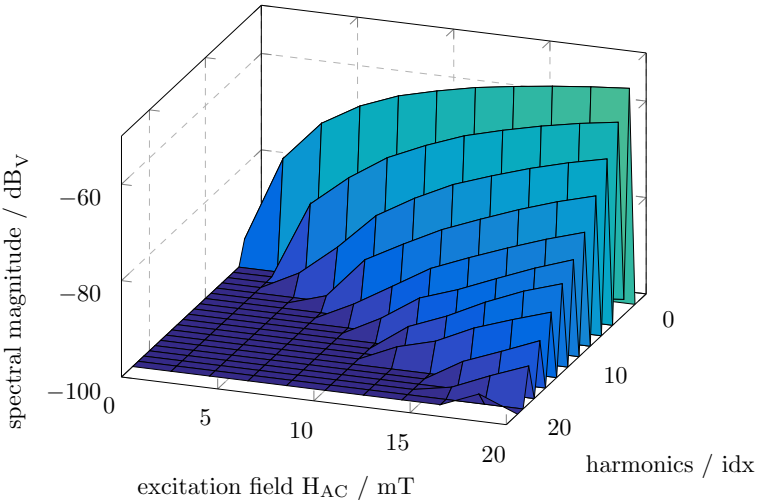

Figure 3.10: AC field dependence of the harmonic spectrum excited at $f = \omega/2\pi = 9.96\,\mathrm{kHz}$ ($H_{DC} = 0$).

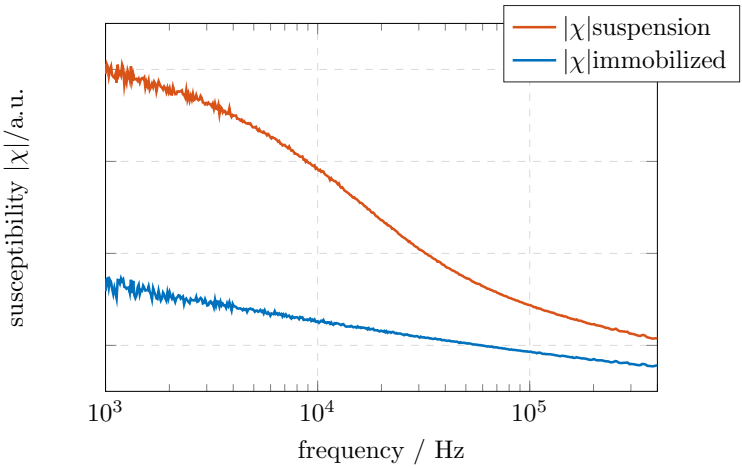

Figure 3.11: Magnitude of ac susceptibility (excitation field amplitude $H_{AC} = 95\,\mu\mathrm{T}$) measured on mobile (suspension) and immobile SHP-25 particles.

frequency dependence of the harmonic spectra measured on the MNP suspension – proposed that the MNP's magnetic moments are at least partially blocked, i.e. $\tau_B < \tau_N$. To explore the excitation field frequency dependence, the excitation frequency should be in the range of the Brownian characteristic frequency.
To illustrate this point, Fig. 3.11 depicts the magnitude of the ac susceptibility (ACS) measured with our high-frequency ac susceptometer [131]. It is clearly seen that – for a suspension of the SHP-25 nanoparticles – the absolute value of the susceptibility drops significantly around 10 kHz. This loss in amplitude can be conceived from the limited hydrodynamic mobility of the particles. The transition frequency for a Brownian particle is high for small particles and it is shifted to lower frequencies with increasing hydrodynamic particle diameter. For comparison, the ACS spectrum is also shown for SHP-25 particles immobilized by freeze-drying, so that Brownian motion is inhibited. In this case, the susceptibility is minimal over the whole frequency range since the Néel characteristic frequency of particles with 25 nm core diameter is well below 1 kHz.

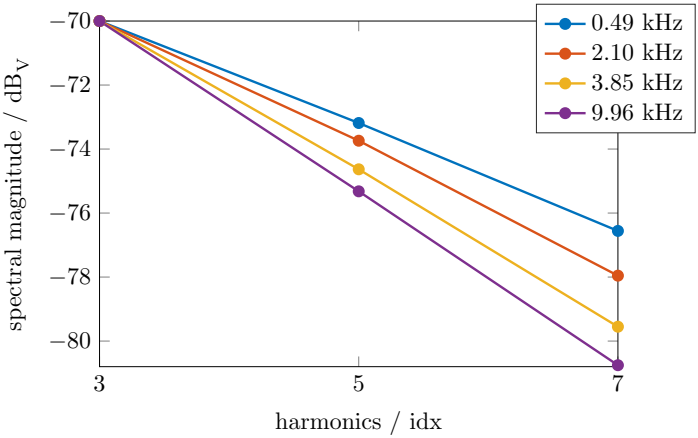

Figure 3.12: Spectral magnitude of $3f$ to $7f$ harmonics for different excitation frequencies (frequency-corrected and normalized to $3f$).

This principle also applies to an MPS measurement, where the harmonic spectrum is recorded on the particle suspension for different excitation frequencies in the frequency range around the transition frequency. The frequency range where significant changes in the harmonic spectra are expected might be shifted toward higher frequencies as a consequence of the field-dependent Brownian relaxation time (→ Sec. 2.2.2). Looking at the magnitudes of the $3f$ to $7f$ harmonics for various excitation frequencies in Fig. 3.12, a frequency-related decay is clearly observed.
As highlighted in Fig. 3.13, the mean magnitudinal decay of the odd harmonics referred to the harmonic index decreases with increasing frequency.

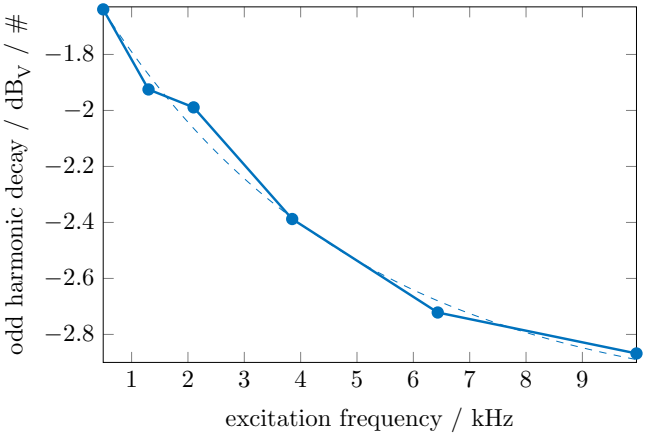

Figure 3.13: Decay of the odd harmonics (linear regression on magnitudes of $3f$ to $7f$, see Fig. 3.12) of the MPS spectrum for different excitation frequencies (normalized per harmonic index #). Dotted line is guide to the eye.

Because only particles whose characteristic frequency is in the range or above the excitation frequency contribute to the signal, a frequency-weighting or size selection happens on the particle size. As a result, the curvature of the magnetization curve changes with frequency as well. For low excitation frequencies one observes a high overall amplitude, as discussed before (→ Fig. 3.11), and all particles contribute to the signal. Consequently, the magnetization curve is dominated by large particles, leading to a steep magnetization curve, a large number of higher harmonics and a slow harmonic decay. Only smaller particles contribute to the signal for excitation frequencies above the transition frequency, which leads to a shallow slope of the magnetization curve and to a stronger decay of harmonics in the spectrum. Also, for Néel-dominated particles above a certain size, where they are no longer superparamagnetic, the hysteresis increases with increasing frequency.

Multivariate Parameter Estimation

Multivariate parameter estimation is performed based on the Levenberg-Marquardt algorithm. This algorithm provides a second-order approach for least squares problems [144–149] and its primary application is for least squares curve fitting. Given a set of M data pairs $(x_\mathrm{i}, y_\mathrm{i})$, it optimizes the parameters β of the model curve $f(x, \beta)$ so that the sum of squares of the deviations, the error term $E_\mathrm{t}(\beta)$, becomes minimal:

$$E_\mathrm{t}(\beta) = \sum_\mathrm{i} \left[y_\mathrm{i} - f(x_\mathrm{i}, \beta) \right]^2 = min \tag{3.6}$$

For MPS x_i equals to the harmonic index and the y_i are the spectral magnitudes of the harmonics. The model function $f(x, \beta)$ is given by a suitable magnetization model (→ Sec. 2.4) in combination with a simulated signal chain (→ Sec. 3.1). The key to multivariate parameter estimation is that the above equation is valid for each individual dataset, i.e. for each measurement with a defined set of measuring parameters a corresponding set of model parameters can be found. However, not all model parameters are definite from a single dataset. That is where the 'stacked matrix' approach comes into play. Because all multivariate MPS measurements are performed on the same sample (as a boundary condition) the procedure can be modified to include all measurements at once, the model function $f(x, \beta)$ is then required to satisfy all measurement from a single set of model parameters β. Due to (possible) ambiguity of parameter dependencies, an explicit Jacobian of the model function is typically required to solve the problem, which can be challenging for more complex numerical magnetization models.
The above approach can be modified to model MPS data dependent on a single parameter, i.e. MPS spectra as a function of viscosity (→ Sec. 3.3.3). A stack of function parameters is correlated with a set of corresponding MPS datasets. Each harmonic as a function of the parameter is modeled with a simple prototype (i.e. a polynomial) resulting in a 'mapping matrix' of parameter values to function parameters. The optimal matrix is obtained by fitting or iteratively adapting the matrix coefficients and differencing the calculated MPS spectra from the model with the actual datasets by means of the same Levenberg-Marquardt algorithms described above.
Alternatively to the Levenberg-Marquardt algorithm for non-linear minimization, Powell's (trust-region) dogleg algorithm is employed for the fit procedure. The dogleg (DL) method was found to be superior to the LM algorithm for the problem at hand in terms of convergence speed (or iteration/evaluation count) by approximately a factor of 3.
Based on the parametric measurement of the harmonic spectrum depicted in Figs. 3.9, 3.10 and 3.12 and utilizing the Levenberg-Marquardt algorithm for least squares curve fitting, the core and hydrodynamic size distribution of the measured particle sample was estimated from the dependencies on ac field amplitude and frequency as well as on a superimposed dc field.
Figure 3.14 shows the resulting log-normal size distributions for the SHP-25 suspension estimated from the MPS spectra. The core size distribution is found with a mean diameter of 23.0 nm and a standard deviation of 0.22, and for the hydrodynamic size distribution a mean diameter of 30.0 nm and a standard deviation of 0.28 were obtained. Both mean values are in good aggreement with the sizes estimated from ACS measurements and with the values given by the manufacturer.
For comparison and to investigate the impact of different magnetization models on the result, the core size distribution parameters of the SHP-25 particles were determined by the above procedure, measured at $H_\mathrm{AC} = 20\,\mathrm{mT}$ for two different excitation frequencies (2.17 kHz and 6.37 kHz) on a mobile and an immobilized SHP-25 sample. The static Langevin model

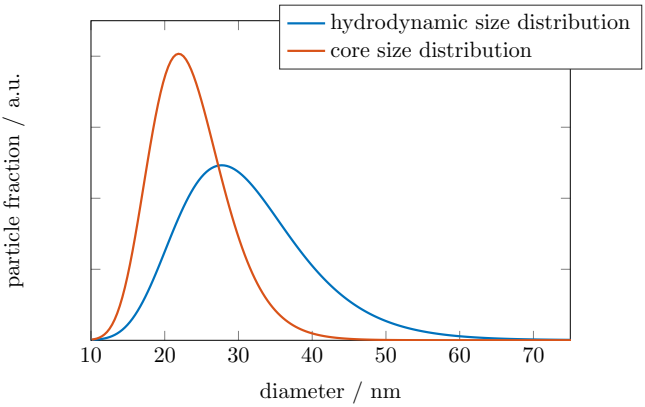

Figure 3.14: Size distributions obtained from multi-variate regression analysis based on parametric MPS measurements (in Figs. 3.9 - 3.13).

(→ Sec. 2.4.1) and the non-linear Debye approximation model (→ Sec. 2.4.4) were applied to determine the distribution parameters. The fitting results are summarized in Table 3.6. As can be seen, ignoring the particle dynamics (static Langevin model) results in too large core diameters. Additionally, the mean core diameter values determined for the particle suspension are larger than the ones obtained for the immobilized sample. This difference is caused by the fact that the mean harmonic decay does not only depend on excitation frequency f (see Fig. 3.12) but also on the mobility of the particles: the mean magnitudinal decay of the odd harmonics referred to the harmonic index amounts to $-1.139\,\mathrm{dB/\#}$ for the suspension and $-1.337\,\mathrm{dB/\#}$ for the immobilized reference sample measured for $f = 2.17\,\mathrm{kHz}$. If the particle dynamics are correctly taken into account, values close to those from the multivariate fit are obtained.

Table 3.6: Summary of core size distribution fit parameters for SHP-25 particles in multi-variate MPS.

Model	Langevin (static)				Non-linear Debye (dynamic)			
Sample	mobile		immobile		mobile		immobile	
f / kHz	2.17	6.37	2.17	6.37	2.17	6.37	2.17	6.37
μ_c / nm	27.3	25.4	26.6	24.2	24.7	23.2	24.0	22.0
σ_c	0.25	0.17	0.22	0.20	0.23	0.28	0.22	0.21

Our MPS setup enables the evaluation of the harmonic spectrum in dependence of the static field level H_{DC}, the excitation field amplitude H_{AC} and excitation frequency f. The results show that all three parameters have exceptional influence on the harmonic spectrum. While the amplitude of

the static and sinusoidal fields is mainly responsible for changes in the spectrum reflecting the core properties, the dynamic behavior of the particle sample can be measured by applying different excitation frequencies and by taking the field-dependence of the relaxation time constants into account. Using a whole set of measurements with different parameters, it is possible to estimate the core and hydrodynamic properties of the sample under test.
In the multivariate fit two measurements on the same particle sample at two different ac amplitudes will result in an identical core size distribution (a boundary condition in the 'stacked matrix' approach). Because the shape of the magnetization curve is known from the model and the slope of the Langevin function is unique as a function of the field (→ Sec. 2.1.2), the matrix system is overdetermined and can be used e.g. to determine the exact absolute magnitude of the excitation field. This way, the MPS system is self-calibrating in regard to the absolute excitation field which is important in context of field-dependent relaxation time constants.
The inverse approach can be used to explicitly distinguish two samples based on their core diameter. This is a prearrangement for multi-color MPI, where multiple particles with different core sizes (or core size distributions) are distinguishable from the MPI reconstruction [13].

3.3.3 BioAssays / Viscosity

Bioanalytics describes a set of analytical techniques in the context of biotechnological research. Especially in bioanalysis, analytical chemical methods are used to quantitatively determine biological molecules, such as proteins, DNA, metabolites or molecular drugs. Chromatographic methods in conjunction with mass spectrometry or nuclear magnetic resonance (NMR) are most prominent. These methods are supplemented by ligand binding assays. The enzyme-linked immunosorbent assay (ELISA) is routinely used as a specific antigen-antibody test where the target substance is identified by color change. Alternatively, radioactively labeled markers, fluorescent dyes or quantitative PCR (polymerase chain reaction) can be used for detection. Depending on the type of assay, free markers have to be quantitatively distinguished from markers bound to the analyte. Here, a magnetic marker (magnetic bead or nanoparticle) is advantageous. In magnetic immunoassays (MIA) the binding state of the marker is evident in dynamic measurements via its relaxation time constant [150–158]. Ideally, a free marker is subject to Brownian rotational motion with the Brownian time constant τ_B and a bound marker responds via the Néel mechanism with the Néel time constant τ_N.
For particles with a large enough core diameter (around 20 – 25 nm), the Néel time constant is much larger compared to the Brownian time constant. The event of particle binding to a large analyte or being incorporated into a cross-linked mesh is then congruent with the transition from Brownian to Néel type magnetization response.
Similarly, magnetic particle spectroscopy (MPS) is sensitive to both the Néel time constant τ_N and the Brownian time constant τ_B. In the context of estimating the core properties of the particles (→ Sec. 3.3.2) this can

lead to undesired results. Thus, measurements are typically performed on a mobile (Brownian) sample and on an immobilized (Néel) sample, which allows one to account for both contributing particle fractions and/or time constants. On the other hand, sensitivity to Brownian rotation motion of the particles and its suppression in case of binding or immobilization enables explicit experiments to determine the viscosity or the binding state of particles in MPS as part of a magnetic immuno- or binding-assay. The Brownian time constant τ_B (→ Sec. 2.2.2) is a function of the hydrodynamic volume V_h of the particles and the viscosity η of the surrounding medium (repeated here from (2.16) for convinience):

$$\tau_\mathrm{B} = \frac{3\eta V_\mathrm{h}}{k_\mathrm{B}T} \tag{3.7}$$

More precisely, the Brownian time constant τ_B is directly proportional to the hydrodynamic volume V_h and the viscosity η:

$$\tau_\mathrm{B} \propto \eta \qquad \text{or} \qquad \tau_\mathrm{B} \propto V_\mathrm{h}$$

A change in viscosity is – in effect – equivalent to a change in hydrodynamic volume. For a magnetic immunoassay, the increase of the hydrodynamic particle diameter is typically observed. However, for the investigation of such an assay, variation of viscosity of a homogenous particle sample is usually more accessible and easier to control. A viscosity series (based e.g. on a water-glycerol mixture) is used as a reference or model system for emulating an actual assay.
For the realization of a magnetic immunoassay, particles should be selected to show a significant difference in Brownian and Néel response, which is synonymous to a large difference between the Brownian and Néel time constants. Arguing from Fig. 3.11, the ACS spectrum of a SHP-25 sample, there is a pronounced difference in the responses of mobile and immobile particles in the frequency range around and below 10 kHz. An MPS measurement taken at small excitation frequencies (well below 10 kHz) should therefore qualify to detect a binding state change.
Not only the particles must be selected with care, also the measurement parameters of the MPS have direct influence on the ability to record bindings. In general, there is a trade-off between the sensitivity of the MPS (which increases proportionally with the excitation frequency according to the induction law) and reduction of the Brownian signal contribution above $\omega > 1/\tau_\mathrm{B}$ due to the limited Brownian particle dynamics. Many of the MPS measurements in this section are therefore taken at low excitation frequencies, although the standard MPS is operating at 10 kHz.
The feasibility of conducting a binding assay with MPS as a detector is demonstrated at an excitation frequency of 3.78 kHz with the V2 configuration of the MPS (→ Tab. 3.1). The kinetics of the binding reaction of 5 µL fluidMag-Streptavidin (CCCR) particles in 145 µL suspension with biotin-agarose-beads are shown in Fig. 3.15.

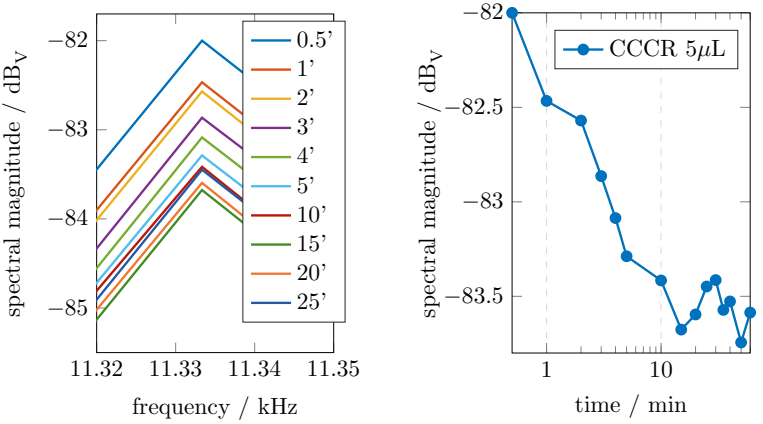

(a) Zoom on $3f$ **(b)** $3f$ over time

Figure 3.15: Kinetic MPS measurements ($3f$ evolution in time) on fluidMag-Strepdavidin at an excitation frequency of 3.78 kHz.

The $3f$ component of the MPS magnitude spectrum (→ Fig. 3.15a) is affected by the binding and decreases as the reaction progresses. In Fig. 3.15b the $3f$ level is plotted over reaction time. After about 15 min no further change in magnitude is observed and the reaction is considered complete.
As a conclusion, we find that MPS is capable of observing binding reactions and because the measurement time is short (about 1 s with 100-fold averaging) the binding kinetics of the reaction can be resolved.
At this point, MPS has been established as a detection method for magnetic immunoassays. However, the quantitativeness of the approach is not clear, i.e. only the magnitude of the $3f$ spectral component had been observed over time. Following a stability study to guarantee that the streptavidin-functionalized particles are stable, i.e. they do not aggregate and only bind in presense of biotin, a concentration series was prepared. 5 µL fluidMag-Streptavidin and variable amounts of biotin-agarose were mixed and the vacant volume (in the 150 µL vial) was filled up with PBS buffer or de-ionized water. All samples were periodically stirred (eppendorf Thermomixer) every 2.5 min for 5 s at 1400 rpm and at room temperature over a 2 h interval to ensure optimal binding.
For reference, the entire series was measured with magnetorelaxometry (MRX). Figure 3.16a shows the complete magnetization and relaxation cycle of the MRX experiment. Except for the immobilized reference, all relaxation curves are stacked in order of increasing biotin-agarose (BA) content (→ Fig. 3.16b). In a congenial series with streptavidin-functionalized and biotin-agarose (on a different batch of particles), the experiment was repeated in the MPS measuring setup. Figure 3.17a shows

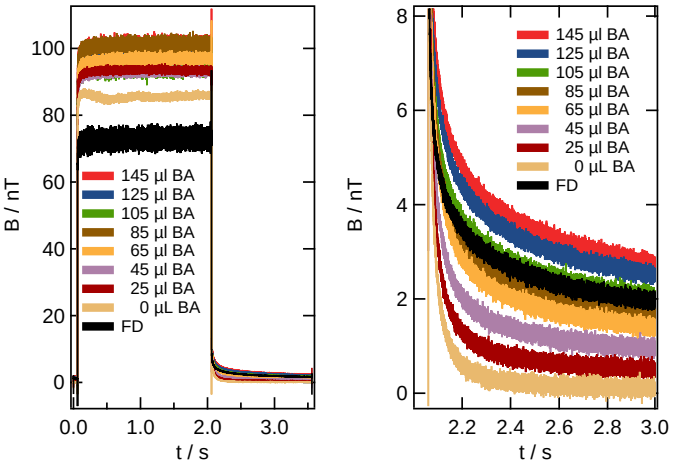

(a) Complete cycle **(b)** Relaxation only

Figure 3.16: MRX curves on the fluidMag-Streptavidin concentration series (with biotin-agarose beads).

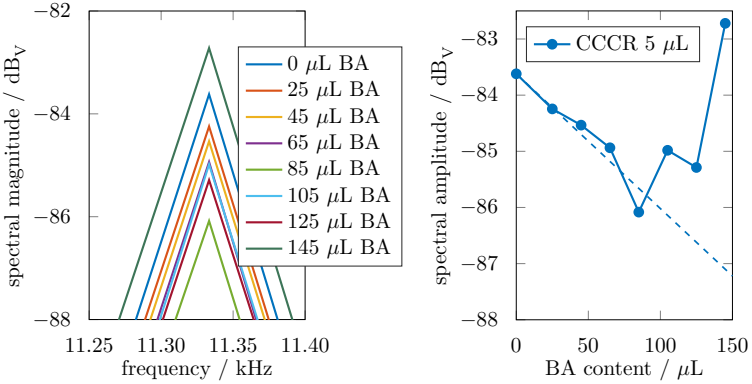

(a) Zoom on $3f$ **(b)** $3f$ as a function of BA content

Figure 3.17: MPS measurements $3f$ on fluidMag-Strepdavidin concentration series (with biotin-agarose beads) at 3.78 kHz.

the details of the $3f$ harmonic component for the prepared series. A clear modulation of the $3f$ magnitude is observable from the spectrum. In (→ Fig. 3.17b) the $3f$ magnitude is plotted as a function of the amount of biotin-agarose. In contrast to the expectations, the $3f$ signal does not scale linearly with increasing binding association. Starting from 100 µL BA the $3f$ harmonic reverses trend and its magnitude increases again.
In order to establish a model to quantitatively describe the dependence of the MPS harmonics, i.e. not only a single harmonic component or a ratio of harmonics, on the binding state, experiments were conducted using a viscosity series instead of an actual binding assay. A viscosity series (→ Fig. 3.18) with variable ratio of glycerol ($\eta \approx 1000\,\mathrm{mPa\,s}$) and water ($\eta \approx 1\,\mathrm{mPa\,s}$) is much easier to prepare and typically more stable for storage and repeated use in measurements. Also, the viscosity of glycerol-water mixtures has been studied extensively in literature and formulae were derived to calculated the viscosity as a function of the glycerol/water ratio [159].

Figure 3.18: Photo of water-glycerol viscosity series with FeraSpin™ R in 150 µL vials.

The glycerol-water suspension is prepared from FeraSpin™ R. A validation of the viscosity of each sample in the series is provided from MRX, ACS and rheological measurements. ACS measurement results obtained on the viscosity series are shown in Fig. 3.19. For the mobile sample (0 % glycerol), the maximum of the imaginary part of the ACS spectrum (→ Fig. 3.19b), equivalent to the characteristic frequency of the particle's Brownian rotational motion, is observed around 1.5 kHz. With increasing viscosity the peak of the imaginary part shifts towards lower frequencies, and for the highly viscous samples the peak maximum is outside the measurement range of the ACS device. In the real part (→ Fig. 3.19a), the Brownian contribution is observed to be increasingly suppressed for higher viscosities.
Secondly, the same series is validated using magnetorelaxometry (MRX) measurements. The MRX results (→ Fig. 3.20) confirm the observation from ACS that the Brownian time constant of the particles increases with rising viscosity of the medium. While the water sample from the series relaxes instantaneous, the viscous samples and the Néel (freeze-dried) reference have not relaxed after over 3 s (outside the measuring time window of a standard MRX experiment). The long relaxation times are readily observable in MRX but are way outside the frequency window of the ACS.

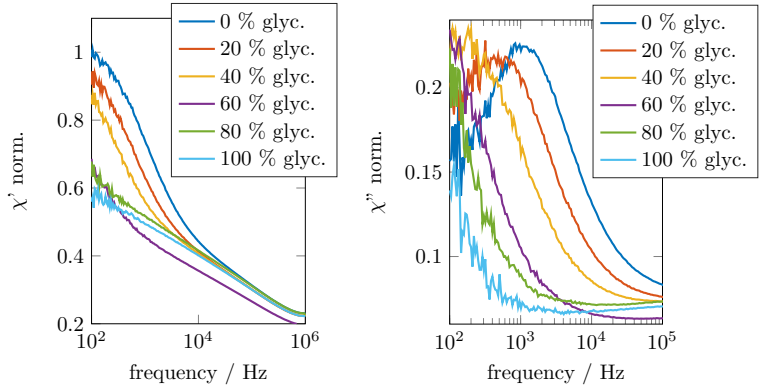

(a) Real part of susceptibility **(b)** Imaginary part of susceptibility

Figure 3.19: AC susceptibility spectra (real and imaginary part) on the FeraSpin™ R viscosity series.

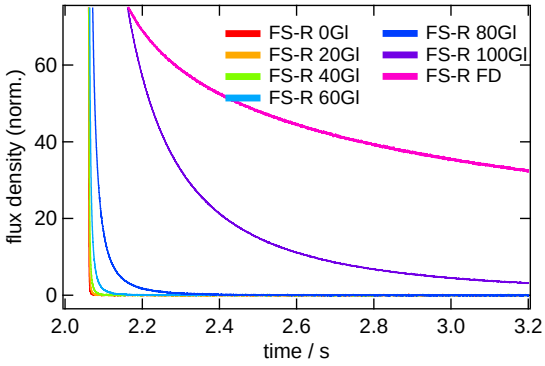

Figure 3.20: MRX measurements on the FeraSpin™ R viscosity series (normalized to the equilibrium flux density level before the magnetizing field was switched off).

Both methods, ACS and MRX, confirm the stability and the successful preparation of the viscosity series. A quantitative comparison of the measurement results is given in Fig. 3.21. The diagram contains the ACS and MRX results alongside with rheological measurements and the calculated viscosity. The plot maps the water/glycerol ratio (or glycerol content) to the viscosity of the medium. All methods deliver comparable results, which are close to the calculated values. Larger deviations for low viscosity in the rheometer and for high viscosity from ACS can be explained from the suitable measurement range of these devices and are to be expected.

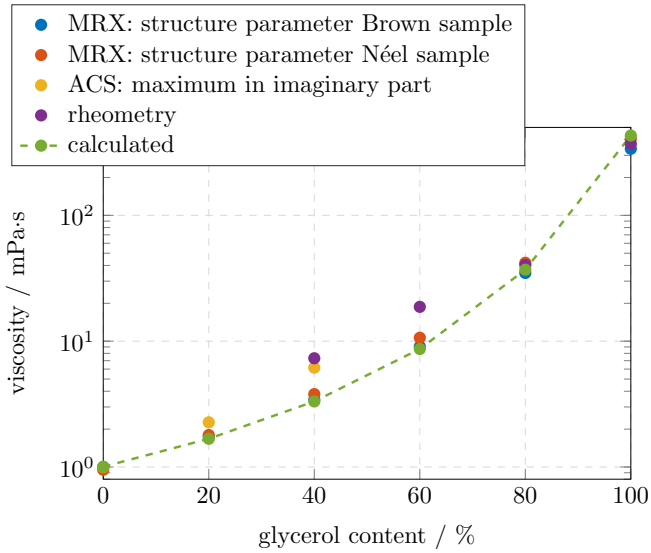

Figure 3.21: Comparison of viscosity estimates from different sources (MRX, ACS, rheometer and calculated).

Magnitude View

A series of MPS measurements (using the MPS V2b setup) at three different excitation frequencies of 1 kHz, 5.05 kHz and 10.05 kHz was performed on the FeraSpin™ viscosity series [160]. Figure 3.22 shows the magnitude spectrum of the MPS data separate for each frequency. The harmonics plot associated with the immobilized sample shows the strongest decay at all frequencies, although the slope of the average harmonic decay increases slightly with frequency.

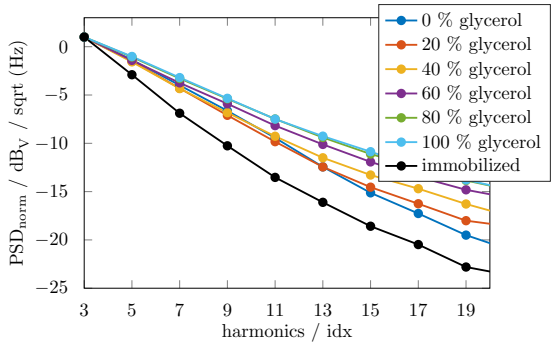

(a) Decay of odd harmonics at 1 kHz

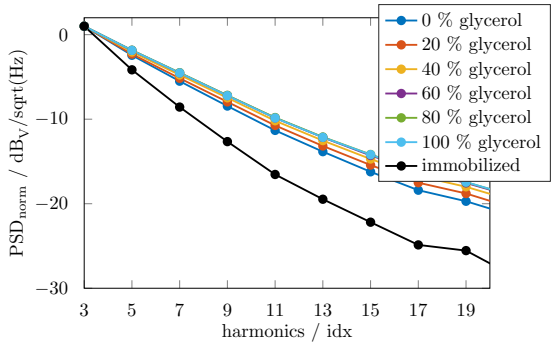

(b) Decay of odd harmonics at 5.05 kHz

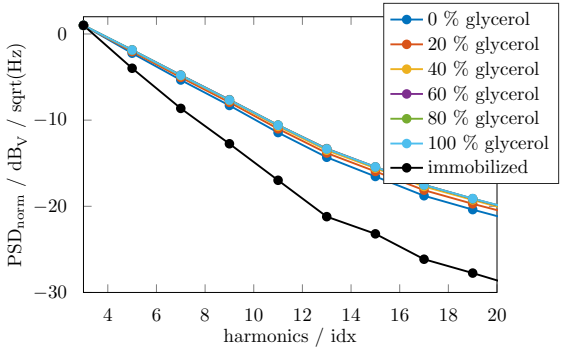

(c) Decay of odd harmonics at 10.05 kHz

Figure 3.22: Magnitude MPS data on FeraSpin™ R viscosity series for different excitation frequencies (frequency-corrected and normalized to $3f$).

All plots show a more or less pronounced modulation of the harmonics as a function of the sample's viscosity. In agreement with the observations from ACS, where a distinctive Brownian contribution in the real part of the susceptibility (the magnitude plot in ACS is dominated by the real part) is only observed in the lower frequency range (below 1 kHz) and only for low-viscosity samples, the span in harmonic decay between the top-most and the bottom-most sample curve scales with the excitation frequency. At 1 kHz, a span at $19f$ of about $10\,\mathrm{dB_V}$ is observed, at 5.05 kHz it is only $4\,\mathrm{dB_V}$ and at 10.05 kHz the curve almost agrees with a residual span of about $2\,\mathrm{dB_V}$.
Applying linear regression analysis on the $3f$ to $11f$ harmonics to yield an average harmonic decay, leads to different representation variants of the datasets (→ Fig. 3.23) visualizing the modulation of the harmonics in dependence of the viscosity.

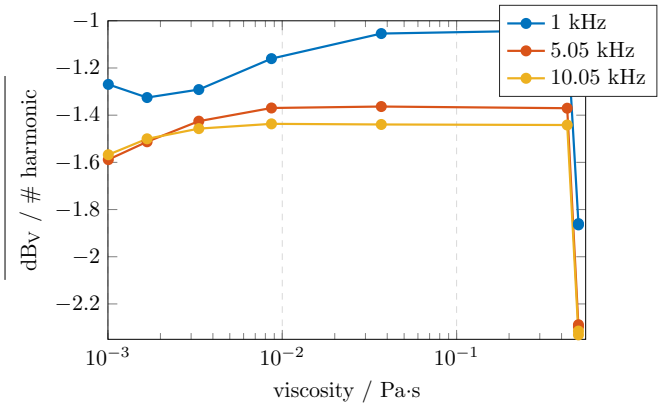

Figure 3.23: Pre-evaluated (decay of odd harmonics) magnitude MPS data on FeraSpin™ R viscosity series (over viscosity), last viscosity point is Néel reference.

Figure 3.23 plots the harmonic decay as a function of viscosity and as such reveals that the harmonics in Fig. 3.22a do not occur strictly in linear order with viscosity. Instead, after a initial decrease, the harmonic decay first increases up to about 2 – 3 mPa s and then reverts towards the 100 % glycerol sample. The modulation at very low viscosities in the 1 kHz measurement can not be observed at higher frequencies. The curves for higher frequenies appear shifted towards lower viscosities, i.e. the parameter $\omega\tau$ stays constant. Similarly, Weaver et al. [161–166] used the 5th to 3rd harmonics ratio ($5f/3f$) on a viscosity series of Feridex in gelatine to observe the effect.

However, in both cases there is no unique relation between the harmonic decay (or $5f/3f$ ratio) to viscosity. Also a transfer of the approach for MPI is not possible, because there the harmonic ratio changes with every point in the FOV as a result of the selection field's dc components. The magnitude spectrum does not provide sufficient data to resolve the ambiguity and complex-valued spectra (or the phase in addition magnitude) have to be considered. While in ACS measurements the complex-valued representation is considered standard, MPS spectra are typically evaluated as a magnitude spectrum. Because of the phase shift from a dc field, the real and imaginary parts in MPS or MPI can also become negative in sign.

Complex-valued View

Based on the Fokker-Planck simulation by Yoshida et al. [75], which was used as a reference for deriving the non-linear Debye Approximation in Sec. 2.4.4, Fig. 2.16d shows the theoretical curve progression of the complex-valued harmonics as a function of viscosity. Because the simulations include the Brownian contribution only, they are not directly comparable to the MPS results on FeraSpin™ R. As observed in Fig. 2.12, only one fraction of FeraSpin™ R shows Brownian relaxation. The largest fraction of MPS-visible particles is Néel-dominated. As a simplistic approach, the Brownian and Néel mechanisms are assumed to be completely independent of each other. Although this is not exactly true, neither in realitity nor in Fokker-Planck or LLG-based simulations, the same assumption is made to express the effective relaxation time (→ Sec. 2.2.3) as a superposition of the individual time constants. Superposition implies that a particle exhibits either Brownian or Néel relaxation, so that the observed magnetization is also a superposition of both contributions. In this case, the Néel contribution can simply be substracted (maintaining the correct phase relation) from the total signal. The result (including scaling adjustments of the dataset to match the simulation) is depicted in Fig. 3.24. The $3f$ (→ Fig. 3.24a) and $5f$ (→ Fig. 3.24b) components are shown as an overlay to the simulation data.
Except for baseline deviations, which could be related to an imperfect Néel compensation or residual effects from the MPS measurement setup, the measured curves are in good overall agreement with the simulations. It has been shown in this section, that MPS is a useful tool for the characterization of magnetic nanoparticles. It is suitable for detecting changes in the hydrodynamic diameter of the particles from binding reactions or in the viscosity of the medium. Especially, the results from the FeraSpin™ R viscosity series constitute a promising step towards the numerical description of the MPS measurement data via an appropriate dynamic magnetization model.

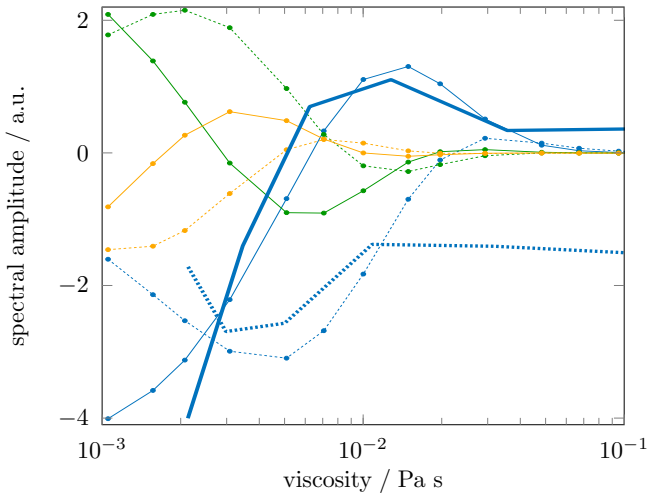

(a) 3rd harmonic overlay (thick lines) of experimental data on Fokker-Planck simulations (thin lines)

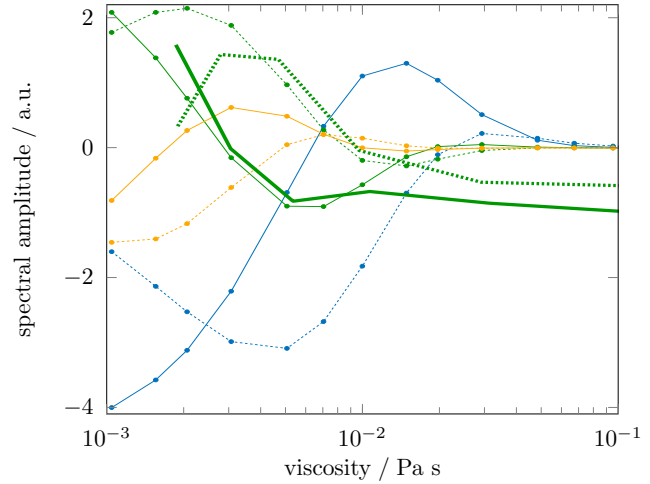

(b) 5th harmonic overlay (thick lines) of experimental data on Fokker-Planck simulation (thin lines)

Figure 3.24: Complex-valued MPS data ($3f$, $5f$, $7f$) on FeraSpin™ R viscosity series in comparison with Fokker-Planck simulation data (from [75] for $3f$ and $5f$). Real part as solid lines, imaginary part as dashed lines.

4 Magnetic Particle Imaging

The chapter on Magnetic Particle Imaging (MPI) starts with the fundamental principles by extending the theory on MPS to include spatial encoding. The imaging process of MPI is discussed, reconstruction and resolution limits are explored. The application section then covers MPI imaging of phantoms and the so-called 'Mobility MPI' approach (→ Sec. 4.5.2) which additionally registers the particle mobility or binding state in the field of view (FOV).
MPI is a tracer-based imaging modality. While magnetic nanoparticles, typically superparamagnetic iron oxide particles (SPIOs), are used as a contrast agent for Magnetic Resonance Imaging (MRI) to enhance the contrast, in MPI there is no contrast at all without the particles being present in the imaging volume. Therefore, the MNPs are called a tracer, and it's non-linear magnetization curve forms the basis for any MPI experiment.

4.1 Basics

The basic ingredients for an MPI experiment are the following:

- sinusoidal/harmonics drive field: ac magnetic field with a sufficiently large amplitude
- MNPs as tracer: excited by the drive field into non-linear range of the magnetization curve, thus generating higher harmonics
- magnetic field sensor: detecting the rich harmonic spectrum from the tracer
- selection field: modulating the magnetization response depending on spatial position

We first take a look at the various field contributions for an MPI experiment, the drive field and the selection field (→ Fig. 4.1). The selection field takes the shape of a gradient field created by two opposing coils or magnets, where the field contributions from the hemispheres cancel each other out in a single point in space (Fig. 4.1, left). That point is therefore called the field-free point (FFP). The drive field is homogenous

in space and it is superimposed on the selection field by one or more additional coil sets. Because its magnitude is comparable to the dc field level in the imaging volume, it effectively moves the FFP around. For a 1-dimensional MPI experiment, a single drive field coilset/axis is used and the FFP moves along a line (Fig. 4.1, right). For two dimensions, two orthogonal drive fields are superimposed and consequently the FFP moves along a 2-dimensional trajectory. And for three dimensions, a third drive field axis is required to create a 3-dimensional movement of the FFP.

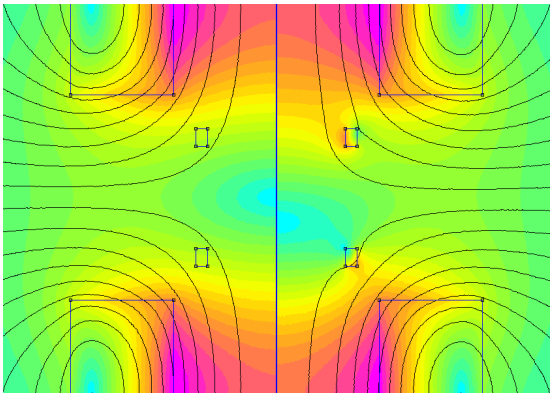

Figure 4.1: Selection field geometry of an FFP MPI scanner, (left) FFP in origin of the FOV and (right) FFP in deflected position from the drive field.

Because there is no sustained resonance effect for the magnetization (dampening constants are too large), like the nuclear magnetic resonance in MRI, simultaneous excitation and detection is required in MPI. Separation of the excitation signal from the particle magnetization response then happens in the frequency domain. For that, a pure sinusoidal excitation is used, which contributes a single spectral component to the received signal. All other frequencies, which are basically the overtones (harmonics) of the excitation frequency (or fundamental frequency), are originating from the MNP tracer. Because the fundamental component is large compared to the MNP signal, a filter is required to remove or at least reduce it. The remaining series of higher harmonic components constitutes the raw signal that is used for image reconstruction.
It should be noted that recovering the fundamental component is possible at additional cost and is desired for certain reconstruction schemes (→ Sec. 4.1.3).
The entire process is shown schematically in Fig. 4.2. So far, this is all identical to the MPS experiment introduced in Sec. 3.1. The only difference in practice is the small filling factor of the MPI receive system, so

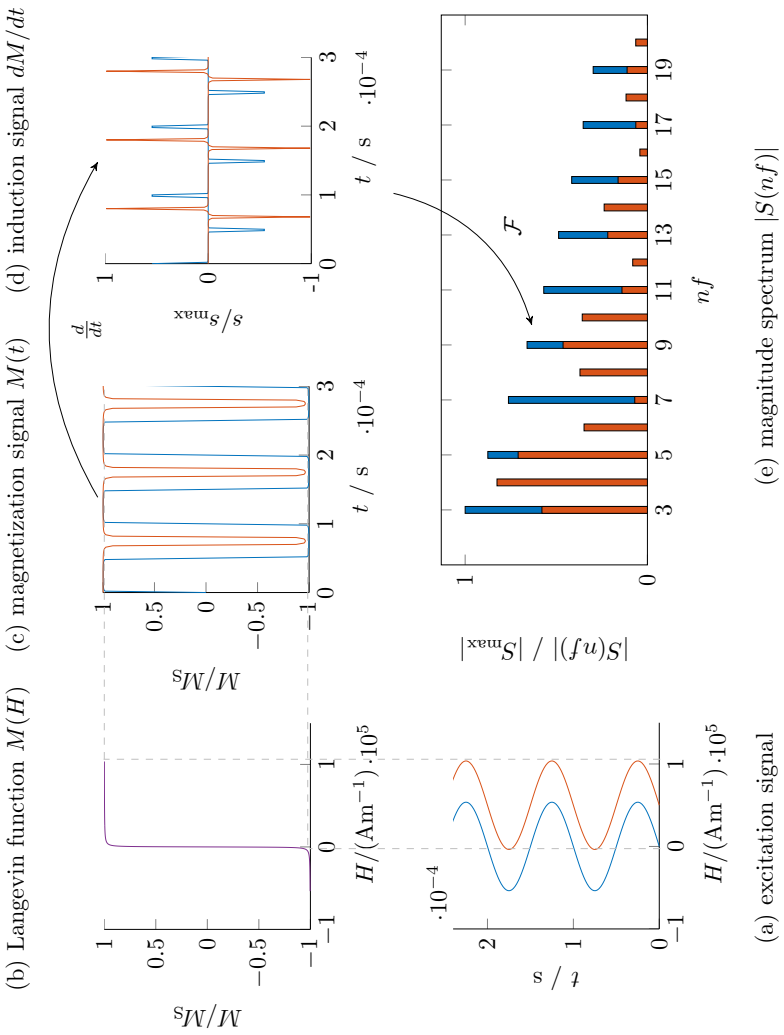

Figure 4.2: Principle of MPI: A sinusoidal drive field (a) applied to particles with Langevin magnetization curve (b) causes the magnetization to commute between the saturation levels (c). An inductive receiver picks up the time-derivative of the magnetization (d) and a Fourier-transform reveils higher harmonics (e).

that the particle signal is at least 3 orders of magnitude smaller compared to the fundamental than it is in an MPS system. For that reason, there are some additional technical challenges in the realization of an MPI scanner (→ Sec. 4.2).

Figure 4.2 is in principle valid only for particles in a stationary FFP, where the dc component contributed from the encoding field is zero. Everywhere else in the imaging volume, there is a defined dc level attributive to each point in space. The particle response from that spots is modulated by the additional dc field, entailing a different, yet unique spectral signature for the corresponding points (→ Sec. 4.1.2). Far away from the FFP center of the imaging volume, where the dc selection field level is larger (better 2-times larger) than the ac amplitude from the drive field, the magnetic nanoparticles are steadily saturated and no higher harmonic components are evident in the detection signal (→ Fig. 4.2). Hence, the FFP is a special point in space to be distinguished in signal from other spots in the volume.

The above description applies, if the ac amplitude is small compared to the dc field from the encoding gradient, i.e. the ac modulation does not move the FFP significantly, and the ac amplitude is large enough to cause the generation of higher harmonics to be detected. In that case, a step-wise dc shift (or equivalently a shift of the object) can be used to generate an image of the object by scanning the FFP with the dc offset through the volume. Because at each point along the way a full spectrum has to be acquired (although in that case a single overtone could suffice) the imaging process becomes slow. This mode is typically refered to as 'slow scan' mode and it is often used to cover a large area, which otherwise would not be captured with a single MPI scan pass.

However, if the ac amplitude is large, so that the FFP moves a certain distance in the volume by applying the drive field, the entire path covered by the FFP passing over is mapped in the process. This mode is then called 'fast scan' mode. Because all points covered by the FFP path are mingled together in Fourier space a reconstruction approach is required in order to obtain the image (→ Sec. 4.1.2 and Sec. 4.1.3). The path imposed on the FFP by the drive fields is called the trajectory of the field-free point (FFP) and the region it covers during its pass is called the field of view (FOV). In order to pick-up the receive signal over a large distance in the FOV a minimal excitation amplitude is needed (in order to generate harmonics and because the signal is proportionl to the FFP velocity). That is another reason to go with a 'fast scan' mode in MPI and use 'slow scan' only to increase spatial coverage. The required dc offset is called the 'focus field' because it moves the focus point of the 'fast scan' FOV around [24]. The resulting field of views are also refered to as the drive field FOV (DF-FOV) or partial FOV (pFOV) and the focus field FOV (FF-FOV) or global FOV.

Starting from (3.1), an additional term is included for the focus field $\boldsymbol{H}_{\mathrm{DC}} = \boldsymbol{H}_{\mathrm{SF}} + \boldsymbol{H}_{\mathrm{FF}}$, where SF stands for the selection field and FF

for the focus field. The focus field components are neglected in further discussions because they add an additional low-frequency modulation, that is not required for the understanding of MPI technology.

$$\boldsymbol{H}(t) = \boldsymbol{H}_{\mathrm{DC}} + \boldsymbol{H}_{\mathrm{AC}} \cos(\boldsymbol{\omega}_{\mathrm{x}} t) \tag{4.1a}$$
$$= [\boldsymbol{H}_{\mathrm{SF}} + \boldsymbol{H}_{\mathrm{FF}}] + \boldsymbol{H}_{\mathrm{DF}} \cos(\boldsymbol{\omega}_{\mathrm{x}} t) \tag{4.1b}$$
$$= \frac{1}{\mu_0} \bar{\boldsymbol{G}} [\boldsymbol{x} + \boldsymbol{x}_{\mathrm{center}}] + \boldsymbol{H}_{\mathrm{x}} \cos(\boldsymbol{\omega}_{\mathrm{x}} t) \tag{4.1c}$$

For the drive field, a sine or cosine formalism could be used. Since the drive field function in MPI is equivalent to the trajectory of the FFP, a sine function has a starting/resting point in the center of the FOV, whereas the cosine starts at the edge of the FOV. $\boldsymbol{H}_{\mathrm{x}}$ and $\boldsymbol{\omega}_{\mathrm{x}}$ are representative for a 3-component vector, corresponding to (x, y, z) components in the system's cartesian coordinate system (origin at the center of the bore, equal to idle/resting position of the FFP).
With the gradient tensor $\bar{\boldsymbol{G}}$ (in T/m) the selection field and focus field contributions can be expressed as $\mu_0 \boldsymbol{H}_{\mathrm{SF}} = \bar{\boldsymbol{G}} \boldsymbol{x}$ and $\mu_0 \boldsymbol{H}_{\mathrm{FF}} = \bar{\boldsymbol{G}} \boldsymbol{x}_{\mathrm{center}}$ respectively in (4.1c). The function of the FFP's movement $\boldsymbol{x}_0(t)$ can be infered from (4.1c) by setting it **null** and solving it for $\boldsymbol{x}$:

$$\boldsymbol{H}(t) = \frac{1}{\mu_0} \bar{\boldsymbol{G}} \boldsymbol{x} + \boldsymbol{H}_{\mathrm{x}} \cos(\boldsymbol{\omega}_{\mathrm{x}} t) \stackrel{!}{=} \boldsymbol{0} \tag{4.2a}$$
$$\longrightarrow \qquad \boldsymbol{x}_0(t) = -\frac{\mu_0 \boldsymbol{H}_{\mathrm{x}}}{\bar{\boldsymbol{G}}} \cos(\boldsymbol{\omega}_{\mathrm{x}} t) \tag{4.2b}$$
$$= -\mu_0 \bar{\boldsymbol{G}}^{-1} \boldsymbol{H}_{\mathrm{x}} \cos(\boldsymbol{\omega}_{\mathrm{x}} t) \tag{4.2c}$$

The FFP is found to travel within the boundaries of $\left[-\frac{\mu_0 \boldsymbol{H}_{\mathrm{x}}}{\bar{\boldsymbol{G}}}, +\frac{\mu_0 \boldsymbol{H}_{\mathrm{x}}}{\bar{\boldsymbol{G}}}\right]$.
Apparently, $\bar{\boldsymbol{G}}$ is expected to be invertible in (4.2c), which is true for the Maxwell gradient geometry used in most scanner designs (→ Sec. 4.2.2).

4.1.1 Encoding

In this section, a more detailed discussion on MPI's spatial encoding is provided. The harmonic spectrum which results from inserting (4.1c) into (3.2) and detecting it's time-derivative is evaluated either in Fourier-domain (F-space) or in the filtered time-domain, which is equivalent to spatial coordinates (x-space) by means of (4.2c). $\boldsymbol{x}_0(t)$ maps time to points in the FOV and consequently $\boldsymbol{x}_0^{-1}(t)$ maps from x-space back to the time-domain. While in F-space an actual reconstruction is needed to obtain the image, for x-space MPI the signal is simply mapped to it's point of origin (a process called 'gridding', → Sec. 4.1.3).
As defined in (4.2c), the field-free point traverses only a finite interval in space. A new symbol $\boldsymbol{\kappa}$ is introduced, that defines the ratio of gradient

strength to drive field amplitude in units of 1/m and it is called the reciprocal FOV:

$$\boldsymbol{\kappa} = \frac{\bar{\boldsymbol{G}}}{\mu_0 \boldsymbol{H}_\mathrm{x}} \tag{4.3}$$

The spatial interval can then be written as $[-1/\boldsymbol{\kappa}, +1/\boldsymbol{\kappa}]$. The expression can also be normalized by using a parameter $\hat{\boldsymbol{x}}$ so that $\boldsymbol{\kappa}\hat{\boldsymbol{x}}$ stays within the dimensionless range of $[-\mathbf{1}, +\mathbf{1}]$, where $\hat{\boldsymbol{x}}$ is called the field of view (FOV) and $\boldsymbol{x} \in [-\hat{\boldsymbol{x}}, +\hat{\boldsymbol{x}}]$.
The purpose of this section is to find an expression that describes the encoding process in MPI. As a first step, we can write down the time-dependent net magnetic field $\boldsymbol{H}(t)$ at a point $\boldsymbol{x}$ in the FOV as the function $\boldsymbol{H}(x, t)$:

$$\boldsymbol{H}(\boldsymbol{x}, t) = \frac{1}{\mu_0} \bar{\boldsymbol{G}} \boldsymbol{x} + \boldsymbol{H}_\mathrm{x}(t) \quad \xrightarrow{(4.2c)} \quad \boldsymbol{H}(\boldsymbol{x}, t) = \frac{1}{\mu_0} \bar{\boldsymbol{G}} \left[\boldsymbol{x} - \boldsymbol{x}_0(t)\right] \tag{4.4}$$

By rewriting the drive field $\boldsymbol{H}_\mathrm{x}$ into the FFP location (4.2c), the function $\boldsymbol{H}(\boldsymbol{x}, t)$ evolves into (4.4).
The magnetization contributed by a point $\boldsymbol{x}$ is obtained by inserting (4.4) into a magnetization model $\boldsymbol{M}(\boldsymbol{H})$ ($\rightarrow$ Sec. 2.4). The simplest example is the Langevin model ($\rightarrow$ Sec. 2.4.1), which neglects all particle dynamics and assumes an instant response to the applied field. The result is a function $\boldsymbol{M}(\boldsymbol{x}, t)$ that describes the evolution of magnetization $\boldsymbol{M}$ over time t for a single spot $\boldsymbol{x}$ in the FOV. Inserting (4.4) into (2.25) gives:

$$\boldsymbol{M}(\boldsymbol{x}, t) = v_\mathrm{f} M_\mathrm{S} \, \tilde{\boldsymbol{L}}(\boldsymbol{H}(\boldsymbol{x}, t)) \tag{4.5}$$

The magnetization of two particles in the FOV is simply the superposition of two individual particle's magnetization.
The signal detected in MPI is proportional to the time-derivative of the magnetization by means of Faraday's induction law, because an induction coil is used as a sensor. This means, that the susceptibility is observed as a function of a space-variant magnetic field (i.e. the selection field) and a homogenous time-dependent field. Therefore, the point-spread-function (PSF) of the imaging process is found in the derivative $d\boldsymbol{M}/d\boldsymbol{H}$ of the above function. The abscissa of such a plot can be rescaled into spatial coordinates with $\boldsymbol{H} = \bar{\boldsymbol{G}}\boldsymbol{x}$.
Both the magnetization $\boldsymbol{M}$ and the susceptibility $d\boldsymbol{M}/d\boldsymbol{H}$ are a function of the dimensionless parameter $\xi = \frac{\mu_0 m H}{k_\mathrm{B} T}$ (2.5). A minimal $\Delta\xi$ can be derived in Fig. 4.3 by applying the full-width at half-maximum (FWHM) criterion to the PSF ($\rightarrow$ Eq. (4.6a)).
Using a vector-valued expression for ξ makes no sense, because the Langevin model is intrinsically non-vectorial. The general idea of estimating the

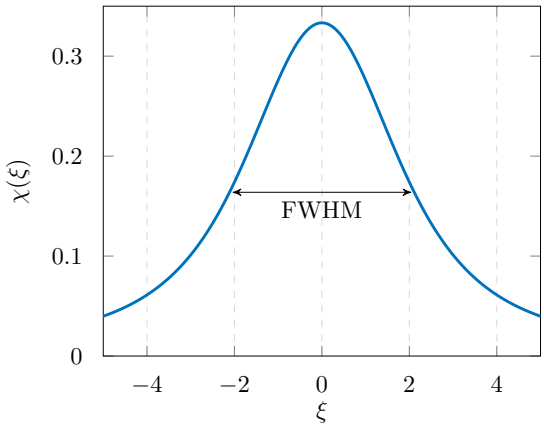

Figure 4.3: MPI Resolution via the full-width at half-maximum (FWHM) criterion on the 1D PSF (proportional to the susceptibility of the particles).

resolution from a magnetization model, can however be transfered to more general models, even if a closed-expression can generally not be obtained. For the purpose of finding a simple expression for the MPI resolution, a 1-dimensional case (where the gradient and the field are scalars) is considered in (4.6b).
Replacing $\Delta H = Gx$ in $\Delta\xi$ and m with (2.4), gives an expression for the spatial resolution limit Δx:

$$\Delta\xi = \frac{\mu_0 m \Delta H}{k_\mathrm{B} T} \quad \stackrel{!}{=} 4.16 \tag{4.6a}$$

$$\xrightarrow{\Delta H = Gx} \quad \Delta x \; = 4.16 \frac{k_\mathrm{B} T}{mG} \approx \frac{8 k_\mathrm{B} T}{M_\mathrm{S} d_\mathrm{c}^3 G} \tag{4.6b}$$

From (4.6b), the resolution improves for particles with larger core diameters $\Delta x \propto 1/d_\mathrm{c}^3$ and for a stronger gradients $\Delta x \propto 1/G$.
It must be noted, that estimating the MPI resolution as above does not paint the whole picture. As mentioned, the Langevin model is a simplistic approach for modelling the particle's magnetization. Especially, it does not consider any magnetization dynamics. It is these magnetization dynamics which are responsible for two things:
First, the time constants describing the dynamic particle behaviour become slower with increasing particle size. According to (2.13), the Néel time constant that is connected to the core diameter d_c, scales exponentially with the core diameter: $\tau_\mathrm{N} \propto exp(d_\mathrm{c}^3)$ (→ Sec. 2.2.1). The time constants cause an additional blurring in the PSF, that limits the resolution for larger particle diameters.

Second, the finite time constants cause a lag between the exciting magnetic field and the particle's response which violates the linear and time-invariant (LTI) properties of the imaging process, because it leads to different responses depending on the magnetization history of the particles in each point.

Trajectory

The selection field geometry has direct impact on the point spread function, because the gradient field determines the dc field component of a particular point in space. Typically, a selection field constituting a field-free point (FFP) is used, where the FFP highlights a defined region in the FOV to contribute to the signal. As an alternative, a field-free line can be utilized, which has the advantage of a full line in space contributing to the signal, leadings to an increase in signal-to-noise ratio. In any case, the field-free region is moved over the FOV by modulating magnetic fields. The path it covers is referred to as the 'trajectory' [167].
As mentioned previously, signal separation, i.e. distinguishing between the drive field 'feed-through' and the particle magnetization signal, required by the simultaneous transmit and receive pattern in MPI happens in the frequency domain. For that, the drive field spectrum has to be as pure as possible in terms of higher harmonic content, so that all harmonics can be assumed to originate from the imaging object in the FOV.
By using three orthogonal and sinusoidal excitation waveforms at slightly different frequencies, a 3-dimensional trajectory can be formed that describes a Lissajous pattern in the field of view (FOV). Besides being a purely harmonic excitation, a Lissajous figure rapidly covers the entire FOV. The 3-dimensional drive field $\boldsymbol{H}(t)$ for a Lissajous trajectory can be written as:

$$\boldsymbol{H}(t) = \begin{pmatrix} H_\mathrm{x}\ \cos(\omega_\mathrm{x} t) \\ H_\mathrm{y}\ \cos(\omega_\mathrm{y} t) \\ H_\mathrm{z}\ \cos(\omega_\mathrm{z} t) \end{pmatrix} \tag{4.7}$$

The field-free point (FFP) of a selection field with gradient $\bar{\boldsymbol{G}}$ then follows a trajectory $\boldsymbol{x}_0(t)$.

$$\boldsymbol{x}_0(t) = -\mu_0 \bar{\boldsymbol{G}}^{-1} \boldsymbol{H}_\mathrm{x}\ \cos(\boldsymbol{\omega}_\mathrm{x} t) \tag{4.8a}$$

$$= -\mu_0 \bar{\boldsymbol{G}}^{-1} \begin{pmatrix} H_\mathrm{x} \\ H_\mathrm{y} \\ H_\mathrm{z} \end{pmatrix} \cos(\begin{pmatrix} \omega_\mathrm{x} \\ \omega_\mathrm{y} \\ \omega_\mathrm{z} \end{pmatrix} t) \tag{4.8b}$$

Frequency components for the trajectory are typically derived from a base frequency $f_0 = \omega_0/2\pi$ divided by integer numbers $(m_\mathrm{x}, m_\mathrm{z}, m_\mathrm{z})$:

$$\begin{pmatrix} \omega_\mathrm{x} \\ \omega_\mathrm{y} \\ \omega_\mathrm{z} \end{pmatrix} = \begin{pmatrix} 1/m_\mathrm{x} \\ 1/m_\mathrm{y} \\ 1/m_\mathrm{z} \end{pmatrix} \omega_0 \tag{4.9}$$

With this design, the Lissajous figure repeats with constant repetition frequency f_{rep}. In other words, it takes the repetition interval T_{rep} for the trajectory to complete a single pass through the FOV (lcm denotes the least common multiple of the arguments).

$$T_{\text{rep}} = \frac{1}{f_{\text{rep}}} = \frac{2\pi}{\omega_0}\,\text{lcm}(m_{\text{x}}, m_{\text{y}}, m_{\text{z}}) \tag{4.10}$$

For the 10 kHz MPI system in this thesis, the parameters for the Lissajous trajectory were chosen according to Tab. 4.1.

Table 4.1: Lissajous parameters for the 10 kHz MPI system.

FOV	30 mm	non-isotropic	
m_{x}	72	f_{x}	10.416 kHz
m_{y}	75	f_{y}	10.000 kHz
m_{z}	78	f_{z}	9.615 kHz
f_{rep}	32.0 Hz	T_{rep}	31.2 ms
Density	0.4 mm	Min/Max	0.38 – 0.42 mm

The resulting Lissajous figure is depicted in Fig. 4.4. The density of the Lissajous trajectory in non-uniform across the FOV. The lowest density region is located at the FOV center, whereas the edges of the FOV are well covered (→ Fig. 4.4a). The density function of Lissajous figure is the cosecant function $csc(x)$ (→ Fig. 4.4b).

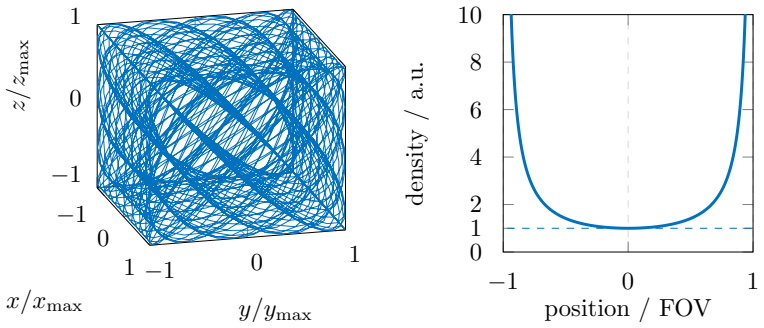

(a) Lissajous trajectory **(b)** Density function

Figure 4.4: Lissajous trajectory and corresponding density function in coordinates of the FOV.

The density of the central part of the trajectory is required to exceed a certain minimal density threshold. This means, that the distance between the nodes of the trajectory, i.e. the points in space where the FFP path

intersects itself, is required to be smaller than the expected resolution limit of the MPI scanner.
The number of nodes in a Lissajous figure corresponds to the frequency dividers m and the number of loops is m (for even dividers) or $m-1$ (for odd dividers). For example, a 2-dimensional Lissajous trajectory with a frequency ratio of $4:5$, can be observed to have 4 holes in each direction. As a rule of thumb, the average density of the trajectory can then be calculated by dividing the size of the FOV by the number of holes (this is a valid approximation, because as seen from Fig. 4.4b the trajectory density is almost constant over a large central area of the FOV). In the above example of a $4:5$ trajectory with a FOV of 10 mm x 10 mm, the average density is $10\,\text{mm}/4 = 2.5\,\text{mm}$. The actual density can then be calculated from the density function for each point in the FOV.

4.1.2 Reconstruction (F-space)

While the FFP is moving over the FOV, each particle-containing point in space contributes to the detection signal. As a result, reconstruction is required to un-fold the various contributions and to recover the spatial distribution of particles in the volume. This can be achieved by using the unique spectral signature found for each point in the FOV [11].
In Fig. 4.5, the spatial dependence of the second and third harmonic component of a 1-dimensional MPI experiment is shown.

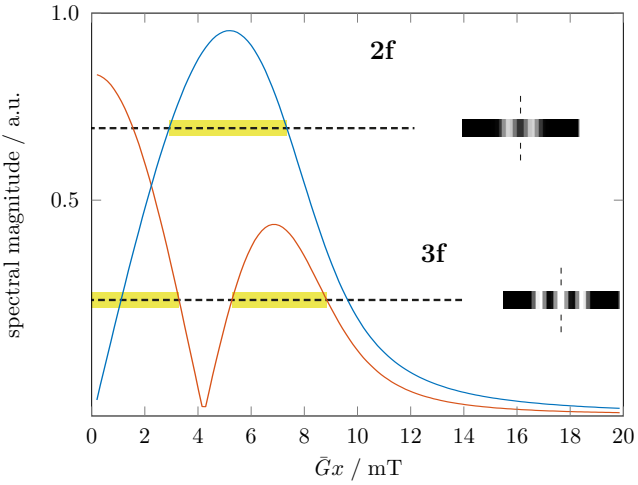

Figure 4.5: Illustration of the 1-dimensional MPI F-space encoding scheme: $2f$ and $3f$ component are modulated as result of the selection field gradient.

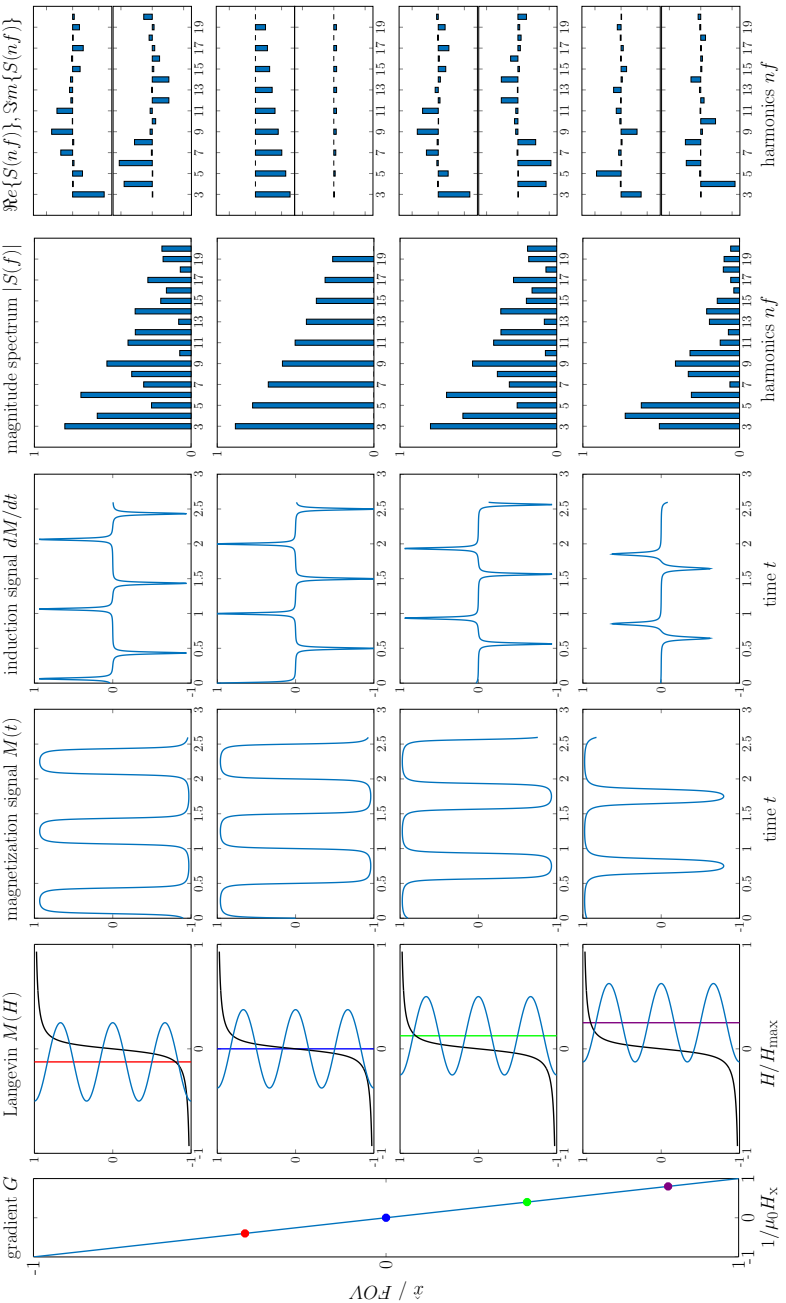

Figure 4.6: Spatial encoding in F-space MPI (see text for details).

At the center of the FOV (at coordinate 0) the 3f signal shows a strong maximum and a second smaller maximum appears at a larger distance to the center. In contrast, the 2f signal has a minimum at the center and only a single maximum (in between the two maxima of the 3f signal). For harmonic components of higher order, the picture looks similar, with the number of maxima identical to the order, i.e. the 5f signal has odd symmetry to the origin and 5 maxima, a 4f signal has even symmetry to the origin and 4 maxima. More details on the structure of the system matrix are found in Sec. 4.4.
The illustration in Fig. 4.5, which shows a *single frequency component over all spatial positions*, gives a good idea on how MPI encoding works. But in order to understand the system matrix approach for reconstruction, a different representation is advantageous. Figure 4.6 examplifies the signal generation process and shows *all frequency components for a single point in space* (the opposite of the above). These spectra are the F-space 'fingerprints' of the respective points in the FOV.
By arranging all spectral signatures for all points in the FOV into matrix form a system matrix is assembled, which can then be used in a matrix equation to reconstruct the inverse problem.
The magnitude spectrum is not suffient to form a system matrix, because two points symmetrically to the origin, i.e. with dc levels of identical magnitude but with opposite sign, exhibit an identical magnitude spectrum with opposite phase. Therefore, the rows of the system matrix are complex-valued spectra.

The imaging process can be expressed in matrix form as a simple linear equation:

$$\boldsymbol{A}\boldsymbol{x} = \boldsymbol{b} \tag{4.11}$$

The trivial solution is to left-multiply (4.11) with the inverse of matrix $\boldsymbol{A}^{-1}$ as follows:

$$\boldsymbol{A}^{-1}\boldsymbol{A}x = \boldsymbol{A}^{-1}\boldsymbol{b} \quad \rightarrow \quad \boldsymbol{x} = \boldsymbol{A}^{-1}\boldsymbol{b} \tag{4.12}$$

Unfortunately, in practice it is not that simple and we will get into why in a moment. First, consider the symbols in the above expressions. The matrix $\boldsymbol{A}$ is the system matrix, that basically defines an operation transforming the spatial points vector $\boldsymbol{x}$ into a measurement signal vector $\boldsymbol{b}$. The points vector $\boldsymbol{x}$ contains all n points in the FOV. For a 2-/3-dimensional problem, the points are reshaped into a single dimension. The measurement vector $\boldsymbol{b}$ is made up of all m frequency components that are detected from the object.

$$\boldsymbol{A} = \begin{pmatrix} a_{1,1} & a_{1,2} & \cdots & a_{1,n} \\ a_{2,1} & a_{2,2} & \cdots & a_{2,n} \\ \vdots & \vdots & \ddots & \vdots \\ a_{m,1} & a_{m,2} & \cdots & a_{m,n} \end{pmatrix} \in \mathbb{C}^{m \times n}$$

$$\boldsymbol{x} = \begin{pmatrix} x_1 \\ x_2 \\ \vdots \\ x_n \end{pmatrix} \in \mathbb{C}^n \quad \boldsymbol{b} = \begin{pmatrix} b_1 \\ b_2 \\ \vdots \\ b_m \end{pmatrix}^T \in \mathbb{C}^m$$

Apparently, $m \geq n$ is required to be able to solve the equation. This means, the number of frequency components must be at least the same as the number of spatial points to be reconstructed. Due to noise in the measurement vector, some extra frequency components are typically required.

In a 1-dimensional FOV, the frequency components are exactly the higher harmonics of the drive field frequency. For that reason, reconstructing a line with n points requires at least n harmonics to be recorded. For 2-/3-dimensional imaging the situation looks slightly different. For example, a $n \times n$ pixels FOV (with n^2 total number of pixels), requires at least n^2 frequency components for reconstruction. However, these frequency components do not have to be integer harmonics of the drive field frequencies. In 2-dimensional MPI there are two distinct drive field frequencies associated with the two axes. Detecting the same number of harmonics as in the 1-dimensional case above (or in other words with the same detection bandwidth) gives twice the number of frequency components ($2n$). But due to the non-linearity of the particle's magnetization curve a large number of mixing components are generated (in all off-axis positions), e.g. $(2f_\mathrm{x} + 3f_\mathrm{y})$ or $(3f_\mathrm{x} + 5f_\mathrm{y})$, and the like. For that reason, the detection bandwidth for 2-/3-dimensional MPI is not necessarily higher than for the 1-dimensional case, but then the requirements on dynamic detection range and the signal-noise-ratio are higher.

The above stated problem is generally over-determined, i.e. there are more frequency components in the system matrix than there are points in the FOV. However, due to a significant noise contribution in the detection signal $\tilde{b} = b + b_\mathrm{noise}$ many frequency components are not usable in reconstruction (matrix always has full rank, but a large number of components with small signal-to-background ratio are observed). It also means, that a simple matrix inversion is not possible. Therefore, the image reconstruction requires some level of regularization. The image is found as a solution to the least squares problem $\min_\mathrm{x} \|\boldsymbol{A}\boldsymbol{x} - \boldsymbol{b}\|_2$ or using the well-known Tikhonov regularization $\min_\mathrm{x} \left\{ \|\boldsymbol{A}\boldsymbol{x} - \boldsymbol{b}\|_2^2 + \lambda^2 \|\boldsymbol{x}\|_2^2 \right\}$.

4.1.3 Reconstruction (X-Space)

The x-space formalism of MPI, introduced by Goodwill et al. [13, 14, 168–170], expresses the signal in real space rather than in Fourier-space. It provides an elegant set of equations connecting the observed magnetization signal with the particle concentration in the FOV and the scanning trajectory. The time-domain magnetization produced at a point $\boldsymbol{x}$ under a trajectory $\boldsymbol{x}_0(t)$ is obtained by inserting (4.4) into (4.5):

$$\boldsymbol{M}(\boldsymbol{x},t) = v_\mathrm{f}(\boldsymbol{x}) M_\mathrm{S}\, \tilde{\boldsymbol{L}}\left(\frac{1}{\mu_0}\bar{\boldsymbol{G}}\left[\boldsymbol{x}-\boldsymbol{x}_0(t)\right]\right) \tag{4.13a}$$

$$\begin{aligned}\boldsymbol{\Phi}(t) &= -\mu_0 M_\mathrm{S} \int_V v_\mathrm{f}(\boldsymbol{r})\, \tilde{\boldsymbol{L}}\left(\frac{1}{\mu_0}\bar{\boldsymbol{G}}\left[\boldsymbol{r}-\boldsymbol{x}_0(t)\right]\right) \mathrm{d}\boldsymbol{r} \\ &= -\mu_0 M_\mathrm{S}\, v_\mathrm{f}(\boldsymbol{x}) * \tilde{\boldsymbol{L}}\left(\frac{1}{\mu_0}\bar{\boldsymbol{G}}\boldsymbol{x}\right)\Bigg|_{\boldsymbol{x}=\boldsymbol{x}_0(t)}\end{aligned} \tag{4.13b}$$

The magnetic flux $\boldsymbol{\Phi}(t)$ is detected by the MPI receive coils as a time derivative of (4.13b) with coil sensitivity S_x:

$$\begin{aligned}\boldsymbol{s}(t) &= -S_\mathrm{x}\frac{\mathrm{d}}{\mathrm{d}t}\boldsymbol{\Phi}(t) \\ &= S_\mathrm{x}\, M_\mathrm{S}\, v_\mathrm{f}(\boldsymbol{x}) * \dot{\tilde{\boldsymbol{L}}}\left(\frac{1}{\mu_0}\bar{\boldsymbol{G}}\boldsymbol{x}\right)\Bigg|_{\boldsymbol{x}=\boldsymbol{x}_0(t)} \bar{\boldsymbol{G}}\dot{\boldsymbol{x}}(t)\end{aligned} \tag{4.14a}$$

The receive signal $s(t)$ is scaled with the FFP velocity $\dot{\boldsymbol{x}}(t)$. That leads to maximum sensitity at the center of the FOV where the FFP velocity is fastest. The above equation (4.13b) is the x-space equivalent of the matrix equation as it describes the receive signal in dependence on the particle concentration in the FOV. In contrast to the F-space formalism, the x-space equation explicitly include the trajectory path and an accessible point spread function for the experiment in form of the derivative of the magnetization curve.

4.2 Hardware

For this thesis, two generations of Magnetic Particle Imaging (MPI) systems were build. The first (legacy) MPI system (→ Sec. 4.5) was considered a proof-of-principle design. The technical challenges in the realization of our own MPI system had to be discovered in a live system. The second and final MPI scanner setup (in the timeframe of this thesis) was designed to be 3D-capable and its design is described in this chapter [171, 172].
An overview of the MPI hardware evolution and a comparison of the technical specifications is listed in Tab. 4.2.

Table 4.2: Generations of MPI devices.

	Generation V1	Generation V2	Generation V2b
H_{typ}	12.5 mT	25 mT (max. 30 mT)	
f	2 kHz	10 kHz	
G	2 – 3.5 T/m	3 – 7 T/m (adjustable)	
FOV	10 mm × 10 mm	25 mm × 15 mm × 25 mm	
Axes	1(+1)	2(+1)	1(+1)
Shielding	none	none (copper cover)	shielded room
D/A	NI PCI-6733 (1 MHz, 16 bit)		
PA	Custom (470 W, <0.04 %)	img StageLine STA-3000 (1500 W, <0.1 %)	AE Techron 7548 (3.3 kW$_{\text{RMS}}$, <0.1 %)
BPF	series	series	series + parallel (LC resonant)
TxC X	N = 3x270 (3.0 mT/A)	4x360N (519.58 µH, 0 mT/A)	
TxC Y	N = 3x270 (3.0 mT/A)	4x360N (1.27 mH, 3.02 mT/A)	
TxC Z		4x360N (7.32 mH, 3.02 mT/A)	
RxC X	N = 20	N = 35 (143.1 µH)	
RxC Y	N = 20	N = 35 (99.89 µH)	
RxC Z		N = 35 (103.2 µH)	
BSF	BP (3.14 – 102 kHz)	6th-order (LC resonant)	12th-order (LC resonant)
ULNA	LT1028	AD797 (parallel, $e_{\text{n}} = 0.6\,\text{nV}/\sqrt{\text{Hz}}$)	INA103 ($e_{\text{n}} = 3.84\,\text{nV}/\sqrt{\text{Hz}}$)
A/D	NI PCI-4462 (205 kS/s, 24 bit)	NI PCI-6133 (2.5 MS/s, 14 bit)	
Rx BW	100 kHz (25 kHz)	12 – 500 kHz	1 MHz

The design of our Magnetic Particle Imaging system was inspired by the FFP scanner design from the initial publication on MPI by Gleich et al. [1]. A small 30 mm bore – suitable to fit a mouse – in a three-dimensional coil system, supplemented by a strong gradient of more than 3 T/m (up to 6 T/m). Focussing on a small size, was key for keeping the system efficient and compact and complexity of the overall system manageable. With drive field frequencies around 10 kHz the system was constructed in a cost effective way, using audio power amplifiers and cooling components for PCs.

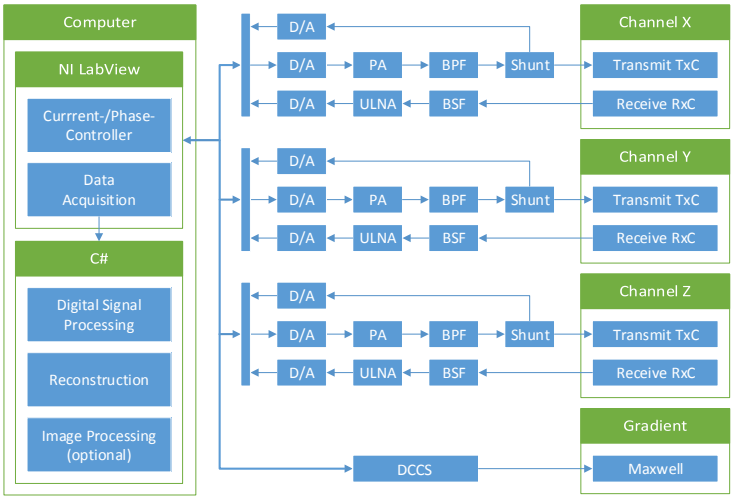

Figure 4.7: Block diagram of MPI system components.

Figure 4.7 shows a block diagram of the entire system. A break-down of the system components reveals three major pillars. The column on the left (Fig. 4.7, Computer) is the workstation controlling the system. It runs a NI LabView 2014 module that generates the digital transmit signals for selection and drive fields (Fig. 4.7, Current-/Phase Controller) and performs the synchronized data acquisition (Fig. 4.7, Data Acquisition). The control PC also runs a suite of components (written in C#, see Sec. 4.3) which are responsible for providing a graphical user interface for the operator and performing all essential computations to finally obtain an MPI image. That includes digital signal processing (Fig. 4.7, Digital Signal Processing), the reconstruction of the image from the raw (or pre-processed) data stream (Fig. 4.7, Reconstruction) and any post-processing steps, e.g. projection or volume rendering, on the reconstructed MPI data (Fig. 4.7, Image Processing).

The right column represents the coils assembly (→ Sec. 4.2.2), containing three sets of field generators for the drive field (Fig. 4.7, Transmit TxC) and the receive coils (Fig. 4.7, Receive RxC), and the selection field generator (Fig. 4.7, Gradient/Maxwell).
The central space of the diagram covers all digital and analog electronics required to operate the system. Each channel contains a transmit path (middle row), supplemented by the feedback path (top row) and a receive path (bottom row). For transmission (from left to right), a D/A converter card (Fig. 4.7, D/A) generates the low-level signals, followed by a linear power amplifier (Fig. 4.7, PA) and an analog band-pass filter (Fig. 4.7, BPF) feeding the transmit coils (TxC) through a shunt (Fig. 4.7, Shunt), which enables a feedback loop (Fig. 4.7, D/A (top row)) to control phase and amplitude of the drive field current. The receive path (from right to left) removes the feed-through from the transmit side via a band-stop filter (Fig. 4.7, BSF). The remaining signal is then fed into an (ultra) low noise amplifier (Fig. 4.7, ULNA) in order to be amplified to a level suitable for A/D conversion (Fig. 4.7, D/A (bottom row)). Transmit and receive path are discussed in more detail in chapters Sec. 4.2.3 and Sec. 4.2.4, respectively. The encoding gradient is powered from a dc current source (Fig. 4.7, DCCS).
A photo of the realized MPI system V2 is shown in Fig. 4.8. The rack on the left side contains (from bottom to top) two dc current supplies (Agilent 6674A) for the selection field, three linear power amplifier (img StageLine STA-3000, 2x 1.5 kW @ 4 Ω) and three transmit filter stages for the drive field, a surveillance unit, a universal dc power supply unit and a set of line filters. The coils assembly is seen on the right, mounted on a wooden shelf. A number of cables and tubes emerge from the PVC-enclosed coils. The tubes belong to a water circulation and cooling unit. Forced-air radiators with fans and the water expansion reservoirs are visible inside the shelf. The upper-left quadrant of the shelf contains the receive filters and low noise amplifiers. For the latest revision of our MPI system (with best sensitivity so far), the depicted coils assembly was moved into a shielding chamber [173, 174], the transmit filters were adapted to the common ground and the audio amplifiers (img StageLine STA-3000) were replaced with industrial amplifiers (AE Techron 7548).
For the description of the MPI scanner in the upcoming sections, the individual axes of the system are typically referred to with x, y and z. The nomenclature and orientation of the instrument's axes in relation to the anatomical planes of the object under investigation (e.g. a mouse) need to be defined. For most medical imaging methods, the principal axis of the system is referred to as the z-axis. The z-axis is also typically the symmetry axis of the instrument and oriented along the bore. This is true for the two most prominent modalities, CT and MRI . However, in MPI the symmetry axis of the mechanical setup (i.e. the bore) is not (necessarily) identical to the symmetry axis of the FOV, which is given by the encoding gradient. For the MPI design in this thesis, the main axis was defined as the symmetry axis of the encoding gradient, which in most MPI designs is perpendicular to the bore.

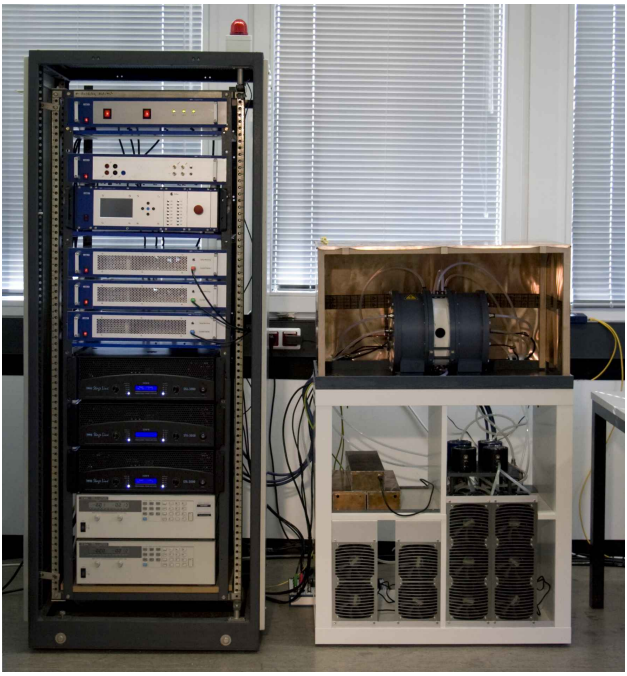

Figure 4.8: Photo of the MPI component rack (left) and coils assembly with cooling (right). The coils assembly was later moved into a shielded room.

For the subject, which is assumed to be a mouse-sized animal or phantom, the anatomical planes are related to the instrument's axes as follows:

- saggital plane (vertical section, left/right) $\rightarrow x/y$
- coronal plane (horizontal section, dorsal/ventral or back/front or posterior/anterior) $\rightarrow x/z$
- transverse plane (cross section, cranial/caudal or head/tail) $\rightarrow y/z$

The axial or transverse plane is by definition perpendicular to the body long axis.

4.2.1 Calibration robot

In order to perform a calibration scan (or system matrix acquisition) for a system matrix based reconstruction scheme (→ Sec. 4.1.2), a custom-build calibration robot is used (→ Fig. 4.9). The robot was assembled from three linear bearings with trapezoidal/ball screw thread and NEMA

17 stepper motors. Traveling distance of the sliders is about 40 mm with a positioning precision of <50 µm. Stepper motor drivers are digitally controlled over a serial line (with USB adapter). The calibration procedure can be fully automated, so that the robot steps through all spatial positions and the control software triggers an MPI data acqisition at each point.

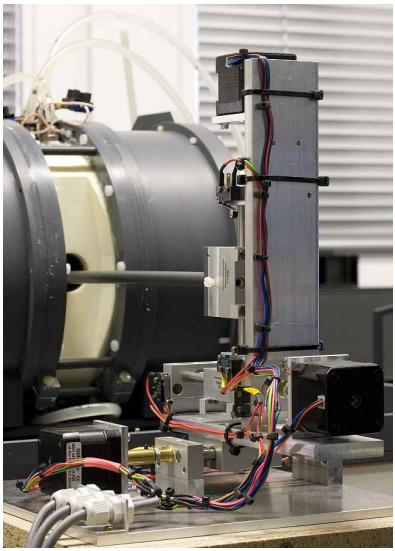

Figure 4.9: Photo of the calibration robot (positioned in front of the bore).

The calibration robot is build to move a sample, in most cases a (point-like) delta sample, within the boundaries of the field of view (FOV). The robot is required to be mechanically stable, so that there are as little oscillations/vibrations as possible from the robot's motion. Also, the movements must be reproducible in space with a high positioning precision. Precision limits are dictated by the resolution of the imaging system, which means that you should not be able to resolve any difference in signal when approaching a single spatial point repeatedly.
The robot must not have any feedback onto the MPI experiment. Because the robot is the only active, externally-supplied component within the shielding boundaries, and even close to the coils system, the dc power supply and especially the USB connection (transients from digital signals) are critical. For that reason, the robot has to be adequately grounded, it is erected at a 'safe' distance from the coils assembly and the sample is mounted onto a plastic arm, that reaches into the bore (→ Fig. 4.10).

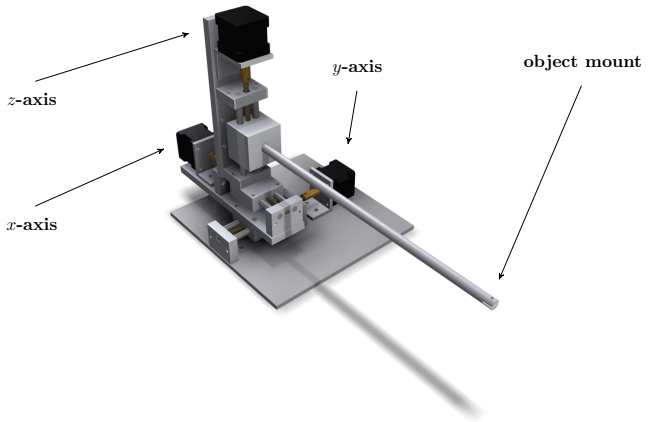

Figure 4.10: CAD rendering of the 3-axes calibration robot construction.

4.2.2 Coils System

The coils assembly is a central part of every MPI system. It constitutes the interface of the imaging system with the subject under investigation. As such, it must be designed to accommodate the subject by enabling access to the bore (preferably from both sides), but at the same time it must also satisfy the engineering requirements regarding field geometry, sensitivity and reliable operation. The coils assembly houses the field generators for the drive and selection fields as well as the receive coils. Due to high electric power and thermal losses in the resistive coils, the coils assembly must be designed with cooling needs in mind. As an interface, the coils assembly should also conform basic safety standards, for both the subject and the operator. The subject is to be kept at sensible ambient conditions (no overheating from the surrounding heat dissipation of the coils and no under-cooling). For the operator, the bore should be accessible without risk of electric shock or burns. For safety regarding radiation exposure and limits the software controller of the system is responsible.
Receive coils are not considered an integral part of the coils assembly, i.e. the system uses dedicated receive coils, which can be replaced easily for testing and advancement.
A close-up view of the MPI coils assembly is provided in Fig. 4.11.
The gray cylindric side parts made from PVC (polyvinylchloride), left and right of the opening), hold the gradient coils. The white center piece made from ABS (acrylonitrile butadiene styrene) contains the drive field coils. The assembly is modular, though not meant for frequent dis-/reassembly, and all pieces are connected by O-rings to seal the assembly waterproof.

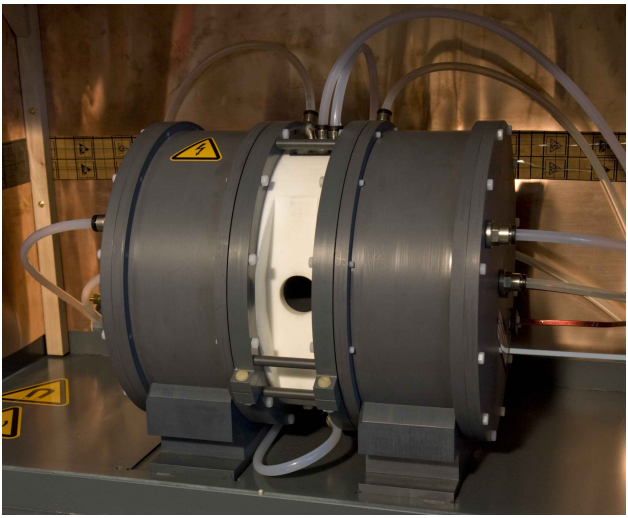

Figure 4.11: Photo of the MPI V2 coils assembly in copper shielding box with connected cooling tubes.

The tubes leading from/to the assembly belong to a water circulation system, which is used for water-cooling the drive field and selection field coils. The cooling is subdivided into multiple closed cooling circuits, so that heat dissipation from individual components can be controlled separately. As shown earlier in Fig. 4.8, the cooling happens over forced air radiators without active cooling. Only the inner most circuit around the bore features a Peltier-based active cooling system. The ambient air radiators are able to keep temperature of the cooling agent (water) around 40 – 45 °C at standard operating parameters. In the center of the coils assembly the 30 mm bore is visible.
The coils assembly must be designed as robust and mechanically stable as possible. Drive field coils (→ Sec. 4.2.2) produce a field in the range of 25 mT within the dc field gradient of the selection field (→ Sec. 4.2.2). As a result, the coils assembly produces mechanical vibrations, which in turn cause mechanical stress on the components. To handle this, the coils assembly was designed as a modular yet rigid system, without any gaps or weak points in the structure. However, the compactness turned out to be challenging during assembly and repair. Especially, the inner-most part framing the drive field coils has been manufactured in a rapid prototyping process.
Figure 4.12a shows a (simplified) CAD rendering of the coils system. The corresponding internal structure is visible in Fig. 4.12b. According to Sec. 4.1.1, three types of coils are required for Magnetic Particle Imaging. The yellow cylinders are the gradient coils augmented by the permanent

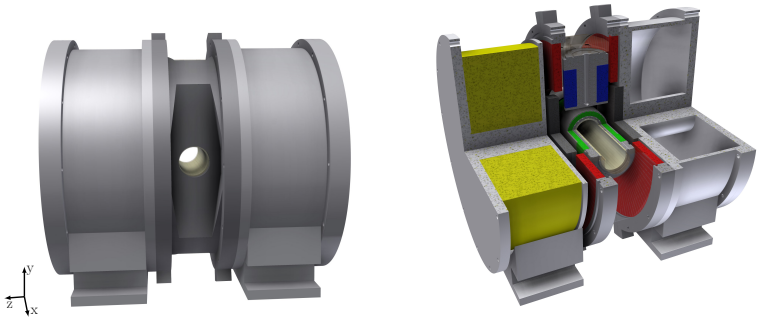

(a) Exterior assembly view **(b)** Inside coil positions

Figure 4.12: Insight into the coils assembly: Drive field coils are colored to show the field generators for the x- (green), y- (blue) and z-axis (red). Gradient coils are shown in yellow with permanent magnets in black.

magnets (Fig. 4.12b, black discs) to produce a selection field. The field-free point (FFP) is steered through the FOV by the drive field coils. The drive field coils for the three axes are shown in green (x-axis), blue (y-axis) and red (z-axis).
In the next sections, the individual coils are described in more detail.

Selection Field / Gradient

The encoding field in MPI is provided by the time-invariant gradient field. The gradient could form a field-free point (FFP) or a field-free line (FFL). The scanner in this thesis uses a field-free point design with a linear encoding gradient. A good selection field generator should be mechanically stable and it should produce a gradient field that is constant over time, even in the presence of other strong magnetic fields, i.e. the drive fields. Also, a strong gradient with more than 3 T/m is desirable, because the resolution in MPI is directly proportional to the gradient strength (→ Sec. 4.1.1). For such strong gradients, a design based purely on electromagnets (esp. without core material) is quite challenging. A permanent magnet on the other hand is capable of generating fixed gradients of that order. By combining a permanent magnet with an electromagnet, one obtains an adjustable gradient without moving parts, i.e. without shifting the magnets. Also, a shift field or focus field can be implemented in the main gradient direction by using individual dc power supplies for the gradient coils.
The adjustable encoding gradient for the described scanner with a maximum gradient strength of about 7 T/m along the z-axis is created by a combination of NeFeB permanent magnets and a pair of Maxwell coils. A schematic view of the gradient unit is shown in Fig. 4.13.

The gradient coils are made from a solid copper wire with a rectangular cross section of 6 mm x 2 mm. The wire is wound onto a 50 mm tenon and fills the entire space to an outer diameter of about 220 mm. Cable ties have been used to induce regular spacing into the coil package where cooling water can flow through.

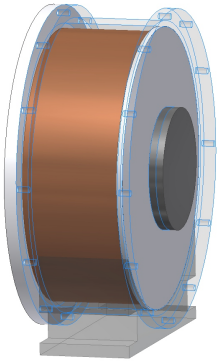

Figure 4.13: CAD rendering of the gradient coils (copper) and the NdFeB permanent magnet (black disc).

The coil's geometry resembles a Maxwell coil. A Maxwell coils pair consists of two coils each with radius r, spaced by a distance of $\sqrt{3}\,r$. The current in the two loops flows in opposite directions. The field gradient in a Maxwell coil has a uniformity of 5% within a sphere of radius $0.5r$ at the center of the coil pair [175].

Table 4.3: Specifications of the gradient coils.

Wire gauge	10 mm^2 (⌀ 5×2 mm)
Outer Diameter	220 mm
Windings	16
Layers	24
Inductance	23 mH
Coil constant	66.7 mT/(m A)
Current (typ.)	30/60 A ($\widehat{=}$ 2 T/m* / 4 T/m*) * excluding NdFeB magnets
NdFeB magnet	D100x12 mm (N45H)

The gradient coils pair as shown in Fig. 4.13 is complemented by a pair of neodymium permanent magnets (Fig. 4.13, black disc). These magnets are rare-earth magnets made of sintered alloy of neodymium-iron-boron ($Nd_2Fe_{14}B$). The saturation magnetization on the surface is up to 1.3 T ($BH_{max} = 200 - 400\,kJ/m^3$) [176].

Drive Field

The drive field coils are to generate a deflection field for the FFP with sufficient amplitude to move the FFP to the edges of the FOV and to (at least partially) saturate the magnetic nanoparticle tracer. For generating the three orthogonal drive fields, which are required for 3-dimensional spatial encoding in MPI, coils in Helmholtz-type configuration are used on the y- and z- axes, while the x-axis is designed as an elongated solenoid ($\rightarrow$ Fig. 4.14) [177]. On the principal (gradient) axis a maximum field amplitude of 60 mT can be generated, while on the other axes up to 30 mT are achievable. Typically, lower drive field amplitudes around 20 – 25 mT are used as standard operating parameters.
The drive field coils – as mentioned above – are enclosed in a water-sealed housing to enable water-cooling (see Fig. 4.14a for geometric reference). For thermally stable operation duty cycles are introduced during data acquisition. The effectiveness of the cooling strongly depends on the coil geometry. However, the geometry of the coil package is primarily driven by the required field geometry. A compromise between cooling efficiency, field uniformity and electrical parameters (such as impedance) must be found. Luckily, the requirement for the drive field to adhere to a precise field geometry are in the range of a few percent for MPI. According to (4.2c), a field variation leads to a proportional (via the selection field gradient) displacement of the FFP in the FOV. For small field deviations, the FFP displacement is below the spatial resolution limit of the scanner. For F-space reconstruction (based on a system matrix), imperfections in field geometry can also be accounted for via calibration.

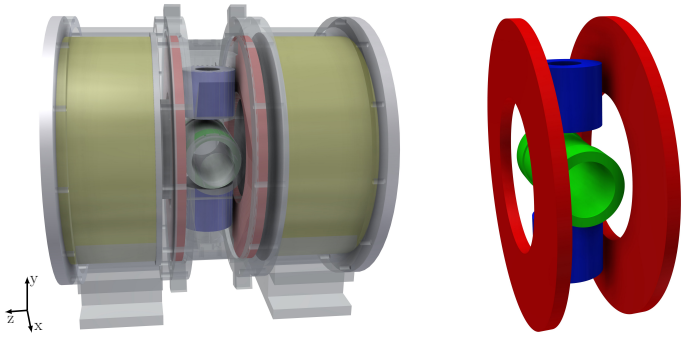

(a) Assembly coil positions **(b)** Drive field coils

Figure 4.14: Schematic view of the drive field coils and positions in the coils assembly: Drive field coils are colored to show the field generators for the x- (green), y- (blue) and z-axis (red).

Due to the ac currents of about 10 kHz and amplitudes of about 25 A running through the drive field coils, the thermal losses are quite significant.

For that reason, the drive field coils are made of Litz wire [178, 179]. The skin depth of copper at the drive field frequency is about 0.6 mm. As a result, there is no homogenous current density in a solid wire. The increased current density close to the surface of the wire in comparison to the wire's core results in a decrease of the effective, current-carrying diameter. A Litz wire is made of dozens of isolated strands to mitigate this effect. It minimizes the skin effect in order to increase the effective diameter of the wire (also affected by the proximity effect, which is an eddy current coupling between neighboring strands) [180, 181].
The following sections give more details on the design of individual axes, especially on the shape/type of the coils and the design of the cooling channels. An isolated view of the drive coils geometry is given in Fig. 4.14b.

Drive Field X

The drive field in x-direction is generated by a single elongated solenoid. Specifications of the field generator in that axis are given in Tab. 4.4.

Table 4.4: Specifications of the x drive coils.

Wire gauge	1.41 mm^2 ($\varnothing$ 45×0.031 mm)
Litz type	45×0.2 mm (wrapped with silk thread)
Outer Diameter	54 mm
Length	100 mm
Layers	3 (+1)
Windings	55 (+2×11)
Coil constant	2.07 mT/A
Current (typ.)	15 A ($\widehat{=}$ 31 mT)

The x drive coil is designed as a solenoid, as this shape ensures a high coil constant while at the same time resulting in a compact package that yields high homogeneity close to the center. Homogeneity is further increased by the addition of an extra layer near both ends of the coil, resulting in a dumbbell-shaped winding area. This allows to reduce the length of the coil and increases the field strength per unit current, while still achieving ±0.2% homogeneity within the FOV.
As a result, this axis exhibits better ac characteristics (such as smaller thermal losses) under operating conditions than the y and z drive coils. Cooling is achieved by channels embedded in the coil carrier that allows coolant flow orthogonal to the winding direction. Coolant agent enters the coil below the winding area at one end of the coil and flows in axial direction. It returns above the winding area to the same end of the coil. A mylar sheet between the windings prevents coolant from returning directly to the sink and provides additional electrical inter-layer isolation.
Above mentioned design considerations are confirmed by impedance measurements (→ Fig. 4.16), where the x-axis shows a lower real part of the

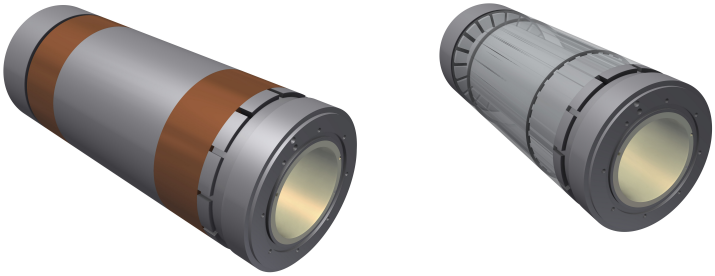

(a) CAD rendering of the x drive coil

(b) Cooling channels below the winding area

Figure 4.15: CAD rendering of the x drive field generator and embedded cooling channels.

impedance compared to other axes. The inductance of the coil, determined from fits to the impedance plot, is $L_S = 519.0\,\mathrm{mH}$. Equivalent circuit parameters of the coil are fitted as well and give a parallel capacitance of $C_P = 7.5\,\mathrm{nF}$, a parallel resistance of $R_P = 350\,\Omega$ and a series resistance of $R_S = 280\,\mathrm{m}\Omega$. The real part at the drive field frequency (without the effect of coolant) is $0.41\,\Omega$.
For the minimum gradient, using only the NdFeB magnets ($4.4\,\mathrm{T/m}$ in z-direction), a typical excitation current of $15\,\mathrm{A}$ results in a FOV of $2.066\,\mathrm{mT/A} \cdot 15\,\mathrm{A_{pk}} \cdot (\frac{1}{2}\ 4.4\,\mathrm{T/m})^{-1} = \pm 14.08\,\mathrm{mm}$.

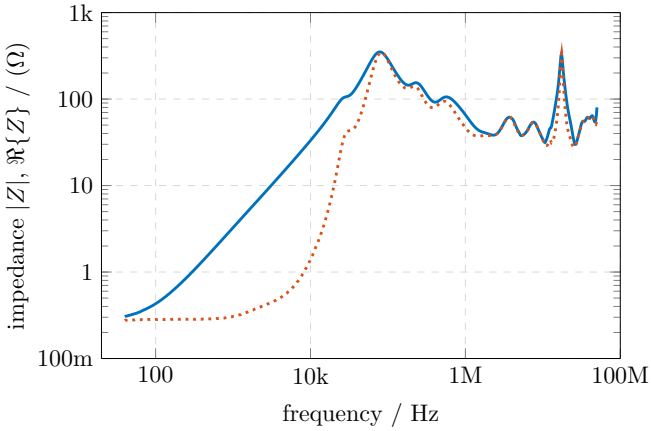

Figure 4.16: Impedance plot of the x drive field coil, magnitude (solid) and real part (dotted).

Drive Field Y

The drive field in y-direction is generated by a Helmholtz-type coils pair. Specifications of the field generator in that axis are given in Tab. 4.5.

Table 4.5: Specifications of the y drive coils.

Wire gauge	$1.41\,\mathrm{mm}^2$ ($\varnothing$ 45×0.031 mm)
Litz type	45×0.2 mm (wrapped with silk thread)
Outer Diameter	52 mm
Length	43 mm (each)
Layers	8
Windings	25
Coil constant	1.24 mT/A
Current (typ.)	25 A ($\widehat{=}$ 31 mT)

Due to limited space between the gradient coils, which is further reduced by the volume occupied by the z drive coils, the radius of the coils is insufficient compared to their axial spacing. Consequently, this axis shows the lowest homogeneity (±29.4%) of the drive system. This compromise was made to ensure high homogeneity in the direction of the highest gradient (z-direction), which would have been impossible to achieve with a better Helmholtz design in y-direction.
Fig. 4.17 shows the CAD model of the y coils pair. Both coils are embedded within the central supporting structure of the coils system and feature separate coolant influx and drainage (connected in series externally).

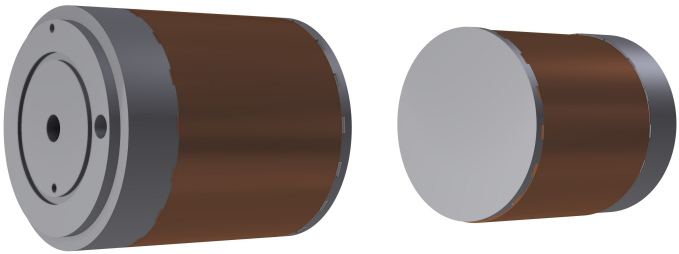

Figure 4.17: CAD rendering of the y drive field generator.

Parameter fits to the impedance plot (→ Fig. 4.2.2) yield equivalent circuit parameters of $C_P = 467\,\mathrm{pF}$, $R_P = 15.6\,\mathrm{k\Omega}$ and $R_S = 1.27\,\Omega$. The inductance of the y coil is measured as $L_S = 1.27\,\mathrm{mH}$.

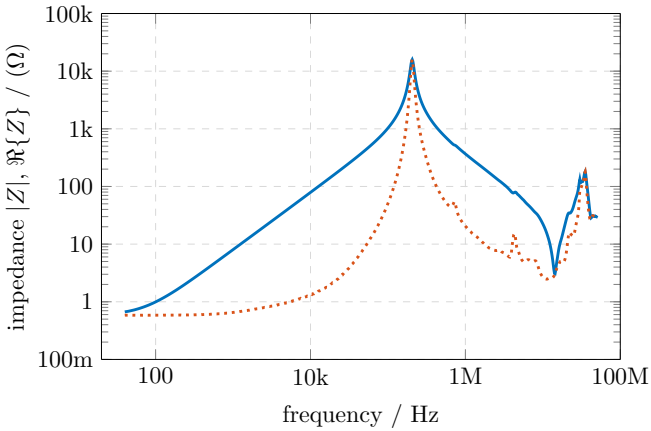

Figure 4.18: Impedance plot of the y drive field coil, magnitude (solid) and real part (dotted).

Due to its compact design, the y drive coils achieve only satisfying ac performance, which is greatly inferior to the x-axis.

Drive Field Z

The drive field in z-direction is generated by a Helmholtz-type coils pair. Specifications of the field generator in that axis are given in Tab. 4.6.

Table 4.6: Specifications of the z drive coils.

Wire gauge	1.41 mm^2 (⌀ 45×0.031 mm)
Litz type	45×0.2 mm (wrapped with silk thread)
Outer Diameter	203 mm
Length	9 mm (each)
Layers	30
Windings	5
Coil constant	2.44 mT/A
Current (typ.)	25 A ($\widehat{=}$ 61 mT)

Similar to the y-direction, the drive coils in the z-axis are constructed as Helmholtz pairs. Because this axis has the highest gradient strength, homogeneity of the drive field is a major design effort. Although the z coils have high winding counts and short lengths, the effective radius could be realized as the Helmholtz radius.

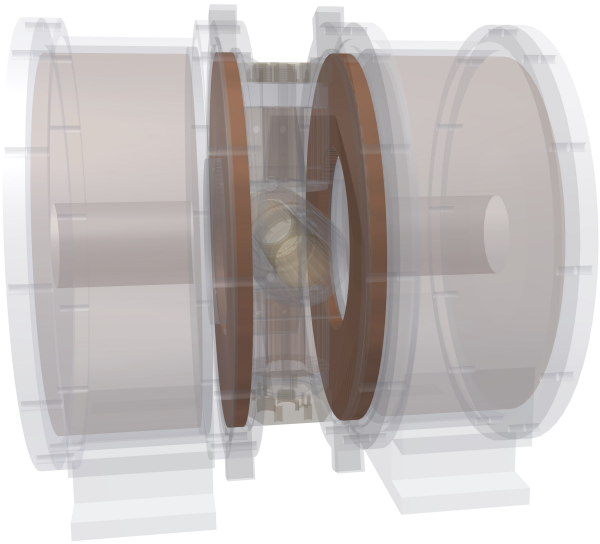

Figure 4.19: CAD rendering of the z drive field generator (in context of the coils assembly).

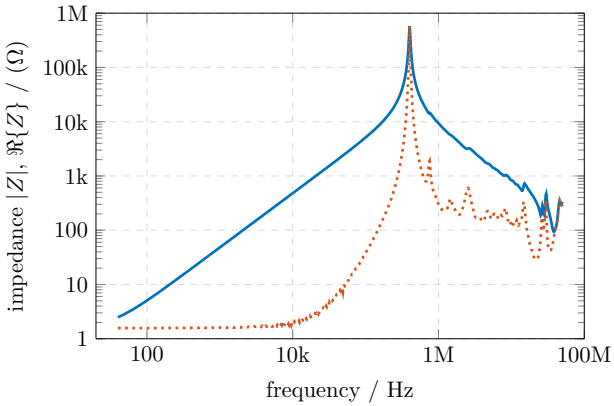

Figure 4.20: Impedance plot of the z drive field coil, magnitude (solid) and real part (dotted).

Coolant for this axis is channeled along the radial direction, with a drilling at the inner radius connecting both coils. Therefore one side is connected to the coolant influx, while the other coil returns the coolant.

Featuring a homogeneity of ±0.8%, the z-axis is on a par with the x-direction. Due to the large distance from the FOV and the large coil diameter resulting from geometric Helmholtz coil requirements, this axis shows the highest inductance ($L_S = 7.32\,\mathrm{mH}$) of all drive field coils. A fit to the impedance data (→ Fig. 4.20) determines the equivalent circuit parameters as $C_P = 402\,\mathrm{pF}$, $R_P = 4.64\,\mathrm{k\Omega}$ and $R_S = 1.7\,\mathrm{m\Omega}$. The real part of the impedance at the drive frequency is $1.82\,\Omega$, making this axis unsuitable for large ac amplitudes. However, it can be used for precise dc-shifts of the FFP over large distances, i.e. focus field generator in z-direction, due to the high homogeneity.

Receiver

The receive coils pick up the particle response and therefore directly affect imaging quality through their sensitivity and noise characteristics. Achieving a good SNR was a key consideration and led to the construction of dedicated receive coils [182, 183]. This allows for optimizations with respect to the investigated object and intended application. For general-purpose studies, a default detection system was built that allows (independent) detection of the three spatial field components of the particle signal.

Table 4.7: Specifications of the receive coil system.

Wire	$0.02\,\mathrm{mm}^2$ (⌀ 0.16 mm)
Radius	16 mm
Windings	x-axis: 35 y-axis: 30 z-axis: 30
Coil constant	x-axis: 0.96 mT/A

Specifications of the receive coils system are given in Tab. 4.7. The detection system consists of a Helmholtz pair in x-direction as well as additional saddle coils for y and z components [184–186], which are wound on a PVC coil former (→ Fig. 4.21). The wires are kept in position by epoxy resin which also acts as protective cover during assembly.
Measurements of the impedance for the x coils (→ Fig. 4.22) yield an inductance of $L_S = 143.1\,\mu\mathrm{H}$ and a series resistance of $R_S = 13\,\Omega$. The self resonance frequency, which limits the detection bandwidth, is $f_{\mathrm{srf,x}} = 931\,\mathrm{kHz}$. For the y and z detection coils (saddle coils) the inductance values are $L_{S,y} = 103.2\,\mu\mathrm{H}$ and $L_{S,z} = 99.9\,\mu\mathrm{H}$, respectively (→ Fig. 4.23). The resonances occur at $f_{\mathrm{srf,y}}$ =1.34 MHz and $f_{\mathrm{srf,z}}$ =1.39 MHz. Both coils have approximately $14\,\Omega$ of series resistance.

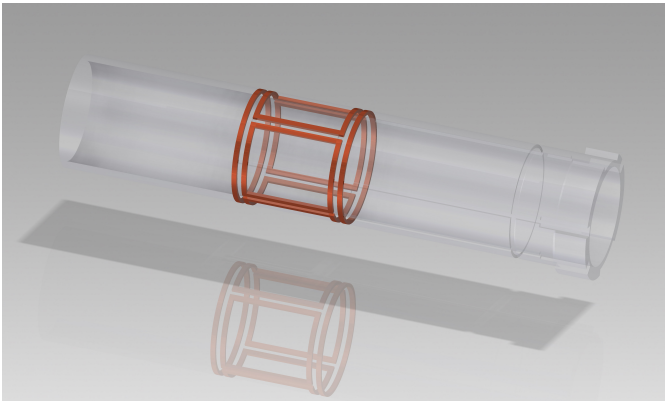

Figure 4.21: CAD rendering of the receive coils, a Helmholtz coil pair in x-direction and saddle coils in y and z.

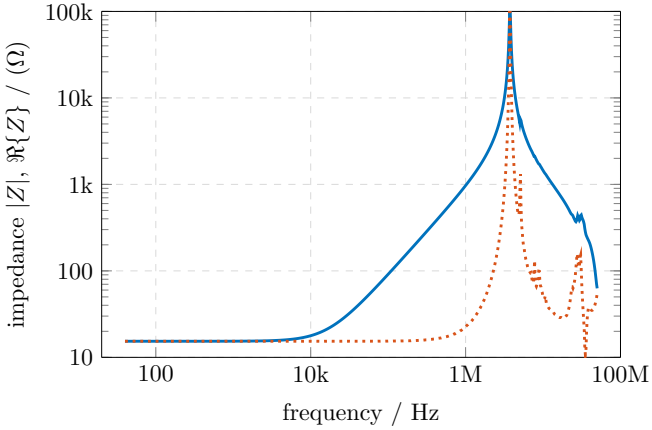

Figure 4.22: Impedance plot of the x receive coils, magnitude (solid) and real part (dotted).

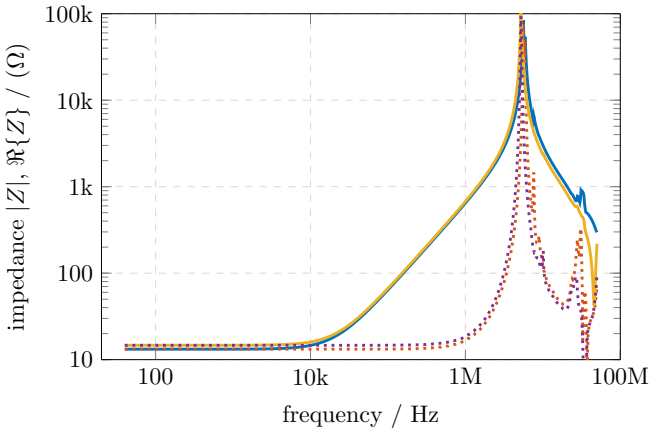

Figure 4.23: Impedance plot of the y (blue, red) and z (yellow, purple) receive coils, magnitude (solid) and real part (dotted). Due to the identical construction, these two receive axes show very similar properties.

4.2.3 Transmit Chain (Tx)

The sinusoidal ac signals for the scanning axes are generated by a D/A converter card (NI PCI-6733, 3x 16 bit @ 1 MS/s), amplified by three audio power amplifiers (AE Techron 7548, 5.5 kW @ 1 Ω, DC – 30 kHz) and passed through a resonating band-pass filter network (BPF) tuned to drive field frequencies around 10 kHz (→ Fig. 4.24). The current revision of the system achieves a spectral purity with THD $< 0.002\,\%$ ($> 94\,\mathrm{dB_C}$). Temperature drift of the analog power circuits is monitored (Shunt plus A/D converter, NI PCIe-6320, 3x 16 bit @ 250 kS/s) correcting current amplitude and phase of each drive field axis separately by adjusting the D/A generated signals appropriately.

Transmit Filters

The transmit filters ensure low harmonic distortion for the drive coil currents in the presence of distorting power amplifiers by providing suppression for all frequency components outside a narrow bandwidth around the drive field frequency. A classical resonating LC-band-pass ladder filter is used here [187, 188]. The filter components are tuned to the drive field frequencies of the corresponding channels. Component parameters are selected from design constraints (currents, voltages, available space, etc.) without adhering to a specific filter characteristic (such as Butterworth or Bessel). In order to achieve good suppression of high frequency components, the filter is cascaded with a 1^{st} order RC low-pass filter that provides a high stopband attenuation in presence of component parasitics.

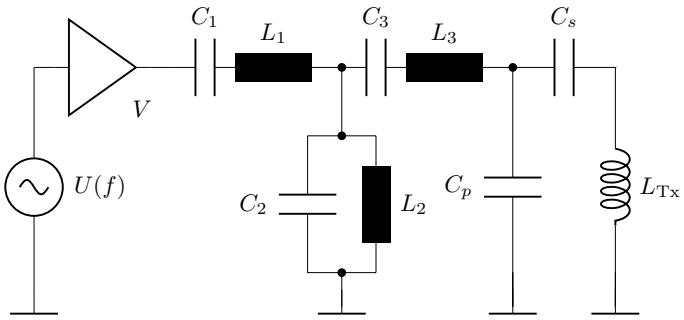

Figure 4.24: Transmit filter circuit of the MPI drive field system. The filter is designed as a band-pass filter stage and a series LC resonator with the transmit coil.

Another need for transmit filters arises from the impedance mismatch between the power amplifier and the drive coils at higher frequencies. Forming a resonant LC circuit with the drive coil, the transmit filter cancels the reactive part of the drive coil impedance and therefore reduces the mismatch with the (approximate) resistive low impedance amplifier output. Tab. 4.8 lists the specifications of a transmit filter stage.

Table 4.8: Specifications of the transmit filters.

Type	Band-pass (+ low-pass)
Order	6th order + 1st order low-pass
Center Frequency	10.0 kHz
Corner Frequency	39.7 kHz
Bandwidth	525 Hz ($Q = 19$)

The transmit filters require heavy duty components due to elevated voltages and currents at the resonant operating point. Therefore solid 2 mm copper wires and high-power Vishay series MKP1839 capacitors (metallized polypropylene film capacitors) were chosen for the filter components [189]. Inductors were wound in a toroidal shape to reduce stray fields [190]. This is essential as highly permeable core materials usually employed to reduce flux leakage cannot be used within MPI drive systems because of their non-linear properties.
The filters are built as a rigid construction with resin supporting the coil wires to reduce mechanical vibrations. Fig. 4.25 shows the impedance plot of such a filter (from the x-axis). The resonant design ensures narrow bandwidth and high stopband attenuation.

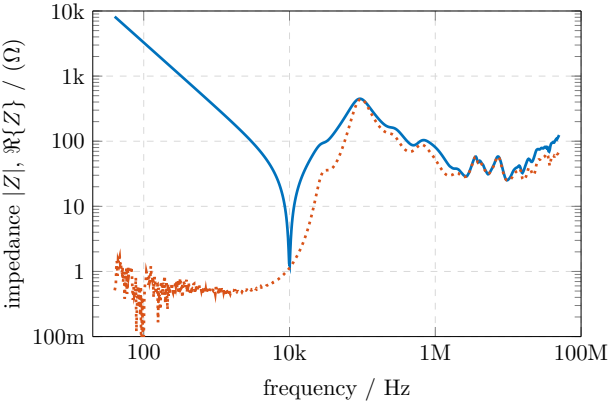

Figure 4.25: Impedance plot of the transmit band-pass filter of the x channel, magnitude (solid) and real part (dotted).

4.2.4 Receive Chain (Rx)

For detection, three pairs of detection coils close to the surface of the bore are used. The induction signals are passed through a passive, resonating band-stop filter (BSF), amplified by a custom-build low noise amplifier (en $< 4\,\mathrm{nV}/\sqrt{\mathrm{Hz}}$, bandwidth 1 MHz) [191–193] and finally digitized by a high-speed A/D converter card (NI PCI-6133, 3x 14 bit @ 2.5 MS/s).

Receive Filters

Due to feed-through from the drive field, additional filtering is required for the detection signal to reduce dynamic range requirements. Otherwise a dynamic range exceeding 120 dB would be required to detect a sufficient number of higher harmonics (or mixing frequency components) for MPI image reconstruction. Therefore, additional band-stop or notch filters are inserted to remove the unwanted drive field frequency component from the detection signal. A summary of the receive filter specifications is given in Tab. 4.9 and their design is sketched in Fig. 4.26.

Table 4.9: Specifications of the receive filters.

Type	Bandstop / Notch
Order	1 box: 6th order, 2 boxes: 12th order
Center Frequency	10.0 kHz
Bandwidth	1.06 kHz ($Q = 9.5$)

In order to build a receive filter with high suppression, similar concepts as for the transmit filters are employed. A resonant LC ladder band-stop filter (with no specific filter characteristic) is used to remove the

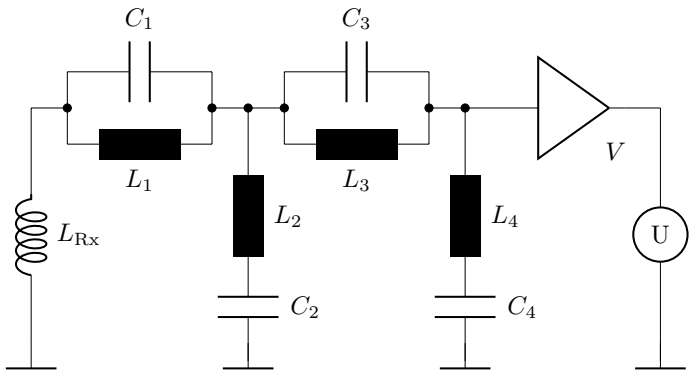

Figure 4.26: Receive filter circuit of the MPI system. The receive chain is composed of a band-stop filter and a low noise amplification stage.

drive field frequency component. Although an impedance match to the (wideband) detection system cannot be achieved, the input impedance of the band-stop filter is critical as it loads the detection coil [194–196]. The receive filters are built from toroidal wire wound coils (0.5 mm solid wire for high inductance toroids, 45x 0.2 mm Litz wire for subsequent filter stages) which are mounted together with their matched capacitors in a common copper enclosure.

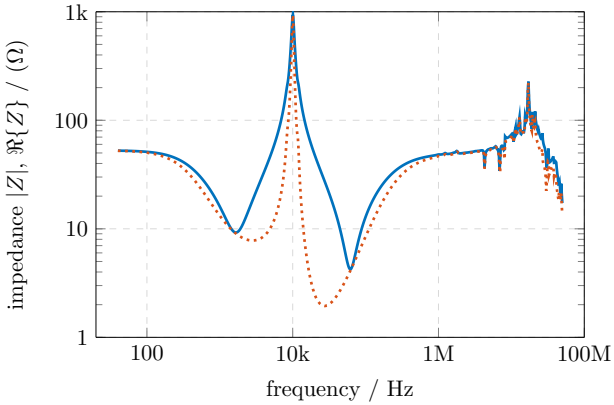

Figure 4.27: Impedance plot of the notch filters, magnitude (solid) and real part (dotted).

To avoid mutual inductance coupling between the coils, every filter stage is isolated in a separate compartment. Because the capacitors have to be highly linear, high voltage capacitors (Vishay MKP1813 series) are used. Fig. 4.27 depicts the typical input impedance characteristic of such a filter. At the resonance point, the input impedance is high (approximately 1 kHz) in order to prevent excessive current flow through the detection coil.

4.3 Software

The MPI imaging modility and the MPS particle characterization method – as most modern measuring setups – do not function without software (and possibly firmware). Specifically, MPI requires signal processing, image reconstruction and visualization to actually work. To provide the necessary support on the software side, a software package has been developed as part of the project. In the MPI block diagram (→ Fig. 4.7) approximately 1/3 of the space is taken by the software stack, which is also roughly equivalent to the effort and complexity of the software components in relation to the entire system.
The screenshot of the 'MPIControl' panels in Fig. 4.28 is representative for the MPI control software. It shows the main user interface (with mode selection, sample/object management, measurement parameters, etc.) and a 'display' window that contains a 'view' on the simulated or measured dataset. The application is designed to be agnostic to different measurement or simulation modes. While the user interface and the data structures are optimized for use in MNP -related projects, the actual methods (e.g. MPI, MPS, ACS, ...) are realized as composable modules.

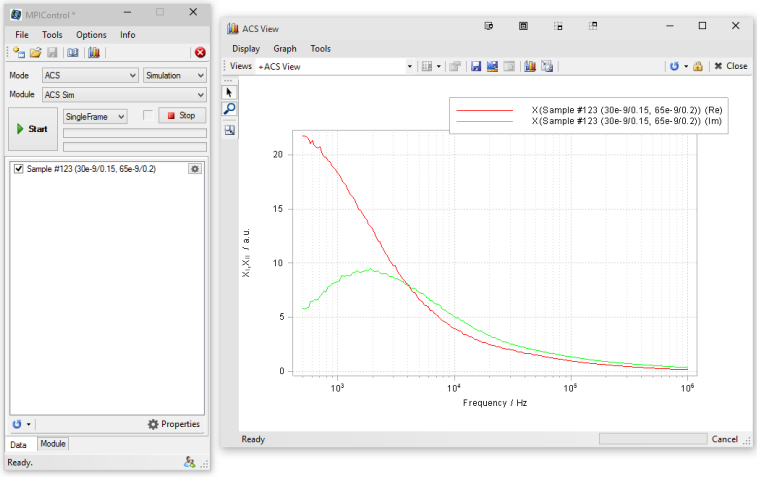

Figure 4.28: User Interface of the main "MPIControl" application.

The MPI and MPS modules build on top of NI LabVIEW 2014 as the I/O layer. Because the system uses data acquisition (A/D) and generation (D/A) cards from National Instruments using LabVIEW as a control interface was obvious. The digital transmit waveforms are generated in LabVIEW and then passed to the D/A card. In combination with an A/D card to record reference signals from the three transmit coils, a current- and phase-controller is implemented to adjust the transmit signals in order to generate a stable trajectory. The data acquisition from the high-speed A/D card is synchronized to the signal generators and the digitized data is stored to disk or passed to the control software. The LabVIEW interfaces are also especially useful for low-level system and signal tests.
The MPI control software itself is written in C#, which provides a good balance between ease of implementation and efficient runtime execution. All math routines are based on the compute engine from the ILNumerics library (http://ilnumerics.net/), and most of the data visualization is implemented with their graphics engine. ILNumerics delivers an efficient memory management and high performance math primitives (from LAPACK, BLAS, etc.) similar to the MathWorks MATLAB environment. Other external libraries include VTK/ITK for image and volume visualization, and BerkeleyDB, MongoDB and HDF5 as storage backends. The entire project tree spans about 70 000 lines of custom C# code.
As a high-level overview, the C# components provide a graphical user interface, object and data management, digital signal processing, MPI image reconstruction, post- and image-processing, curve fitting for MPS and ACS and a universal simulation and processing framework for MNP -related tasks. The framework currently implementes the following reconstruction algorithms: Kaczmarz (in classical and randomized version), Tikhonov and Truncated SVD. Additionally all particle magnetization models from Sec. 2.4 are available.
For large-scale MPI simulation or fitting procedures with compute-intensive algorithms the framework supports a distributed computing model to leverage idle (heterogenous) machines in the local network. Alternatively, some of the computations for this thesis were executed as a Microsoft Azure Batch project in the cloud.

4.4 System Matrix

Generally, as described in Sec. 4.1, there are two options for obtaining an image from the recorded data of an MPI experiment. One can either use the x-space approach (→ Sec. 4.1.3), i.e. observing the time-domain signal and mapping it into the FOV, or the F-space reconstruction (→ Sec. 4.1.2) based on a system matrix. The system matrix describes the entire imaging process and contains details on field geometries, the trajectory, the operating frequency, the particles, the transfer function of transmit and receive filters, the power amplifiers and low-noise amplifiers, etc. It implicitely covers all components of the system's signal path and the tracer

as well. Typically, the system matrix is measured in the actual imaging system by using a calibration robot that moves a point-like reference sample through the FOV and acquires a reference response signal at each point (→ Sec. 4.2.1).

Of course, the system matrix can also be derived theoretically or computed numerically from appropriate models. There are various ways for obtaining the system matrix:
A synthetic (calculated) system matrix can be used for reconstruction. While the calculated system matrix is 'perfect' in terms of signal-noise-ratio (SNR), it is typically inferior regarding the resulting image quality. A reconstruction approach based purely on a modelled system matrix has been studied by Knopp et al. [197], but was found to be inferior to the calibration-based approach. The calculations for a synthetic system matrix have to incorporate all of the above mentioned properties of the imaging system and the tracer, which is difficult to achieve because we do not have access to all relevant parameters. Also, imperfections of the physical system or the available numerical models make it even more difficult.
As an alternative, a hybrid approach can be employed that combines empirical measurements on the actual system and numerically calculated data into a hybrid system matrix. For that, the transfer function of all system components is taken into account and/or the particle model is advanced with data from MPS measurements (→ Sec. 4.4.1) [198].

The next section shows examples of synthetic and measured system matrices. Different approaches and models are compared with regard to reconstruction quality. Also, the effect of noise on the reconstruction process is demonstrated. Most of the fore-mentioned topics are dealt with in the 1-dimensional domain.

4.4.1 1D System Matrix

The system matrix of a 1-dimensional MPI experiment is easily explained: It is a complex-valued matrix where the rows contain all available harmonics acquired on the sample and the columns match the indexed spatial points in the FOV. In 1D MPI, only a single receive channel (aligned with the only transmit channel) is used, and the detection signal contains only integer harmonics of the drive field frequency.

For a hypothetical experiment with 10 pixels in the 1-dimensional FOV and detection conditions suitable to receive 15 harmonics (above the noise floor), the system matrix is a 15×10 matrix. In principle, this means that the matrix equation for reconstruction is over-determined and should be solvable with an appropriate regularization scheme. For a 1-dimensional FOV the system matrix can be visualized as a surface plot with the spatial positions along the x-axis, the frequency components along the y-axis and

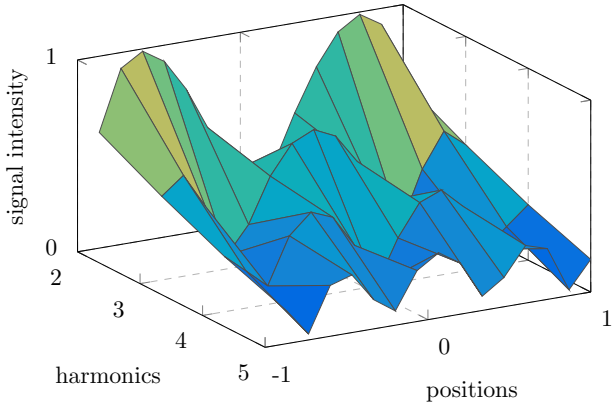

Figure 4.29: 1D system matrix with 5 harmonics (magnitude of system matrix components) demonstrates the MPI encoding scheme as a function of spatial position and harmonic index.

the spectral amplitude/magnitude on the z-axis. Figure 4.29 illustrates such a 1D system matrix including the first five harmonics only and with the spatial positions normalized to the field of view (FOV).

1D Synthetic System Matrix

The simplest model that can be utilized to calculate a system matrix is the Langevin model (→ Sec. 2.4.1). The Langevin model does not include any particle magnetization dynamics and implies an instant response to the applied drive field. Figure 4.30 shows a system matrix calculated with this model in the surface plot representation introduced above.

It is apparent from the figure that there is a distinct modulation of the magnitude signal as a function of the spatial coordinates within the FOV and of the harmonic index. The characteristic pattern provides the basis for spatial encoding in MPI . Although the prototype of the system matrix looks simple in a magnitude plot, there is a lot to find in a more detailed analysis of the system matrix properties of a 1-dimensional MPI experiment.

The side-view (→ Fig. 4.31a) of the previous plot shows the modulation width of the individual harmonics, i.e. the span between the maximum and the minimum spectral magnitude for all positions. It also depicts the near-exponential decay of the signal towards higher harmonics, which corresponds to the falling slope in an MPS experiment (→ Sec. 3.1 and Fig. 3.6). A reduced view (top-view onto the surface plot) reveals the

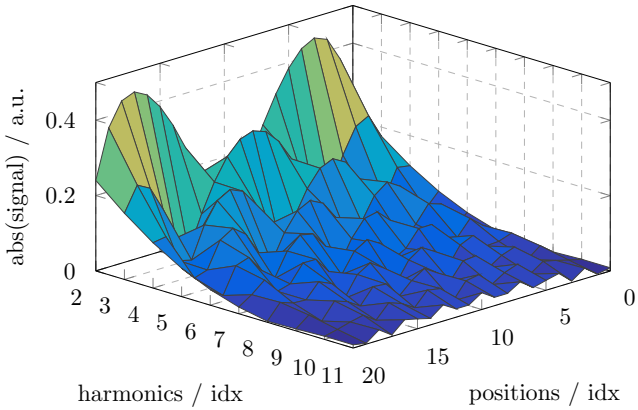

Figure 4.30: Synthetic 1D system matrix (magnitude) in orthographic projection view.

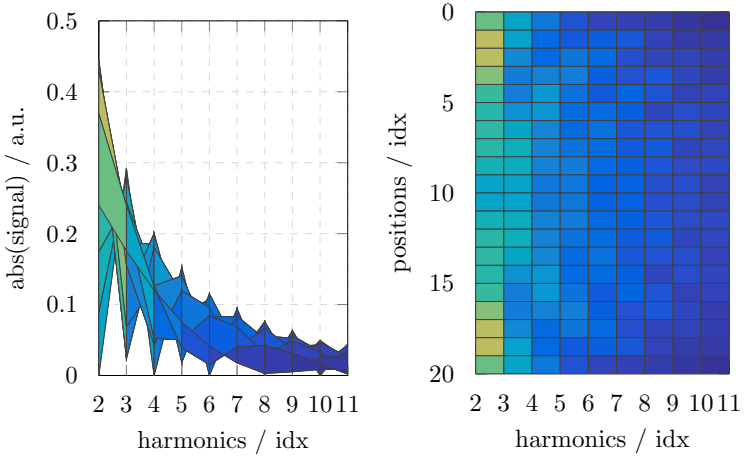

(a) side-view **(b)** top-view

Figure 4.31: Synthetic 1D system matrix (magnitude): side-view reveals decay in magnitude towards higher harmonics, the top-view shows the symmetry around the FOV center (position index 10).

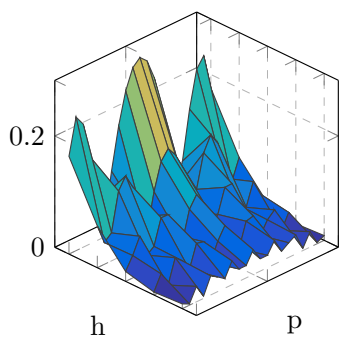

(a) Odd: Magnitude

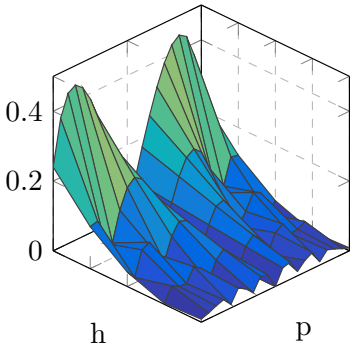

(b) Even: Magnitude

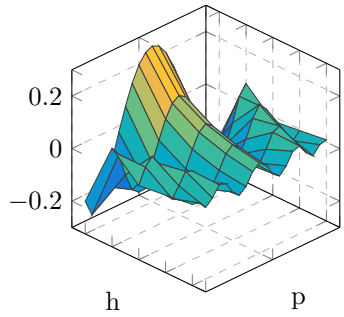

(c) Odd: Real

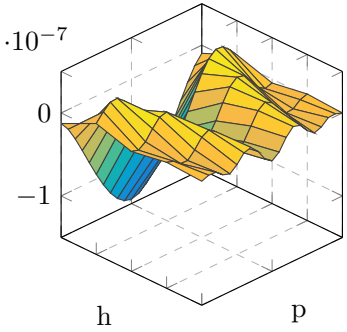

(d) Even: Real

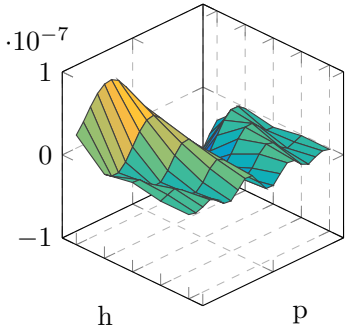

(e) Odd: Imaginary

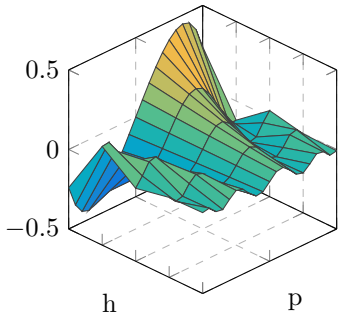

(f) Even: Imaginary

Figure 4.32: Complex-valued components of the synthetic 1D system matrix (for odd and even harmonics).

pattern emerging from the system matrix more clearly (→ Fig. 4.31b). Especially, it identifies a perfect symmetry of the left and right hemisphere of the FOV, i.e. positions 0 – 10 and 10 – 20, where position 10 marks the origin of the FOV. It is the symmetry which requires a complex-valued system matrix for reconstruction, because – obviously – the magnitude of the system matrix is ambiguous.

Symmetries in the 1D MPI system matrix are found in comparison of real versus imaginary components and in odd versus even frequency indices. All subfigures in Fig. 4.32 are divided into odd and even harmonics plots. The magnitude plots are similar to previous plots, only that the separation of odd (→ Fig. 4.32a) and even (→ Fig. 4.32b) harmonics clarifies that all odd harmonics and all even harmonics each have a similar spatial dependency, i.e. the signal maxima/minima form continuous ridges instead of being interrupted by elements from the other sort (as in Fig. 4.30). Figures 4.32c and 4.32d visualize the real parts of the complex-valued system matrix, and figures 4.32e and 4.32f show the imaginary parts. These plots show the left-right, hemispherical symmetry more obviously. It is apparent that the real part reveals an axis-symmetry between left and right, whereas the imaginary part carries a point-symmetry towards the origin of the FOV. Also, in an ideal system matrix only one type of harmonics (odd or even) contributes significantly to the real and imaginary parts, respectively. The even/real (→ Fig. 4.32d) and odd/imaginary (→ Fig. 4.32e) contributions are negligible (note the 10^{-7} scale on the plots). As a result, all harmonics are required for reconstruction in MPI, especially the odd/real and even/imaginary components contribute to the system matrix. This idealistic picture does not apply for any real-world systems, where the distribution of system matrix components is altered due to the transfer functions of the transmit and receive system components (especially their phases) and MNP magnetization dynamics. As a note, the symmetry of the system matrix to the origin of the FOV can be used during calibration to pinpoint the physical origin of the system.

The above figures have illustrated the system matrix components. The surface plots are suited for 1-dimensional MPI, because they capture all relevant dependencies into a single plot. More generally, there are two possible representations to express the spatial dependence of frequency components. Typically, a view containing all frequency components for a single point in the FOV is shown (cp. Fig. 4.6). For F-space reconstruction, i.e. based on the system matrix of complex-valued frequency components, this gives the spectral 'fingerprint' for each point in space. An alternative view shows the spatial contribution for a single frequency component, i.e. a single frequency encodes details from multiple points in the FOV. The spatial system matrix components in 1D translate directly into contributions of a single harmonic frequency to indiviual points in space.

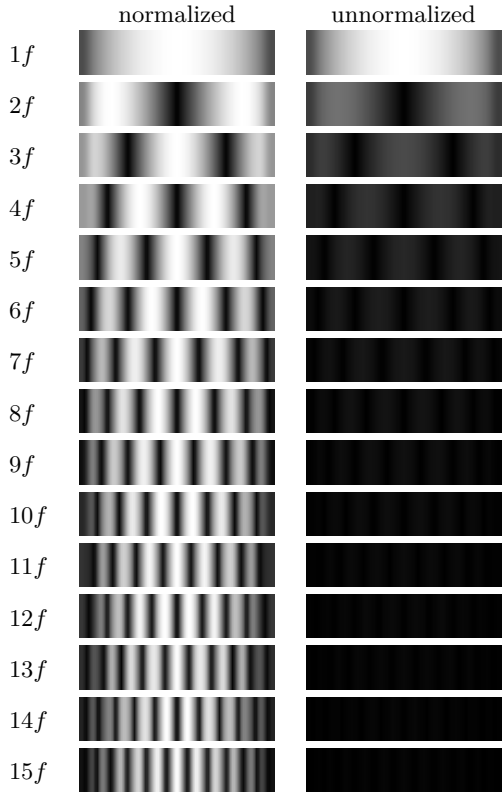

Figure 4.33: Spatial frequencies from the synthetic 1D system matrix. The 'normalized' column scales each frequency component individually, while the 'unnormalized' column visualizes signal decrease in higher harmonics.

Figure 4.33 shows the spatial contributions of individual harmonics to the MPI signal. The fundamental frequency $1f$ is usually not observed in an MPI experiment (due to filtering of the direct feed-through, see Sec. 4.2.4) but it is included here to show the theoretical contribution. The $1f$ component gives a coarse (but direct) localization of the object/particles. The second harmonic $2f$ shows two intensity maxima symmetrically to both sides of the FOV center. Similar to the fundamental, the third harmonic $3f$ is again centered, but it has two additional maxima to both sides of the origin (in addition to one broad central maximum for $1f$). The component $4f$ looks comparable to the $2f$ component, but with two additional maxima at the edges of the FOV. In general, the odd/even symmetry described above is observed here as well, but it is also quite evident that there is a 'spatial frequency' associated with each harmonic

frequency. The lower harmonics allow for an approximate reconstruction of the object's location and the higher harmonics contribute the finer structure of the MPI image.
While the left side of Fig. 4.33 shows the spatial system matrix components individually scaled to optimal contrast, the right column of Fig. 4.33 depicts the spatial components as they appear from the raw (Fourier-transformed) detection signal. Although higher harmonics contribute high spatial frequencies to the reconstruction, the signal decay towards higher harmonics (→ Fig. 4.31a) results in a weaker contribution as the system matrix components are naturally scaled with the signal magnitude. As a result, re-scaling the system matrix components is critical for successful MPI reconstruction. But care must be taken not to over-amplify higher harmonics as they tend to have lower signal-to-noise ratio (SNR).

1D Reference System Matrix

Continuing the discussion on the synthetic 1-dimensional system matrix above, here a 1-dimensional system matrix measured in a calibration scan (→ Sec. 4.2.1) on the actual MPI system hardware is shown. The system matrix was acquired on a FeraSpin™ R sample at original concentration (500 mM). The magnitude of the obtained system matrix is shown in Fig. 4.34. The harmonic decay of the reference particles in the measured system matrix is shown in Fig. 4.35.

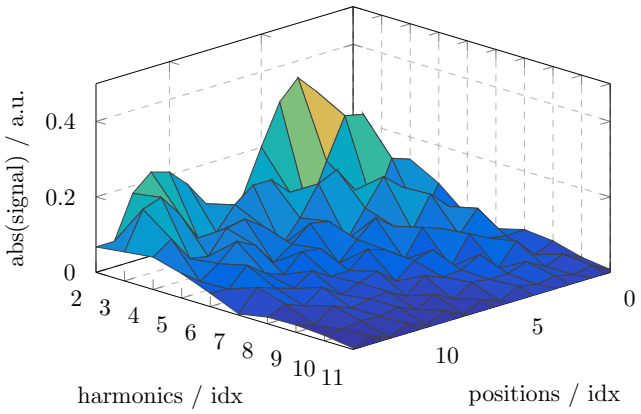

Figure 4.34: Calibration-based 1D system matrix (magnitude) in orthographic projection view.

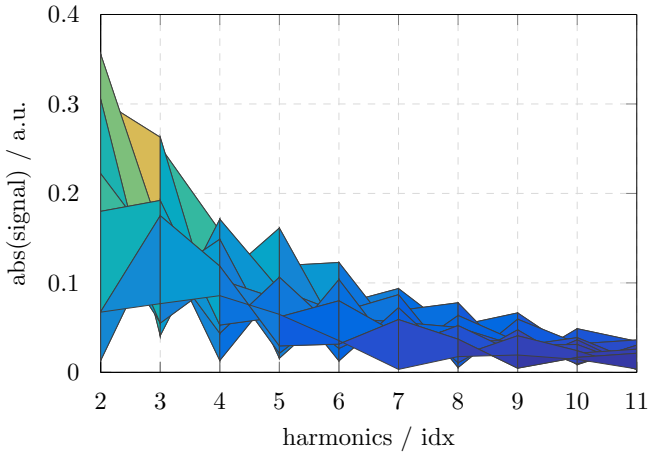

Figure 4.35: Calibration-based 1D system matrix (magnitude, side-view).

In style of the previous section, the odd/even and real/imaginary plots are also shown (→ Fig. 4.36). The same fundamental symmetries are observed as in the simulated system matrix. Only the signal-to-noise ratio SNR is worse (compared to near-infinite SNR for the simulation, only limited by dynamic range / numerical precision) which makes the system matrix features in the plots to appear disturbed. In Fig. 4.36a and Fig. 4.36b, an over-expressed signal magnitude in the right half (higher spatial indices) of the plots is visible.

Figure 4.37 shows the spatial system matrix components for the measured system matrix. In agreement with Fig. 4.33, spatial frequencies are observed to increase towards higher harmonics. The overall structure of the components looks as expected, including a small overscan (region covered by calibration robot is larger than the FOV from the drive field), only a small misalignment between the bands for individual frequencies is evident. Such irregularities (as seen from Fig. 4.36 as well) in the system matrix of a physical MPI system are the reason, why reconstruction based on a measured system matrix is still superior to model-based reconstructions.

A comparison of the artificial, simulated system matrix (→ Sec. 4.4.1) and the measured one (→ Sec. 4.4.1) makes it clear, that there are pros and cons for both approaches. The synthetic system matrix has optimal SNR, but lacks features most of system properties (i.e. transfer functions) and the correct modelling of the tracer properties remains challenging as well. The calibration-based approach on the other hand, represents the physical system and the actual tracer, but obtaining a high SNR for the

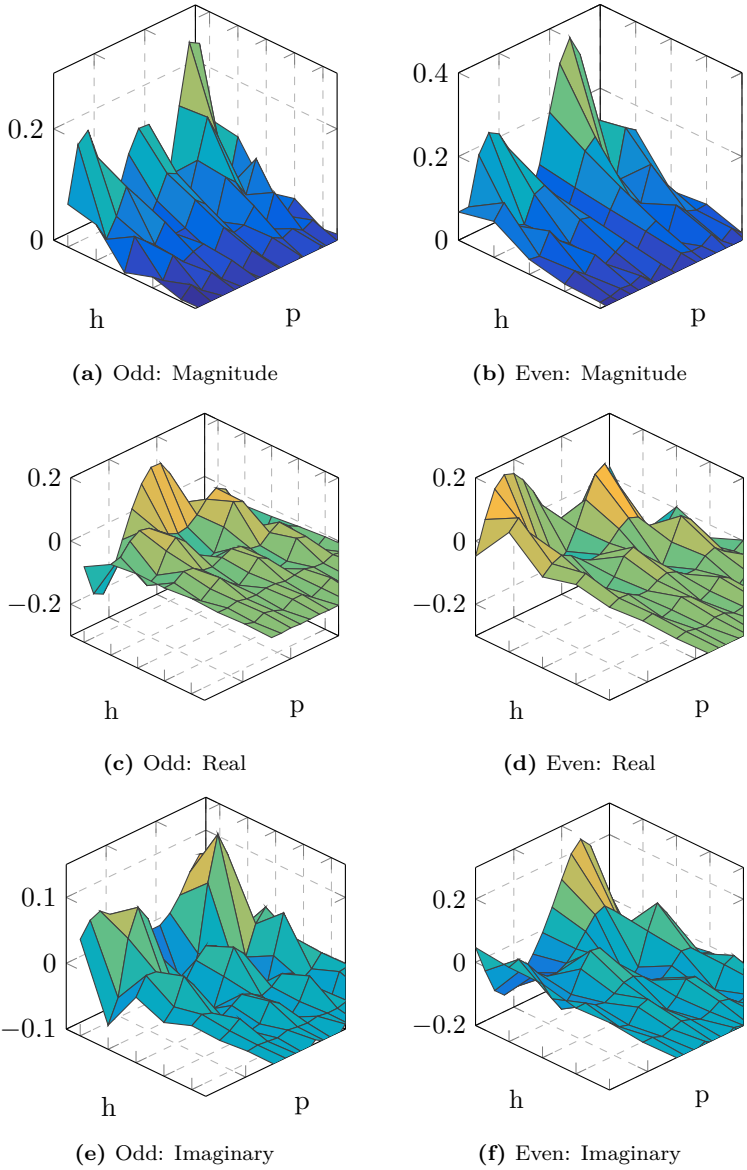

(a) Odd: Magnitude

(b) Even: Magnitude

(c) Odd: Real

(d) Even: Real

(e) Odd: Imaginary

(f) Even: Imaginary

Figure 4.36: Complex-valued components of the calibration-based 1D system matrix (for odd and even harmonics).

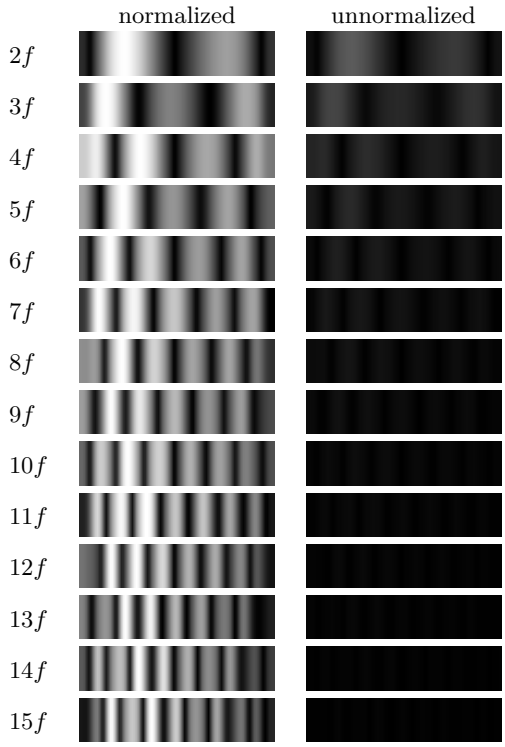

Figure 4.37: Spatial frequencies from the calibration-based 1D system matrix. The 'normalized' column scales each frequency component individually, while the 'unnormalized' column visualizes signal decrease in higher harmonics.

system matrix is time-consuming or not practical due to constraints of the hardware (i.e. maximum time in continuous operation). Hybrid system matrix approaches (→ Sec. 4.4.1) or compressed-sensing techniques [199, 200] can help here.

1D Hybrid System Matrix

A system matrix for MPI can practically be acquired in two ways. First, using the MPI scanner on a reference sample by utilizing a calibration robot (or dc field coils to circumvent the mechanical movement) scanning the sample through the FOV. The advantage here is – of course – that the system matrix can be used as is for reconstruction, because it implicitly contains all details of the system and the sample properties. However, the SNR of the matrix is limited by SNR of the scanner. It can be improved by averaging multiple spectra obtained from a single point, but the

acquisition time for a full system matrix increases proportionally to the number of averages. Typically, reference spectra are obtained for every single point in the field of view. By exploiting symmetries of the system matrix, as revealed before, the total number of required reference scans can be reduced significantly [199]. Another option to improve the system matrix involves MPS measurements. MPS has the advantage of a much larger filling factor (at least 1000-fold) compared to the MPI scanner. A 1-dimensional MPI system matrix can be assembled from MPS measurements on the particle sample with static offset fields to emulate different positions in the FOV, which are otherwise defined by a distinct dc field level from the selection field (gradient field) [198]. The disadvantage of this approach is found in the differences between then system design of MPS and MPI. The frequency response has to be adjusted to match the MPI system and even then the field geometry between MPS and MPI is quite different, i.e. in MPS the dc field is always parallel/perpendicular to the drive field, whereas in MPI the selection field has vectorial character and the principal dc field direction depends on the actual position in the FOV.

One other approach to the question on wether to use a calibration-based or a model-based approach for MPI reconstruction is the hybrid system matrix. Depending on the implementation, a hybrid system matrix blends the simulated (model-based) and the acquired (calibration-based) ones into a combined matrix. For our purposes, a hybrid system matrix is not assembled from actual measurements (MPI calibration or MPS with static field emulation), it is a modelled system matrix which is adjusted to a reference matrix in least-squares sense without inheriting the noise properties of the measured reference system matrix [201]. Good noise properties are essential for obtaining a good approximation of a pseudo-inverse of the system matrix as it is constructed by some reconstruction algorithms (Tikhonov, TSVD, etc.).

As a basis for the hybrid system matrix any dynamic particle model can be used (→ Sec. 2.4). For methodical simplicity and computational efficiency the simple Langevin model has been used. Therefore, the ideal system matrix depicted in Fig. 4.38a is equivalent to Sec. 4.4.1, as calculated for a tracer with 25 nm core diameter. The synthetic system matrix appears smooth, i.e. noise free, and because it is computed it can be easily interpolated or extrapolated for different FOVs or higher/lower resolution. If compared to a measured system matrix (→ Fig. 4.38b) there are some distinct differences and the ideal system matrix does not reproduce the encoding structure of the experimental system matrix correctly. The extent of the calculated FOV is not correct (apparently in the experiment we exceed the defined FOV marginally), which leads to a different width of the humps.
To account for all deviations (except noise contributions – of course) the model is fitted to the measured system matrix. There are different ways to achieve such a fit. For the purpose of producing a noise-free equivalent of the reference system matrix, it is not important to obtain physically meaningful model parameters. For that reason, the approach here does

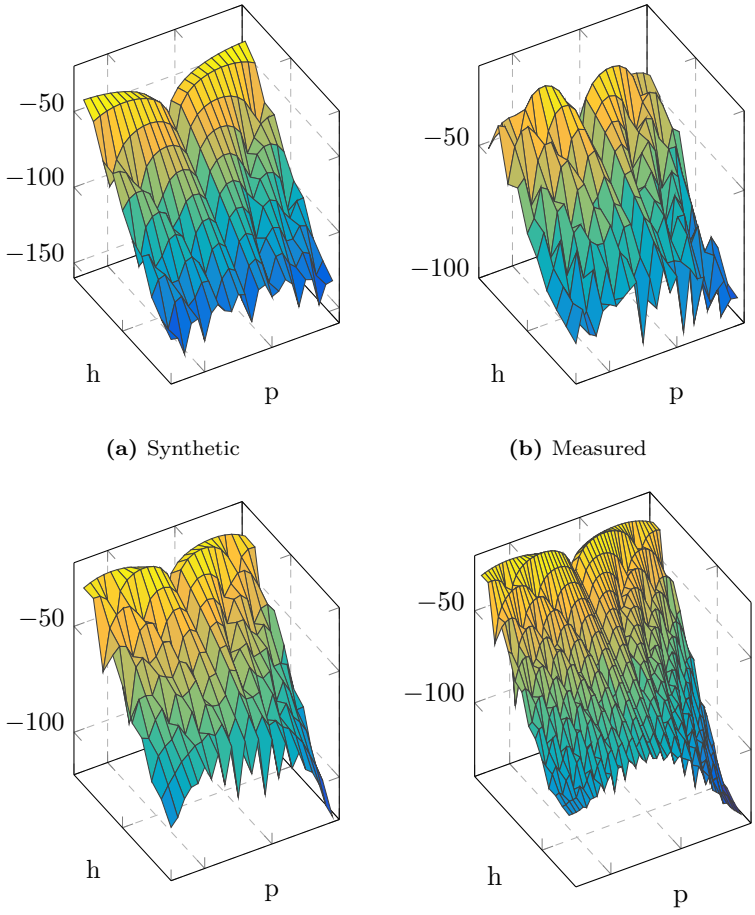

(a) Synthetic **(b)** Measured

(c) Hybrid **(d)** Hybrid (inter-/extra-polated)

Figure 4.38: Comparison of 1D system matrices: Synthetic (a) and calibration-based system matrix (b) on FeraSpin™ R show significant differences. Applying the fitting routine, a hybrid system matrix is obtained (c), which can easily be inter-/extrapolated to different grid sizes (d).

not consider the actual particle and system properties, it merely adjusts the geometry of the artificial system matrix to match the reference.
The system matrix can be analyzed along two main directions, where both axes can be considered independent of each other in terms of the observed deviations:
Along the harmonics axis (for a fixed point in the FOV) all deviations between the simulated and the measured system matrix are attributed to either a different tracer response, i.e. the model does not provide an adequate approximation of the dynamic magnetization response of the tracer, or the MPI signal chain, i.e. transfer function or residual harmonics of system components.
The axis along the positions in the FOV (for a fixed harmonic index) is considered dominant for MPI encoding. All deviations in that axis are attributed to field geometries and imperfections of the selection field, the drive field and the sensitivity distribution of the receiving induction coils. It is this axis which is altered in the fitting process. The least-squares fitting adjust the zero-crossings and the maxima/minima of the system matrix components.
First, the selection field geometry is estimated from the measured system matrix by detecting zero-crossings and maxima/minima. Second, a least-squares approach for fitting magnitude values of the supporting points is applied, which covers inter-harmonic ratios (slope), tilting and skewing of the supporting points in the FOV. Another implementation uses radial basis functions (RBFs) in the supporting points as an interpolation scheme, which allows for a 2-dimensional adjustment of the system matrix components. In contrast to a least-squares approach on the matrix columns, the RBF version does not support spatially under-sampled data, because it requires that all supporting points (zero-crossing and minima/maxima) are present in the measured system matrix for reference. Other system matrix disturbances, e.g. interference on individual frequency components (from lab equipment or radio stations), must be dealt with manually and thus not treated as part of the fitting process. Typically affected frequency components are blacklisted and removed before system matrix assembly (or before reconstruction).

The resulting hybrid system matrix is shown in Fig. 4.38c. It combines the smoothness (noiseless) of a synthetic system matrix with the geometrical properties obtained from the reference matrix. The specific features of the measured system matrix are well reproduced, e.g. the front-right corner shows a drop in signal magnitude in the experiment and in the hybrid matrix as well. As mentioned earlier, the obtained set of parameters representing the hybrid system matrix can be used to produce system matrices with different spatial mesh size and density (for higher or lower resolutions) as long as the geometry of the selection field and the MPI signal chain are not modified. With the least-squares approach it is even possible to create a full-span system matrix from a set of spatially under-sampled reference scans or calibration that does not span the entire FOV. An example of such an interpolated system matrix is given in Fig. 4.38d.

Figure 4.39 provides a visual proof of the effectiveness of the hybrid system matrix approach. The two images at the top (Fig. 4.39a and Fig. 4.39b) show the reconstruction obtained from measured system matrices. The system matrix obtained without averaging in Fig. 4.39a leads to poor results because of a low SNR. By 10-fold averaging during calibration the reconstruction quality improves at the cost of a 10-times longer reference acquisition time. Reconstruction using the hybrid system matrix gives a superior result, mostly because of the drastically improved SNR, which is a limiting factor in the MPI reconstruction (→ Fig. 4.39c). Building a hybrid matrix from an averaged reference dataset only marginally improves the results (→ Fig. 4.39d). Reconstruction based on a purely synthetic system matrix (without adjustments to the actual system and tracer) is not shown here, but it does not result in a recognizable image.

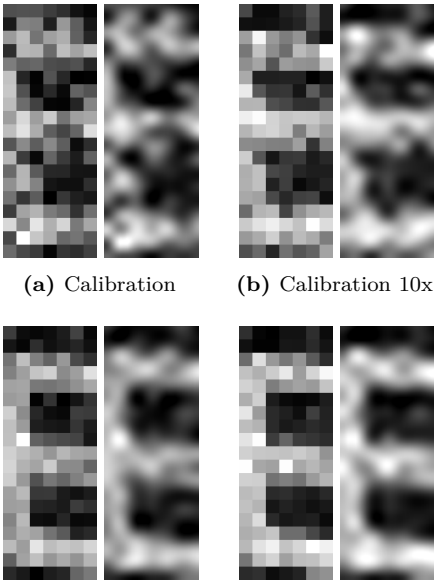

(a) Calibration **(b)** Calibration 10x

(c) Hybrid **(d)** Hybrid 10x

Figure 4.39: Reconstruction of the 'E' phantom with a calibration-based (a),(b) versus the hybrid (c),(d) system matrix. To demonstrate the effect of averaging (increase in SNR) 10-fold average system matrices are used for reconstruction in (b),(d). Upsampled image with bicubic interpolation to the right of each native image.

A high signal-to-noise ratio SNR is essential for the F-space reconstruction (matrix inversion is sensible to noise). The SNR can be improved by constructional measures, i.e. low-noise filters and electronic design, or via operational parameters, such as averaging. For a 10-fold averaging

as shown in Figs. 4.39b and 4.39d the frame time increases linearly from 20 ms for the non-averaged case to 200 ms. For later experiments (→ Sec. 4.5.1), 10-fold averaging is used as a standard operating parameter. Overall, the hybrid system matrix approach seems promising for reducing calibration time and at the same time for improving image quality in reconstruction (due to SNR improvements). Unfortunately, the method currently does not work (unmodified) for 2D/3D MPI system matrices which is a major disadvantage and multi-dimensional approaches remain an area of research for the future.

4.4.2 2D/3D System Matrix

In this section, a short discussion of system matrices for 2-/3-dimensional MPI experiments is given. The minimum size of a system matrix can generally be described as a function of the FOV size. For a quadradic (in 2D) field of view with n pixels per spatial dimension, the minimum size is $N_{2D} = n^2 \times n^2 = n^4$, for a cubic FOV (in 3D) the number of system matrix entries is $N_{3D} = n^3 \times n^3 = n^6$. A 3D system matrix for a 10^3 pixels cube contains at least 10^6 (1 million) entries, for a 30^3 pixels cubic FOV already 729 million entries. For that reason, numerical treatment and reconstruction for large 2D/3D MPI is challenging. The large matrix size typically eliminates all options for a SVD-based reconstruction (e.g. Tikhonov) and only iterative algorithms (e.g. Kaczmarz) are usable.

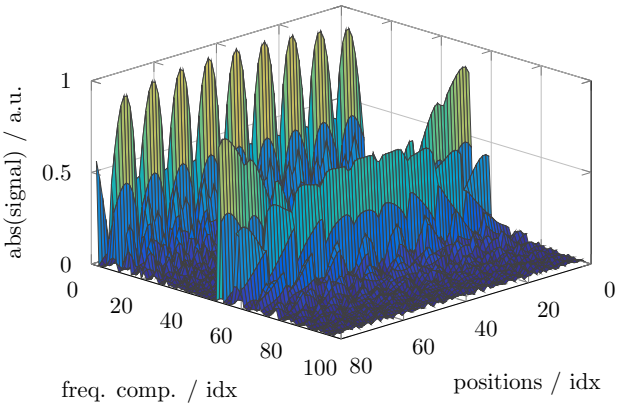

Figure 4.40: Synthetic 2D system matrix (channel x at indices 0-50 and channel y ranging indices 51-100)

The majority of additional frequency components in a 2D/3D system matrix (compared to 1D) contain mixing frequencies of the 2/3 MPI drive field frequencies, e.g. $(2f_x + 3f_y)$ (→ Fig. 4.40).

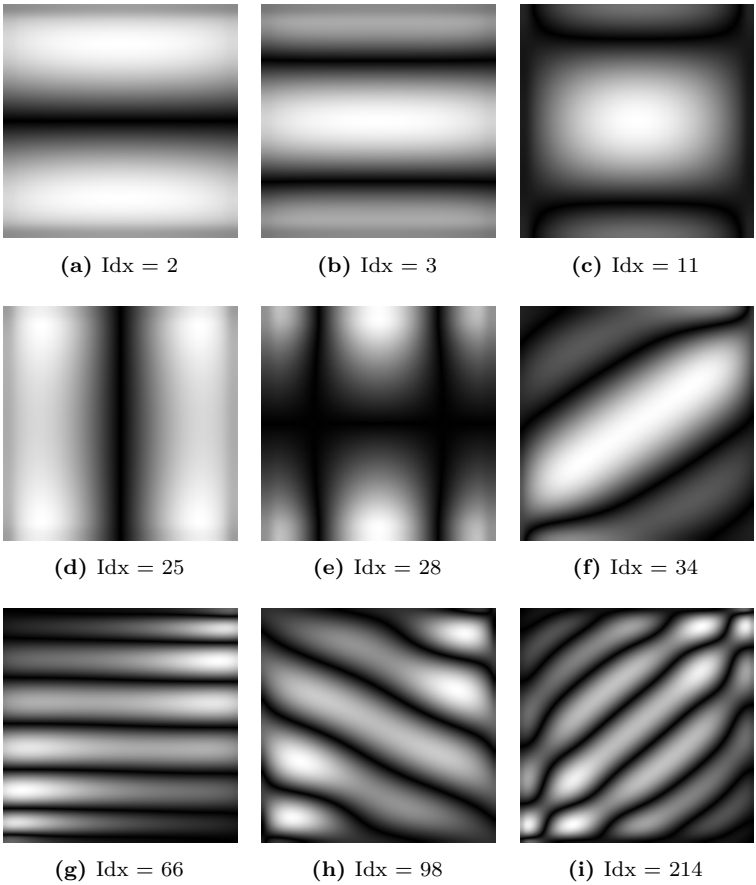

(a) Idx = 2 **(b)** Idx = 3 **(c)** Idx = 11

(d) Idx = 25 **(e)** Idx = 28 **(f)** Idx = 34

(g) Idx = 66 **(h)** Idx = 98 **(i)** Idx = 214

Figure 4.41: Spatial frequencies from a synthetic 2D system matrix, frequency components are sorted descending by energy (or mixing order) and random indices were selected. The low index components (with high energy) reveal coarse spatial frequencies. High index components (with lower energy) are contributing high spatial frequencies (compare to 1D above).

Similar to weighting of integer harmonics in the 1D case, also the mixing components are associated with a weighting factor $1/n$ that – in general – is approximately proportional to the mixing order $n(f)$ of the component. For a frequency f that is made up of linear combination of the drive field frequencies $(f_\mathrm{x}, f_\mathrm{y}, f_\mathrm{z})$ (4.15a), the mixing order $n(f)$ is the sum of coefficient (a, b, c):

$$f = af_\mathrm{x} + bf_\mathrm{y} + cf_\mathrm{z} \tag{4.15a}$$

$$n(f) = |a| + |b| + |c| \tag{4.15b}$$

As an example, a frequency $f_\mathrm{test} = 2f_\mathrm{x} + 3f_\mathrm{y}$ has a mixing oder of $n(f_\mathrm{test}) = 5$.

Figure 4.41 shows the spatial components for selected frequency components, analog to Fig. 4.33 and Fig. 4.37. For a 2D system matrix, a single frequency component is visualized as a 2D image.

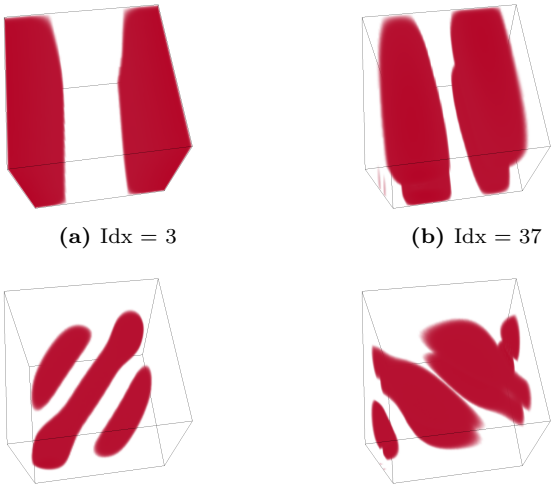

(a) Idx = 3 **(b)** Idx = 37

(c) Idx = 86 **(d)** Idx = 153

Figure 4.42: Spatial frequencies from a synthetic 3D system matrix, frequency components are sorted descending by energy (or mixing order) and random indices were selected. The low index components (with high energy) reveal coarse spatial frequencies. High index components (with lower energy) are contributing high spatial frequencies (compare 1D and 2D above).

Integer harmonics of the drive field frequencies manifest in shapes of horizontal or vertical bands (akin to the frequency component equivalent in a 1D system matrix). Mixing components, e.g. $(2f_x + 3f_y)$ are observed as a superposition of the contributing 1D system matrix components. A $2f_x$ spatial component, with a minimum at the center and two maxima towards the edges, and a $3f_y$ spatial component, with a maximum in the center and two additional maxima towards the edges, are effectively merged into a new 2-dimensional spatial component inheriting the spatial features from their 1D contributors. As in the 1D case, the spatial patterns in the 2D system matrix represent the spatial encoding in 2D MPI [197].
High frequency components relating to high spatial frequencies are observed to show similarities with the trajectory responsible for their generation. That way, the high spatial components give direct evidence of the trajectory used during the experiment and it also allows to validate the trajectory's geometry, i.e. correct frequency ratio for drive fields and no 'holes' in the trajectory's spatial pattern.

Similarly, spatial system matrix components of a 3D experiment can be visualized as a 3D volume as depicted in Fig. 4.42 [10].

4.5 Applications

In the upcoming application section, the MPI system introduced in Sec. 4.2 is put to use. The system was designed to be 3D-capable, but only two axes were actually used. Most of the following MPI image data was even acquired in 1D mode, i.e. with only one fast-scanning axis operating. By using a dc offset field (focus field) or by mechanically moving the object perpendicular to the fast-scanning axis, 2D and/or 3D images were acquired. All experiments, except for Legacy MPI (→ Sec. 4.5), were performed on Resovist® or FeraSpin™ R (which are mostly interchangeable). FeraSpin™ R is an iron oxide nanoparticle tracer, consisting of a multicore structure with primary core diameter (of the crystallites) around 5 – 7 nm (effective core diameter is larger due to moment interactions) and a hydrodynamic diameter in the range of 50 – 80 nm. Further details on the tracer are described in the MPS chapter (→ Sec. 3.3).

MPI images in this thesis are typically shown in two variants: a) in native resolution and b) resampled using bicubic interpolation. The native resolution corresponds to the image size as it is obtained directly from the reconstruction, i.e. the image points map directly to the spatial points in the reference scan during calibration. Because for an image with typically only 20 pixels it is difficult to reason about the image quality, the images are alternatively resampled using bicubic interpolation (bicubic interpolation means that a pixel is the weighted average of pixels in the nearest 4x4 neighborhood) to provide a smoother more appealing notion to the reader's eyes. All images (native and resampled) are shown without any image post-processing, i.e. no masking, no sharpening, no contrast enhancements, etc.

Legacy MPI

The 'Legacy MPI' section shows the first MPI scanner ('V1') that was built as a proof-of-principle system (→ Fig. 4.43) [202, 203].

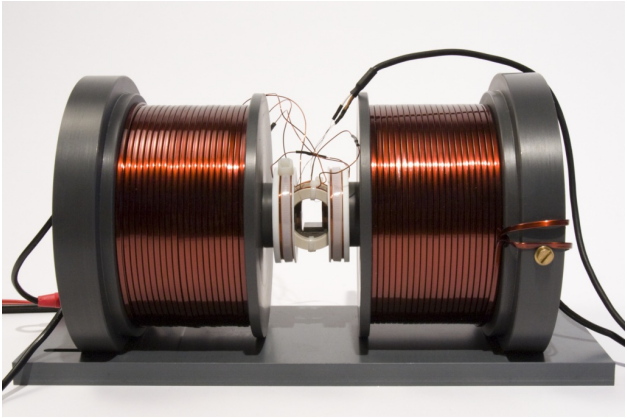

Figure 4.43: Photo of the first (legacy) MPI scanner capable of 1+1D imaging on Vitrovac.

Originally, the system used a combination of one fast-scanning axis and a dc focus field (step function to address individual lines) to provide a 2-dimensional field of view of 10 mm × 10 mm. For the images below (→ Fig. 4.44), an actual 2D Lissajous trajectory with $f_x = 2\,\text{kHz}$ and $f_y = 1.81\,\text{kHz}$ and a repetition time of $t_r = 5.5\,\text{ms}(f_r = 181\,\text{Hz})$ was used. The MPI signal was averaged over 250 repetition periods and 20 reconstructed images were averaged again, resulting in a total acquisition time of 26 s for the final image. Vitrovac 6025Z was used as a tracer material. Vitrovac is an amorphous cobalt-based metal alloy with soft magnetic properties characterized by a low coercitivity field strength and high permeability. Detection of magnetic nanoparticles was not possible due to limited spectral purity of the transmit signal (with minimalistic passive filters, LC series resonant circuit only). The filling factor of the receive coils was somewhat larger than in the later MPI scanner ('V2'), which enabled the detection of up to 10 harmonics, using a differential amplifier with prefixed phase-shift/allpass circuit based on the LT1028 (instead of a passive band-stop filter).
Plastic (PVC) cubes with holes at different positions were used as an object for calibration and scanning. The holes (diameter 1 mm) were equipped with a small piece of Vitrovac (→ Fig. 4.44d). With a maximum of 10 harmonics (+ mixing components) detectable above the noise floor, MPI reconstruction succeeded on a 6x6 grid (→ Fig. 4.44) using a Tikhonov regularization scheme. The performance of the system was poor compared to today's standards, but it showed that MPI imaging was indeed possible.

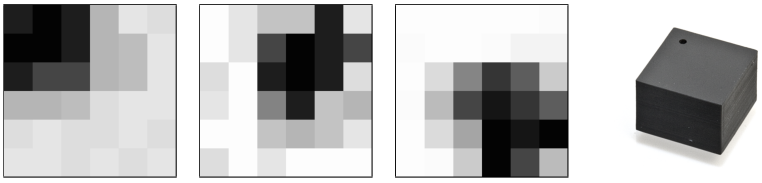

(a) Top-left **(b)** Top-right **(c)** Bottom-right **(d)** Photo

Figure 4.44: Reconstruction results (Tikhonov) from a delta sample on a 6x6 grid (a-c) and a photo of a sample cube (d).

The system included a full signal chain with all relevant transmit and receive components, a 2D coils assembly and it demonstrated a successful reconstruction approach.

4.5.1 Phantoms

The 'Phantoms' section shows results produced with the second generation MPI scanner in its original state ('V2') and with its improved version ('V2b'), where the transmit filters and receive amplifiers have been replaced. The V2 scanner is the first scanner designed with three axes and a reasonable large bore of 30 mm diameter. A detailed description of the scanner hardware was given in Sec. 4.2.
The images are mostly reconstructed using the F-space (system matrix-based) approach, except where explicitely noted. The recorded time-domain signal is Fourier-transformed to obtain the frequency spectrum and 'dead' frequencies (interference from radio stations or lab equipment) are removed. No other pre-processing of the data is performed. For reconstruction typically the Kaczmarz algorithm family (Kaczmarz, randomized Kaczmarz, etc.) is used, except for the 1-dimensional case where SVD-based methods are applicable and can provide additional insights into the properties of the system matrix.

Double Dash (1D)

The most basic phantom is a plastic (PVC or acrylic) cube or plate which contains two stripes of magnetic nanoparticles with a distance of approximately 5 mm to each other, internally refered to as double dash ('DDash') phantom. The two stripes are engraved into two individual cuboids, so that one can mix-and-match between mobile (→ Fig. 4.45a) and immobilized (→ Fig. 4.45b) versions.
Performing a 1-dimensional MPI scan at a central line over the phantom reveals two maxima where the scan line intersects with the magnetic nanoparticle stripes (→ Fig. 4.46).

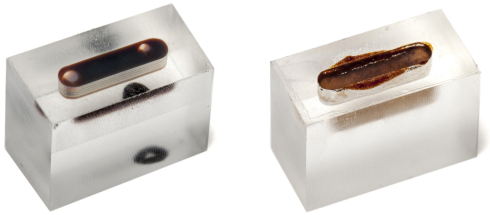

(a) mobile **(b)** immobilized

Figure 4.45: Photo of two (mobile and immobilized) dash phantoms. A side-by-side arrangement of both samples is referred to as a double dash 'DDash' phantom.

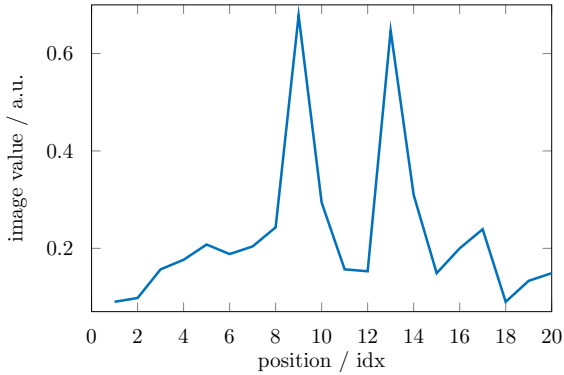

Figure 4.46: MPI image profile through the center line of the 'DDash' phantom.

Shifting Double Dash (1D)

The double dash phantom is also used to test the MPI system and to ensure that reconstruction is functional. For that, the phantom is moved along the 1-dimensional FOV and an MPI image is acquired for each position. The procedure is identical to the 1-dimensional calibration scan, only that the point-like reference sample is replaced by the slightly more complex double dash phantom. The advantage of imaging the phantom at all possible locations is that it allows to compare system response and reconstruction for the entire FOV. Also, by stitching the individual images side-by-side, a 2D image is created which makes a visual inspection easier (compared to a profile plot). The shifting double dash phantom

is frequently used to compare the MPI performance, both in terms of speed and image quality, of different reconstruction techniques including variations in their parameter sets.

The following three different reconstruction and regularization algorithms are used for MPI image reconstruction in this thesis [12, 204–208]:

a) Kaczmarz and randomized Kaczmarz (as default) [209–211]

b) Truncated SVD [212, 213]

c) Tikhonov [214, 215]

Figure 4.47 shows a comparison of the reconstruction results of the shifting 'DDash' phantom for the different algorithms. Whenever the raw signal SNR is not sufficient (Figs. 4.47 (a), (b) and (c)), reconstructed image quality is also poor for all algorithms.

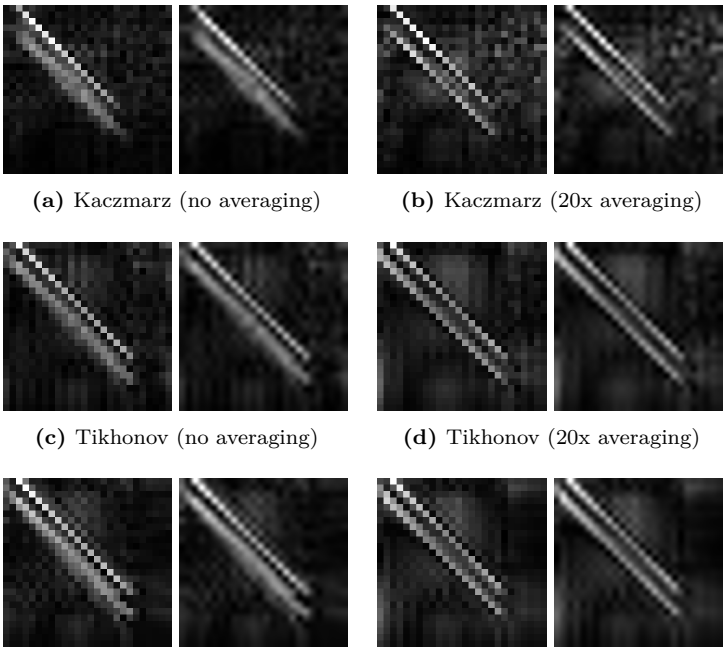

(a) Kaczmarz (no averaging) **(b)** Kaczmarz (20x averaging)

(c) Tikhonov (no averaging) **(d)** Tikhonov (20x averaging)

(e) TSVD (no averaging) **(f)** SVD (20x averaging)

Figure 4.47: Comparison of three different F-space reconstruction algorithms (Kaczmarz, Tikhonov, TSVD) on the 'DDash' phantom with and without 20-fold averaging.

With 20-fold averaging (in time or frequency domain) of the receive signal before reconstruction all algorithms are capable of recovering the two dashes of the 'DDash' phantom correctly. From visual inspection the Kaczmarz (→ Fig. 4.47b) and Tikhonov (→ Fig. 4.47d) options reveal comparable results. Kaczmarz is found to obtain slightly 'sharper' images, but with stronger artifacts. It should be noted, that the Kaczmarz family is the only algorithm that it used at scale for 2-/3-dimensional reconstruction, especially for large images (and system matrices).
Noise properties of the MPI system and noise propagation through reconstruction is very important as it defines the signal-to-noise ratio of the resulting image.

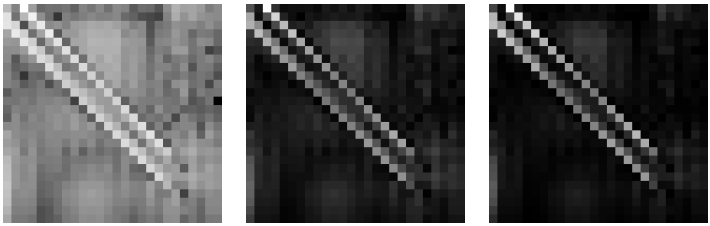

(a) noise contrast **(b)** original **(c)** with denoising

Figure 4.48: Noise properties in F-space reconstruction: noise boosted with $\gamma = 4$ (a) to reveal residual noise structure, an MPI image reconstructed with standard parameters (b) and MPI image with pre-FFT wavelet-thresholding (c).

Figure 4.48 visually approaches the problem of image noise. The original image as obtained from a Tikhonov regularized reconstruction is shown in Fig. 4.48b. In Fig. 4.48a the image's gamma encoding has been set to $\gamma = 4$ to amplify the noise. Ideally, the noise background should be uniformly gray and it should not show any structure that maps back to the acquisition system or the reconstruction itself. Here, the background is not perfectly uniform, but it does not reveal any characteristic patterns either, which would be a point of concern. An attempt to reduce noise prior to reconstruction by using wavelet thresholding on the time signal as a noise-reduction technique is depicted in Fig. 4.48c [216–218]. The wavelet technique takes advantage of the local/short-time structure of the signal to remove noise contributions independent of global/periodic Fourier components, which is especially effective for short-time variations within a repetition frame (in 2D and 3D imaging). In effect, the approach is comparable to a basis change in compressed sensing reconstruction [199].
Unfortunately, the signal-to-noise ratio of an image is impossible to determine if no noise-free reference is available (which is usually the case). An estimate of the signal-to-background ratio (SBR) can be obtained from a line profile (→ Fig. 4.49a). For the origianl (un-filtered) Tikhonov reconstruction an estimate of $SBR_{\text{original}} = 0.611/0.090 = 6.7$ and for

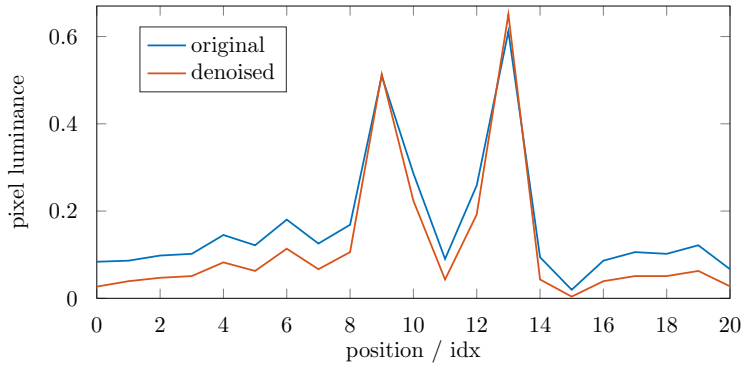

(a) MPI Line Profile (through the center of the 'DDash' phantom)

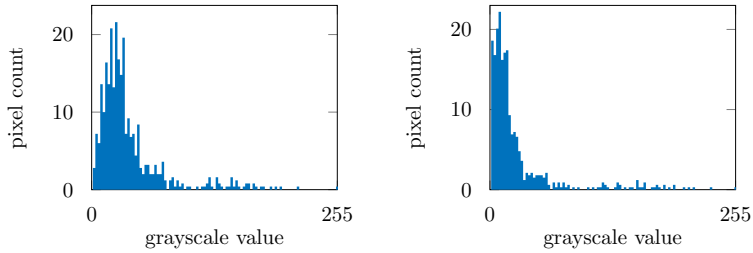

(b) Tikhonov **(c)** Denoised Tikhonov

Figure 4.49: Noise estimates for reconstructed images. Denoising shows an improvement in image contrast (a). The image background shifts to lower values in the histograms (from (b) to (c)).

the denoised image profile $SBR_{\text{denoise}} = 0.650/0.043 = 15.1$ are calculated. The SBR estimates confirm the visual impression, that the wavelet denoising has a positive effect on the image noise properties after reconstruction. Another option for a noise estimate is given by the histogram of the images (Figs. 4.49b and 4.49c). Ideally, the image should contain only white and black pixels. The dark/black pixels from the background represent the majority of pixels in the image, so that the histogramm should contain a large and narrow peak at low gray values (0 = black, 255 = white). Again, the histograms confirm the visual impression. The histogram of the denoised image (→ Fig. 4.49c) shows a more confined peak compared to the histogram of the original reconstruction (→ Fig. 4.49b).

Especially in cases with limited SNR the F-space reconstruction generates artifacts, which can generally be attributed to the system matrix

(pseudo-)inversion being sensitive to noise [219]. The x-space reconstruction approach promises resiliency in low SNR scenarios [170]. For that reason (and because of access to relaxation properties in context of Mobility MPI (→ Sec. 4.5.2)), the x-space reconstruction is also considered for certain applications in this thesis. X-space reconstruction has been implemented, but it's use is currently limited mainly to simulated MPI datasets. X-space reconstruction is very sensitive to phase instability of the receive chain and without compensation of the transfer function of the MPI hardware results from x-space are heavily distorted, i.e. especially the receive band-stop filters contribute a strong phase shift in the lower harmonics $(2f, 3f, ...)$.

E-Phantom (1D and 1.5D)

Following a 'tradition' in MPI where people image letters representing their affiliation, i.e. 'P'hilips in their original publication on MPI and Berkeley with the letters 'CAL' for California, the letter 'E' for EMG was used in our group to introduce the new scanner in 2011/2012. The scanner configuration used for the experiment accords with generation V2 (→ Sec. 4.2) specification.

(a) MPI Image **(b)** Inverted image **(c)** 'E' phantom

Figure 4.50: MPI images and photo of the 'E' gelatine phantom.

For the initial 'E' scan, the detection bandwidth was constricted to a range of 12 – 500 kHz and a frequency-proportional (high-pass) gain from $G_{10\,\mathrm{kHz}} = 250$ to $G_{500\,\mathrm{kHz}} = 1000$ was used. With that restriction both the drive field frequency of 10 kHz and the objectionable AM radio signal at 756 kHz (DLF, 'Deutschlandfunk') were skipped. The gradient was set to 4.5 T/m with a combination of permanent magnets and gradient coils (at a 10% duty cycle). The peak drive field amplitude was 20 mT (same duty cycle).
The data acquisition used an averaging of 150 periods accounting to 6 s for a 1-dimensional FOV with 20 pixels, i.e. with a single fast-scanning

axis. The 2D images were assembled with a perpendicular dc offset (from the z drive field coils) to acquire 5 individual lines, resulting in a total acquisition time of 30 s. Reconstruction was performed using Tikhonov regularization, with manual tuning of the regularization parameter γ according to best visual results.
The 'E' phantom was made of 8 holes in a gelatine matrix, filled with 4 – 5 µL of undiluted Resovist®. The 'E' had a dimension of 13 mm in height and 6 mm in width.

The MPI scanner was able to resolve the dots in vertical direction, but the dots in horizontal direction remained intersecting (→ Fig. 4.50). However, the overall features of the letter 'E' are well recognizable and the image can be considered a successful 'first light' (expression from astronomy) of the V2 scanner design. It should be noted, that the resolution in the scanner is non-isotropic, i.e. the resolution is different for both directions according to the gradient strength of the selection field in the different directions. The horizontal line was oriented parallel to the system's z-axis, i.e. the axis with the strongest gradient and consequently with the best theoretical resolution, but the dots were still not resolvable.

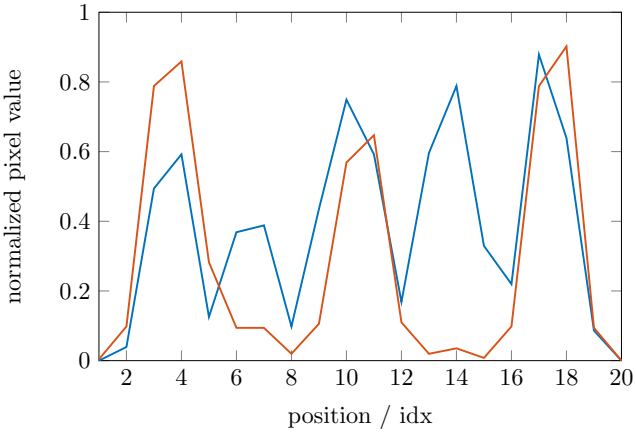

Figure 4.51: Selected line profiles from the MPI image of the 'E' phantom, through the three tips (orange) and the left bar (blue) of the letter 'E'.

Figure 4.51 shows two selected line profiles along the vertical direction of the letter 'E'. The blue line in Fig. 4.51 cuts the left bar of the 'E' and shows 5 distinct maxima matching the 5 individual holes in the gelatine the line is made of. The orange profile in Fig. 4.51 shows the profile

across the leads/tips of the 'E'. Here, 3 maxima corresponding to the baseline, the center line and the top line of the letter are apparent.
Another scan of the letter 'E' was conducted after the scanner was renewed from V2 to V2b, i.e. the transmit filters and the receive amplifiers were replaced. The scanner was again functional with one active (fast-scanning) axis and the vertical direction was scanned by mechanically moving the object through the field of view (with the calibration robot). Also the scan time was reduced to 20 averages of 200 ms 1-dimensional scans, resulting in a total acquisition time of 4 s.
The phantom was made of a PVC plate engraved with the letter 'E' and filled with undiluted Resovist®. Reconstruction was performed in F-space using the unmodified Kaczmarz algorithm.

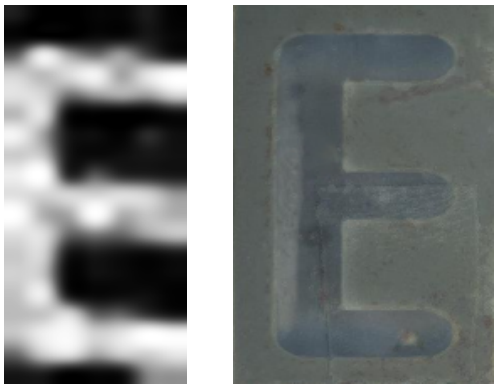

(a) **(b)**

Figure 4.52: MPI image and photo of a second (large) 'E' phantom.

The results are show in Fig. 4.52. The features of the letter are well defined in the obtained MPI image and a $SBR = 9.0$ is estimated from a profile. This is comparable with the SBR before modification of the scanner (→ Fig. 4.50a) but with an almost 10 times faster acquisition.

Helix (2D and 2.5D)

The MPI scanner built and operated in the context of this thesis is prepared for a 2+1D mode, with two fast-scanning axes and a dc focus field in the third axis. This operation mode is similar to sequential slice selection in MRI. The image was acquired with the scanner in configuration V2 (V2b has only one fast scanning axis). A Lissajous trajectory with a repetition time of $T_{\text{rep}} = 31.2\,\text{ms}$ (→ Tab. 4.1) was used and a 100-fold average (10×10) of the spatial trajectory was acquired, resulting in a total acquisition time for a single plane of 3.12 s (plus duty cycle).

Reconstruction was performed with the system matrix approach and Tikhonov regularization scheme – as before – but this time using the system matrix of a 2-dimensional MPI experiment with 14×7 pixels in the plane. In order to assemble a 3-dimensional FOV, 5 planes were acquired independently (with the focus field) and stacked to form a $14 \times 7 \times 5$ pixels volume.
The phantom used for 3D imaging was a helix made of a capillary tube (diameter 1 mm) spiraled around a paper barrel (diameter 10 mm). The capillary tube was filled with approximately 200 µL of undiluted Resovist®. The phantom is displayed in Fig. 4.53.

Figure 4.53: Photo of the helix phantom, capillary tube filled with MNPs and wound around kartonage.

The image quality of the reconstructed MPI images is sufficient to identify characteristic features of the helical phantom. Figure 4.54 shows three selected planes from the 5 planes stack. The central plane (#3) is shown in Fig. 4.54b. The four white spots at the top and again at the bottom of the plane are visible, which correspond to the four loops of the capillary tube intersecting the central plane. The central plane is a simple cross-section of the spiral. The upper-most (top) and lowest (bottom) planes show diagonal patterns \\ and // (mirror-reversed to each other) representative of the helical windings. All slices can be joint together to show the 3-dimensional structure of the helix.

(a) bottom **(b)** center **(c)** top

Figure 4.54: Reconstructed MPI slices of the helix phantom.

Finally, the stack of planes forming a 3-dimensional volume is visualized as an iso-surface rendering in Fig. 4.55. The threshold for the surface is set to 0.75 of the maximum pixel luminance.

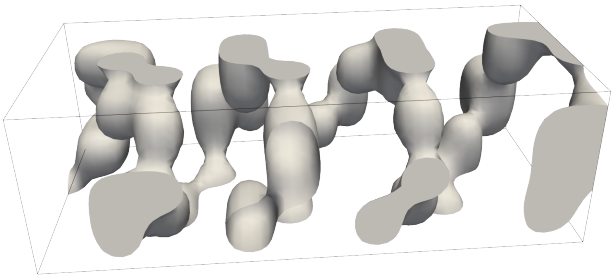

Figure 4.55: Iso-surface rendering of the helix phantom (threshold 75%).

The iso-surface representation was selected instead of the usual maximum intensity projection (MIP), because in a still image it provides a better depth perception. The rendering in Fig. 4.55 shows indeed a good approximation of a helix, although some small gaps in the spiral are evident.

4.5.2 Mobility MPI (mMPI)

MPI is recognized as a tracer-based imaging modality that delivers images with high spatial and temporal resolution. Early in the development of our own Magnetic Particle Imaging scanner and with a background on magnetization dynamics of magnetic nanoparticles, from other methods like magnetorelaxometry (MRX) or ac susceptometry (ACS), the idea of bringing a functional imaging aspect to MPI seemed promising. The dynamic magnetization behaviour of the nanoparticular tracer is governed by two different relaxation mechanisms, the Néel relaxation (→ Sec. 2.2.1) and the Brownian relaxation (→ Sec. 2.2.2). While the Néel mechanism is confined to properties and the structure of the magnetic core, the Brownian rotational motion is influenced by the particle's environment. Especially, the Brownian time constant is susceptible to changes in viscosity of the surrounding medium or to molecules attaching/detaching to their (functionalized) shell, i.e. the hydrodynamic diameter changes as a result of a chemical binding process. If it was possible to translate the environmental responsivity into MPI image contrast (in addition to the concentration/density-weighted image), MPI would be promoted to a functional imaging modality.

This chapter gives insights into the development of this approach and its current state. Because it is the goal to capture information about the particle's mobility, where mobility includes both the viscosity η and the hydrodynamic particle diameter V_h and is therefore equivalent to the Brownian time constant τ_B, the method is called 'mobility MPI' (or mMPI in analogy to fMRI, functional MRI). The Brownian time constant shows the following proportionality:

$$\tau_\mathrm{B} \propto \eta V_\mathrm{h} \tag{4.16}$$

From the Debye model (→ Sec. 2.4.3) it is known, that the magnetization (or susceptibility) of the particles can only be observed when the ac frequency of the excitation signal is in the same range ($\omega\tau = 1$) or below ($\omega\tau < 1$) the equivalent characteristic $1/\tau$ time constant of the particles. At higher frequencies the particle's response amplitude gradually drops to zero according to (2.32) and as visualized in Fig. 2.14.
The typical Brownian time constant for particles with a hydrodynamic diameter of 40 nm is 24 µs (= 41 kHz), 60 nm gives 82 µs (= 12 kHz) and for 80 nm we find 200 µs (= 5 kHz). The connection between hydrodynamic diameter and the time constant or characteristic frequency of the particles is plotted in Fig. 2.8. It should be noted, that the time constant additionally depends on the field amplitude of the ac drive fields and dc selection field. The field-dependence lowers the time constant for large field levels.

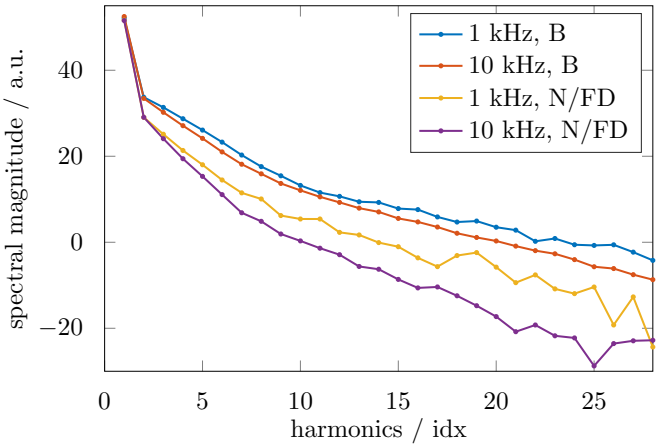

Figure 4.56: MPS spectrum of FeraSpin™ R in mobile (B) and immobilized (N/FD) state measured at 1 kHz and 10 kHz.

The MPI scanner presented in this thesis operates at drive field frequencies around 10 kHz, in a range where Brownian rotation of typical particles is

still evident. Sensitivity for particle mobility estimation strongly degenerates beyond a transition frequency ($\omega\tau = 1$), which for 10 kHz is located around 75 nm (without considering field-dependence). For Resovist®, which has a mean hydrodynamic diameter in the range of 60 – 80 nm, the 10 kHz system is sensitive to changes in viscosity or hydrodynamic diameter. An MPS dataset measured on FeraSpin™ R at 1 kHz and 10 kHz is given in Fig. 4.56. It shows a clear separation of different viscous samples, i.e. in water, glycerol and immobilized, at these frequencies.
The frequency range susceptible to deliver mobility information is defined as a function of $\omega\tau$. However, as mentioned before, there are two competing relaxation mechanisms (Néel and Brownian relaxation). It depends on the properties of the particle sample at hand, whether the Brownian mechanism is (at least partially) dominant as required for mMPI. Based on that criterion the following condition list can be arranged:

- $\tau_N < \tau_B$: mobility not detectable (Brownian relaxation recessive)
- $\tau_N > \tau_B$: mobility state detectable
  - $1/\omega \geq \tau_B$: mobility MPI regime
  - $1/\omega \leq \tau_B$: standard MPI regime (modulation required)

As mentioned above, the mMPI approach strives to find options for accessing the Brownian time constant of the particles in the FOV. Four different approaches for the practical realization of mobility MPI (mMPI) have been pursued so far:

Multi-Frequency mMPI (→ Sec. 4.5.2)

The idea for multi-frequency mMPI is based on the observations in ac susceptometry. For low frequencies ($\omega\tau \leq 1$) a strong difference between a mobile (Brownian) and immobilized (Néel) is observed, but for high frequencies ($\omega\tau \gg 1$) the suceptibilities of the two samples match up. In the simplest realization, an MPI scanner with two frequencies is built and the mobility information is extracted from the delta/difference in image contrast.

F-space mMPI (→ Sec. 4.5.2)

In order to realize mMPI in the Fourier domain, the effect of mobility, i.e. viscosity changes or binding, on the system matrix is studied. As it turns out, the system matrix of a mobile sample is an approximate composite of two system matrices, one for the contributions of the mobile (Brownian) and one for the immobile (Néel) particles.

x-space mMPI (→ Sec. 4.5.2)

In x-space it is observed that – for particles with limited magnetization dynamics – the x-space kernel becomes asymmetric, which can be modeled via an additional exponential relaxation term. The direct spatial mapping in x-space allows one to explore the temporal structure of the receive signal.

Direct mMPI (→ Sec. 4.5.3)

> The direct approach does not explicitely require reconstruction in order to obtain mobility information. This approach is based on the magnetization vector being observed in x-space detecting the misalignment (or better delayed alignment) in reference to the exciting magnetic field vector. The vector difference is a direct indicator for the particle mobility.

The goal in mMPI is to reconstruct two (independent) images for a) the concentration and b) the mobility of the tracer. The different approaches to mMPI are discussed in more details in the subsequent sections.

Multi-Frequency Approach

The multi-frequency approach is based on the fact, that the MPI image contrast changes as a function of the parameter $\omega\tau$ [220, 221]. Assuming that the Brownian relaxation is faster than the Néel mechanism, i.e. Brownian dominance, a simulation is conducted based on the effective field model (→ Sec. 2.4.2) [222]. The core diameter is fixed to $d_c = 25\,\text{nm}$ and only the Brownian time constant is considered.

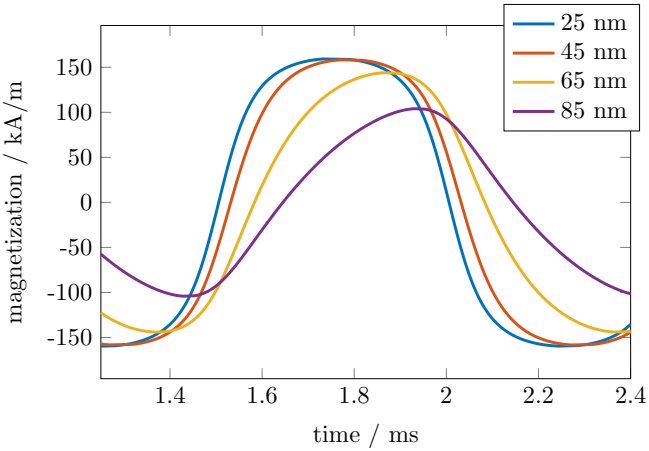

Figure 4.57: Time-domain signal of an effective-field simulation on particles with $d_c = 25\,\text{nm}$ and different hydrodynamic diameters in the range of $25 - 85\,\text{nm}$. For larger diameters, the increasing Brownian time constant causes a delay and decrease in peak magnitude of the magnetization response.

For small particles (below 30 nm hydrodynamic diameter), the fast relaxation time constant allows for an almost instantaneous magnetization of the particles (→ Fig. 4.57). With increasing hydrodynamic diameter

the relaxation starts to take effect on the time-domain signal and the originally symmetric curve becomes asymmetrically distorted due to limited magnetization response of the particles. The break in time-domain symmetry also maps to an altered spectral response.
In agreement with the linear Debye model (→ Sec. 2.4.3), the magnitude of the magnetization decreases towards higher frequencies for a fixed particle size (→ Fig. 2.14). As a different visualization, the magnetization magnitude can be plotted over the hydrodynamic diameter, which gives the same result due to a commutative $\omega\tau$ relationships (→ Fig. 4.58).

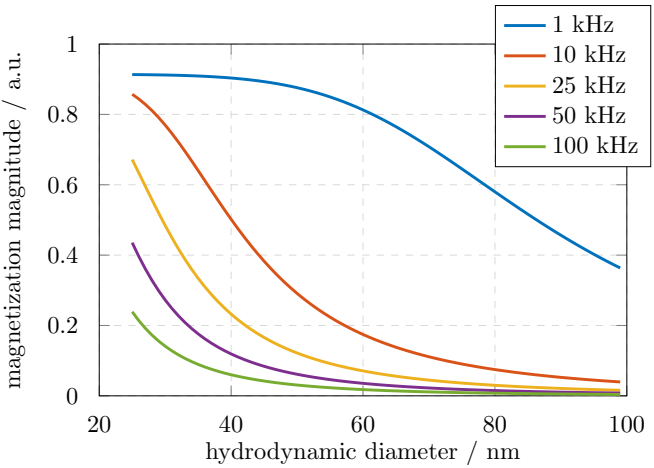

Figure 4.58: Magnetization magnitude as a function of the hydrodynamic diameter simulated with the effective-field model (particles with $d_c = 25\,\text{nm}$) for different excitation frequencies in the range of 1 – 100 kHz.

Figure 4.58 also includes the frequency dimension as a series of curves in the range of 1 kHz to 100 kHz. For 1 kHz, there is a strong change in magnitude with increasing hydrodynamic diameter. For higher frequencies, the change is only observable for smaller diameters and it is much less pronounced for frequencies above 10 kHz.
Similarly to the magnitude, an analog behavior can also be observed for the phase of the magnetization (→ Fig. 4.59). Small particles show an almost instant response to the applied field, resulting in a small phase angle. For larger particles, the angle tends towards 90°, equivalent to only a minimal displacement of the magnetization vector from the excitation field. Again, the strongest dependence on the hydrodynamic diameter is observed for low excitation frequencies.
The two plots (Figs. 4.58 and 4.59) give the motivation on how to realize mMPI. Using multiple frequencies to acquire MPI data should lead to images with different contrast. A MPI image acquired with a high drive field frequency (e.g. 50 kHz or 100 kHz), should mostly be unsusceptible

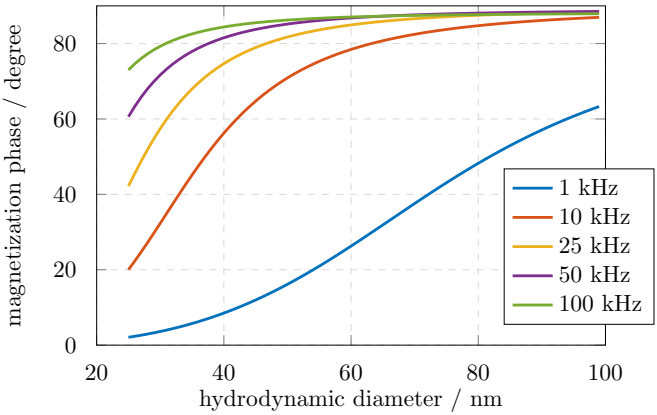

Figure 4.59: Magnetization phase as a function of the hydrodynamic diameter simulated with the effective-field model (particles with d_c = 25 nm) for different excitation frequencies in the range of 1 – 100 kHz.

to contributions from Brownian rotational motion. In contrast, an MPI image obtained at a lower drive field frequency (e.g. 1 kHz or 10 kHz) should result in a strong Brownian contribution. The basic idea here is to take multiple images at different frequencies. The difference in contrast between those images can then be attributed to the Brownian rotational motion.

Ideally, the system would be capable of getting images at many different frequencies, similar to an ac susceptometry measurement. The system would be adjustable to different particle sizes and would allow adjustable weighting for the Brownian contribution. However, because MPI requires a linear, spectrally pure drive field signal, band-pass filters are employed and tailored to the drive field frequency. For that reason, mMPI can also be realized based on only two distinct frequencies instead of many, so that only two transmit and two receive filters are required. The frequencies must be chosen to match the particle's Brownian time constant. The best choice requires $1/\omega_1 \geq \tau_B \geq 1/\omega_2$, but some variation is still possible.

To demonstrate the idea of 2-frequency mMPI, a simulation is performed for a 5×5 pixels phantom containing four spots with particles (→ Fig. 4.60). As before, the core diameter is fixed to 25 nm and Brownian rotation dominates. The upper row contains particles with a hydrodynamic diameter of 40 nm, the lower row is filled with 90 nm particles. The left and right column differs in concentration only, i.e. concentration in the right column is twice as much as in the left column.

The simulation results are depicted in Fig. 4.61. The naive reader expects that the right columns (with double concentration) are always twice as bright as the left columns. However, that is only the case at 100 kHz. At a high frequency there is no Brownian contribution, i.e. there is also

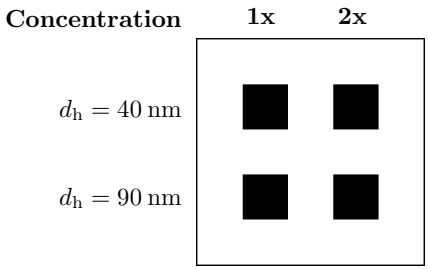

Figure 4.60: Illustration of a test object used for simulation of the multi-frequency mMPI approach.

no contrast between different hydrodynamic diameters (→ Fig. 4.61c), and the grayscales map directly to the concentration. The phases are close to 90° because the Brownian time constant is much too slow in reference to the drive field (→ Fig. 4.61f). At a frequency of 1 kHz, the MPI grayscale image does no longer represent the concentration. For example, the 40 nm single concentration point in Fig. 4.61a (top-left) has about the same grayscale value as the 90 nm point with twice the concentration (bottom-right). The limited relaxation dynamics of the large 90 nm particles reduce the magnitude observed in the image, while the smaller particles contribute to the full magnitude. In the phase image (→ Fig. 4.61f), which is independent of the concentration, the two particle sizes can be clearly distinguished. For the phases, the grayscale is white for 0° and black for 90° phase angle. While the small particles show a small phase angle (white), the larger particles' grayscale value indicates a significant phase of approximately 50 – 60°. At 10 kHz the Brownian contribution is noticeable, but much less pronounces compared to 1 kHz. However, in the phase image, the two particle sizes are still different.
Because the phase images are not directly accessible from the MPI F-space reconstruction, two of the above images have to be combined in order to obtain both the correct concentration as well as mobility information. For example, substracting Fig. 4.61a (1 kHz) from Fig. 4.61c (100 kHz) leaves no rest in the upper row, i.e. the particles relax fast enough for both frequencies in order to not introduce a difference in contrast, and the concentration estimate is accurate. The lower row leaves a rest of a low grayscale value, which represents a contrast difference that maps to a certain relaxation time constant. The correct concentration estimate is only found for the higher frequency, while the concentration from the lower frequency has to be corrected to account for the particle mobility. The exact time constant can only be obtained from the contrast difference via prior-knowledge from ACS or multi-frequency MPS measurements (→ Sec. 3.3.2). It should be noted, that the Néel contribution is not present in the

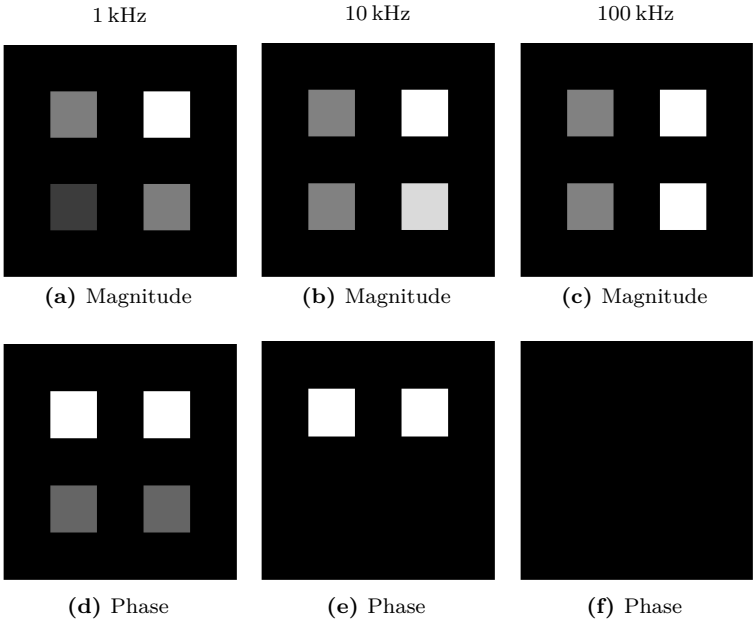

Figure 4.61: Magnitude and phase visualization represents simulation results of the multi-frequency mMPI approach. Magnitudes are scaled for each frequency individually, the phases encode a 0 (white) to 90° (black) range for comparison.

difference image, because it is nearly constant in the relevant frequency range. The Néel contribution is therefore referred to as 'baseline' image contribution. The experimental demonstration of the approach remains to be shown while a 2-frequency MPI scanner is being constructed.

F-Space Approach

The F-space approach to mMPI analyzes the dependence of the system matrix on changes in particle mobility. For the experimental implementation the mobility state is modeled via the viscosity of the medium. For this, a series of FeraSpin™ R samples were prepared with a variable ratio of de-ionized water and glycerol/glycerol to obtain a controllable viscosity for each sample. The viscosity ranges from 1 mPa s for water to approximately 1 Pa s for glycerol. A freeze-dried immobilized sample is used for reference, where only the Néel mechanism is contributing. The samples are confined enough to qualify as a localized (point-like) δ-sample.

For the experiment, a full 1-dimensional system matrix is acquired on each sample. Since all samples are made from the same batch of FeraSpin™ R and they are measured in an identical fashion, a strong congruence between the individual system matrices is expected. While the overall spatial structure is indeed comparable, there are some discriminable nuances which are best observed by computing the difference between pairs of system matrices. Figure 4.62 visualizes two selected Δ-matrices.

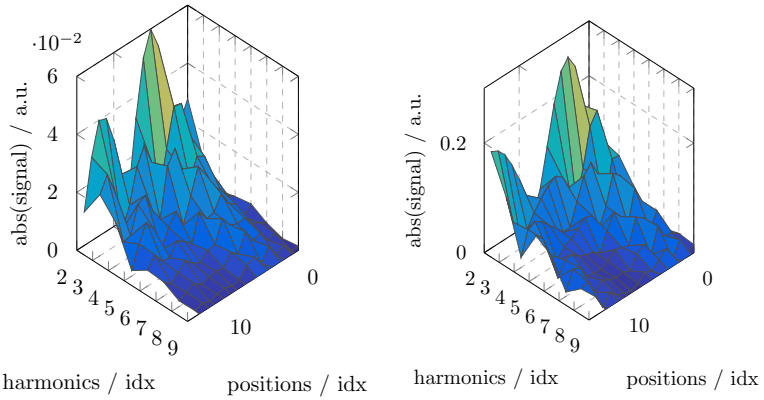

(a) 40% - 60% **(b)** 100% - 0%

Figure 4.62: Δ-matrices from calibrations of particles with different viscosities (0%, 40%, 60% and 100% glycerol + MNPs).

The magnitude views of the difference matrices reveal full MPI system matrices on their own. The structure is similar to real and imaginary parts contributing to the spatial frequency image, but an additional phase is observed representative of the different particle dynamics in the original system matrices.
For all considerations in this section, it is assumed that the relaxation times are fast enough so that they are not carried over to neighboring pixels, which would change the spatial structure of the system matrix fundamentally. However, the currently achieved resolution and the typical time constant of FeraSpin™ satisfy the aforesaid requirement.
In order to analyze the effect of a mobility mismatch between the system matrix and a phantom, different combinations were tested in F-space reconstruction (→ Fig. 4.63). A mobility mismatch is evident, when the system matrix was acquired for a viscosity that is different from the one found in the phantom. That is a common scenario in clinical MPI measurements because typically the particles (injected into the body) are found in many different physiological environments with vastly different viscosities, i.e. tissue versus blood stream.

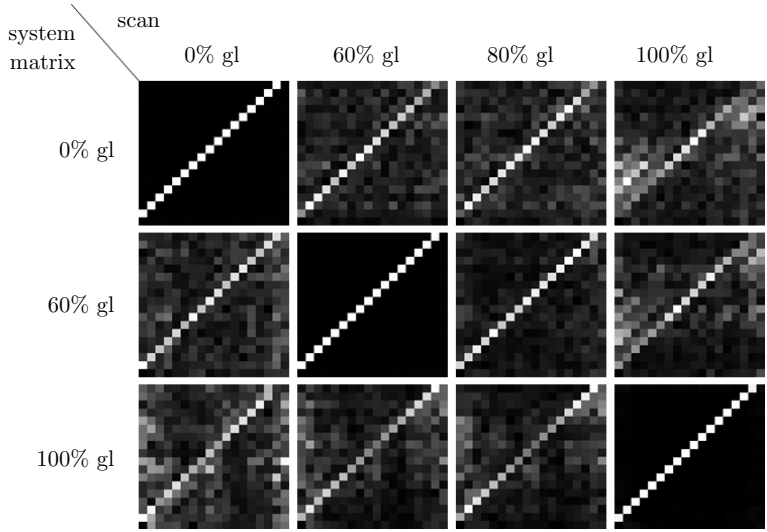

Figure 4.63: Reconstruction artifact caused by a mismatch between the viscosity during calibration and for the image scan.

If the phantom matches the viscosity of the system matrix, a near-perfect reconstruction is obtained. However, the larger the viscosity deviation between phantom and system matrix becomes, the more severe artifacts are observed from F-space reconstruction. Also, the artifacts are more prominent towards the edges of the FOV, whereas reconstruction of the center appears quite definite.
The additional phase observed in the difference matrices (→ Fig. 4.62) was identified to follow an explicit correlation with the corresponding viscosity (and it is also position-dependent). If all system matrices for the individual viscosities are referenced to the common Néel reference, the resulting phase (at an arbitrary point in the FOV) can be plotted as a function of the viscosity (→ Fig. 4.64). Because of induction law the phase difference is multiplied with the harmonic index, i.e. the phase angle in the 9th harmonics is approximately 3-times larger than in the 3rd harmonic.
The resulting phase plot in Fig. 4.64 shares strong similarity to an arctangent function, which is also observed in the Debye model for the phase angle $\phi = \arctan(\chi''/\chi')$ over frequency. This observation leads to the conclusion, that the difference matrix is indeed an approximate full 1-dimensional system matrix of the Brownian contribution. In order to proof that, a synthetic system matrix has been calculated using the extended (non-linear) Debye model (→ Sec. 2.4.4) and with a Brownian relaxation time constant for the known viscosity of the sample. The calculated system

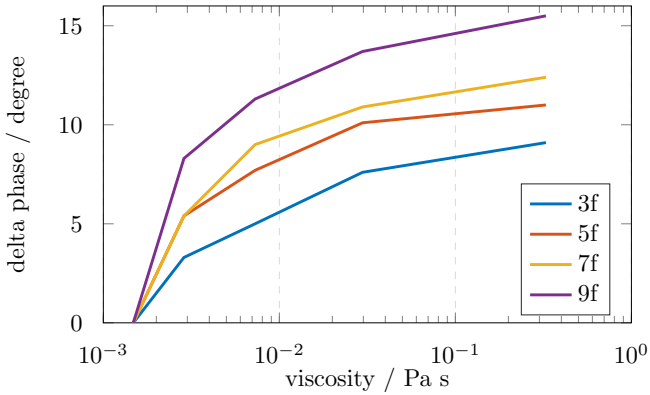

Figure 4.64: Phase shifts from the $3f - 9f$ system matrix component as a function of the sample viscosity (native resolution and upsampled image).

matrix was added to the Néel baseline matrix to obtain a combined system matrix that covers both the Néel and the viscous Brownian contributions. Results from applying the combined system matrix in an F-space reconstruction are depicted in Fig. 4.65. For the figure, a 0 % glycerol scan was reconstructed a) with the Néel baseline system matrix (showing strong artifacts from mismatch between calibration and scan), b) with the combined system matrix created before ('model-based') and c) with a calibration-based system matrix with adjusted viscosity. The model-based system matrix clearly shows an improvement and significant reduction in the artifacts compared to the baseline reconstruction. The calibration-based method still obtains the best results. However, given the naive approach and a simplistic particle model (non-linear Debye model), the agreement of the synthetic system matrix with the calibration-based one is promising.

The above experiment does not (yet) provide a recipe on how to realize mMPI in the F-space domain. But it shows that a good agreement of the system matrix and the actual environment from which to acquire images is critical. At least for our 10 kHz MPI scanner, which is more sensitive to Brownian contribution compared to the standard 25 kHz systems, care must be taken to characterize the tracer and the system matrix in a relevant environment (which includes both the concentration and viscosity of the calibration sample).

The reconstruction in standard MPI relies on constant tracer properties, which can not be guaranteed in a physiological environment. As a result, MPI might over-/underestimate the particle concentration making MPI less quantitative. A possible approach for correcting the concentration-weighted images is given as a side-effect of mMPI research.

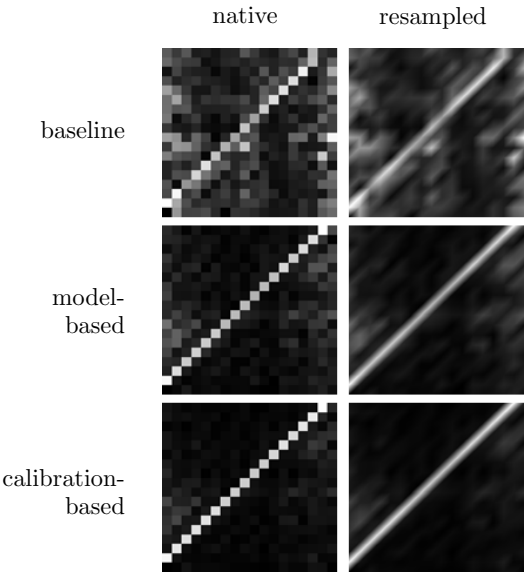

Figure 4.65: MPI images reconstructed with the Néel baseline matrix, a model-based and a calibration-based system matrix on a sample with different viscosity.

X-Space Approach

Another mobility estimation arises from the x-space reconstruction approach. In x-space MPI the native image is described as a convolution of the spatial particle distribution and a convolution kernel that is typically derived from Langevin theory and is closely related to the susceptibility curve of the tracer particles [223–225].
By using the same simulation framework as for the multi-frequency section above (→ Sec. 4.5.2), namely the effective field model (→ Sec. 2.4.2), a dynamic convolution kernel can be calculated. The core diameter is fixed to $d_c = 25\,\text{nm}$ and only the Brownian time constant is considered.
Figure 4.66 shows the resulting kernel for a multitude of different hydrodynamic diameters in the range 20 nm to 100 nm. For the small sizes a symmetric kernel is obtained. The larger the hydrodynamic diameter of the simulated particles, the more pronounced the relaxation effect becomes and the kernel takes an asymmetric form as relaxation happens into the direction of the FFP movement ('scan direction').
A different representation of the same kernel is given in Fig. 4.67. The distortion of the kernel into the scan direction is more apparent in this false color plot. The figure also gives a good impression that for large particle ($> 50\,\text{nm}$) the maximum of the signal is shifted against it's point

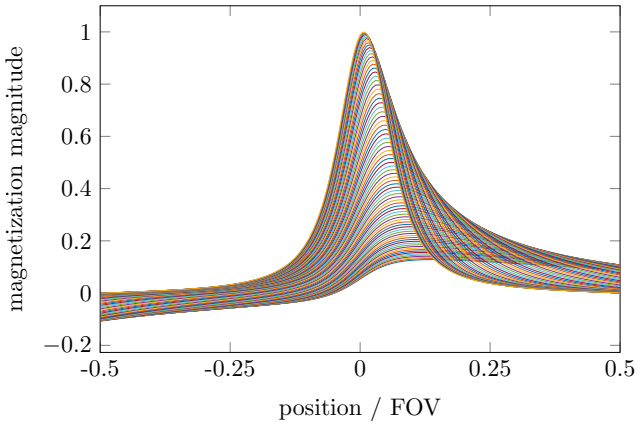

Figure 4.66: 1D x-space (convolution) kernel for different Brownian relaxation time constants. Maximum shifted to the right (scan direction) for slow relaxing particles.

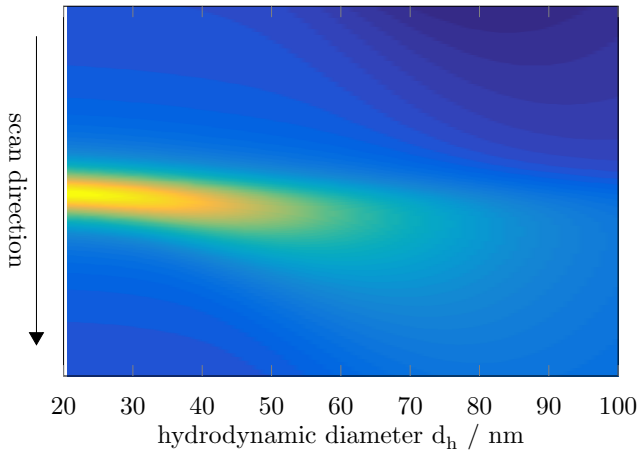

Figure 4.67: 1D x-space kernel for different Brownian relaxation time constants shows the scan direction of the FFP and the deformation caused by the limited time constant.

of origin (horizontal center line). Without proper compensation a point would be reconstructed at a displaced location. For that reason, x-space reconstruction uses the forward and the backward scan direction to pinpoint the original particle location (see below). Alternatively, the obtained kernel can be utilized for deconvolving the x-space signal as part of the reconstruction.

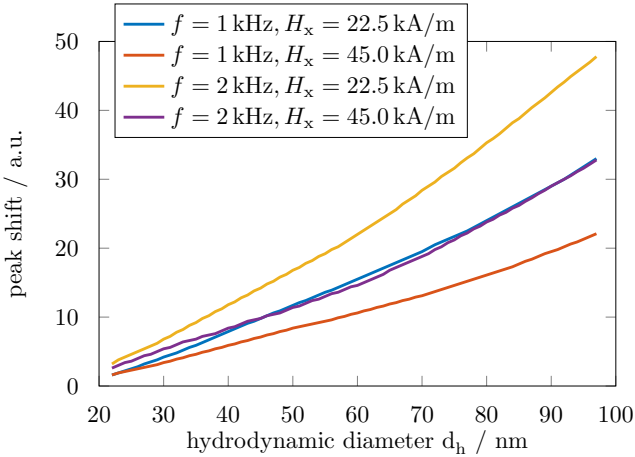

Figure 4.68: Shift of the maximum of the x-space kernel in dependence on the hydrodynamic particle diameter (for different excitation conditions, drive field frequency and amplitude).

The shift in the kernel (or point-spread-function, PSF) can be displayed as a function of the hydrodynamic diameter (→ Fig. 4.68). It strongly depends on the drive field amplitude and frequency. The peak shift is smaller for a large drive field amplitude, because the torque on the particle's magnetic moment is proportional to the applied field amplitude. A smaller shift is also noticed for low drive field frequencies, which corresponds to the observation of an increasing phase lag towards higher frequencies in Fig. 4.59 due to limited magnetization dynamics.
To demonstrate the approach on an actual particle sample, the MPS was modified so that the (optional) Helmholtz coils (usually used to generate a dc offset field to simulate an MPI system matrix acquisition) produce a field-free point (FFP) with a gradient strength of 0.48 T/m. The MPS was operated at 1 kHz and a FeraSpin™ R sample was place in the measuring setup. The x-Space PSF was then acquired on three samples with 0 %, 40 % and 100 % glycerol and the freeze-dried Néel sample for reference (→ Fig. 4.69). All PSFs exhibit a strongly asymmetric shape (→ Fig.

4.69a). The curve of the immobilized sample shows the strongest displacement, equivalent to the slowest relaxation time constant. For the (mobile) viscous samples, the Brownian time constant decreases as the viscosity approaches that of water ('0 % glycerol'). Consequently, the peak shift becomes smaller and the magnitude increases. Again, the freeze-dried sample serves as a baseline contribution to which the Brownian contribution adds a faster time constant and the peak displacement between forward scan (right maximum) and backward (left maximum) scan direction shortens.

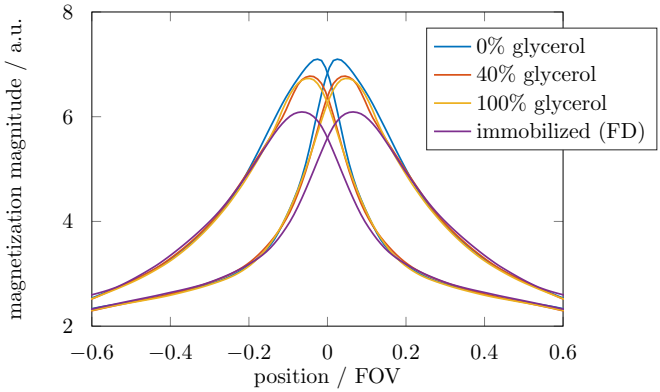

(a) Point-spread functions of different viscous samples

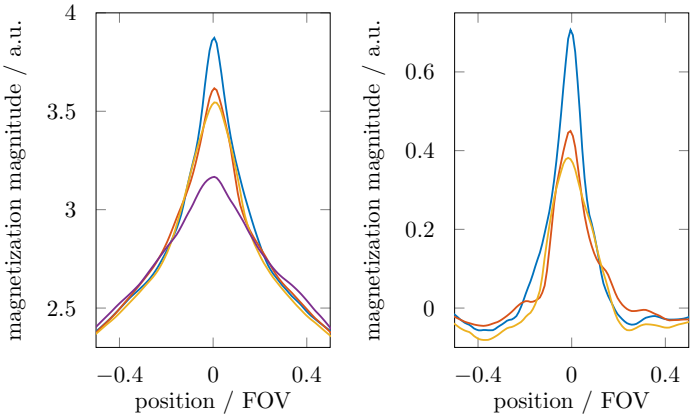

(b) Forward + backward scan **(c)** Néel compensation

Figure 4.69: 1D x-space PSFs measured in MPS on different viscous samples (glycerol-water series on FeraSpin™ R).

The standard x-space reconstruction is still applicable with the Brownian contribution present, provided that the forward and backward scans in Fig. 4.69a are merged into Fig. 4.69b. The composite PSF shows a single maximum at the center location, a prerequisite for successful reconstruction of the original tracer location. The order of the curve's magnitudes from different viscosities is preserved. It should be noted, that in addition to a larger signal of the less viscous samples, the FWHM of their PSF is also advantageous. While reconstruction is possible with all PSFs, a loss in resolution can be observed deteriorating with increasing viscosity.
Since mMPI seeks to isolate the Brownian contribution, which leads to the particle's mobility state (viscosity and hydrodynamic diameter), the baseline contribution as represented by the immobilized sample is substracted from the point spread function. The remaining PSF typifies only the Brownian contribution and can be denoted as the 'Brownian PSF'. In contrast to the multi-frequency approach, the removal of the baseline contribution is an explicit post-processing step in x-space MPI.
In summary, a valid localization of particles under a relaxation-induced shift in 1-dimensional x-space MPI is possible when the forward and backward scans are combined, i.e. the two curves are added so that the maximum of the joint curve appears centered. As an additional information, the PSF displacement maps directly to the hydrodynamic diameter (or particle mobility) according to (→ Fig. 4.68). However, for 2D/3D mMPI with the x-space approach a more complex evaluation scheme is required in order to separate the mobility information in the imaging and reconstruction process.
The residual signal for FeraSpin™ R that makes up the 'Brownian PSF' has a magnitude of about 5 % of the total signal magnitude. Given a limited dynamic range of the acquisition system and a minimal SNR margin for low particle concentrations, it is currently challenging to measure. Also, for x-space evaluation the phase stability of the MPI system is a limiting factor. While the F-space mMPI ideas, especially the multi-frequency approach, promise a high contrast on particle mobility, only limited contrast is expected from x-space mMPI. Of course, that can be different with an alternative particle system. The modulations from changes in particle mobility are best observed in higher harmonics (due to a cumulative effect on the phase), which is more easily done in F-space because of the log-scale representation of the magnetization harmonics. For FeraSpin™ the first few harmonics (up to around $9f$ to $11f$) are almost unaffected by viscosity changes and the PSF is mostly represented by the lower harmonics.

4.5.3 3-dimensional data acquisition

For a 1-dimensional MPI experiment, typically a coil arrangement with one principal axis is used. The drive field axis is aligned with the inductive receiver and only a single vector component parallel to the receive coil axis is recorded. However, even for a 1-dimensional drive field, i.e. a sinusoidal signal on one axis, a magnetization vector can be observed over time, that covers at least 2-dimensions of the MPI receive space. This

observation has already been made when the multi-dimensional x-space MPI was derived by Goodwill et al. [14]. However, the x-space equations do not consider the magnetization dynamics, i.e. particle relaxation.
A detailed analysis of the system function for 1-dimensional MPI reveals that a systematic deviation can be observed between experimental data and the particle magnetization models we are using, i.e. the Langevin and non-linear Debye (or effective field) models. The error was attributed to a continuous re-alignment of the magnetization axis in reference to the drive field direction. Simulations based on the Landau-Lifschitz-Gilbert equation (2.14) are supporting that. For a 2-dimensional Lissajous trajectory, the magnetization vector for particles with a finite relaxation time constant (in the order of the drive field periodicity) does not cover the entire 360° plane (→ Fig. 4.70a). The void in certain directions is a direct consequence of the limited magnetization dynamics of the particles. It is also highly dependent on the magnetization history of the particles. Similarly, for a 3-dimensional Lissajous trajectory a complex pattern is observed (→ Fig. 4.70b). For Brownian-dominated particles (with small Brownian time constants) the effect is negligible, but for immobilized (Néel-dominated) particles it is quite pronounced.

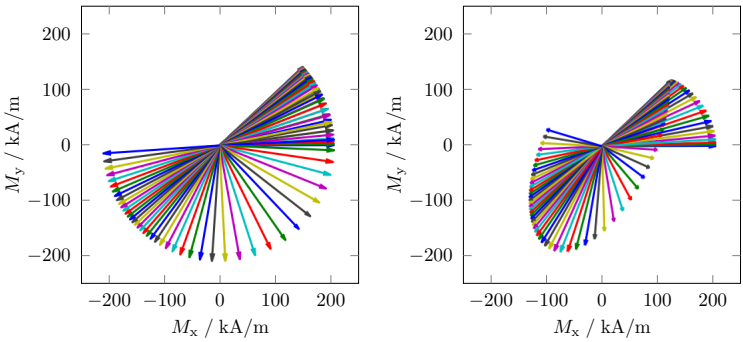

(a) 2D trajectory **(b)** 3D trajectory

Figure 4.70: Landau-Lifschitz-Gilbert (LLG) simulation results for a 2D/3D Lissajous trajectory (single drive field period, $\omega\tau = 0.6$).

Simulations show – in accordance with the Debye model – that at the point $\omega\tau = 1$, with effective relaxation time τ of the particles and drive field frequency $f = \omega/2\pi$, a transition occurs. For faster relaxing particles only a small lag between the particle magnetization vector and the drive field vector is observed. For slower particles the described effect becomes more definitive.
By recording all three components of the magnetization vector, the actual, vectorial magnetization can be observed as a function of the applied trajectory. Also, the specificity of the Lissajous-driven magnetization cycle

is highly dependent on the ratio of the effective relaxation time constant and the drive field frequency. Figure 4.71 illustrates the evolution of the magnetization vector for the same 3-dimensional Lissajous trajectory but for particles with different relaxation time constants, with different $\omega\tau$ ratios.

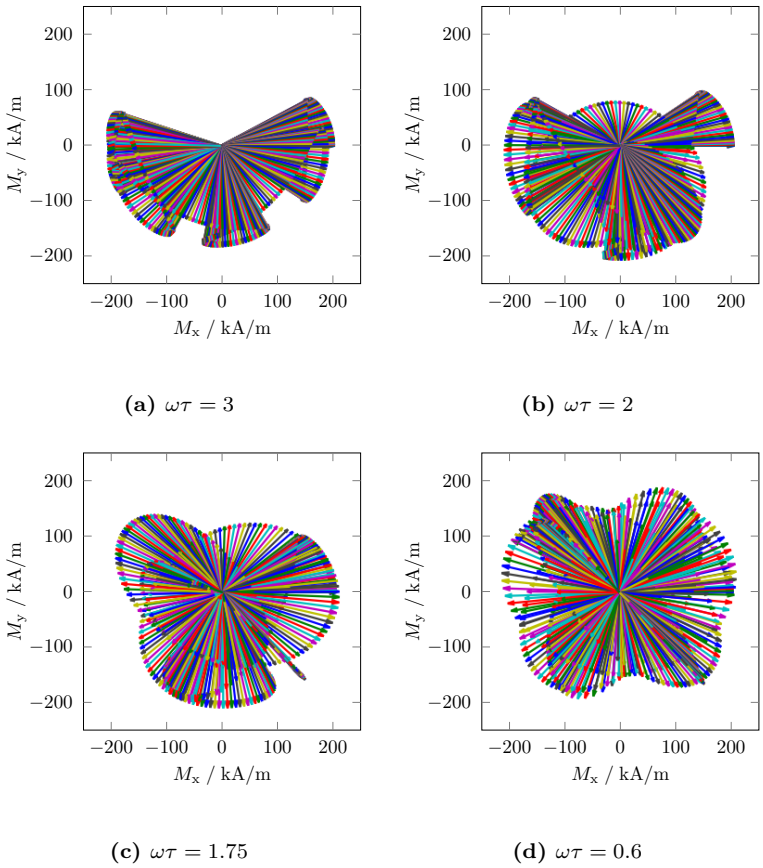

(a) $\omega\tau = 3$ **(b)** $\omega\tau = 2$

(c) $\omega\tau = 1.75$ **(d)** $\omega\tau = 0.6$

Figure 4.71: Landau-Lifschitz-Gilbert (LLG) simulation results for Lissajous trajectory 2D/3D (five drive field periods) for different $\omega\tau$.

In cases where the drive field frequency is around or above the characteristic frequency of the relaxing particles, a complex motion pattern can be observed. The magnetization vector does not simply follow the Lissajous excitation, but it renders additional loops that are explicit for a certain combination of particles and trajectory. Consequently, the orthogonality of the system matrix is affected and an MPI image can be reconstructed from alternate projections in the receive coils.

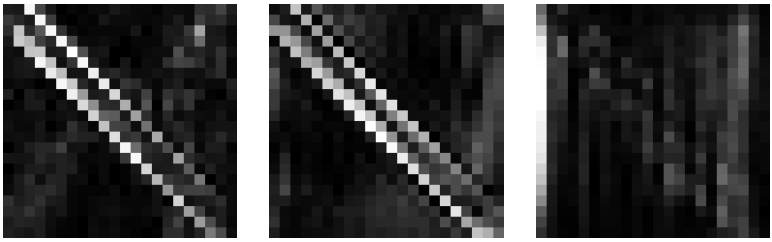

(a) x receive coil **(b)** y receive coil **(c)** z receive coil

Figure 4.72: Reconstruction of the 'DDash' phantom from x, y and z receive coil only.

To show the postulated effect, a 3-dimensional system matrix acquisition for a 1-dimensional FOV has been performed with the MPI scanner. In other words, a 1-dimensional system matrix was measured independently in all three receive directions (with the x, y and z receive coils) for a drive field in x-direction only. Figure 4.72 displays the images reconstructed by standard F-space means via the individual channels.
In addition to the image in x-direction, which is the standard MPI arrangement, also the y-image nicely reproduces the phantom. The receive coils in z-direction do not pick up enough signal to restore an image. One may conclude that over time the trajectory-driven motion of the magnetization vector covers mostly the X/Y-plane. The reason for that is given by the geometry of the selection field. The 1-dimensional (shift phantom) images were acquired along the x-axis in a centered position and slightly above the origin (in y-direction). As a result the predominant direction of the dc component (or gradient direction) is aligned with the y-axis. That is, the observed X/Y-plane is spanned by the dc and ac axes.

Direct Approach to Mobility MPI (mMPI)

The direct vector-based approach constitutes the latest iteration on 'Mobility MPI' in this thesis. Continuing the thoughts from the previous chapter (→ Sec. 4.5.3), the selection field geometry was recognized to play a very important role in MPI. It defines (together with the drive field) the extend and orientation of the field of view (FOV) and it has impact on the particle relaxation behavior.
The gradient field for a FFP MPI system is visualized in Fig. 4.73. Magnitude and direction of the dc field components are different in every point in space, although there are several symmetries in the selection field, e.g. mirror-points from the left and right hemisphere have identical magnitude but the direction is symmetric to a vertical center line. As a note, those spatial symmetries are directly related to the symmetries described for

the system matrix in Sec. 4.4. In conjunction with the drive field, the selection field manifests a specific orientation angle between dc and ac field that varies for different positions in the FOV. Also, if the dc and ac fields are about the same magnitude, i.e. the edges of the FOV are defined as the points where the dc field level equals the ac amplitude (→ Sec. 4.1.1), the dc field component is on average dominant against the drive field (which oscillates around the dc direction with zero time-average). As a consequence, the idle state or resting direction of the magnetization vector is inherent from the selection field gradient, and the principal direction of it depends on the position within the field of view (→ Fig. 4.73). A position-dependent phase offset observed in the system matrix, that was regarded as a model limitation for the F-space approach (→ Sec. 4.5.2), is now put into new context and it is a consequence of the above statements.

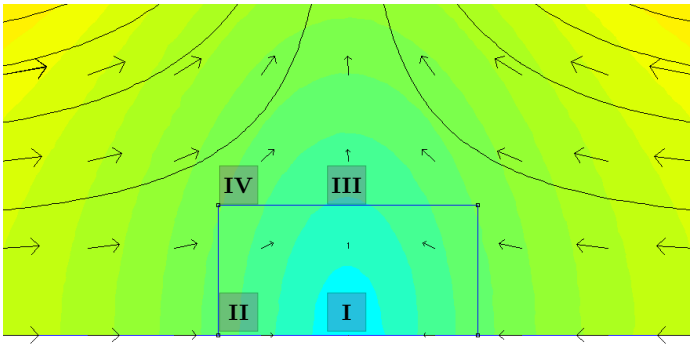

Figure 4.73: Selection field geometry of an FFP MPI scanner visualizing the DC selection field gradient at various points in the FOV (generated with FEMM [127]). Each point shows a unique field vector (magnitude and direction).

The idea for a time-domain, vector-based realization of mMPI can be viewed as a relaxation experiment. Similar to the particle relaxation in a magnetorelaxometry (MRX) experiment, where the particles relax as response to a step(-down) function, a continuing relaxation is observed for a Lissajous excitation pattern. The challenge here is to find ways of measuring the relaxation time constant while the vectorial alignment progresses. One observation in Fig. 4.71 was a $\omega\tau$ dependency of the magnetization response. As such, the 'vectorial relaxation' could be monitored by observing the difference vector between an instantaneous alignment and the actual magnetization vector of the particles.
For the experimental validation, an 'off-axis' 1-dimensional MPI scan is performed, where the FOV is chosen not to pass through the center point of the system but with a small offset to it, i.e. the dc dominance and with

it the expected deflection is greater in some distance to the origin. As introduced in Sec. 4.5.3, all three vector components are recorded for the 1-dimensional MPI experiment. The magnetization vector is estimated from the time-domain signals. The magnetization vector can not be recorded directly because only the time-derivative is available from an inductive receiver. Therefore, several assumptions are made. First, for a sampling rate much faster than the relaxation process (in our case the sampling frequency is 2 – 2.5 MS/s and the expected characteristic frequency of the particles is below 50 kHz) the difference vector is assumed to be perpendicular to the field vector, i.e. the difference is small. Second, the relaxation is assumed to be fast enough (in reference to the trajectory), so that an instantaneous response and the actual particle response map to the same pixel in the resulting image (no pixel carry-over).
In order to extract the mobility information from the difference vector, the effective field approximation with parallel and perpendicular time constants is applied (→ Sec. 2.4.2). Also, the field-dependence of the Brownian time constant is critical for an effective analysis (→ Sec. 2.2.2). Figure 4.74 shows the results of the experiment. A standard MPI image can be obtained either via the F-space or the x-space reconstruction. In any case, limitations apply as to the distortion of the standard MPI image from variable viscosity. The problem is observed already on reconstructing the acquired dataset via the F-space approach with a system matrix calibrated on a baseline/immobile reference sample (→ Fig. 4.74a) or on a mobility sample (→ Fig. 4.74b). Similarly to the reconstruction, also adaptation, i.e. the mapping of the magnetization vector difference to a pixel in the image, can be performed by either methods as a post-processing step. For the adapted images (Figs. 4.74c and 4.74d), the pixel luminance value is weighted by the estimated time constant (alternatively a false-color time constant map could be produced). Depending on the choice of parameters for the effective field calculation, the weighting process can lead to an over-compensation of the Brownian contribution in the image (→ Fig. 4.74c) or an under-compensation (→ Fig. 4.74d). For a known sample, the parameters can be adjusted manually to obtain a optimal separation. In a difference image of the standard (unmodified) MPI image and the image after adaptation, the effect of the procedure becomes apparent (→ Fig. 4.74e). Finally, the mobility information (or time constant map) can be inserted as a false-color overlay onto the unmodified image (→ Fig. 4.74f). Yellow denotes Brownian particles and blue marks the Néel contributions.
Figure 4.74f clearly shows, that it is possible to realize the 'mobility MPI' paradigm by using a time-domain vector-acquired dataset. The contrast for particle mobility discrimination depends strongly on the particles and the drive field frequency of the MPI scanner (as suggested by Fig. 4.71). Especially, for systems operating at 25 kHz the loss in sensitivity for detecting changes in particle mobility is about 10 – 20 % compared to a 10 kHz design (for the particles tested here). One possible solution could be the introduction of a temporal or spatial modulation. Alternatively to

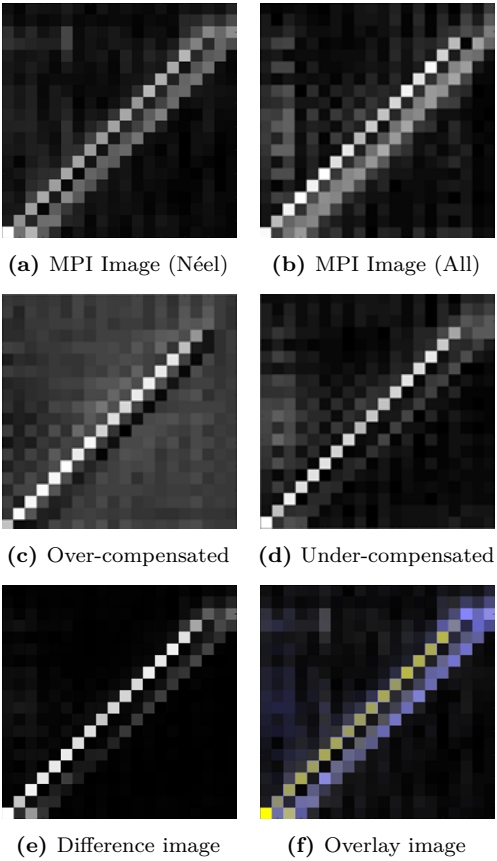

(a) MPI Image (Néel) **(b)** MPI Image (All)

(c) Over-compensated **(d)** Under-compensated

(e) Difference image **(f)** Overlay image

Figure 4.74: mMPI direct approach: MPI standard F-space reconstructed images with system matrix from baseline Néel sample (a) and from mobile sample (b). Images after adaptation via the time-domain vector-difference (c), (d). Difference image between original and adapted image (e) and false color overlay image (yellow = Brownian, blue = Neel) from mMPI.

the 'vectorial relaxation' one could impose a step field (as in MRX) to induce a global relaxation over the entire trajectory. In an MPI scanner this could be achieved by step-wise shifting of the FOV via the focus fields, provided that the focus field generators are capable of creating a sufficiently short-timed field-step in a time frame of about 100 µs to 1 ms (or better).
Also, for quantitative evaluation of particle mobility (not just grayscale contrast), which might be desirable for certain applications, the field-dependence of relaxation time constants must be taken into account. Unfortunately, due to the geometry of the selection field, the relaxation time constants become position-dependent, i.e. the specific ac and dc field levels at each point lead to a specific field-dependent time constant, which then is no longer uniform over the entire FOV.

5 Conclusion and Outlook

This thesis is concerned with the functional imaging aspect of MPI, where the particle mobility, representative of the particle binding state or local changes in the viscosity environment, is made accessible in addition to the standard concentration-weighted images. The dynamic magnetization response of the tracer plays a central role and is studied in the context of MPS and MPI experiments.

For that purpose, a Magnetic Particle Spectroscopy (MPS) setup was constructed and put into operation, that allows one to study the particle's harmonic spectrum as a function of the excitation field amplitude and frequency, as well as a dc magnetic field. This multivariate MPS provides an universal tool for studying the dynamic particle magnetization and to determine core and hydrodynamic properties of the particle sample. It is found, that a unique correlation between the magnitude spectrum and the sample's viscosity can not be established. Consequently, the phenomenological non-linear Debye model is derived and validated, which highlights the need for a complex-valued evaluation of MPS data. It is observed, that FeraSpin™ R (or Resovist®) works well for binding detection, once the Néel baseline contribution is compensated. The remaining Brownian response is in good agreement with the model.

To provide an experimental platform for MPI, a 10 kHz water-cooled MPI scanner with two active axes is designed, realized and employed for various applications. The system proofs ready to deliver phantom images in 1D, 2D and 2+1D (with focus field in the 3rd axis). The idea of the so-called 'Mobility MPI' (mMPI) is introduced and different options for the practical realization of the method are explored. The issue of providing a proper separation between a concentration-weighted image (standard MPI) and an additional mobility estimate is discussed. So far, the two-frequency mMPI variant, which requires specialized hardware, and the direct time-domain approach seem most promising.

Magnetic Particle Imaging (MPI) is currently an active field, where new scanner hardware and new methods are developed. In perspective, MPI could also bring value for technical (or generally non-clinical) applications. The biocompatibility of iron oxide would not be a requirement and alternative tracer compositions could be applied. For the use of MPI in the

clinical and biomedical field, optimization of the tracer has some potential to further improve the sensitivity and spatial resolution of MPI, but requires of course that the tailored tracer gets approved for human use.
The mMPI method has to take a next step, where binding assays are performed in 3-dimensional volume and target-specific markers are tested.
An alternative approach to separate the Néel and Brownian contribution in mMPI, is the concurrent use of different core sizes in 'multi-color MPI' (cMPI). However, a major advantage of mMPI over multi-color MPI (cMPI) for the distinction of labeled and unlabeled particles is the question of biodistribution, i.e. the different particles sizes are not guaranteed to show equal distribution in biological tissue, because cells are selective on particle size. As an alternative, the cMPI reconstruction could be used on the combined system matrices from F-space mMPI (Neel baseline + computed/calibrated Brownian contribution) to obtained a joint reconstruction of different viscosities.
A key point for enabling more functional imaging scenarios in MPI is a deeper understanding of the role of the tracer as part of the imaging process. In x-space, an over-simplified view is rendered and the tracer properties are not considered beyond a simple exponential relaxation model. In F-space, the tracer dynamics are implicitly contained in the system matrix and no attention is typically paid to them. The challenges in bringing mMPI forward are a) the transition from 1-dimensional to 2-/3-dimensional evaluation schemes and b) a better approximation of the particle's dynamic response for multi-core particle systems, like Resovist® and FeraSpin™ R.

List of Figures

List of Tables

References

[1] B. Gleich and J. Weizenecker, "Tomographic imaging using the nonlinear response of magnetic particles", *Nature*, vol. 435, no. 7046, pp. 1214–1217, 2005 (pages 1, 8, 84).

[2] B. Gleich, J. Weizenecker, and J. Borgert, "Experimental results on fast 2D-encoded magnetic particle imaging", *Physics in Medicine and Biology*, vol. 53, no. 6, N81–4, 2008 (page 1).

[3] C. Bontus, J. Rahmer, B. Gleich, J. Weizeneeker, and J. Borgert, "Cardiac MPI of mice over the complete heart cycle", *2009 IEEE Nuclear Science Symposium Conference Record (NSS/MIC)*, 2009 (page 1).

[4] J. Weizenecker, B. Gleich, J. Rahmer, H. Dahnke, and J. Borgert, "Three-dimensional real-time in vivo magnetic particle imaging", *Physics in medicine and biology*, vol. 54, no. 5, pp. L1–L10, 2009 (pages 1, 8).

[5] J. Rahmer, B. Gleich, and C. Bontus, "Rapid 3d in vivo magnetic particle imaging with a large field of view", *Proc. Intl. Soc. Mag. Reson. Med.*, vol. 1217, no. 2005, p. 3285, 2011 (pages 1–2).

[6] I. Schmale, J. Rahmer, B. Gleich, J. Kanzenbach, J. D. Schmidt, C. Bontus, O. Woywode, and J. Borgert, "First phantom and in vivo MPI images with an extended field of view", *Medical Imaging 2011: Biomedical Applications in Molecular, Structural, and Functional Imaging*, J. B. Weaver and R. C. Molthen, Eds., p. 796 510, 2011 (page 1).

[7] J. Borgert, J. D. Schmidt, I. Schmale, J. Rahmer, C. Bontus, B. Gleich, B. David, R. Eckart, O. Woywode, J. Weizenecker, J. Schnorr, M. Taupitz, J. Haegele, F. M. Vogt, and J. Barkhausen, "Fundamentals and applications of magnetic particle imaging", *Journal of Cardiovascular Computed Tomography*, vol. 6, no. 3, pp. 149–153, 2012 (page 1).

[8] E. U. Saritas, P. W. Goodwill, L. R. Croft, J. J. Konkle, K. Lu, B. Zheng, and S. M. Conolly, "Magnetic particle imaging (MPI) for nmr and MRI researchers", *Journal of Magnetic Resonance (San Diego, Calif.)*, vol. 229, pp. 116–126, 2013 (page 1).

[9] S. Biederer, T. Knopp, T. F. Sattel, K. Lüdtke-Buzug, B. Gleich, J. Weizenecker, J. Borgert, and T. M. Buzug, "Magnetization response spectroscopy of superparamagnetic nanoparticles for magnetic particle imaging", *Journal of Physics D: Applied Physics*, vol. 42, no. 20, p. 205 007, 2009 (pages 1, 37).

[10] J. Rahmer, J. Weizenecker, B. Gleich, and J. Borgert, "Analysis of a 3-D system function measured for magnetic particle imaging", *IEEE Transactions on Medical Imaging*, vol. 31, no. 6, pp. 1289–1299, 2012 (pages 1, 123).

[11] J. Rahmer, J. Weizenecker, B. Gleich, and J. Borgert, "Signal encoding in magnetic particle imaging: Properties of the system function", *BMC Medical Imaging*, vol. 9, no. 1, p. 4, 2009 (pages 1, 78).

[12] J. Lampe, C. Bassoy, J. Rahmer, J. Weizenecker, H. Voss, B. Gleich, and J. Borgert, "Fast reconstruction in magnetic particle imaging", *Physics in Medicine and Biology*, vol. 57, no. 4, pp. 1113–1134, 2012 (pages 1, 127).

[13] P. W. Goodwill and S. M. Conolly, "The x-space formulation of the magnetic particle imaging process: 1-D signal, resolution, bandwidth, SNR, SAR, and magnetostimulation", *IEEE Transactions on Medical Imaging*, vol. 29, no. 11, pp. 1851–1859, 2010 (pages 1, 58, 82).

[14] P. W. Goodwill and S. M. Conolly, "Multidimensional x-space magnetic particle imaging", *IEEE Transactions on Medical Imaging*, vol. 30, no. 9, pp. 1581–1590, 2011 (pages 1, 82, 150).

[15] P. W. Goodwill, E. U. Saritas, L. R. Croft, T. N. Kim, K. M. Krishnan, D. V. Schaffer, and S. M. Conolly, "X-space MPI: Magnetic nanoparticles for safe medical imaging", *Advanced Materials*, vol. 24, no. 28, pp. 3870–3877, 2012 (page 1).

[16] J. Weizenecker, B. Gleich, and J. Borgert, "Magnetic particle imaging using a field free line", *Journal of Physics D: Applied Physics*, vol. 41, no. 10, p. 105 009, 2008 (page 2).

[17] T. Knopp, T. F. Sattel, S. Biederer, and T. M. Buzug, "Field-free line formation in a magnetic field", *Journal of Physics A: Mathematical and Theoretical*, vol. 43, no. 1, p. 012 002, 2010 (page 2).

[18] J. Konkle, P. Goodwill, and S. Conolly, "Development of a field free line magnet for projection MPI", *Medical Imaging 2011: Biomedical Applications in Molecular, Structural, and Functional Imaging*, vol. 7965, J. B. Weaver and R. C. Molthen, Eds., p. 79650X, 2011 (page 2).

[19] J. J. Konkle, P. W. Goodwill, O. M. Carrasco-Zevallos, and S. M. Conolly, "Projection reconstruction magnetic particle imaging", *IEEE Transactions on Medical Imaging*, vol. 32, no. 2, pp. 338–347, 2013 (page 2).

[20] E. U. Saritas, P. W. Goodwill, G. Z. Zhang, and S. M. Conolly, "Magnetostimulation limits in magnetic particle imaging", *IEEE Transactions on Medical Imaging*, vol. 32, no. 9, pp. 1600–1610, 2013 (page 2).

[21] O. Dössel and J. Bohnert, “Safety considerations for magnetic fields of 10mT to 100mT amplitude in the frequency range of 10kHz to 100kHz for magnetic particle imaging”, *Biomedizinische Technik*, vol. 58, no. 6, pp. 611–621, 2013 (page 2).

[22] J. Bohnert and O. Dössel, “Effects of time varying currents and magnetic fields in the frequency range of 1kHz to 1MHz to the human body - a simulation study”, *Annual International Conference of the IEEE Engineering in Medicine and Biology Society*, pp. 6805–6808, 2010 (page 2).

[23] I. Schmale, B. Gleich, J. Schmidt, J. Rahmer, C. Bontus, R. Eckart, B. David, M. Heinrich, O. Mende, O. Woywode, J. Jokram, and J. Borgert, “Human PNs and SAR study in the frequency range from 24 to 162kHz”, *2013 International Workshop on Magnetic Particle Imaging*, vol. 7965, no. May 2012, p. 1, 2013 (page 2).

[24] J. Rahmer, B. Gleich, J. Schmidt, I. Schmale, C. Bontus, J. Kanzenbach, J. Borgert, O. Woywode, and J. Weizenecker, “Increased volume coverage in 3D magnetic particle imaging”, *Proceedings of the 4th International Symposium on Applied Sciences in Biomedical and Communiction Technologies*, vol. C, no. 1, pp. 1–5, 2011 (pages 2, 72).

[25] D. Eberbeck, F. Wiekhorst, S. Wagner, and L. Trahms, “How the size distribution of magnetic nanoparticles determines their magnetic particle imaging performance”, *Applied Physics Letters*, vol. 98, no. 18, p. 182 502, 2011 (pages 2, 24).

[27] T. Yoshida, N. B. Othman, and K. Enpuku, “Characterization of magnetically fractionated magnetic nanoparticles for magnetic particle imaging”, *Journal of Applied Physics*, vol. 114, no. 17, p. 173 908, 2013 (pages 2, 24–25).

[28] R. Ferguson, A. Khandhar, S. Kemp, H. Arami, E. Saritas, L. Croft, J. Konkle, P. Goodwill, A. Halkola, J. Rahmer, J. Borgert, S. Conolly, and K. Krishnan, “Magnetic particle imaging with tailored iron oxide nanoparticle tracers”, *IEEE Medical Imaging*, vol. 34, no. 5, pp. 1077–1084, 2015 (pages 2, 24).

[29] R. M. Ferguson, A. P. Khandhar, H. Arami, L. Hua, O. Hovorka, and K. M. Krishnan, “Tailoring the magnetic and pharmacokinetic properties of iron oxide magnetic particle imaging tracers”, *Biomedizinische Technik*, vol. 58, no. 6, pp. 493–507, 2013 (pages 2, 24).

[30] Starmans, Lucas W. E., D. Burdinski, Haex, Nicole P. M., Moonen, Rik P. M., G. J. Strijkers, K. Nicolay, and H. Grüll, “Iron oxide nanoparticle-micelles (IOn-micelles) for sensitive (molecular) magnetic particle imaging and magnetic resonance imaging”, *PloS one*, vol. 8, no. 2, e57335, 2013 (page 2).

[31] R. M. Ferguson, K. R. Minard, and K. M. Krishnan, “Optimization of nanoparticle core size for magnetic particle imaging”, *Journal of Magnetism and Magnetic Materials*, vol. 321, no. 10, pp. 1548–1551, 2009 (pages 2, 24).

[32] K. M. Krishnan, "Biomedical nanomagnetics: A spin through possibilities in imaging, diagnostics, and therapy", *IEEE Transactions on Magnetics*, vol. 46, no. 7, pp. 2523–2558, 2010 (page 5).

[33] Q. A. Pankhurst, J. Connolly, S. K. Jones, and J. Dobson, "Applications of magnetic nanoparticles in biomedicine", *Journal of Physics D: Applied Physics*, vol. 36, no. 13, R167–R181, 2003 (page 5).

[34] Q. A. Pankhurst, Thanh, N. T. K., S. K. Jones, and J. Dobson, "Progress in applications of magnetic nanoparticles in biomedicine", *Journal of Physics D: Applied Physics*, vol. 42, no. 22, p. 224 001, 2009 (page 5).

[35] A. Ito, M. Shinkai, H. Honda, and T. Kobayashi, "Medical application of functionalized magnetic nanoparticles", *Journal of Bioscience and Bioengineering*, vol. 100, no. 1, pp. 1–11, 2005 (pages 5, 7).

[36] S. Laurent, D. Forge, M. Port, A. Roch, C. Robic, L. Vander Elst, and R. N. Muller, "Magnetic iron oxide nanoparticles: Synthesis, stabilization, vectorization, physicochemical characterizations, and biological applications", *Chemical Reviews*, vol. 108, no. 6, pp. 2064–2110, 2008 (pages 5–6).

[37] Y.-X. J. Wang, S. M. Hussain, and G. P. Krestin, "Superparamagnetic iron oxide contrast agents: Physicochemical characteristics and applications in MR imaging", *Eur Radiol*, vol. 11, no. 11, pp. 2319–2331, 2001 (page 5).

[38] P. Reimer and T. Balzer, "Ferucarbotran (resovist): A new clinically approved res-specific contrast agent for contrast-enhanced MRI of the liver: Properties, clinical development, and applications", *European Radiology*, vol. 13, no. 6, pp. 1266–1276, 2003 (pages 5, 8).

[39] D. Schüler, "Molecular analysis of a subcellular compartment: The magnetosome membrane in magnetospirillum gryphiswaldense", *Archives of Microbiology*, vol. 181, no. 1, pp. 1–7, 2004 (page 6).

[40] I. Šafařík and M. Šafaříkov, *Magnetic nanoparticles and biosciences*. 2002, vol. 133 (page 6).

[41] C. C. Berry, "Progress in functionalization of magnetic nanoparticles for applications in biomedicine", *Journal of Physics D: Applied Physics*, vol. 42, no. 22, p. 224 003, 2009 (pages 6–7).

[42] A.-H. Lu, E. L. Salabas, and F. Schüth, "Magnetic nanoparticles: Synthesis, protection, functionalization, and application", *Angewandte Chemie International Edition*, vol. 46, no. 8, pp. 1222–1244, 2007 (pages 6–7).

[43] L. H. Reddy, J. L. Arias, J. Nicolas, and P. Couvreur, "Magnetic nanoparticles: Design and characterization, toxicity and biocompatibility, pharmaceutical and biomedical applications", *Chemical Reviews*, vol. 112, no. 11, pp. 5818–5878, 2012 (pages 6–7).

[44] Bishop, Kyle J. M., C. E. Wilmer, S. Soh, and B. A. Grzybowski, "Nanoscale forces and their uses in self-assembly", *Small (Weinheim, Germany)*, vol. 5, no. 14, pp. 1600–1630, 2009 (page 7).

[45] J. Faraudo, J. S. Andreu, and J. Camacho, "Understanding diluted dispersions of superparamagnetic particles under strong magnetic fields: A review of concepts, theory and simulations", *Soft Matter*, vol. 9, no. 29, p. 6654, 2013 (page 7).

[46] A. G. Roca, R. Costo, A. F. Rebolledo, S. Veintemillas-Verdaguer, P. Tartaj, T. González-Carreño, M. P. Morales, and C. J. Serna, "Progress in the preparation of magnetic nanoparticles for applications in biomedicine", *Journal of Physics D: Applied Physics*, vol. 42, no. 22, p. 224 002, 2009 (page 7).

[47] C. Hoskins, A. Cuschieri, and L. Wang, "The cytotoxicity of polycationic iron oxide nanoparticles: Common endpoint assays and alternative approaches for improved understanding of cellular response mechanism", *Journal of Nanobiotechnology*, vol. 10, no. 1, p. 15, 2012 (page 7).

[48] M. Mahmoudi, H. Hofmann, B. Rothen-Rutishauser, and A. Petri-Fink, "Assessing the in vitro and in vivo toxicity of superparamagnetic iron oxide nanoparticles", *Chemical Reviews*, vol. 112, no. 4, pp. 2323–2338, 2012 (page 7).

[49] C. C. Berry and Curtis, Adam S. G., "Functionalisation of magnetic nanoparticles for applications in biomedicine", *Journal of Physics D: Applied Physics*, vol. 36, no. 13, R198–R206, 2003 (page 7).

[50] J.-H. Lee, Y.-M. Huh, Y.-w. Jun, J.-w. Seo, J.-t. Jang, H.-T. Song, S. Kim, E.-J. Cho, H.-G. Yoon, J.-S. Suh, and J. Cheon, "Artificially engineered magnetic nanoparticles for ultra-sensitive molecular imaging", *Nature Medicine*, vol. 13, no. 1, pp. 95–99, 2007 (page 7).

[51] H. Weinmann, R. Brasch, W. Press, and G. Wesbey, "Characteristics of gadolinium-DTPA complex: A potential NMR contrast agent", *American Journal of Roentgenology*, vol. 142, no. 3, pp. 619–624, 1984 (page 9).

[52] S. Bedanta and W. Kleemann, "Supermagnetism", *Journal of Physics D: Applied Physics*, vol. 42, no. 1, p. 013 001, 2009 (pages 10, 15).

[53] L. Tauxe, *Essentials of paleomagnetism*. University of California Press, 2010 (page 10).

[54] R. Jedynak, "Approximation of the inverse Langevin function revisited", *Rheologica Acta*, vol. 54, no. 1, pp. 29–39, 2015 (page 12).

[55] A. Aharoni and I. Eisenstein, "Theoretical relaxation times of large superparamagnetic particles with cubic ansiotropy", *Physical Review B*, vol. 11, no. 1, pp. 514–519, 1975 (page 14).

[56] D. V. Berkov, N. L. Gorn, R. Schmitz, and D. Stock, "Langevin dynamic simulations of fast remagnetization processes in ferrofluids with internal magnetic degrees of freedom", *Journal of Physics: Condensed Matter*, vol. 18, no. 38, S2595–S2621, 2006 (page 14).

[57] W. T. Coffey, P. J. Cregg, and Y. U. P. Kalmykov, "On the theory of debye and néel relaxation of single domain ferromagnetic particles", *Advances in Chemical Physics*, vol. 83, pp. 263–464, 2009 (pages 14, 29, 32, 34).

[58] W. Brown, "Thermal fluctuations of a single-domain particle", *Physical Review*, vol. 130, no. 5, pp. 1677–1686, 1963 (pages 14, 26).

[59] Martsenyuk, "On the kinetics of magnetization of suspensions of ferromagnetic particles", *Soviet Physics*, vol. 38, no. 2, pp. 413–416, 1974 (page 14).

[60] I. Eisenstein and A. Aharoni, "Asymptotic superparamagnetic time constants for cubic anisotropy. ii. negative anisotropy constant", *Physical Review B*, vol. 16, no. 3, pp. 1285–1290, 1977 (page 14).

[61] I. Eisenstein and A. Aharoni, "Asymptotic superparamagnetic time constants for cubic anisotropy. i. positive anisotropy", *Physical Review B*, vol. 16, no. 3, pp. 1278–1284, 1977 (page 14).

[62] P. C. Fannin and S. W. Charles, "The study of a ferrofluid exhibiting both brownian and neel relaxation", *Journal of Physics D: Applied Physics*, vol. 22, no. 1, pp. 187–191, 1989 (pages 14, 18).

[63] M. I. Shliomis and V. I. Stepanov, "Rotational viscosity of magnetic fluids: Contribution of the brownian and néel relaxational processes", *Journal of Magnetism and Magnetic Materials*, vol. 122, no. 1-3, pp. 196–199, 1993 (page 14).

[64] J. García-Palacios and F. Lázaro, "Langevin-dynamics study of the dynamical properties of small magnetic particles", *Physical Review B*, vol. 58, no. 22, pp. 14 937–14 958, 1998 (pages 16, 25–26, 35).

[65] C. Tannous and J. Gieraltowski, "The stoner–wohlfarth model of ferromagnetism", *European Journal of Physics*, vol. 29, no. 3, pp. 475–487, 2008 (page 16).

[66] J. Carrey, B. Mehdaoui, and M. Respaud, "Simple models for dynamic hysteresis loop calculations of magnetic single-domain nanoparticles: Application to magnetic hyperthermia optimization", *Journal of Applied Physics*, vol. 109, no. 8, p. 083 921, 2011 (page 16).

[67] P. C. Fannin, L. Kinsella, and S. W. Charles, "On the influence of a uniform magnetic field on the néel relaxation of a colloidal suspension of nanometre-sized particles", *Journal of Physics D: Applied Physics*, vol. 30, no. 16, pp. 2292–2297, 1997 (page 16).

[68] P. C. Fannin, Scaife, B. K. P., and S. W. Charles, "The field dependence of the complex frequency-dependent susceptibility of magnetic fluids", *Journal of Physics D: Applied Physics*, vol. 21, no. 3, pp. 533–534, 1988 (pages 16–17).

[69] M. A. Chuev and J. Hesse, "Nanomagnetism: Extension of the stoner–wohlfarth model within néel's ideas and useful plots", *Journal of Physics: Condensed Matter*, vol. 19, no. 50, p. 506 201, 2007 (page 16).

[70] A. Aharoni, "Effect of a magnetic field on the superparamagnetic relaxation time", *Physical Review*, vol. 177, no. 2, pp. 793–796, 1969 (page 17).

[71] W. Coffey, D. Crothers, Y. Kalmykov, and J. Waldron, "Constant-magnetic-field effect in néel relaxation of single-domain ferromagnetic particles", *Physical Review B*, vol. 51, no. 22, pp. 15 947–15 956, 1995 (pages 17, 26).

[72] R. J. Deissler, Y. Wu, and M. A. Martens, "Dependence of brownian and néel relaxation times on magnetic field strength", *Medical Physics*, vol. 41, no. 1, p. 012 301, 2014 (pages 17, 26).

[73] P. C. Fannin, S. W. Charles, C. Mac Oireachtaigh, and S. Odenbach, "Investigation of possible hysteresis effects arising from frequency- and field-dependent complex susceptibility measurements of magnetic fluids", *Journal of Magnetism and Magnetic Materials*, vol. 302, no. 1, pp. 1–6, 2006 (page 17).

[74] P. C. Fannin, B. Scaife, and S. W. Charles, "A study of the complex ac susceptibility of magnetic fluids subjected to a constant polarizing magnetic field", *Journal of Magnetism and Magnetic Materials*, vol. 85, no. 1-3, pp. 54–56, 1990 (page 17).

[75] T. Yoshida and K. Enpuku, "Simulation and quantitative clarification of AC susceptibility of magnetic fluid in nonlinear brownian relaxation region", *Japanese Journal of Applied Physics*, vol. 48, no. 12, p. 127 002, 2009 (pages 18, 26, 28, 32, 34, 67–68).

[76] R. E. Rosensweig, "Heating magnetic fluid with alternating magnetic field", *Journal of Magnetism and Magnetic Materials*, vol. 252, pp. 370–374, 2002 (page 23).

[77] F. Burrows, C. Parker, Evans, R. F. L., Y. Hancock, O. Hovorka, and R. W. Chantrell, "Energy losses in interacting fine-particle magnetic composites", *Journal of Physics D: Applied Physics*, vol. 43, no. 47, p. 474 010, 2010 (page 23).

[78] R. Hergt, R. Hiergeist, I. Hilger, W. Kaiser, Y. Lapatnikov, S. Margel, and U. Richter, "Maghemite nanoparticles with very high AC-losses for application in RF-magnetic hyperthermia", *Journal of Magnetism and Magnetic Materials*, vol. 270, no. 3, pp. 345–357, 2004 (page 23).

[79] R. Hergt, R. Hiergeist, M. Zeisberger, G. Glöckl, W. Weitschies, L. Ramirez, I. Hilger, and W. Kaiser, "Enhancement of AC-losses of magnetic nanoparticles for heating applications", *Journal of Magnetism and Magnetic Materials*, vol. 280, no. 2-3, pp. 358–368, 2004 (page 23).

[80] H. Mamiya and B. Jeyadevan, "Hyperthermic effects of dissipative structures of magnetic nanoparticles in large alternating magnetic fields", *Scientific Reports*, vol. 1, p. 157, 2011 (page 23).

[81] J. Weizenecker, B. Gleich, J. Rahmer, and J. Borgert, "Micromagnetic simulation study on the magnetic particle imaging performance of anisotropic mono-domain particles", *Physics in Medicine and Biology*, vol. 57, no. 22, pp. 7317–7327, 2012 (pages 23, 25, 35).

[82] A. R. Muxworthy and W. Williams, "Critical superparamagnetic / single-domain grain sizes in interacting magnetite particles: Implications for magnetosome crystals", *Journal of The Royal Society Interface*, vol. 6, no. 41, 2009 (page 24).

[83] L. Tauxe, T. A. T. Mullender, and T. Pick, "Potbellies, wasp-waists, and superparamagnetism in magnetic hysteresis", *Journal of Geophysical Research: Solid Earth*, vol. 101, no. B1, pp. 571–583, 1996 (page 24).

[84] D. J. Dunlop, "Theory and application of the day plot (mrs/ms versus hcr/hc)", *Journal of Geophysical Research: Solid Earth*, vol. 107, no. B3, pp. 41–422, 2002 (page 24).

[85] D. Eberbeck, C. L. Dennis, N. F. Huls, K. L. Krycka, C. Gruttner, and F. Westphal, "Multicore magnetic nanoparticles for magnetic particle imaging", *IEEE Transactions on Magnetics*, vol. 49, no. 1, pp. 269–274, 2013 (page 24).

[86] R. M. Ferguson, A. P. Khandhar, H. Arami, S. M. Conolly, and K. M. Krishnan, "Assessing the limits of MPI tracer performance", *Magnetic Particle Imaging*, vol. 111, no. 7, p. 1, 2013 (page 24).

[87] F. Ludwig, D. Eberbeck, N. Löwa, U. Steinhoff, T. Wawrzik, M. Schilling, and L. Trahms, "Characterization of magnetic nanoparticle systems with respect to their magnetic particle imaging performance", *Biomedizinische Technik*, vol. 58, no. 6, pp. 535–545, 2013 (page 24).

[88] R. M. Ferguson, A. P. Khandhar, and K. M. Krishnan, "Tracer design for magnetic particle imaging (invited)", *Journal of Applied Physics*, vol. 111, no. 7, 7B318–7B3185, 2012 (page 24).

[89] R. M. Ferguson, K. R. Minard, A. P. Khandhar, and K. M. Krishnan, "Optimizing magnetite nanoparticles for mass sensitivity in magnetic particle imaging", *Medical Physics*, vol. 38, no. 3, p. 1619, 2011 (page 24).

[90] V. Schaller, G. Wahnström, A. Sanz-Velasco, S. Gustafsson, E. Olsson, P. Enoksson, and C. Johansson, "Effective magnetic moment of magnetic multicore nanoparticles", *Physical Review B*, vol. 80, no. 9, p. 092 406, 2009 (pages 24, 47).

[91] V. Schaller, G. Wahnström, A. Sanz-Velasco, P. Enoksson, C. Johansson, U. Häfeli, W. Schütt, and M. Zborowski, "Determination of nanocrystal size distribution in magnetic multicore particles including dipole-dipole interactions and magnetic anisotropy: A Monte Carlo study", *AIP Conference Proceedings*, pp. 42–50, 2010 (pages 24, 47).

[92] A. Weddemann, A. Auge, D. Kappe, F. Wittbracht, and A. Hütten, "Dynamic simulations of the dipolar driven demagnetization process of magnetic multi-core nanoparticles", *Journal of Magnetism and Magnetic Materials*, vol. 322, no. 6, pp. 643–646, 2010 (page 24).

[93] R. Chantrell, N. Walmsley, J. Gore, and M. Maylin, "Calculations of the susceptibility of interacting superparamagnetic particles", *Physical Review B*, vol. 63, no. 2, p. 024 410, 2000 (page 24).

[94] R. W. Chantrell, "Agglomerate formation in a magnetic fluid", *Journal of Applied Physics*, vol. 53, no. 3, p. 2742, 1982 (page 24).

[95] T. Rheinländer, R. Kötitz, W. Weitschies, and W. Semmler, "Magnetic fractionation of magnetic fluids", *Journal of Magnetism and Magnetic Materials*, vol. 219, no. 2, pp. 219–228, 2000 (page 25).

[96] T. Rheinländer, D. Roessner, W. Weitschies, and W. Semmler, "Comparison of size-selective techniques for the fractionation of magnetic fluids", *Journal of Magnetism and Magnetic Materials*, vol. 214, no. 3, pp. 269–275, 2000 (page 25).

[97] M. Büttner, P. Weber, F. Schmidl, P. Seidel, M. Röder, M. Schnabelrauch, K. Wagner, P. Görnert, G. Glöckl, and W. Weitschies, "Investigation of magnetic active core sizes and hydrodynamic diameters of a magnetically fractionated ferrofluid", *Journal of Nanoparticle Research*, vol. 13, no. 1, pp. 165–173, 2011 (page 25).

[98] D. R. Kelland, "Magnetic separation of nanoparticles", *IEEE Transactions on Magnetics*, vol. 34, no. 4, pp. 2123–2125, 1998 (page 25).

[99] D. Fletcher, "Fine particle high gradient magnetic entrapment", *IEEE Transactions on Magnetics*, vol. 27, no. 4, pp. 3655–3677, 1991 (page 25).

[100] H. Pfister, "Magnetische Separation mit hohen Flussdichte-", *Journal of Magnetism and Magnetic Materials*, vol. 13, no. 1-2, pp. 1–10, 1979 (page 25).

[101] W. T. Coffey, Y. P. Kalmykov, and J. T. Waldron, "The Langevin equation", vol. 14, 2004 (pages 25–26, 28, 35).

[102] R. J. Deissler, M. A. Martens, Y. Wu, and R. Brown, "Brownian and néel relaxation times in magnetic particle dynamics", *2013 International Workshop on Magnetic Particle Imaging*, vol. 1677, p. 1, (pages 25–26, 35).

[103] D. B. Reeves and J. B. Weaver, "Simulations of magnetic nanoparticle brownian motion", *Journal of Applied Physics*, vol. 112, no. 12, p. 124 311, 2012 (pages 25–26, 35).

[104] M. A. Martens, R. J. Deissler, Y. Wu, L. Bauer, Z. Yao, R. Brown, and M. Griswold, "Modeling the brownian relaxation of nanoparticle ferrofluids: Comparison with experiment", *Medical Physics*, vol. 40, no. 2, p. 022 303, 2013 (pages 25, 32, 34–35).

[105] N. Löwa, D. Eberbeck, U. Steinhoff, F. Wiekhorst, and L. Trahms, "Potential of improving MPI performance by magnetic separation", *Springer Proceedings in Physics*, vol. 140, T. M. Buzug and J. Borgert, Eds., pp. 73–78, 2012 (page 25).

[106] T. Gilbert, "A phenomenological theory of damping in ferromagnetic materials", *IEEE Transactions on Magnetics*, vol. 40, no. 6, pp. 3443–3449, 2004 (page 26).

[107] J. L. Garca-Palacios, "On the statics and dynamics of magnetoanisotropic nanoparticles", *Advances in Chemical Physics*, vol. 112, pp. 1–210, 2009 (page 26).

[108] W. T. Coffey and Y. P. Kalmykov, "Thermal fluctuations of magnetic nanoparticles: Fifty years after brown", *Journal of Applied Physics*, vol. 112, no. 12, p. 121 301, 2012 (pages 26, 28).

[109] J. Li, Y. Huang, X. Liu, Y. Lin, L. Bai, and Q. Li, "Effect of aggregates on the magnetization property of ferrofluids: A model of gaslike compression", *Science and Technology of Advanced Materials*, vol. 8, no. 6, pp. 448–454, 2007 (page 27).

[110] Y. L. Raikher and M. I. Shliomis, "The effective field method in the orientational kinetics of magnetic fluids and liquid crystals", *Adv. Chem. Phys*, vol. 87, no. 1994, pp. 595–751, 1994 (pages 27–28).

[111] Y. Kalmykov and W. Coffey, "Transverse complex magnetic susceptibility of single-domain ferromagnetic particles with uniaxial anisotropy subjected to a longitudinal uniform magnetic field", *Physical Review B*, vol. 56, no. 6, pp. 3325–3337, 1997 (page 28).

[112] B. H. Erne, K. Butter, B. W. M. Kuipers, and G. J. Vroege, "Rotational diffusion in iron ferrofluids", *Langmuir*, vol. 19, no. 20, 2003 (page 29).

[114] T. Yoshida, K. Ogawa, A. K. Bhuiya, K. Enpuku, U. Häfeli, W. Schütt, and M. Zborowski, "Nonlinear behavior of magnetic fluid in brownian relaxation", pp. 102–110, 2010 (page 32).

[115] S. Biederer, T. Sattel, T. Knopp, K. Lüdtke-Buzug, B. Gleich, J. Weizenecker, J. Borgert, and T. M. Buzug, "A spectrometer for magnetic particle imaging", vol. 22, pp. 2313–2316, (page 37).

[123] J. Jin, *Electromagnetic analysis and design in magnetic resonance imaging*. CRC Press, 1998 (page 39).

[124] V. Kuperman, *Magnetic resonance imaging: Physical principles and applications*. Academic Press, 2000 (page 39).

[125] D. I. Hoult, "The principle of reciprocity in signal strength calculations?a mathematical guide", *Concepts in Magnetic Resonance*, vol. 12, no. 4, pp. 173–187, 2000 (page 39).

[126] A. C. Fraser-Smith, *The magnetic field gradiometer*, Technical Report E723-1. Stanford University, 1983 (page 43).

[127] D. C. Meeker, *Finite element method magnetics*, 2006 (pages 44, 153).

[128] P. Ripka, "Electric current sensors: A review", *Measurement Science and Technology*, vol. 21, no. 11, p. 112 001, 2010 (page 45).

[129] J. A. Pettinga and J. Siersema, "A polyphase 500kA current measuring system with rogowski coils", *IEE Proceedings B, Electric Power Applications*, no. February, pp. 4–7, 1983 (page 45).

[130] V. Luckow, "Eine praxisorientierte Bestimmung der Nachweisgrenze", *Fresenius' Zeitschrift für Analytische Chemie*, vol. 303, no. 1, pp. 23–25, 1980 (page 49).

[131] F. Ludwig, A. Guillaume, M. Schilling, N. Frickel, and A. M. Schmidt, "Determination of core and hydrodynamic size distributions of cofe[sub 2]o[sub 4] nanoparticle suspensions using ac susceptibility measurements", *Journal of Applied Physics*, vol. 108, no. 3, p. 033 918, 2010 (pages 51, 54).

[132] M. Büttner, P. Weber, C. Lang, M. Röder, D. Schüler, P. Görnert, and P. Seidel, "Examination of magnetite nanoparticles utilising the temperature dependent magnetorelaxometry", *Journal of Magnetism and Magnetic Materials*, vol. 323, no. 9, pp. 1179–1184, 2011 (page 51).

[133] D. Eberbeck, C. Bergemann, F. Wiekhorst, U. Steinhoff, and L. Trahms, "Quantification of specific bindings of biomolecules by magnetorelaxometry", *Journal of Nanobiotechnology*, vol. 6, p. 4, 2008 (page 51).

[134] D. Eberbeck, F. Wiekhorst, U. Steinhoff, K. O. Schwarz, A. Kummrow, M. Kammel, J. Neukammer, and L. Trahms, "Specific binding of magnetic nanoparticle probes to platelets in whole blood detected by magnetorelaxometry", *Journal of Magnetism and Magnetic Materials*, vol. 321, no. 10, pp. 1617–1620, 2009 (page 51).

[135] D. Eberbeck, F. Wiekhorst, U. Steinhoff, and L. Trahms, "Quantification of biomolecule agglutination by magnetorelaxometry", *Applied Physics Letters*, vol. 95, no. 21, p. 213 701, 2009 (page 51).

[136] D. Eberbeck, C. Bergemann, S. Hartwig, U. Steinhoff, and L. Trahms, "Binding kinetics of magnetic nanoparticles on latex beads studied by magnetorelaxometry", *Applied Organometallic Chemistry*, vol. 18, no. 10, pp. 542–547, 2004 (page 51).

[137] N. L. Adolphi, D. L. Huber, H. C. Bryant, T. C. Monson, D. L. Fegan, J. Lim, J. E. Trujillo, T. E. Tessier, D. M. Lovato, K. S. Butler, P. P. Provencio, H. J. Hathaway, S. A. Majetich, R. S. Larson, and E. R. Flynn, "Characterization of single-core magnetite nanoparticles for magnetic imaging by squid relaxometry", *Physics in Medicine and Biology*, vol. 55, no. 19, pp. 5985–6003, 2010 (page 51).

[141] A. M. Rauwerdink, E. W. Hansen, and J. B. Weaver, "Nanoparticle temperature estimation in combined ac and dc magnetic fields", *Physics in Medicine and Biology*, vol. 54, no. 19, pp. L51–5, 2009 (page 51).

[142] Min-Cheol Kim, Do-Kyung Kim, Se-Hee Lee, M. S. Amin, Il-Han Park, Charn-Jung Kim, and M. Zahn, "Dynamic characteristics of superparamagnetic iron oxide nanoparticles in a viscous fluid under an external magnetic field", *IEEE Transactions on Magnetics*, vol. 42, no. 4, pp. 979–982, 2006 (page 51).

[144] D. M. Glover, W. J. Jenkins, and S. C. Doney, *Modeling methods for marine science.* Cambridge University Press, 2011 (page 55).

[145] P. C. Hansen, V. Pereyra, and G. Scherer, *Least squares data fitting with applications.* Johns Hopkins University Press, 2012 (page 55).

[146] G. H. Golub and C. F. V. Loan, *Matrix computations.* Johns Hopkins University Press, 2012 (page 55).

[147] C. T. Kelley, *Iterative methods for optimization*, ser. Frontiers in applied mathematics. Philadelphia, Pa.: Society for Industrial and Applied Mathematics, 1999, vol. 18 (page 55).

[148] A. Tarantola, *Inverse problem theory and methods for model parameter estimation.* Society for Industrial and Applied Mathematics, 2005 (page 55).

[149] K. Madsen, H. Bruun, and O. Tingleff, *Methods for non-linear least squares problems.* 1999 (page 55).

[150] A. P. Astalan, F. Ahrentorp, C. Johansson, K. Larsson, and A. Krozer, "Biomolecular reactions studied using changes in brownian rotation dynamics of magnetic particles", *Biosensors and Bioelectronics*, vol. 19, no. 8, pp. 945–951, 2004 (page 58).

[151] S.-H. Chung, A. Hoffmann, K. Guslienko, S. D. Bader, C. Liu, B. Kay, L. Makowski, and L. Chen, "Biological sensing with magnetic nanoparticles using brownian relaxation (invited)", *Journal of Applied Physics*, vol. 97, no. 10, 10R101, 2005 (page 58).

[152] K. Enpuku, K. Soejima, T. Nishimoto, H. Tokumitsu, H. Kuma, N. Hamasaki, and K. Yoshinaga, "Liquid phase immunoassay utilizing magnetic marker and high t[sub c] superconducting quantum interference device", *Journal of Applied Physics*, vol. 100, no. 5, p. 054 701, 2006 (page 58).

[153] K. Enpuku, T. Tanaka, T. Matsuda, F. Dang, N. Enomoto, J. Hojo, K. Yoshinaga, F. Ludwig, F. Ghaffari, E. Heim, and M. Schilling, "Properties of magnetic nanoparticles in the brownian relaxation range for liquid phase immunoassays", *Journal of Applied Physics*, vol. 102, no. 5, p. 054 901, 2007 (page 58).

[154] K. Enpuku, T. Tanaka, T. Matsuda, H. Kuma, N. Hamasaki, F. Dang, N. Enomoto, J. Hojo, K. Yoshinaga, F. Ludwig, F. Ghaffari, E. Heim, and M. Schilling, "Liquid phase immunoassay using magnetic markers and superconducting quantum interference device", *Japanese Journal of Applied Physics*, vol. 46, no. 11, pp. 7524–7529, 2007 (page 58).

[155] K. Enpuku, K. Soejima, T. Nishimoto, T. Matsuda, H. Tokumitsu, T. Tanaka, K. Yoshinaga, H. Kuma, and N. Hamasaki, "Biological immunoassays without bound/free separation utilizing magnetic marker and hts squid", *IEEE Transactions on Applied Superconductivity*, vol. 17, no. 2, pp. 816–819, 2007 (page 58).

[156] K. Enpuku, T. Tanaka, Y. Tamai, F. Dang, N. Enomoto, J. Hojo, H. Kanzaki, and N. Usuki, "Size distribution of magnetic marker estimated from AC susceptibility in solution for biosensor application", *Japanese Journal of Applied Physics*, vol. 47, no. 10, pp. 7859–7865, 2008 (page 58).

[157] K. Enpuku, T. Tanaka, Y. Tamai, and M. Matsuo, "AC susceptibility of magnetic markers in suspension for liquid phase immunoassay", *Journal of Magnetism and Magnetic Materials*, vol. 321, no. 10, pp. 1621–1624, 2009 (page 58).

[158] S. H. Chung, A. Hoffmann, S. D. Bader, C. Liu, B. Kay, L. Makowski, and L. Chen, "Biological sensors based on brownian relaxation of magnetic nanoparticles", *Applied Physics Letters*, vol. 85, no. 14, p. 2971, 2004 (page 58).

[159] N.-S. Cheng, "Formula for the viscosity of a glycerol−water mixture", *Industrial & Engineering Chemistry Research*, vol. 47, no. 9, pp. 3285–3288, 2008 (page 62).

[161] J. B. Weaver, M. Harding, A. M. Rauwerdink, and E. W. Hansen, "The effect of viscosity on the phase of the nanoparticle magnetization induced by a harmonic applied field", vol. 7626, R. C. Molthen and J. B. Weaver, Eds., p. 762 627, 2010 (page 66).

[162] J. B. Weaver and E. Kuehlert, "Measurement of magnetic nanoparticle relaxation time", *Medical Physics*, vol. 39, no. 5, pp. 2765–2770, 2012 (page 66).

[163] J. B. Weaver, A. M. Rauwerdink, and E. W. Hansen, "Magnetic nanoparticle temperature estimation", *Medical Physics*, vol. 36, no. 5, p. 1822, 2009 (page 66).

[164] J. B. Weaver and A. M. Rauwerdink, "Chemical binding affinity estimation using MSB", vol. 7965, J. B. Weaver and R. C. Molthen, Eds., 79650Y, 2011 (page 66).

[165] A. M. Rauwerdink and J. B. Weaver, "Measurement of molecular binding using the brownian motion of magnetic nanoparticle probes", *Applied Physics Letters*, vol. 96, no. 3, p. 033 702, 2010 (page 66).

[166] A. M. Rauwerdink and J. B. Weaver, "Viscous effects on nanoparticle magnetization harmonics", *Journal of Magnetism and Magnetic Materials*, vol. 322, no. 6, pp. 609–613, 2010 (page 66).

[167] T. Knopp, S. Biederer, T. Sattel, J. Weizenecker, B. Gleich, J. Borgert, and T. M. Buzug, "Trajectory analysis for magnetic particle imaging", *Physics in Medicine and Biology*, vol. 54, no. 2, pp. 385–397, 2009 (page 76).

[168] P. W. Goodwill and S. M. Conolly, "Experimental demonstration of x-space magnetic particle imaging", *Medical Imaging 2011: Biomedical Applications in Molecular, Structural, and Functional Imaging*, vol. 7965, J. B. Weaver and R. C. Molthen, Eds., 79650U, 2011 (page 82).

[169] K. Lu, P. Goodwill, B. Zheng, and S. Conolly, "The impact of filtering direct-feedthrough on the x-space theory of magnetic particle imaging", *Medical Imaging 2011: Biomedical Applications in Molecular, Structural, and Functional Imaging*, vol. 7965, J. B. Weaver and R. C. Molthen, Eds., p. 79652I, 2011 (page 82).

[170] P. W. Goodwill, K. Lu, B. Zheng, and S. M. Conolly, "An x-space magnetic particle imaging scanner", *Review of Scientific Instruments*, vol. 83, no. 3, p. 033 708, 2012 (pages 82, 130).

[173] J. Moser, "An empirical study of elf and vlf shield cans", *IEEE Transactions on Electromagnetic Compatibility*, vol. EMC-10, no. 1, pp. 112–125, 1968 (page 85).

[174] H. W. Ludwig, "Shielding effect of materials in the ulf, elf and vlf region", *International Journal of Biometeorology*, vol. 17, pp. 207–211, 1973 (page 85).

[175] S. Hidalgo-Tobon, "Theory of gradient coil design methods for magnetic resonance imaging", *Concepts Magn. Reson.*, vol. 36A, no. 4, pp. 223–242, 2010 (page 91).

[176] D. Brown, B.-M. Ma, and Z. Chen, "Developments in the processing and properties of NdFeb-type permanent magnets", *Journal of Magnetism and Magnetic Materials*, vol. 248, no. 3, pp. 432–440, 2002 (page 91).

[177] R. G. Medhurst, "HF resistance and self-capacitance of single-layer solenoids", *Wireless Engineer*, 1947 (page 92).

[178] C. R. Sullivan, "Optimal choice for number of strands in a litz-wire transformer winding", *IEEE Transactions on Power Electronics*, vol. 14, no. 2, pp. 283–291, 1999 (page 93).

[179] D. W. Knight, "The self-resonance and self-capacitance of solenoid coils", *G3YNH. info*, vol. 08, no. July, pp. 2006–2013, 2010 (page 93).

[180] J. Lammeraner and M. Štafl, *Eddy currents*. CRC Press, 1966 (page 93).

[181] D. C. Meeker, "An improved continuum skin and proximity effect model for hexagonally packed wires", *Journal of Computational and Applied Mathematics*, vol. 236, no. 18, pp. 4635–4644, 2012 (page 93).

[182] S. Tumanski, "Induction coil sensors – a review", *Measurement Science and Technology*, vol. 18, no. 3, R31–R46, 2007 (page 98).

[183] J. Wang, A. Reykowski, and J. Dickas, "Calculation of the signal-to-noise ratio for simple surface coils and arrays of coils", *IEEE Transactions on Bio-medical Engineering*, vol. 42, no. 9, pp. 908–917, 1995 (page 98).

[184] D. Belohrad and M. Kasal, “Saddle coil for MRI”, 2000 (page 98).

[185] Salmon, Carlos Ernesto Garrido, Vidoto, Edson Luiz Gea, M. J. Martins, and A. Tannús, “Optimization of saddle coils for magnetic resonance imaging”, *Brazilian Journal of Physics*, vol. 36, no. 1a, pp. 5–7, 2006 (page 98).

[186] B. H. Suits and A. N. Garroway, “Optimizing surface coils and the self-shielded gradiometer”, *Journal of Applied Physics*, vol. 94, no. 6, p. 4170, 2003 (page 98).

[187] G. Groenewold, “Optimal ladder filters”, *IEEE Transactions on Circuits and Systems II: Express Briefs*, vol. 56, no. 2, pp. 147–151, 2009 (page 100).

[188] A. Casson and E. Rodriguez-Villegas, “A review and modern approach to LC ladder synthesis”, *Journal of Low Power Electronics and Applications*, vol. 1, no. 3, pp. 20–44, 2011 (page 100).

[189] H. R. van Maanen, “Non-linear distortions in capacitors”, *124th Convention Audio Engineering Society*, 2008 (page 101).

[190] P. N. Murgatroyd and D. P. Eastaugh, “Optimum shapes for multilayered toroidal inductors”, *IEE Proceedings - Electric Power Applications*, vol. 147, no. 1, p. 75, 2000 (page 101).

[191] R. B. Hallgren, “Paralleled transconductance ultralow-noise preamplifier”, *Review of Scientific Instruments*, vol. 59, no. 9, p. 2070, 1988 (page 102).

[192] G. M. Gutt, J. S. Kim, M. R. Condron, J. M. Lockhart, and B. Muhlfelder, “An ultralow noise amplifier for superconductive detectors”, *Superconductor Science and Technology*, vol. 4, no. 11, pp. 633–636, 1991 (page 102).

[193] B. Neri, B. Pellegrini, and R. Saletti, “Ultra low-noise preamplifier for low-frequency noise measurements in electron devices”, *IEEE Transactions on Instrumentation and Measurement*, vol. 40, no. 1, pp. 2–6, 1991 (page 102).

[194] R. M. Fano, “Theoretical limitations on the broadband matching of arbitrary impedances”, *Journal of the Franklin Institute*, no. 41, 1950 (page 103).

[195] E. A. Faulkner, “The principles of impedance optimization and noise matching”, *Journal of Physics E: Scientific Instruments*, vol. 8, no. 7, pp. 533–540, 1975 (page 103).

[196] D. G. Lukoschus, “Optimization theory for induction-coil magnetometers at higher frequencies”, *IEEE Transactions on Geoscience Electronics*, no. 3, pp. 56–63, 1979 (page 103).

[197] T. Knopp, S. Biederer, T. F. Sattel, J. Rahmer, J. Weizenecker, B. Gleich, J. Borgert, and T. M. Buzug, “2D model-based reconstruction for magnetic particle imaging”, *Medical Physics*, vol. 37, no. 2, p. 485, 2010 (pages 106, 123).

[198] M. Gruettner, M. Graeser, S. Biederer, T. F. Sattel, H. Wojtczyk, W. Tenner, T. Knopp, B. Gleich, J. Borgert, and T. M. Buzug, "1D-image reconstruction for magnetic particle imaging using a hybrid system function", *2011 IEEE Nuclear Science Symposium Conference Record*, pp. 2545–2548, 2011 (pages 106, 116).

[199] A. Weber and T. Knopp, "Symmetries of the 2D magnetic particle imaging system matrix", *Physics in Medicine and Biology*, vol. 60, no. 10, 2015 (pages 115–116, 128).

[200] A. Weber and T. Knopp, "Reconstruction of the magnetic particle imaging system matrix using symmetries and compressed sensing", *Advances in Mathematical Physics*, vol. 2015, pp. 1–9, 2015 (page 115).

[204] C. Popa, "A hybrid kaczmarz–conjugate gradient algorithm for image reconstruction", *Mathematics and Computers in Simulation*, vol. 80, no. 12, pp. 2272–2285, 2010 (page 127).

[205] M. Hanke, *Iterative regularization techniques in image reconstruction*. 2000 (page 127).

[206] P. C. Hansen, "The discrete picard condition for discrete ill-posed problems", *BIT*, vol. 30, no. 4, pp. 658–672, 1990 (page 127).

[207] C. T. Kelley, *Iterative methods for linear and nonlinear equations*. Society for Industrial and Applied Mathematics, 1995 (page 127).

[208] F. Natterer and F. Wübbeling, *Mathematical methods in image reconstruction*, ser. SIAM monographs on mathematical modeling and computation. Philadelphia: Society for Industrial and Applied Mathematics, 2001 (page 127).

[209] C. Popa and R. Zdunek, "Kaczmarz extended algorithm for tomographic image reconstruction from limited-data", *Mathematics and Computers in Simulation*, vol. 65, no. 6, pp. 579–598, 2004 (page 127).

[210] C. Popa, "Constrained kaczmarz extended algorithm for image reconstruction", *Linear Algebra and its Applications*, vol. 429, no. 8-9, pp. 2247–2267, 2008 (page 127).

[211] T. Knopp, J. Rahmer, T. F. Sattel, S. Biederer, J. Weizenecker, B. Gleich, J. Borgert, and T. M. Buzug, "Weighted iterative reconstruction for magnetic particle imaging", *Physics in Medicine and Biology*, vol. 55, no. 6, pp. 1577–1589, 2010 (page 127).

[212] P. C. Hansen, "The truncatedSVD as a method for regularization", *BIT Springer Science*, vol. 27, no. 4, pp. 534–553, 1987 (page 127).

[213] T. Knopp, S. Biederer, T. Sattel, and T. M. Buzug, "Singular value analysis for magnetic particle imaging", *2008 IEEE Nuclear Science Symposium Conference Record*, pp. 4525–4529, 2008 (page 127).

[214] G. H. Golub and U. V. Matt, "Tikhonov regularization for large scale problems", *Scientific Computing: Proceedings of the Workshop*, 1998 (page 127).

[215] D. P. O'Leary, "Near-optimal parameters for tikhonov and other regularization methods", *SIAM Journal on Scientific Computing*, vol. 23, no. 4, pp. 1161–1171, 2001 (page 127).

[216] A. C. To, J. R. Moore, and S. D. Glaser, "Wavelet denoising techniques with applications to experimental geophysical data", *Signal Processing*, vol. 89, no. 2, pp. 144–160, 2009 (page 128).

[217] A. Jensen and A. la Cour-Harbo, *Ripples in mathematics*. Springer, 2001 (page 128).

[218] V. G. Stamatopoulos, D. A. Karras, and B. G. Mertzios, "On an efficient modification of singular value decomposition using independent component analysis for improved mrs denoising and quantification", *Measurement Science and Technology*, vol. 20, no. 10, p. 104 021, 2009 (page 128).

[219] J. Weizenecker, J. Borgert, and B. Gleich, "A simulation study on the resolution and sensitivity of magnetic particle imaging", *Physics in Medicine and Biology*, vol. 52, no. 21, pp. 6363–6374, 2007 (page 130).

[222] P. C. Fannin, Scaife, B. K. P., A. T. Giannitsis, and S. W. Charles, "Determination of the radius of nano-particles in a magnetic fluid by means of a constant frequency measurement technique", *Journal of Physics D: Applied Physics*, vol. 35, no. 12, pp. 1305–1310, 2002 (page 137).

[223] P. W. Goodwill, A. Tamrazian, L. R. Croft, C. D. Lu, E. M. Johnson, R. Pidaparthi, R. M. Ferguson, A. P. Khandhar, K. M. Krishnan, and S. M. Conolly, "Ferrohydrodynamic relaxometry for magnetic particle imaging", *Applied Physics Letters*, vol. 98, no. 26, p. 262 502, 2011 (page 145).

[224] L. R. Croft, P. W. Goodwill, and S. M. Conolly, "Relaxation in x-space magnetic particle imaging", *IEEE Transactions on Medical Imaging*, vol. 31, no. 12, pp. 2335–2342, 2012 (page 145).

[225] A. Tamrazian, P. Goodwill, L. R. Croft, R. Pidaparth, R. M. Ferguson, K. Krishnan, and S. Conolly, "X-space MPI relaxometry: Methods and initial data", *SPIE Medical Imaging 2011: Biomedical Applications in Molecular, Structural, and Functional Imaging*, vol. 7965, J. B. Weaver and R. C. Molthen, Eds., 79652K, 2011 (page 145).

Contributed Work

[26] F. Ludwig, T. Wawrzik, T. Yoshida, N. Gehrke, A. Briel, D. Eberbeck, and M. Schilling, "Optimization of magnetic nanoparticles for magnetic particle imaging", *IEEE Transactions on Magnetics*, vol. 48, no. 11, pp. 3780–3783, 2012 (pages 2, 24, 37).

[113] T. Wawrzik, T. Yoshida, M. Schilling, and F. Ludwig, "Debye-based frequency-domain magnetization model for magnetic nanoparticles in magnetic particle spectroscopy", *IEEE Transactions on Magnetics*, vol. 51, no. 2, p. 5 300 404, 2015 (pages 31, 33).

[116] F. Ludwig, T. Wawrzik, and M. Schilling, "Characterization of magnetic nanoparticles for magnetic particle imaging by magnetorelaxometry, AC susceptibility, magnetic particle spectroscopy and static magnetization measurements", *Springer Proceedings in Physics*, vol. 140, T. M. Buzug and J. Borgert, Eds., pp. 35–40, 2012 (page 37).

[117] T. Yoshida, K. Enpuku, F. Ludwig, J. Dieckhoff, T. Wawrzik, A. Lak, and M. Schilling, "Characterization of resovist nanoparticles for magnetic particle imaging", *Springer Proceedings in Physics*, vol. 140, T. M. Buzug and J. Borgert, Eds., pp. 3–7, 2012 (page 37).

[118] F. Ludwig, D. Eberbeck, N. Löwa, U. Steinhoff, T. Wawrzik, M. Schilling, and L. Trahms, "Characterization of magnetic nanoparticle systems with respect to their magnetic particle imaging performance", *Biomedizinische Technik*, vol. 58, no. 6, pp. 535–545, 2013 (page 37).

[119] F. Ludwig, C. Kuhlmann, T. Wawrzik, J. Dieckhoff, A. Lak, A. Kandhar, R. Ferguson, S. Kemp, and K. Krishnan, "Dynamic magnetic properties of optimized magnetic nanoparticles for magnetic particle imaging", *IEEE Transactions on Magnetics*, vol. 50, no. 11, 2014 (page 37).

[120] F. Ludwig, H. Remmer, C. Kuhlmann, T. Wawrzik, H. Arami, R. Ferguson, and K. Krishnan, "Self-consistent magnetic properties of magnetite tracers optimized for magnetic particle imaging measured by ac susceptometry, magnetorelaxometry and magnetic particle spectroscopy", *Journal of Magnetism and Magnetic Materials*, vol. 360, pp. 169–173, 2014 (page 37).

[121] N. Gehrke, D. Heinke, D. Eberbeck, F. Ludwig, T. Wawrzik, C. Kuhlmann, and A. Briel, "Magnetic characterization of clustered core magnetic nanoparticles for MPI", *IEEE Transactions on Magnetics*, vol. 51, no. 2, p. 5 300 204, 2015 (page 37).

[122] A. Lak, T. Wawrzik, F. Ludwig, and M. Schilling, "Synthesis of single-core iron oxide nanoparticles as a potential tracer for magnetic particle imaging", *Springer Proceedings in Physics*, vol. 140, T. M. Buzug and J. Borgert, Eds., pp. 91–95, 2012 (page 37).

[138] T. Wawrzik, J. Hahn, F. Ludwig, and M. Schilling, "Magnetic particle spectroscopy for the evaluation of field-dependent harmonics generation", *Magnetic Nanoparticles – Particle Science, Imaging Technology, and Clinical Applications, Proceedings of First International Workshop on Magnetic Particle Imaging*, T. M. Buzug, J. Borgert, T. Knopp, S. Biederer, T. F. Sattel, M. Erbe, and K. Lüdtke-Buzug, Eds., pp. 100–105, 2010 (page 51).

[139] T. Wawrzik, F. Ludwig, and M. Schilling, "Multivariate magnetic particle spectroscopy for magnetic nanoparticle characterization", *AIP Conference Proceedings*, vol. 1311, pp. 267–270, 2010 (page 51).

[140] T. Wawrzik, M. Schilling, and F. Ludwig, "Perspectives of magnetic particle spectroscopy for magnetic nanoparticle characterization", *Springer Proceedings in Physics*, vol. 140, T. M. Buzug and J. Borgert, Eds., pp. 41–45, 2012 (page 51).

[143] C. Kuhlmann, A. Khandhar, R. Ferguson, S. Kemp, T. Wawrzik, M. Schilling, K. Krishnan, and F. Ludwig, "Drive-field frequency dependent MPI performance of single-core magnetite nanoparticle tracers", *IEEE Transactions on Magnetics*, vol. 51, no. 2, 2015 (page 52).

[160] T. Wawrzik, C. Kuhlmann, H. Remmer, N. Gehrke, A. Briel, M. Schilling, and F. Ludwig, "Effect of brownian relaxation in frequency-dependent magnetic particle spectroscopy measurements", *2013 International Workshop on Magnetic Particle Imaging*, 2013 (page 64).

[171] C. Kuhlmann, T. Wawrzik, F. Ludwig, and M. Schilling, "A 3D MPI system for biological studies on mice", *2013 International Workshop on Magnetic Particle Imaging*, 2013 (page 82).

[172] M. Schilling, F. Ludwig, C. Kuhlmann, and T. Wawrzik, "Magnetic particle imaging scanner with 10-kHz drive-field frequency", *Biomedizinische Technik*, vol. 58, no. 6, pp. 557–563, 2013 (page 82).

[201] T. Wawrzik, C. Kuhlmann, F. Ludwig, and M. Schilling, "Scanner setup and reconstruction for three-dimensional magnetic particle imaging", *SPIE Medical Imaging 2013: Biomedical Applications in Molecular, Structural, and Functional Imaging*, vol. 8672, 2013 (page 116).

[202] T. Wawrzik, F. Ludwig, and M. Schilling, "Assembly for one-dimensional magnetic particle imaging", *IFMBE Proceedings*, vol. 25, no. 2, pp. 898–900, 2009 (page 124).

[203] T. Wawrzik, F. Ludwig, and M. Schilling, "Two-dimensional magnetic particle imaging", *Magnetic Nanoparticles – Particle Science, Imaging Technology, and Clinical Applications, Proceedings of First International Workshop on Magnetic Particle Imaging*, T. M. Buzug, J. Borgert, T. Knopp, S. Biederer, T. F. Sattel, M. Erbe, and K. Lüdtke-Buzug, Eds., pp. 100–105, 2010 (page 124).

[220] T. Wawrzik, F. Ludwig, and M. Schilling, "Magnetic particle imaging: Exploring particle mobility", *Springer Proceedings in Physics*, vol. 140, T. M. Buzug and J. Borgert, Eds., pp. 16–23, 2012 (page 137).

[221] T. Wawrzik, C. Kuhlmann, F. Ludwig, and M. Schilling, "Estimating particle mobility in MPI", *2013 International Workshop on Magnetic Particle Imaging*, 2013 (page 137).

Acknowledgements

Firstly, I would like to express my gratitude to my advisor **Prof. Meinhard Schilling** for his continuous support in study and research. And **Dr. Frank Ludwig** for his guidance and motivation. His mentorship was paramount in providing thoughts and experience in the field of magnetic nanoparticles. I am grateful for being allowed to work with such independence for the entire duration of my work.

Besides my advisors, I would like to thank the PhD committee: **Prof. Olaf Dössel** and **Prof. Erwin Peiner**.

Thank you to my fellow labmates for stimulating discussions, for sleepless nights before deadlines, and for the fun we had at work. Especially, **Erik Heim** for introduction to life as a student researcher at EMG, and **Alexander Hirsch** for tips and tricks and entertaining hours. **Christian Kuhlmann** (first as a master student and later) as a partner in the MPI project, for his open/sharp mind and his developer skills in electronics and engineering concepts. **Aidin Lak** for being a great roommate and distinguished materials specialist. **Hilke Remmer** as a long-year student and assistent in nanoparticle preparation and characterization. They have all become friends to my heart.

I would also like to thank all of the members of the research group at the "Institut für Elektrische Messtechnik und Grundlagen der Elektrotechnik" (EMG). The administrative staff at EMG (**G. Weise**, **G. Kurbach**, **K. Franke**, **T. Coenen**), the mechanical workshop (**H. Schmidt**, **J. Pförtner**, **H. Müller**) for making all the measuring setups a reality, and **Ralf Behme** for IT support.

For any project the partners and co-researches are a valueable source of inspiration. Therefore, I thank **Takashi Yoshida** for fruitful discussions and collabortation. I am also thanksful for discussions with other people in the field of MPI from Philips (**B. Gleich**, **I. Schmale**, **J. Rahmer**), Lübeck (**T. Knopp**, **M. Ahlborg**, **K. Gräfe**, **M. Erbe**), and Berkeley (**K. Lu**, **B. Zheng**, **P. Goodwill**).

Thanks to **Nicole Gehrke** at nanoPET Pharma GmbH for providing the materials (FeraSpin™ particles) for my research.

Thanks to the students, who contributed to the success of the MPI project with their theses: **Alexander Guillaume**, **Jan Hahn**, **Tobias Göhring**, **Sebastian Kallenbach**, **Christian Kuhlmann**, **Katharina Olze**, **Nele Petersen**, **Christian Jess**, **Camilo Ramirez**, **Daniel Schmidt**, **Felix Fürstenberger**, **Hilke Remmer**, **Sebastin Draack**, **Klaas Julian Janssen**, and **Yuhang Bao**.

Last but not the least, I would like to thank **my family**: My wife **Julia** and my son **Jonathan**, who had to live with an absent dad for quite some time.

This thesis is dedicated to my parents, which have been great and extraordinary supportive for my technical/scientific hobbies. All the training at home has been a good foundation for my engagement today, which finally culminates in this work.